8-26-2013 12:00 AM

Development and Assessment of an Impact Apparatus and High-Speed Camera Motion Tracking System to Quantify the Effect of Static Muscle Loads on Fracture Threshold Measures in the Distal Radius

Jacob M. Reeves
The University of Western Ontario

Supervisor
Dr. Cynthia Dunning
The University of Western Ontario

Graduate Program in Mechanical and Materials Engineering
A thesis submitted in partial fulfillment of the requirements for the degree in Master of Engineering Science

DEVELOPMENT AND ASSESSMENT OF AN IMPACT APPARATUS AND HIGH-SPEED CAMERA MOTION TRACKING SYSTEM TO QUANTIFY THE EFFECT OF STATIC MUSCLE LOADS ON FRACTURE THRESHOLD MEASURES IN THE DISTAL RADIUS

(Thesis Format: Integrated-Article)

by

Jacob M. Reeves

Graduate Program in Mechanical and Materials Engineering

A thesis submitted in partial fulfillment
of the requirements for the degree of
Master of Engineering Science

The School of Graduate and Postdoctoral Studies
Western University Canada
London, Ontario, Canada

ABSTRACT

Distal radius fractures are prevalent, debilitating, and costly. This thesis conducts an *in vitro* investigation of these injuries, examining the role of static muscle loading on fracture threshold measures (*i.e.*, force, impulse, energy). Initially, an impact apparatus and custom LabVIEW colour-thresholding program were designed and assessed for repeatability and accuracy in quantifying fracture measures and impact kinematics. These tools were then used to test six pairs of cadaveric forearms, with static muscle loads simulated in one specimen from each pair. Distal radius fractures were achieved in 5 pairs, with perilunate dislocations in the remaining pair. None of the fracture threshold measures assessed presented differences attributed to the muscle forces applied. With the appropriate impact apparatus and colour-thresholding techniques now developed and validated, future testing will examine the effects of higher muscle loads to determine if they may have an effect of the fracture threshold of the distal radius.

KEYWORDS:

Distal Radius Fracture, Fracture, Radius, Muscle Force, Perilunate Dislocation, Impact, Colour-Thresholding, Motion Tracking

CO-AUTHORSHIP

This thesis was a result of a collaborative effort. The work presented would not be possible without the assistance of others, whose efforts are documented here.

Chapter 1: Jacob Reeves – wrote manuscript; Timothy Burkhart – edited manuscript; Cynthia Dunning – edited manuscript

Chapter 2: Jacob Reeves – wrote manuscript, study design, apparatus design, data collection and analysis; Timothy Burkhart – edited manuscript, study design, data collection; Cynthia Dunning – edited manuscript, study design, apparatus design

Chapter 3: Jacob Reeves – wrote manuscript, study design, data collection and analysis, LabVIEW programming; Timothy Burkhart – edited manuscript, study design, data collection; Cynthia Dunning – edited manuscript, study design; Stewart McLachlin – LabVIEW programming; Yara Hosein – LabVIEW programming

Chapter 4: Jacob Reeves – wrote manuscript, study design, data collection and analysis; Timothy Burkhart – edited manuscript, study design, data collection and analysis; Cynthia Dunning – edited manuscript, study design; Masao Nishiwaki – Fracture classification, data analysis

Chapter 5: Jacob Reeves – wrote manuscript; Timothy Burkhart – edited manuscript; Cynthia Dunning – edited manuscript

ACKNOWLEDGMENTS

I would like to begin by thanking my supervisor Dr. Cynthia Dunning for providing me with the opportunity to join her laboratory, and for encouraging me to complete a Masters degree. Her continuous support, especially in times of failure, allowed me to see beyond the immediate, and to overcome the many obstacles I faced, beginning with my squeamish nature in the face of cadavers.

Without the daily guidance of Dr. Timothy Burkhart, this thesis would not have been possible. His insight into all-things wrist fracture was simply invaluable, as was his help throughout data collection, analysis and writing.

I would also like to thank Dr. Masao Nishiwaki for his clinical perspective and assistance with fracture classification. He provided a decisive understanding of the true clinical relevance of my work. Additionally, those at University Machine Services (in particular, Clayton Cook) were a pleasure to work with; without them my apparatus designs would have been bound to the paper on which they were conceived.

Moreover, I would like to thank my lab mates, Stewart McLachlin, Yara Hosein, Mark Neuert, Kristyn Leitch, and Sayward Fetterly, who made coming into work a pleasure and always provided a welcome work environment. They have all contributed to helping me through my project and making my graduate experience an exciting one.

Furthermore, this thesis would not have been possible without the external funding provided by the National Science and Engineering Research Council and the Ontario Graduate Scholarship Programs. I would like to thank these organizations for funding me from inspiration through to completion.

Finally, and most importantly, I would like to acknowledge my family and friends for supporting me throughout the past two years, both as an undergraduate and graduate student. You have all put up with my craziness at times, and have loved me all the same. If it weren't for the love and encouragement of my parents over the past 23 years, I would not have had the confidence to take on a degree in engineering, l*et al*one this endeavour. Thank you.

TABLE OF CONTENTS

LIST OF TABLES

LIST OF FIGURES

LIST OF APPENDICES

LIST OF ABREVIATIONS, SYMBOLS AND NOMENCLATURE

"	Inch
°	Degree
%	Percent
@	At
©	Copyright
®	Registered trademark
ε	Engineering strain
$\varepsilon_{1,2}$	Principal strains
$\mu\varepsilon$	Microstrain
ANOVA	Analysis of variance
AO	Arbeitsgemeinschaft für Osteosynthesefragen (Association for the Study of Internal Fixation)
AP	Anterior-posterior
CAD	Computer Aided Design
cm	Centimeter
DAQ	Data Acquisition System
DR	Digital Radiograph
ECU	Extensor Carpi Ulnaris
ECRL	Extensor Carpi Radialis Longus
EMG	Electromyography

FCR	Flexor Carpi Radialis
FCU	Flexor Carpi Ulnaris
F	Force
$\mathbf{F_r}$	Resultant force
$\mathbf{F_x}$	*x*-axis force
$\mathbf{F_y}$	*y*-axis force
$\mathbf{F_z}$	*z*-axis force
$\mathbf{f_c}$	Cutoff frequency
FEA	Finite Element Analysis
Hz	Hertz
ICC	Interclass Correlation Coefficient
$\mathbf{Im_r}$	Impulse arising from the resultant force
$\mathbf{Im_x}$	Impulse arising from force along the *x*-axis
$\mathbf{Im_y}$	Impulse arising from force along the *y*-axis
$\mathbf{Im_z}$	Impulse arising from force along the *z*-axis
J	Joule
kg	Kilogram
Lat	Lateral
m	Meter
M	Moment
mm	Millimetre

ms	Millisecond
$\mathbf{M_x}$	x-axis moment
$\mathbf{M_y}$	y-axis moment
N	Newton
NI	National Instruments
Nm	Newton-meter
Ns	Newton-second
ns	Nanosecond
Pa	Pascal
PCSA	Physiological Cross-Sectional Area
PPC	Proportional Pressure Controller
psi	pounds per square inch
PVC	polyvinyl chloride
R	Resistor
s	Second
$\mathbf{S_{AV}}$	Average of the agreement of individual subjects
SD	Standard Deviation
V	Volt

CHAPTER 1

INTRODUCTION

1.1 THE WRIST[1]

The wrist joint, specifically, the radiocarpal (radius, lunate and scaphoid) and distal radial ulnar joints (DRUJ) (Figure 1.1), is involved in performing essential activities of daily living (*e.g.*, lifting a glass, opening a door, getting dressed). Unfortunately, it is also commonly injured, with distal radius fractures being particularly prevalent.

1.2 DISTAL RADIUS FRACTURES

1.2.1 FRACTURE INCIDENCE

Distal radius fractures (*e.g.,* Smith's, Colles') are among the most prevalent fractures in the body (Shauver *et al*., 2011; Van Staa *et al*., 2001) with an incidence rate (22 per 10,000 person years) nearly twice that of femur/hip fractures and nearly five times the rate of vertebral/spine fractures (Van Staa *et al*., 2001). Smith's fractures commonly arise from falling on flexed wrists with the resulting fracture fragment displacing volarly, while the more common Colles' fractures arise from falling on extended wrists and involve a dorsally displaced fracture fragment (Figure 1.2). A recent review of fall video data (elderly population) has determined that the two most common causes of falls are weight shifts (41%) and trips/stumbles (*i.e.,* foot catching on an object) (21%), and the most common activity associated with falls is forward walking (24%) (Robinovitch *et al*., 2013).

Sport participation, the general workforce, and age have all been identified as risk factors in fall related distal radius fractures. For example, a prospective review of distal radius fractures found that 8 % occurred during sporting activities, with 50 % of those attributed to soccer (Lawson *et al*., 1995). With respect to the general workforce, distal radius

---

[1] Due to the multi-disciplinary nature of this study, the use of medical and anatomical terminology is required. To assist the reader a glossary of medical terms has been provided in Appendix A.

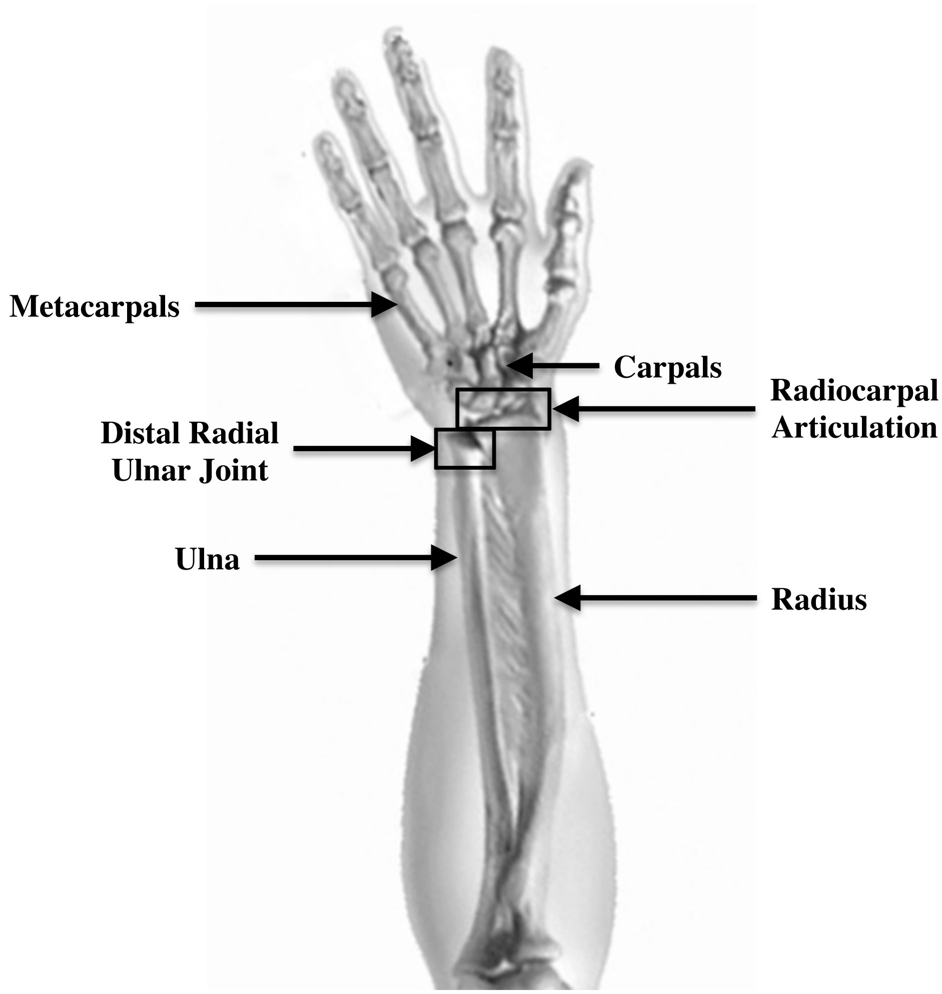

Figure 1.1: Wrist joint
A frontal view of the forearm in supination showing the volar surface of the wrist and the interaction of the bones that articulate to form the wrist joint (*adapted with permission from Tortora, 2011; Appendix B*).

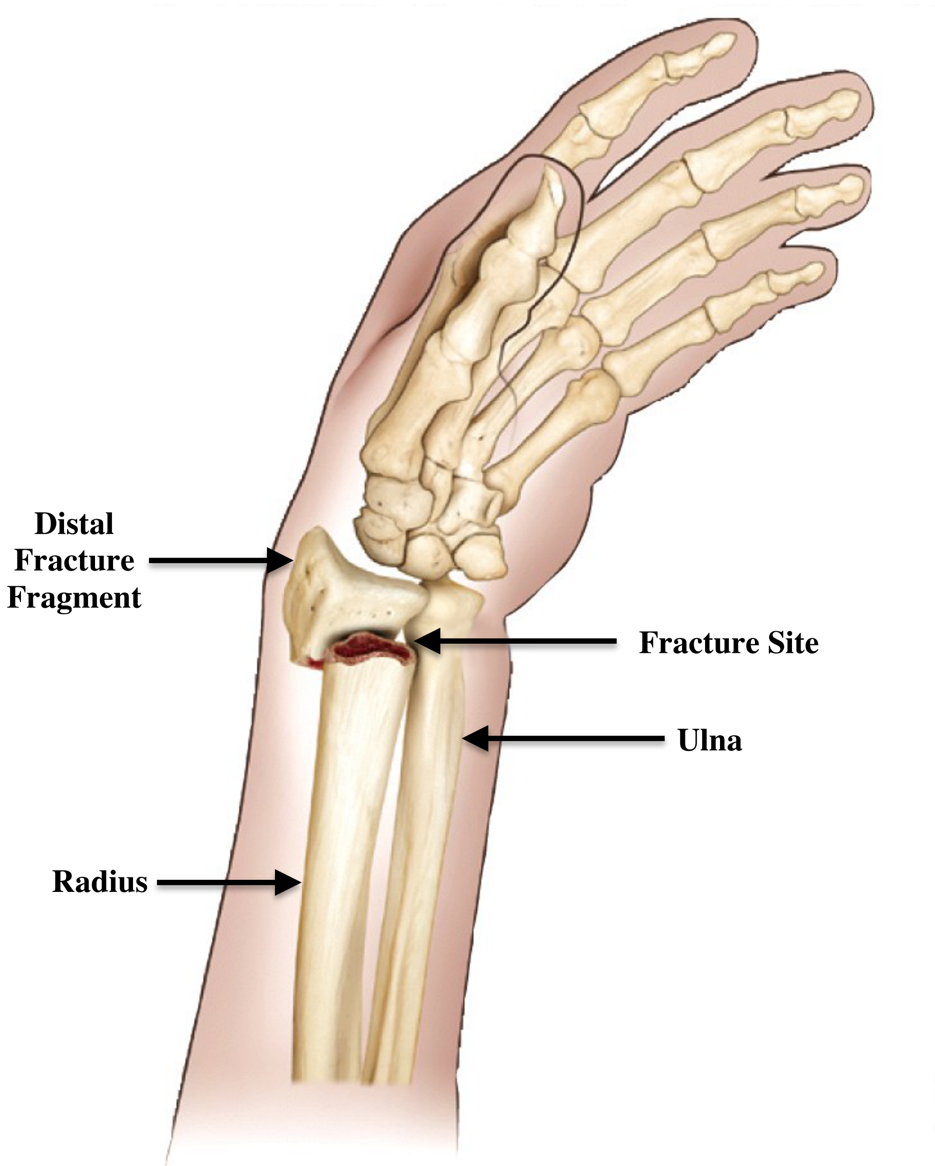

Figure 1.2: Distal radius fracture
Illustration of a Colles' fracture with dorsal displacement of the fracture fragment. Here, the metaphysis of the distal radius has been completely separated from the radial diaphysis (*adapted with permission from Tortora, 2011*).

fractures account for nearly 50 % of all fractures (Róbertsson *et al*., 1990), with manual labourers accounting for 17.6 % of hand and wrist injuries (Hill *et al*., 1998). These findings are further supported by The Workplace Safety and Insurance Board (WSIB), which found that falls were responsible for 22.8 % of all lost time injury claims, with the upper extremity identified as the injury site in 22.7 % of all cases, 18 % being non-specified fractures or sprains (Workplace Safety Insurance Board, 2002). Regarding age, there is a high incidence of distal radius fractures in children 0 – 16 years of age (due to skeletal under-development) (Hill *et al*., 1998; Mann and Rajmaira, 1990) as well as females (< 49 years of age) and males (< 85 years of age) later in life (as a result of decreases in bone density) (O'Neill *et al*., 2001). In fact, it has been estimated that 39 % of forward falls in the elderly (> 65 years of age) will result in a distal radius fracture (Nevitt and Cummings, 1993), with forward falls account for 60 % of elderly falls (O'Neill *et al*., 1994). Fracture incidence and severity have been shown to increase as bone cross sectional area and trabecular density decrease, thus explaining the effect of age. That is, failure load correlates strongly to cortical area (r = 0.7) and trabecular density (r = 0.6) (Lill *et al*., 2003; Myers *et al*., 1993).

1.2.2 ASSOCIATED COSTS

Assessments regarding the costs of distal radius fractures have demonstrated the financial burden that these injuries have on the economy (Gabriel *et al*., 2002; Kakarlapudi *et al*., 2000; Ray *et al*., 1997; Shauver *et al*., 2011). Shauver *et al*. (2011) and Gabriel *et al*. (2002) reported the costs to the affected individual to be approximately $2000 USD per incident, accounting for more than $170 million USD in direct healthcare per year. Furthermore, the costs of forearm fractures attributed to osteoporosis are estimated at $627.8 USD million dollars (Ray *et al*., 1997), 90% of which is due to patient services (*e.g.,* health services) while the remaining 10% is attributed to product consumption (*e.g*., fixation plates) (Kakarlapudi *et al*., 2000). Reducing the incidence can lead to an overall decrease in the economic burden of this injury, as a reduction in the prevalence of distal radius fractures will reduce costs to both patient services and product consumption.

1.2.3 FRACTURE CLASSIFICATION AND TREATMENT

Fracture classification is meant to provide guidance in determining appropriate prognosis and treatment of distal radius fractures (Illarramendi *et al*., 1998). While many distal radius fracture classification systems exist, two of the most common are the Frykman (Frykman, 1967) and Arbeitsgemeinschaft für Osteosynthesefragen (AO) (Muller *et al*., 1990). While the Frykman system is a useful method for fracture classification (Illarramendi *et al*., 1998), the AO system has demonstrated better accuracy and repeatability across experience levels (novices to experienced orthopaedic surgeons) (Lill *et al*., 2003). The AO system (Figure 1.3) allows the observer to separate fractures into three broad categories and subsequently into specific groupings. The initial classification is dependent on the involvement of the radiocarpal articulation such that, A = extra-articular; B = partially articular; and C = completely articular (Henry, 2008; Muller *et al*., 1990). From here, subdivision provides more detail about the fracture, taking into consideration fragment size and degree of comminution (Figure 1.3). Studies have shown that the AO classification can be applied (using anterior-posterior and lateral radiographs) with fair (S_{av} = 0.33) to substantial (S_{av} = 0.68) inter-observer reproducibility, and fair (S_{av} = 0.40) to near perfect (S_{av} = 0.86) intra-observer reproducibility (Kreder *et al*., 1996b).

Despite the long recognition of distal radius fractures as a prominent injury, (Colles, 1814), there is no widespread consensus regarding the proper treatment of these fractures (Colles, 1814; Henry, 2008). In many cases, surgery is required to correct the deformity, but due to the variety of fracture patterns, surgeon bias and patient characteristics, it is often difficult to determine the optimal method of repair (Henry, 2008). For example, stable, low-energy distal radius fractures can often be treated non-surgically (*e.g.,* casting and immobilization) while high-energy fractures frequently require surgical intervention. Some of the most common surgical techniques include: external fixation (*e.g.*, an articular spanning device), internal fragment fixation (*e.g.*, percutaneous pinning), and various plating techniques (*e.g.*, volar fixed angle plate) (Henry, 2008).

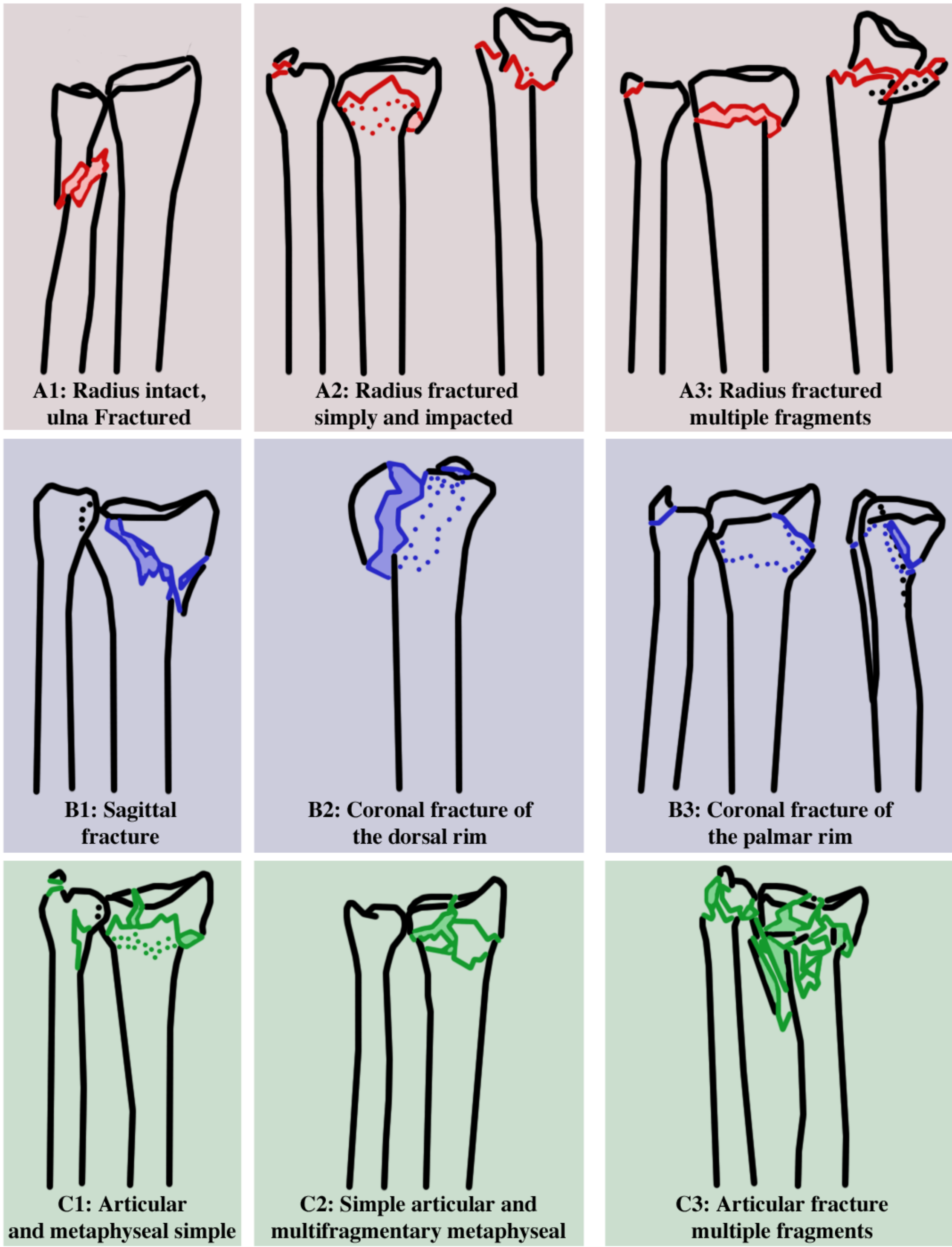

Figure 1.3: AO classification of distal radius and ulna fractures
The AO fracture classification system, where red is extra-articular (A), blue is partial articular (B), and green is complete articular (C). Regardless of severity, fractures become more involved moving from 1 to 3 (adapted from Muller, *et al*. 2007).

1.2.4 COMPLICATIONS

Although generally non-life-threatening, these injuries can lead to long-term deformity and pain for the affected individuals (Altissimi *et al*., 1986; MacDermid *et al*., 2003). McDermind *et al*. (2003) found (using the Patient-rated Wrist Evaluation) that short-term pain and discomfort persist for two to six months following a distal radius fracture. In addition to these short-term effects, median nerve compression can lead to permanent loss of sensation and has been reported as having a 20 % incidence associated with distal radius fractures (Henry, 2008). Furthermore, Altissimi, *et al*. (1986) (using a modified Gartland and Werner demerit point system) reported that 13 % of patients demonstrated fair to poor long-term results over one to six years following a distal radius fracture (Altissimi *et al*., 1986). Knirk and Jupiter (1986) found that 65 % of patients with inter-articular damage arising from a distal radius fracture went on to develop post-traumatic arthritis. The high incidence of distal radius fractures in combination with the poor outcomes have contributed to the World Health Organization listing fracture prevention among its health care priorities (Fardellone, 2008).

1.3 ANATOMY OF THE WRIST

Motion and stability of the wrist are provided through the complex interaction of bones, ligaments and musculotendinous units.

1.3.1 BONES OF THE WRIST

Bone, as a structure, can be divided into two types: cancellous and cortical. Cancellous bone can be described as sponge-like, and makes up the interior structure of bones such as the vertebra, carpals and the radius. Cortical bone on the other hand, is much harder and can primarily be thought of as a continuous solid, forming the outer layer of bones (see McKinley and O'Loughlin, 2006a).

The radius, when viewed in the anatomical position (standing straight with arms by the side, palms facing forward), is located on the lateral aspect of the forearm (Figure 1.4). Proximally, it articulates with the capitulum of the humerus and the radial notch of the

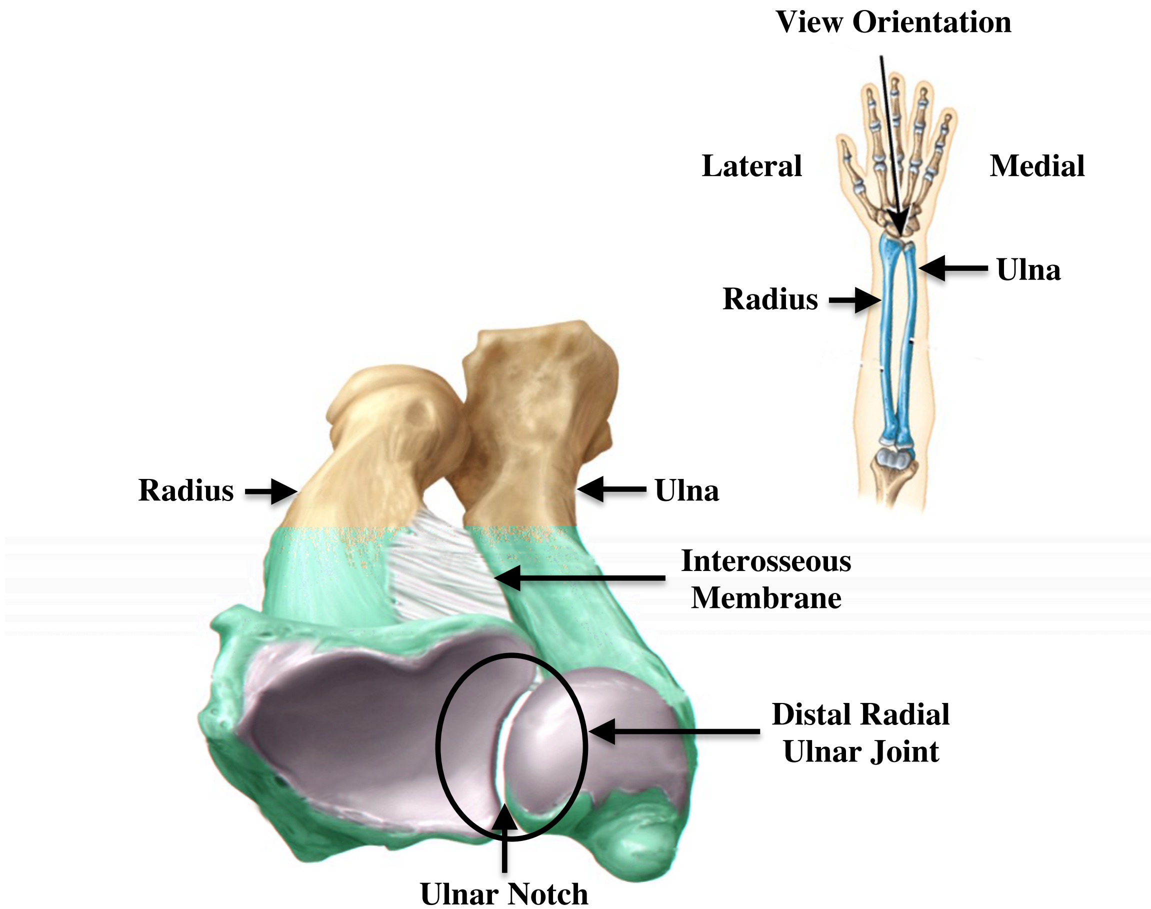

Figure 1.4: Radius and ulna
An axial view of the radius and ulna showing the interosseous membrane and the distal radial ulnar joint (*adapted with permission from Tortora, 2011*).

ulna, while the distal end interacts with both the scaphoid and lunate of the carpals. The distal-lateral portion of the radius comes to a prominence, known as the radial styloid, which aids in the capsulation of the radiocarpal articulation. Research has shown that the radiocarpal joint can bear anywhere from 63 % - 87 % of the load passing through the wrist (Berger, 1996), subjecting it to the majority of loads that travel from the hand to the elbow. In addition to carpal articulation, the distal-medial aspect of the radius (sigmoid fossa) contacts the distal-lateral surface of the ulna (ulnar notch) to form the DRUJ (McKinley and O'Loughlin, 2006b). The connection between the radius and ulna is further supported by the interosseous membrane (IOM), a ligamentous structure that runs between the radius and ulna beginning near the radius' dorsal insertion of abductor pollicis longus and is approximately 10.6 cm in length (McKinley and O'Loughlin, 2006b; Skahen *et al*., 1997). This aids in load transfer by way of the radius and ulna, such that load share is approximately 51 % - 70 % in favor of the radius at the elbow (Birkbeck *et al*., 1997).

The carpals are small irregularly shaped bones that contribute to the structure of the hand. There are a total of eight carpal bones in each hand, stabilized by ligamentous connections. It is through the planar joints between the carpal bones that gliding and pivoting motions of the wrist are permitted (Figure 1.5) (McKinley and O'Loughlin, 2006a).

1.3.2 LIGAMENTS OF THE WRIST

Providing passive stabilization to the radiocarpal articulation are six ligaments: the radioscaphocapitate, the long radiolunate, the short radiolunate, the dorsal radiocarpal, the dorsal radial metaphyseal arcuate and the scapholunate (Berger, 1996). Each of these ligaments attaches to the radius proximally and to the carpals distally (Figure 1.6), forming part of the palmer and the entire radial radiocarpal joint capsule (Berger, 2001). Additionally, the dorsal radioulnar and the dorsal radial metaphyseal arcuate ligaments are the primary supporters of the DRUJ (Figure 1.6B).

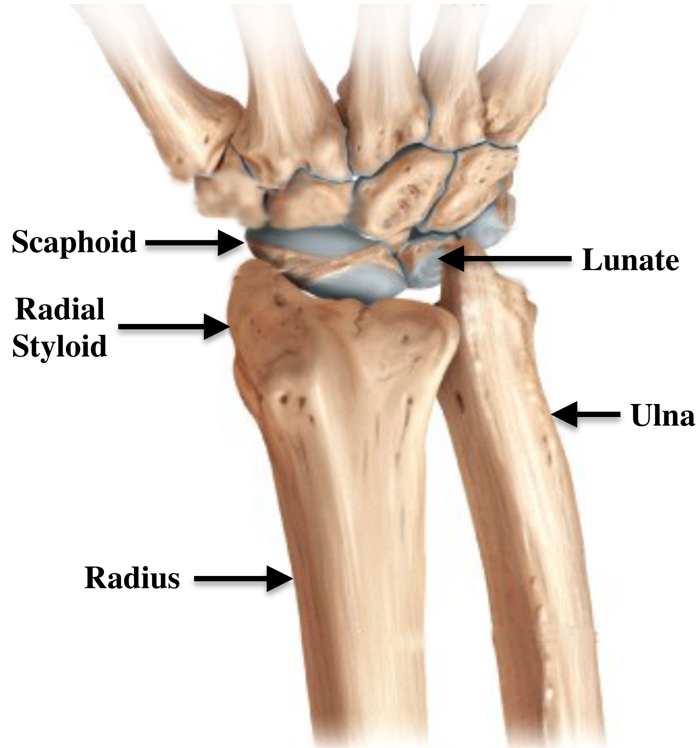

Figure 1.5: Radiocarpal articulation
A dorsal view of the bones that form the radial-carpal articulation, where the radius comes into contact with the scaphoid and lunate (*adapted with permission from Tortora, 2011*).

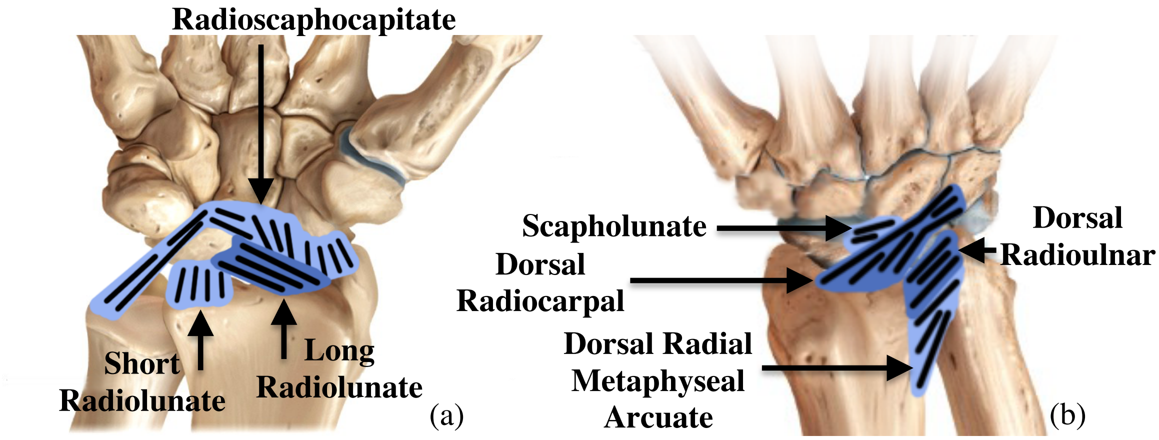

Figure 1.6: Ligaments of the wrist
Depiction of the palmar (a) and dorsal (b) ligaments that passively stabilize the radiocarpal articulation and the DRUJ (*adapted with permission from Tortora, 2011*).

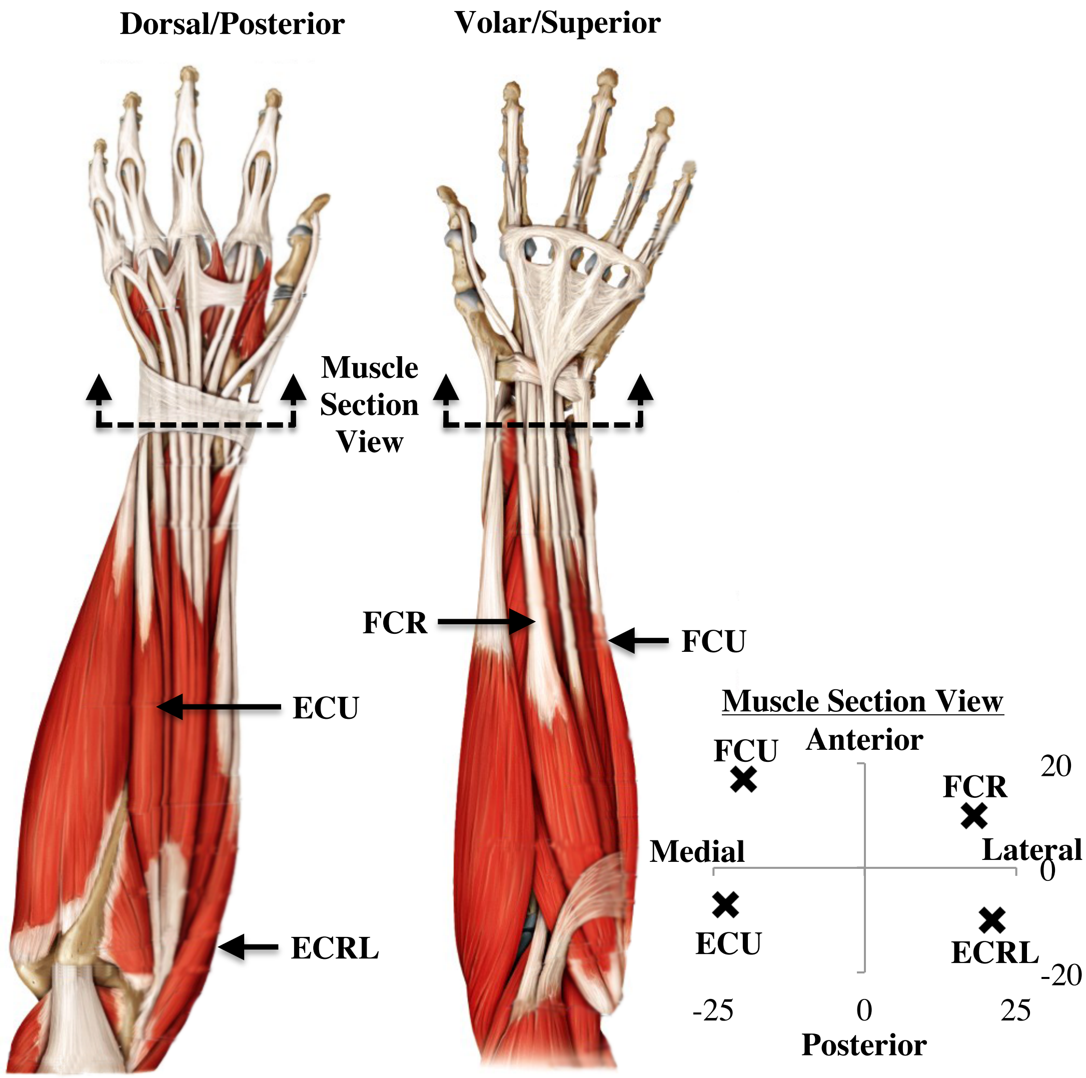

Figure 1.7: Principle flexor and extensor tendons of the wrist
An illustration showing the primary musculotendinous units responsible for wrist flexion, extension, and radial and ulnar deviation; with a depiction of muscle position [mm] at wrist cross-section as per Amis *et al* (1979) (*adapted with permission from Tortora, 2011*).

1.3.3 MUSCULOTENDINOUS UNITS OF THE WRIST

There are a total of 15 musculotendinous units that contribute to the motion of the wrist, with four of particular interest to the present work. Specifically, wrist flexion is achieved through the contraction of flexor carpi ulnaris (FCU) and flexor carpi radialis (FCR), while wrist extension is principally achieved through extensor carpi ulnaris (ECU) and extensor carpi radialis longus (ECRL) (Figure 1.7). These forces have lines of action that are offset from the bone surfaces in the medial-lateral and anterior-posterior axis to create bending moments, which lead to motion (Figure 1.7) (Amis *et al.*, 1979). When acting individually, FCU and ECU cause ulnar deviation, while FCR and ECRL cause radial deviation. Flexion is achieved through FCU and FCR, while extension relies on ECU and ECRL.

The force produced by a muscle is a function of many variables, such as the muscle's contraction length, contraction velocity, physiologic cross-sectional area (pCSA), pennation angle and level of activation (Fukunaga *et al.*, 1997). Through the use of pCSA and specific tension alone, Holzbaur *et al.* (2005) determined the peak forces that can be produced (regardless of activation level) by FCU, FCR, ECU and ECRL to be 128.9 N, 74.0 N, 93.2 N and 304.9 N, respectively.

1.3.4 MOTIONS OF THE WRIST

The radiocarpal joint and the DRUJ permit the range of motion required for the execution of various activities (Figure 1.8) (Berger, 1996; Boone and Azen, 1979; King *et al.*, 1986; Palmer *et al.*, 1985; Panero and Zelnik, 1979; Tilley, 2002). The radiocarpal articulation permits wrist flexion and extension, as well as radial and ulnar deviations, while pronation and supination are principally achieved through the articulation of the DRUJ (in combination with a similar joint at the elbow, called the PRUJ). When simplified, the wrist acts as a universal joint where radial and ulnar deviations combine with extension and flexion to create circumduction (Berger, 1996).

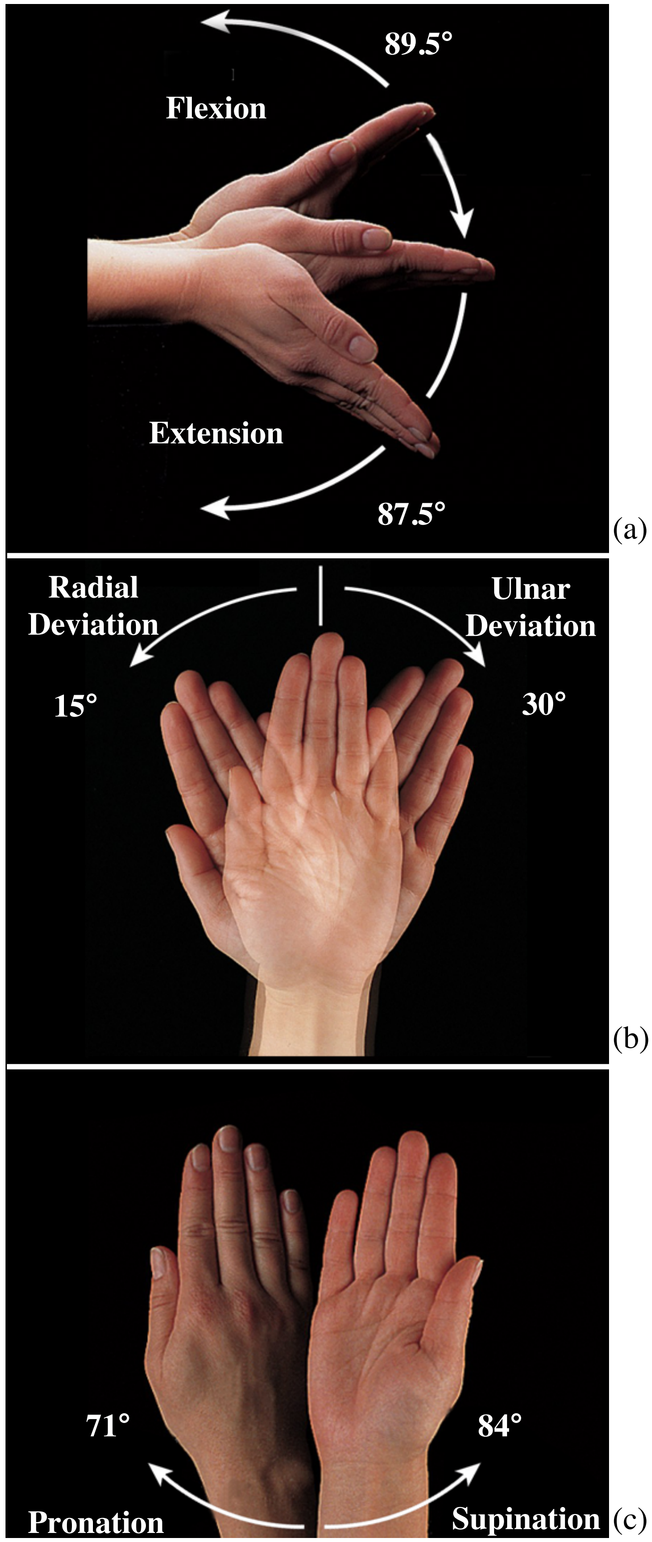

Figure 1.8: Motions about the wrist

Flexion/extension (a), radial/ulnar deviation (b) are motions that occur about the radial carpal joint, while pronation/supination (c) occurs through the articulation of the DRUJ (*adapted with permission from Tortora, 2011*).

1.4 UPPER EXTREMITY IMPACT BIOMECHANICS

1.4.1 IN VIVO TESTING

There is a relatively large body of *in vivo* research focused on quantifying the biomechanics of upper extremity impacts following a forward fall. In an attempt to control the research environment, many studies have investigated participants who fall from either an expected (DeGoede *et al*., 2001; DeGoede and Ashton-Miller, 2002; Dietz *et al*., 1981; Groen *et al*., 2010; Hernandez *et al*., 2013; Lo *et al*., 2003; Troy and Grabiner, 2007a) or unexpected (Hsiao and Robinovitch, 1998; Kim and Brunt, 2013; Kim and Ashton-Miller, 2003; Wojcik *et al*., 1999) state. While studies such as these initiate falls from a static position (*i.e*., the participant is standing still, not walking), more recent studies have accounted for the dynamic nature of *in vivo* forward falls by simulating participant motion prior to fall initiation (Burkhart and Andrews, 2010; Burkhart and Andrews, 2013; Grabiner *et al*., 2008; Robinovitch *et al*., 2013; Robitaille *et al*., 2005; Troy and Grabiner, 2007a; Troy *et al*., 2008).

When a fall occurs, the muscles display a preparatory response that is thought to have an effect on injury, possibly explaining the ability of younger (mean age 24.1 years) adults to react to and arrest falls quicker than their older (mean age 66.4 years) counterparts (Kim and Ashton-Miller, 2003). Through the use of electromyography (EMG), this preparatory response has been documented to plateau prior to peak impact forces in both statically (Dietz *et al*., 1981) and dynamically (Burkhart and Andrews, 2013) initiated forward falls. Specifically, mean (SD) contractions of ECU and FCU were found to be 40 (20) % and 17 (10) % of maximum voluntary muscle contraction, respectively (Burkhart and Andrews, 2013).

In addition, some studies have also demonstrated the importance of upper extremity posture during a forward fall. In particular, it has been noted that participants can self-select a fall arrest posture that significantly reduces peak impact forces compared to natural (168° elbow flexion) and straight-armed falls (174° elbow flexion) by 27 % and 40 % respectively (DeGoede and Ashton-Miller, 2002). Moreover, it has been shown that elbow posture affects peak elbow acceleration magnitude and direction, but has little effect on wrist accelerations during impact (Burkhart and Andrews, 2010). Accordingly, forearm positioning during forward falls is quite subjective and the orientation of the forearm at impact can affect the likelihood of injury.

While dynamically initiated forward fall studies overcome the static nature of previous work, they are not without limitations. Overall, the most evident limitations in any form of *in vivo* fall analyses are the low height from which the fall is initiated (to avoid participant injury), and the fact that the resulting impact is sub-fracture. To address these limitations it is often necessary to rely on alternative research methods (*e.g.*, cadaveric or *in vitro* testing) when studying the injury mechanisms related to distal radius fractures.

1.4.2 IN VITRO TESTING

In vitro research has produced distal radius fractures in an attempt to quantify the mechanisms of this injury. Overall, these studies have been performed under quasi-static or dynamic loading and have simulated either axial (parallel with the long axis of the specimen) (Duma *et al.*, 2003; Horsman and Currey, 1983; Lewis *et al.*, 1997; Lill *et al.*, 2003; Moore *et al.*, 1997; Spadaro *et al.*, 1994; Troy and Grabiner, 2007b) or off-axis (at an angle to the long axis of the specimen) (Augat *et al.*, 1996; Augat *et al.*, 1998; Burkhart *et al.*, 2012b; Burkhart *et al.*, 2011; Giacobetti *et al.*, 1997; Greenwald *et al.*, 1998; Lubahn *et al.*, 2005; McGrady *et al.*, 2001; Myers *et al.*, 1991; Myers *et al.*, 1993; Staebler *et al.*, 1999; Troy and Grabiner, 2007b) load conditions (Table 1.1). With these variations in testing approaches, it is not surprising that a range of fracture forces (1104 N to 3986 N), impulses (14.2 Ns to 82 Ns) and energies (1.09 J to 362 J) to failure have been reported (Table 1.2).

To date, the majority of *in vitro* studies have used quasi-static testing (Augat *et al.*, 1996; Augat *et al.*, 1998; Giacobetti *et al.*, 1997; Horsman and Currey, 1983; Lill *et al.*, 2003; Myers *et al.*, 1991; Myers *et al.*, 1993; Spadaro *et al.*, 1994; Staebler *et al.*, 1999; Wigderowitz *et al.*, 2000; Wu *et al.*, 2000) employing load rates (0.42 to 75 mm/s) lower than what would occur during a forward fall, which has been reported to be approximately 1.5 (0.4) m/s (Burkhart and Andrews, 2013). The majority of these studies correlated fracture forces to distal radius material (*e.g.*, bone mineral density, bone

Table 1.1: Specimen positioning of previous distal radius fracture work.

Author (Year)	Wrist Position	Radial Deviations	Forearm Rotation
General Forward Fall Studies			
Augat *et al* (1996)	Neutral	0°	Neutral
Augat *et al* (1998)	Neutral and Extension (45°)	10°	Neutral
Horsman *et al* (1983)	Neutral	0°	Neutral
Lill *et al* (2003)	Extension (70°)	10°	Pronation (10°)
Myers *et al* (1993)	Extension (75°)	10°	Neutral
Myers *et al* (1991)	Extension (75°)	10°	Neutral
Spadaro *et al* (1994)	Extension (90°)	7°	Neutral
Lubhan *et al* (2005)	Extension (55-75°)	0°	Pronation (Near Complete)
Burkhart *et al* (2011)	Extension (45°)	0°	Neutral
Burkhart *et al* (2012)	Extension (45°)	0°	Neutral
Duma *et al* (2003)	Extension (55 - 62°)	0°	Neutral
Wrist Guard Studies			
Giacobetti *et al* (1997)	Neutral	10°	Pronation (Full)
Staebler *et al* (1999)	Extension (30°)	0°	Pronation (Full)
Greenwald *et al* (1998)	Extension (40°)	0°	Pronation (10°)
Lewis *et al* (1997)	Extension (60-70°)	0°	Neutral
McGrady *et al* (2001)	Extension (30°)	0°	Neutral
Moore *et al* (1997)	Extension (75°)	0°	Neutral

Table 1.2: Mean (SD) reported distal radius fracture forces, impulses and energies.

Author (Year)	Force [N]	Impulse [Ns]	Energy [J]
General Forward Fall Studies			
Augat *et al* (1996)	F: 2008 (913) M: 3773 (1573)	-	F: 1.09 (0.61) M: 2.85 (1.51)
Augat *et al* (1998)	2648 (1489)	-	-
Horsman *et al* (1983)	3600 (1160)	-	-
Lill *et al* (2003)	1630 (860)	-	-
Myers *et al* (1993)	1780 (650)	-	-
Myers *et al* (1991)	3390 (877)	-	-
Spadaro *et al* (1994)	1640 (980)	-	13.2 (10.7)
Lubhan *et al* (2005)	O: 2920 (1197.7) A: 3986 (1991.8)	-	O: 362 (73.1) A: 112 (15.2)
Burkhart *et al* (2012)	2142 (1229)	14.2 (5.5)	45.5 (16)
Duma *et al* (2003)	2820 (1206)	19.9 (8.7)	-
Troy *et al* (2007)	A: 2752 – 2830 O: 1448 – 1521	-	-
Wrist Guard Studies			
Giacobetti *et al* (1997)	G: 2245 (1470 - 4116) N: 2285 (1152 - 4214)	-	-
Greenwald *et al* (1998)	G: 3808 (271) N: 2821 (763)	G: 28 (5) N: 17 (11)	-
Lewis *et al* (1997)	-	G: 176 N: 82	G: 105 (50-145) N: 82 (47-120)
McGrady *et al* (2001)	G: 1082 (168) N: 1104 (119)	G: 42.50 (3.86) N: 38.96 (2.71)	-

F = female; M = male; O = Off-axis; A = Axial; G = Wrist guard; N = No wrist guard mineral content) or geometric properties (*e.g.*, bone cross-sectional area, moment of inertia) (Augat *et al.*, 1996; Augat *et al.*, 1998; Horsman and Currey, 1983; Lill *et al.*, 2003; Myers *et al.*, 1991; Myers *et al.*, 1993; Spadaro *et al.*, 1994). In general, the absence of a consensus regarding the relationship between fracture force and material properties, suggests that geometric properties may be better predictors of distal radius fracture strength (Augat *et al.*, 1996; Augat *et al.*, 1998; Horsman and Currey, 1983; Lill *et al.*, 2003; Myers *et al.*, 1991; Myers *et al.*, 1993; Spadaro *et al.*, 1994).

In an attempt to more accurately represent the *in vivo* conditions that result in a distal radius fracture, dynamic *in vitro* studies have been performed (Burkhart *et al.*, 2012b; Burkhart *et al.*, 2013; Burkhart *et al.*, 2011; Duma *et al.*, 2003; Lubahn *et al.*, 2005). These studies have provided some insight into variations present between off-axis and axial loading of the distal radius, from which it is seen that axial loading (Duma *et al.*, 2003; Horsman and Currey, 1983; Lill *et al.*, 2003; Lubahn *et al.*, 2005; Spadaro *et al.*, 1994) results in a greater mean fracture force (2735 N) compared to off axis loading (2460 N) (Augat *et al.*, 1996; Augat *et al.*, 1998; Burkhart *et al.*, 2012b; Giacobetti *et al.*, 1997; Greenwald *et al.*, 1998; Lubahn *et al.*, 2005; McGrady *et al.*, 2001; Myers *et al.*, 1991; Myers *et al.*, 1993). Furthermore, it has also been shown that wrist guards can increase the mean fracture force of the distal radius from 2070 N to 2378 N (Giacobetti *et al.*, 1997; Greenwald *et al.*, 1998; McGrady *et al.*, 2001). Dynamic *in vitro* testing has also been used to measure distal radius strain in response to impact loading. Through the use of bone-mounted strain gauges, Burkhart *et al* (2012a) reported that compressive radial strain was consistently higher on the dorsal-medial surface during loading, providing a possible explanation for why distal radius fractures are often accompanied by ulnar involvement (Burkhart *et al.*, 2012b; May *et al.*, 2002). Finally, using dynamic impact loading, functions to predict radius fracture risk have been established (Burkhart *et al.*, 2013; Duma *et al.*, 2003). Burkhart *et al.* (2013) found that injury prediction was improved with the inclusion of velocity and impulse terms from multiple axes when compared to force-only (Duma *et al*, 2003) injury prediction models ($R^2 = 0.84$ vs. $R^2 = 0.29$). This highlights the importance of simulating *in vitro* distal radius fractures in a dynamic fashion with a controlled loading direction, including the use of bone-strain gauges in the experimental approach, and measuring multi-directional force components.

While both quasi-static and dynamic *in vitro* distal radius fracture work overcomes some of the limitations of *in vivo* fall studies, they are not without their own limitations. With the exception of Burkhart *et al*. (2012), previous studies have only reported a subset of the three classical fracture measures (force, impulse and energy). Additionally, many studies have not used a formal classification system that would allow for an evaluation of the relationship between fracture measures and the severity of the fracture patterns produced (Augat *et al*., 1996; Duma *et al*., 2003; Horsman and Currey, 1983; McGrady *et al*., 2001; Myers *et al*., 1993; Staebler *et al*., 1999; Troy and Grabiner, 2007b). Furthermore, while McGrady, *et al*. (2001) simulated muscle forces for the purpose of wrist extension, the magnitude of these forces was not reported, and no previous investigations have specifically investigated the effect of anatomically relevant muscle loading on the fracture threshold in the distal radius. Moreover, dynamic studies must be careful not to simulate fracture loads well in excess of the specimen's threshold, to avoid clinically-irrelevant fracture patterns. One-way by which studies have addressed this is through incremental loading, but balanced with the need to avoiding repetitive damage through multiple impacts (Burkhart *et al*., 2012b; Lewis *et al*., 1997). Therefore, future *in vitro* simulation of distal radius fractures should implement systematic dynamic loading, report all of the major fracture measures, use a clinically relevant fracture classification system, and investigate the role that muscle forces have on distal radius fractures.

1.5 APPARATUS DESIGN

As no standardized methodology for the simulation of distal radius fractures (or lower extremities, by comparison) has been established, testing has been conducted using a variety of apparatuses (Tables 1.3 and 1.4). These include materials testing machines (Augat *et al*., 1996; Augat *et al*., 1998; Giacobetti *et al*., 1997; Horsman and Currey, 1983; Lill *et al*., 2003; Myers *et al*., 1991; Myers *et al*., 1993; Spadaro *et al*., 1994; Staebler *et al*., 1999), drop towers (Greenwald *et al*., 1998; Lewis *et al*., 1997; Lubahn *et al*., 2005; McGrady *et al*., 2001; Moore *et al*., 1997), pendulum impactors (Funk *et al*., 2002; Owen and Lowne, 2001; Yoganandan *et al*., 1996; Yoganandan *et al*., 1997), and pneumatic impactors (Burkhart *et al*., 2012b; Burkhart *et al*., 2011; Duma *et al*., 2003; Funk *et al*., 2002; Quenneville *et al*., 2010). In general, these apparatuses differ in terms

Table 1.3: Apparatus description for *in vitro* generalized forward fall studies.

Author (Year)	Quasi-Static, Dynamic	Type of Specimen	Activation Method	Post-Impact Specimen Motion	Muscle Loading	Impact Orientation
General Forward Fall Studies						
Augat *et al* (1996)	Quasi-static	Isolated - Right Radius	Materials Testing Machine	Fixed	none	Off-axis (75°)
Augat *et al* (1998)	Quasi-static	Intact - Fresh Frozen Upper Extremity	Materials Testing Machine	Fixed	none	Off-axis (75°)
Horsman *et al* (1983)	Quasi-static	Isolated - Radius	Materials Testing Machine	Fixed	none	Axial
Lill *et al* (2003)	Quasi-static	Intact - Fresh Frozen Upper Extremity	Materials Testing Machine	Fixed	none	Axial
Myers *et al* (1991, 1993)	Quasi-static	Intact - Fresh Frozen Upper Extremity	Materials Testing Machine	Fixed	none	Off-axis (75°)
Spadaro *et al* (1994)	Quasi-static	Intact - Fresh Frozen Upper Extremity	Materials Testing Machine	Fixed	none	Axial
Lubhan *et al* (2005)	Dynamic	Intact - Fresh Frozen Upper Extremity	Drop Tower	Fixed (drop tower)	none	Axial and Off-axis (45°)
Burkhart *et al* (2011, 2012)	Dynamic	Isolated - Radius	Pneumatic	Linear Translation	none	Off-axis (75°)
Duma *et al* (2003)	Dynamic	Intact - Fresh Frozen Upper Extremity	Pneumatic	Translation and Swing	none	Axial

Table 1.4: Apparatus description for *in vitro* wrist guard and lower extremity studies.

Author (Year)	Quasi-Static, Dynamic	Type of Specimen	Activation Method	Post-Impact Specimen Motion	Muscle Loading	Impact Orientation
Wrist Guard Studies						
Giacobetti *et al* (1997)	Quasi-static	Intact - Fresh Frozen Upper Extremity	Materials Testing Machine	Fixed	none	Off-axis (75°)
Staebler *et al* (1999)	Quasi-static	Intact - Fresh Frozen Upper Extremity	Materials Testing Machine	Fixed	none	Off-axis (75°)
Greenwald *et al* (1998)	Dynamic	Intact - Fresh Frozen Upper Extremity	Drop Tower	Fixed (drop tower)	none	Off-axis (75°)
Lewis *et al* (1997)	Dynamic	Intact - Fresh Frozen Upper Extremity	Drop Tower	Fixed (drop tower)	none	Axial
McGrady *et al* (2001)	Dynamic	Intact - Fresh Frozen Upper Extremity	Drop Tower	Fixed (drop tower)	ECU, ECRB&L	Off-axis (70°)
Moore *et al* (1997)	Dynamic	Intact - Fresh Frozen Upper Extremity	Drop Tower	Fixed (drop tower)	none	Axial
Lower Extremity Studies						
Yoganandan *et al* (1996)	Dynamic	Intact - Fresh Frozen Lower Extremity	Pendulum	Linear Translation	none	Axial
Yoganandan *et al* (1997)	Dynamic	Intact - Fresh Frozen Lower Extremity	Pendulum	Linear Translation	none	Axial
Owen *et al* (2001)	Dynamic	ATD Leg and Intact - Fresh Frozen	Pendulum and Sled	Fixed	Achilles Tendon	Axial and Off-axis
Funk *et al* (2002)	Dynamic	Intact - Foot and Ankle	Pendulum and Pneumatic	Fixed	Achilles Tendon	Axial
McKay *et al* (2009)	Dynamic	Intact - Fresh Frozen Lower Extremity	Not Specified	Free	none	Axial
Quenneville *et al* (2010)	Dynamic	ATD Lower Leg	Pneumatic	Linear Translation	none	Axial

of load application rate and magnitude. The studies that have used materials testing machines often simulate clinically relevant fracture patterns, but use quasi-static loading rates are not indicative of a fall scenario. On the other hand, drop towers recreate the correct impact velocity by using gravity to initiate impact, but do not permit post-impact specimen motion away from the ground. Similarly, pendulum and pneumatic actuation allow for dynamic impacts that can better match the force application rate of a forward fall, but are coupled with the potential for post-impact specimen motion.

While the identification of muscle loading during fall arrest was highlighted in Section 1.4.1, few past impact apparatuses (McGrady *et al*., 2001) have been designed that would allow for the investigation of the effect of muscle loads on radius fractures. Furthermore, the simulation of post-impact specimen motion is varied, ranging from completely fixed (specimen has no degrees-of-freedom) to free (specimen has six degrees-of-freedom). When the hand strikes the ground during a forward fall, the upper extremity is subject to inertial effects. Increasing inertia through body mass has been found to result in a proportionate increase in the secondary force peak seen during *in vivo* fall simulation (Chiu and Robinovitch, 1998). Therefore, for proper *in vitro* simulation of distal radius fractures, a testing apparatus is desired that can incrementally apply controlled dynamic impact forces, allow axial or off-axis specimen orientation, permit muscle force simulation, and allow for specimen specific ballasting to accurately account for inertial effects.

1.6 INSTRUMENTATION REQUIRED FOR IMPACT ASSESSMENT

In addition to the physical structure of the apparatus, there are many other components that are required for comprehensive data collection and analysis.

1.6.1 HIGH-SPEED CAMERAS

In past fracture testing, synchronizing a high-speed camera with load cell data has been used to visually assess the time at which fracture begins (Cristofolini *et al*., 2007), as well as to identify the initial location of crack propagation (de Bakker *et al*., 2009). Due to the rapid nature of bone fracture (*i.e*., fracture load rates of 1029 kN/s, impulse durations of

31 ms) (Burkhart *et al*., 2012b), a high frame rate is necessary to capture all relevant information. There is also a potential to expand the use of high-speed camera data for distal radius fractures beyond observation and into quantification. When used with imaging techniques such as colour-thresholding (McLachlin *et al*., 2011), high-speed camera data can be used to quantify rigid body velocity, as well as apparatus setup (*e.g.*, impact orientation) (Lim *et al*., 2003).

1.6.2 STRAIN GAUGES

A structure deforms in proportion to an applied load and the result (when the deformation is normalized to the initial length of the structure) is referred to as strain. Experimentally, strain is most commonly measured by adhering a strain gauge to the material of interest (Wheeler and Ganji, 2010a). Strain gauges are composed of thin wire foil that is folded many times over a small area and sandwiched between non-conductive materials (Figure 1.9). When gauge deformation occurs the electrical resistance of the foil is altered and can be translated into a strain value. Changes in resistance are often on the same order of magnitude as the resolution of the gauge (Wheeler and Ganji, 2010a), so a Wheatstone bridge is used to accentuate the desired strain signals and attenuate the unwanted components. A Wheatstone bridge allows the change in resistance to be measured rather than the overall magnitude of the resistance (Figure 1.10a) (Wheeler and Ganji, 2010a). In the case of a quarter bridge, where one of the four resistors is variable (strain gauge) and the remaining have fixed resistances, the output voltage will only change when the variable resistance changes; if the bridge is initially balanced, the change in voltage will be proportional to the change in resistance (Wheeler and Ganji, 2010a).

A uniaxial strain gauge can only measure strain in one direction; however, strain of a surface is multi-dimensional. To account for all strain components (two linear strains and one shear strain), a strain gauge rosette can be implemented. Strain gauge rosettes are composed of three uniaxial gauges offset from one another by known angles (the most common being 45° and 60° rosettes). In a 45° rosette (Figure 1.10b), linear strains are taken from the three gauges (Wheeler and Ganji, 2010a) and can be resolved into the minimum and maximum principal strains, which correspond to the peak orthogonal

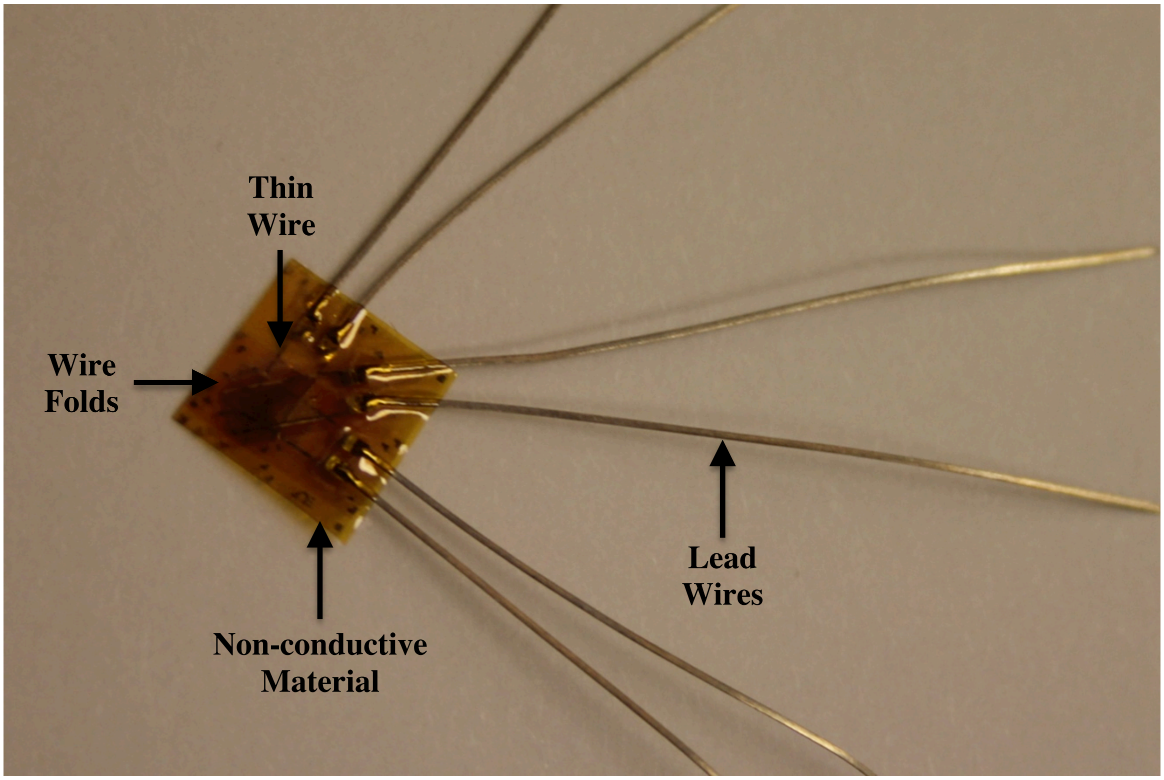

Figure 1.9: Strain gauge
A strain gauge consists of thin wire foil that is folded many times over a small area and sandwiched between non-conductive materials. The gauge shown is a triaxial gauge, where three separate uniaxial gauges, each with their own lead wires, are stacked on top of one another at 45-degree angles.

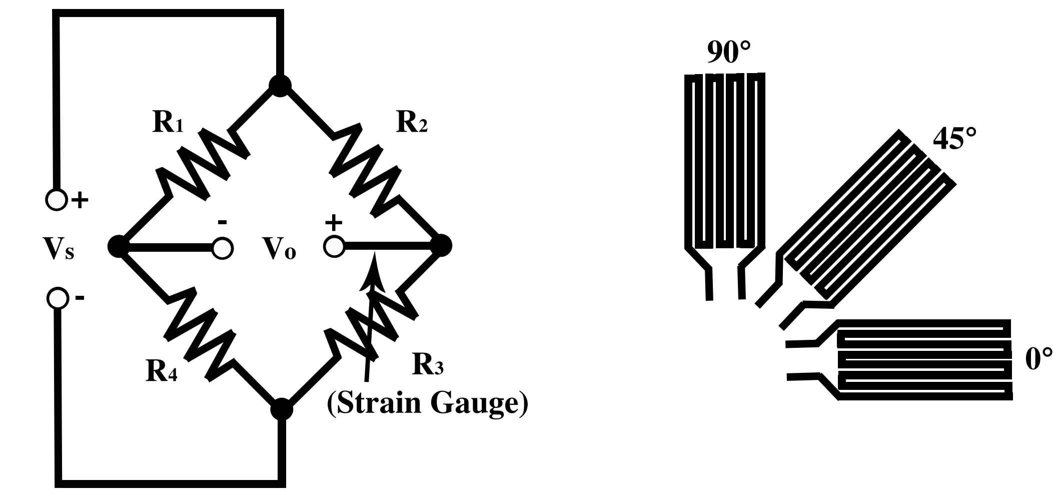

(a) (b)

Figure 1.10: Quarter bridge gauge and 45° rosette configurations
A quarter bridge (a) allows variation in R_3 to produce an output voltage proportional to the change rather than magnitude of strain gauge resistance. 45° rosette strain gauges (b) allow the quantification of principal strains.

strains that exist when shear strain is zero (Eq. 1.1).

$$\varepsilon_{1,2} = \frac{1}{2}(\varepsilon_{0^\circ} + \varepsilon_{90^\circ}) \pm \frac{\sqrt{2}}{2}\sqrt{[(\varepsilon_{0^\circ} - \varepsilon_{45^\circ})^2 + (\varepsilon_{45^\circ} - \varepsilon_{90^\circ})^2]} \tag{1.1}$$

1.6.3 LOAD CELL

In the study of impact loading, the external forces applied to cadaveric specimens must be measured and recorded, generally using load cells. Strain-gauge based load cells are constructed of rigid materials (typically metals) that linearly strain when a force is applied to them (Wheeler and Ganji, 2010b). In order to accurately quantify the strain-force relationship, the load cell is subjected to a known force and the strain that it outputs is recorded through a process known as calibration. Since the strain of the material used in construction is linear, and strain is directly proportional to force via stress, a linear relationship can be formed between the strain output and the applied load. This relationship is then used in future testing to convert the load cell's strain output into a force value.

1.6.4 FRACTURE DETECTION

When specimens are subjected to multiple impacts, it is important to ensure that damage has not accumulated prior to the fracture, as well as to determine when fracture does occur. As such, a variety of methods are available to determine the onset of crack formation in a material. One method makes use of the propagating shock that travels through the bone, as there is a relationship between the shock propagation velocity and the underlying structure of bone (Burkhart and Andrews, 2013; Cheng *et al*., 1995; Cunningham *et al*., 1990; Lafortune *et al*., 1995). The shock propagation velocity is found by attaching two accelerometers or strain gauges to the distal and proximal ends of a specimen at known displacements, and calculating the time between the peak shocks at each location (Cheng *et al*., 1995). Unfortunately, direct application of accelerometers to bone is often necessary to avoid the dampening affects of mounting on soft tissue (Lafortune *et al*., 1995), requiring further dissection of soft tissue.

An alternate fracture detection method is digital radiographic (DR) imaging, which is a standard technique for assessing distal radius fractures clinically and can be used to detect crack development non-invasively (Figure 1.11). The use of anterior-posterior and lateral radiographs in the classification of distal radius fractures has been documented and suggests that DR is a reliable method to assess fracture (Bozentka *et al*., 2002; Illarramendi *et al*., 1998; Kreder *et al*., 1996). One of the limitations associated with the DR is that the contrast is targeted at bone, and therefore this system is unable to provide simultaneous insight into articular cartilage damage during assessment. As well, there is the potential of DR to miss fine details such as trabecular breaks (micro-cracks) due to resolution limitations when trying to image the entire wrist (Forsyth *et al*., 1996). Despite these limitations, due to the non-invasive nature of this technique and its proven reliability, DR imaging is an excellent method for fracture detection in intact cadaveric testing.

1.7 PROJECT SCOPE AND OBJECTIVES

Distal radius fractures have been established as prominent injuries that are expensive to treat (Gabriel *et al*., 2002; Shauver *et al*., 2011) and that can lead to long-term deformity and pain (Altissimi *et al*., 1986; MacDermid *et al*., 2003). Despite *in vivo* studies that indicate muscle forces play a role in the forearm's response to impact, there has been very little *in vitro* investigation regarding the effect of muscle loads on fracture thresholds. Such an *in vitro* investigation would require custom lab equipment capable of simulating a variety of orientations and loads and quantifying the resulting fracture parameters. Accordingly, the **overall purpose** of this work is to determine the effect of static forearm muscle loads on measured fractures parameters in the distal radius following forward fall initiated impact loading. This will be achieved through the following **three specific objectives**:

Objective #1: *Re-design and assess an apparatus to test cadaveric forearm specimens under impact loading.*

To facilitate testing of cadaveric forearms, the redesign and validation of an existing impact loading apparatus is necessary. The new apparatus should allow for easy specimen orientation adjustments, reduced specimen constraint, the application of static muscle loads, and improved overall robustness and repeatability.

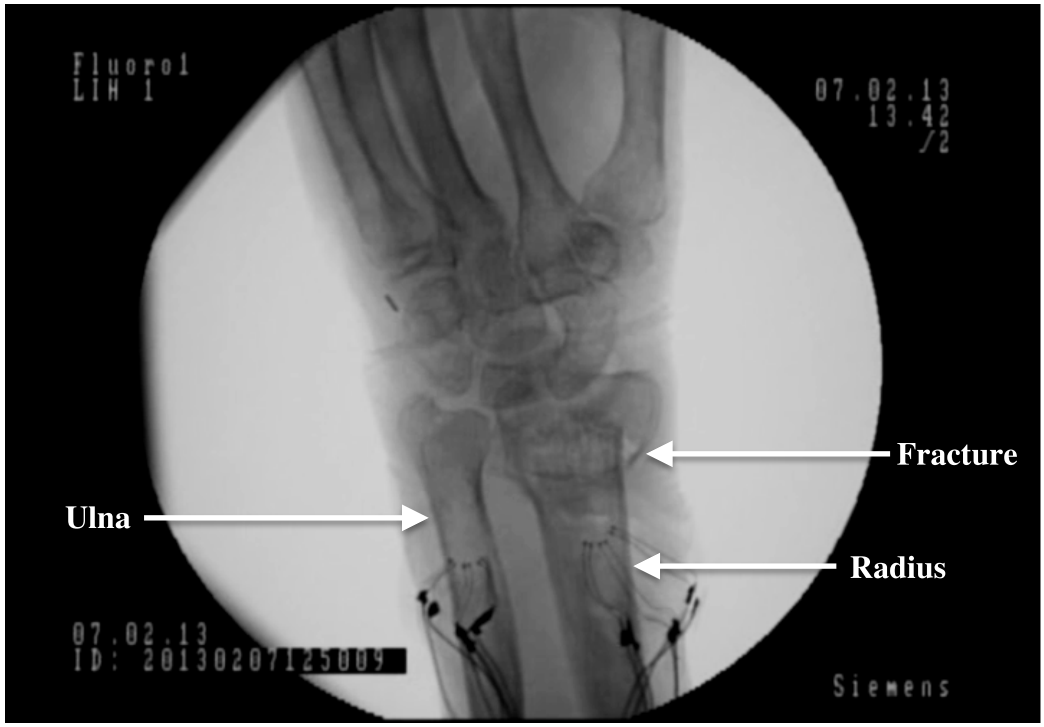

Figure 1.11: Fluoroscopic distal radius fracture image
Transitions from light to dark in digital radiographs represent changes from low to high density, which allows for the visualization of bone structure in the dorsal (anterior-posterior) view of the wrist.

Hypothesis #1: It is hypothesised that pneumatic input pressure will correlate well ($R^2 > 0.8$) with, and that excellent reliability (ICCs > 0.7) will be established for, output parameters of impact force, ram velocity and ram kinetic energy.

Objective #2: Develop and validate a high-speed camera-based measurement system to quantify impact kinematics.

To quantify impact kinematics, the design of a custom motion-tracking program is necessary. Using colour-thresholding, a custom marker can be isolated and its position quantified through sequential frame analysis. To validate the new camera system, a marker will be tracked through a known displacement allowing the direct comparison between camera output measures and an established gold standard.

Hypothesis #2: It is hypothesised that the camera system will function well for documenting marker position and velocity (percent errors < 3 %), but noise amplification through multiple derivatives will have larger errors for acceleration (percent errors < 10 %).

Objective #3: Determine the effect of static forearm muscle loading on in vitro distal radius fracture threshold measures.

A comparison will be made between intact cadaveric forearm specimens with and without muscle loads simulated (*i.e.,* paired specimens will be used). Strain gauges affixed to bone will also allow for the quantification of load sharing between the radius and ulna in response to muscle and impact loading.

Hypothesis # 3: It is hypothesised that muscle loading at magnitudes similar to those observed in *in vivo* studies will have no significant effect on the fracture measures (*i.e.*, fracture force, impulse and energy) of the distal radius.

1.8 REFERENCES

Altissimi, M., Antenucci, R., Fiacca, C., Mancini, G. B., 1986. Long-term results of conservative treatment of fractures of the distal radius. Clinical Orthopaedics and Related Research 206, 202-210.

Amis, A., Dowson, D., Wright, V., 1979. Muscle strengths and musculoskeletal geometry of the upper limb. Engineering in Medicine 8, 41-48.

Augat, P., Reeb, H., Claes, L., 1996. Prediction of fracture load at different skeletal sites by geometric properties of the cortical shell. Journal of Bone and Mineral Research 11, 1356-1363.

Augat, P., Iida, H., Jiang, Y., Diao, E., Genant, H. K., 1998. Distal radius fractures: Mechanisms of injury and strength prediction by bone mineral assessment. Journal of Orthopaedic Research 16, 629-635.

Berger, R. A., 2001. The anatomy of the ligaments of the wrist and distal radioulnar joints. Clinical Orthopaedics and Related Research (383), 32-40.

Berger, R. A., 1996. The anatomy and basic biomechanics of the wrist joint. Journal of Hand Therapy : Official Journal of the American Society of Hand Therapists 9, 84-93.

Birkbeck, D. P., Failla, J. M., Hoshaw, S. J., Fyhrie, D. P., Schaffler, M., 1997. The interosseous membrane affects load distribution in the forearm. The Journal of Hand Surgery 22, 975-980.

Boone, D. C., Azen, S. P., 1979. Normal range of motion of joints in male subjects. J Bone Joint Surg Am 61, 756-759.

Bozentka, D. J., Beredjiklian, P. K., Westawski, D., Steinberg, D. R., 2002. Digital radiographs in the assessment of distal radius fracture parameters. Clinical Orthopaedics and Related Research (397), 409-413.

Burkhart, T. A., Andrews, D. M., 2010. The effectiveness of wrist guards for reducing wrist and elbow accelerations resulting from simulated forward falls. Journal of Applied Biomechanics 26, 281-289.

Burkhart, T. A., Andrews, D. M., Dunning, C. E., 2013. Multivariate injury risk criteria and injury probability scores for fractures to the distal radius. Journal of Biomechanics 46, 973-978.

Burkhart, T. A., Andrews, D. M., Dunning, C. E., 2012. Failure characteristics of the isolated distal radius in response to dynamic impact loading. Journal of Orthopaedic Research : Official Publication of the Orthopaedic Research Society 30, 885-892.

Burkhart, T. A., Andrews, D. M., 2013. Kinematics, kinetics and muscle activation patterns of the upper extremity during simulated forward falls. Journal of Electromyography and Kinesiology 23, 688-695.

Burkhart, T. A., Dunning, C. E., Andrews, D. M., 2011. Determining the optimal system-specific cut-off frequencies for filtering in-vitro upper extremity impact force and acceleration data by residual analysis. Journal of Biomechanics 44, 2728-2731.

Cheng, S., Timonen, J., Suominen, H., 1995. Elastic wave propagation in bone in vivo: Methodology. Journal of Biomechanics 28, 471-478.

Chiu, J., Robinovitch, S. N., 1998. Prediction of upper extremity impact forces during falls on the outstretched hand. Journal of Biomechanics 31, 1169-1176.

Colles, A., 1814. On the Fracture of the Carpal extremity of the Radius. The Edinburgh Medical and Surgical Journal 10, 182-186.

Cristofolini, L., Juszczyk, M., Martelli, S., Taddei, F., Viceconti, M., 2007. In vitro replication of spontaneous fractures of the proximal human femur. Journal of Biomechanics 40, 2837-2845.

Cunningham, J. L., Kenwright, J., Kershaw, C. J., 1990. Biomechanical measurement of fracture healing. Journal of Medical Engineering & Technology 14, 92-101.

de Bakker, P. M., Manske, S. L., Ebacher, V., Oxland, T. R., Cripton, P. A., Guy, P., 2009. During sideways falls proximal femur fractures initiate in the superolateral cortex: Evidence from high-speed video of simulated fractures. Journal of Biomechanics 42, 1917-1925.

DeGoede, K. M., Ashton-Miller, J. A., 2002. Fall arrest strategy affects peak hand impact force in a forward fall. Journal of Biomechanics 35, 843-848.

DeGoede, K. M., Ashton-Miller, J. A., Liao, J. M., Alexander, N. B., 2001. How quickly can healthy adults move their hands to intercept an approaching object? Age and gender effects. The Journals of Gerontology.Series A, Biological Sciences and Medical Sciences 56, M584-8.

Dietz, V., Noth, J., Schmidtbleicher, D., 1981. Interaction between pre-activity and stretch reflex in human triceps brachii during landing from forward falls. The Journal of Physiology 311, 113-125.

Duma, S. M., Boggess, B. M., Crandall, J. R., MacMahon, C. B., 2003. Injury risk function for the small female wrist in axial loading. Accident Analysis and Prevention 35, 869-875.

Fardellone, P., 2008. Predicting the fracture risk in 2008. Joint Bone Spine 75, 661-664.

Forsyth, D., Shaw, W., Richmond, S., 1996. Digital imaging of cephalometric radiography, part 1: advantages and limitations of digital imaging. The Angle Orthodontist 66, 37-42.

Frykman, G., 1967. Fracture of the distal radius including sequelae-shoulder-hand-finger syndrome, disturbance in the distal radio-ulnar joint and impairment of nerve function: a clinical and experimental study. Acta Orthop Scand (Suppl) 108, 1-155.

Fukunaga, T., Ichinose, Y., Ito, M., Kawakami, Y., Fukashiro, S., 1997. Determination of fascicle length and pennation in a contracting human muscle in vivo. Journal of Applied Physiology 82, 354-358.

Funk, J. R., Crandall, J. R., Tourret, L. J., MacMahon, C. B., Bass, C. R., Patrie, J. T., Khaewpong, N., Eppinger, R. H., 2002. The Axial Injury Tolerance of the Human Foot/Ankle Complex and the Effect of Achilles Tension. Journal of Biomechanical Engineering 124, 750-757.

Gabriel, S. E., Gabriel, S. E., Tosteson, A. N. A., Leibson, C. L., Crowson, C. S., Pond, G. R., Hammond, C. S., Melton, I.,L.J., 2002. Direct Medical Costs Attributable to Osteoporotic Fractures. Osteoporosis International 13, 323-330.

Giacobetti, F., Sharkey, P., Bos-Giacobetti, M., Hume, E., Taras, J., 1997. Biomechanical Analysis of the Effectiveness of In-Line Skating Wrist Guards for Preventing Wrist Fractures. The American Journal of Sports Medicine 25, 223-225.

Grabiner, M. D., Donovan, S., Bareither, M. L., Marone, J. R., Hamstra-Wright, K., Gatts, S., Troy, K. L., 2008. Trunk kinematics and fall risk of older adults: Translating biomechanical results to the clinic. Journal of Electromyography and Kinesiology 18, 197-204.

Greenwald, R., Janes, P., Swanson, S., McDonald, T., 1998. Dynamic Impact Response of Human Cadaveric Forearms Using a Wrist Brace. The American Journal of Sports Medicine 26, 825-830.

Groen, B., Smulders, E., Duysens, J., van Lankveld, W., Weerdesteyn, V., 2010. Could martial arts fall training be safe for persons with osteoporosis?: a feasibility study. BMC Research Notes 3, 111. doi: 10.1186/1756-0500-3-111.

Henry, M. H., 2008. Distal Radius Fractures: Current Concepts. Journal of Hand Surgery 33, 1215-1227.

Hernandez, M. E., Ashton-Miller, J. A., Alexander, N. B., 2013. Age-Related Differences in Maintenance of Balance During Forward Reach to the Floor. The Journals of Gerontology.Series A, Biological Sciences and Medical Sciences.

Hill, C., Riaz, M., Mozzam, A., Brennen, M., 1998. A regional audit of hand and wrist injuries: a study of 4873 injuries. The Journal of Hand Surgery: British & European Volume 23, 196-200.

Horsman, A., Currey, J., 1983. Estimation of mechanical properties of the distal radius from bone mineral content and cortical width. Clinical Orthopaedics and Related Research 176, 298-304.

Hsiao, E. T., Robinovitch, S. N., 1998. Common protective movements govern unexpected falls from standing height. Journal of Biomechanics 31, 1-9.

Illarramendi, A., Gonzalez Della Valle, A., Segal, E., De Carli, P., Maignon, G., Gallucci, G., 1998. Evaluation of simplified Frykman and AO classifications of fractures of the distal radius. Assessment of interobserver and intraobserver agreement. International Orthopaedics 22, 111-115.

Kakarlapudi, T. K., Santini, A., Shahane, S. A., Douglas, D., 2000. The cost of treatment of distal radial fractures. Injury 31, 229-232.

Kim, H. D., Brunt, D., 2013. Effect of a change in step direction from a forward to a lateral target in response to a sensory perturbation. Journal of Electromyography and Kinesiology: Official Journal of the International Society of Electrophysiological Kinesiology 23, 851-857.

Kim, K. J., Ashton-Miller, J. A., 2003. Biomechanics of fall arrest using the upper extremity: age differences. Clinical Biomechanics (Bristol, Avon) 18, 311-318.

King, G. J., McMurtry, R. Y., Rubenstein, J. D., Gertzbein, S. D., 1986. Kinematics of the distal radioulnar joint. The Journal of Hand Surgery 11, 798-804.

Kreder, H. J., Hanel, D. P., McKee, M., Jupiter, J., McGillivary, G., Swiontkowski, M. F., 1996. Consistency of AO fracture classification for the distal radius. The Journal of Bone and Joint Surgery.British Volume 78, 726-731.

Lafortune, M. A., Henning, E., Valiant, G. A., 1995. Tibial shock measured with bone and skin mounted transducers. Journal of Biomechanics 28, 989-993.

Lawson, G., Hajducka, C., McQueen, M., 1995. Sports fractures of the distal radius—epidemiology and outcome. Injury 26, 33-36.

Lewis, L. M., West, O. C., Standeven, J., Jarvis, H. E., 1997. Do wrist guards protect against fractures? Annals of Emergency Medicine 29, 766-769.

Lill, C. A., Goldhahn, J., Albrecht, A., Eckstein, F., Gatzka, C., Schneider, E., 2003. Impact of bone density on distal radius fracture patterns and comparison between five different fracture classifications. Journal of Orthopaedic Trauma 17, 271-278.

Lim, C., Ang, C., Tan, L., Seah, S., Wong, E., 2003. Drop impact survey of portable electronic products. In Electronic Components and Technology Conference, 2003. Proceedings. 53rd.

Lo, J., McCabe, G. N., DeGoede, K. M., Okuizumi, H., Ashton-Miller, J. A., 2003. On reducing hand impact force in forward falls: results of a brief intervention in young males. Clinical Biomechanics 18, 730- 736.

Lubahn, J., Englund, R., Trinidad, G., Lyons, J., Ivance, D., Buczek, F. L., 2005. Adequacy of laboratory simulation of in-line skater falls. The Journal of Hand Surgery 30, 283-288.

MacDermid, J. C., Roth, J. H., Richards, R. S., 2003. Pain and disability reported in the year following a distal radius fracture: a cohort study. BMC Musculoskeletal Disorders 4, 24. doi: 10.1186/1471-2474-4-24.

Mann, D. C., Rajmaira, S., 1990. Distribution of physeal and nonphyseal fractures in 2,650 long-bone fractures in children aged 0-16 years. Journal of Pediatric Orthopaedics 10, 713-716.

May, M. M., Lawton, J. N., Blazar, P. E., 2002. Ulnar styloid fractures associated with distal radius fractures: incidence and implications for distal radioulnar joint instability. The Journal of Hand Surgery 27, 965-971.

McGrady, L., Hoepfner, P., Young, C., Raasch, W., Lim, T., Han, J., 2001. Biomechanical effect of in-line skating wrist guards on the prevention of wrist fracture. Journal of Mechanical Science and Technology 15, 1072-1076.

McKinley, M., O'Loughlin, V. D., 2006a. Radiocarpal (Wrist) Articulation. McGraw-Hill, New York, pp. 274-275.

McKinley, M., O'Loughlin, V. D., 2006b. Radius and Ulna. McGraw-Hill, New York, pp. 228-231.

McLachlin, S. D., Al Saleh, K., Gurr, K. R., Bailey, S. I., Bailey, C. S., Dunning, C. E., 2011. Comparative assessment of sacral screw loosening augmented with PMMA versus a calcium triglyceride bone cement. Spine 36, E699-704.

Moore, M. S., Popovic, N. A., Daniel, J. N., Boyea, S. R., Polly, D. W., 1997. The effect of a wrist brace on injury patterns in experimentally produced distal radial fractures in a cadaveric model. The American Journal of Sports Medicine 25, 394-401.

Muller, M., Nazarian, S., Koch, P., Schatzker, J., 1990. The AO classification of long bones. Berlin etc: Springer–Verlag, 74-84.

Myers, E. R., Sebeny, E. A., Hecker, A. T., Corcoran, T. A., Hipp, J. A., Greenspan, S. L., Hayes, W. C., 1991. Correlations between photon absorption properties and failure load of the distal radiusin vitro. Calcified Tissue International 49, 292-297.

Myers, E., Hecker, A., Rooks, D., Hipp, J., Hayes, W., 1993. Geometric variables from DXA of the radius predict forearm fracture load in vitro. Calcified Tissue International 52, 199-204.

Nevitt, M. C., Cummings, S. R., 1993. Type of fall and risk of hip and wrist fractures: the study of osteoporotic fractures. The Study of Osteoporotic Fractures Research Group. Journal of the American Geriatrics Society 41, 1226-1234.

O’Neill, T. W., Cooper, C., Finn, J. D., Lunt, M., Purdie, D., Reid, D. M., Rowe, R., Woolf, A. D., Wallace, W. A., 2001. Incidence of Distal Forearm Fracture in British Men and Women. Osteoporosis International 12, 555-558.

O'Neill, T., Varlow, J., Silman, A., Reeve, J., Reid, D., Todd, C., Woolf, A., 1994. Age and sex influences on fall characteristics. Annals of the Rheumatic Diseases 53, 773-775.

Owen, C., Lowne, R., 2001. Requirements for the evaluation of the risk of injury to the ankle in car impact tests. National Highway Traffic Safety Administration.

Palmer, A. K., Werner, F. W., Murphy, D., Glisson, R., 1985. Functional wrist motion: a biomechanical study. The Journal of Hand Surgery 10, 39-46.

Panero, J., Zelnik, M., 1979. Joint Motion. Whitney Library of Design, New York, pp. 117.

Quenneville, C. E., Fraser, G. S., Dunning, C. E., 2010. Development of an apparatus to produce fractures from short-duration high-impulse loading with an application in the lower leg. Journal of Biomechanical Engineering 132, 014502-1 - 014502-4.

Ray, N. F., Chan, J. K., Thamer, M., Melton, L. J.,3rd, 1997. Medical expenditures for the treatment of osteoporotic fractures in the United States in 1995: report from the National

Osteoporosis Foundation. Journal of Bone and Mineral Research : The Official Journal of the American Society for Bone and Mineral Research 12, 24-35.

Róbertsson, G. O., Jónsson, G. T., Sigurjónsson, K., 1990. Epidemiology of distal radius fractures in Iceland in 1985. Acta Orthopaedica 61, 457-459.

Robinovitch, S. N., Feldman, F., Yang, Y., Schonnop, R., Leung, P. M., Sarraf, T., Sims-Gould, J., Loughin, M., 2013. Video capture of the circumstances of falls in elderly people residing in long-term care: an observational study. Lancet 381, 47-54.

Robitaille, Y., Laforest, S., Fournier, M., Gauvin, L., Parisien, M., Corriveau, H., Trickey, F., Damestoy, N., 2005. Moving forward in fall prevention: an intervention to improve balance among older adults in real- world settings. American Journal of Public Health 95, 2049-2056.

Shauver, M. J., Yin, H., Banerjee, M., Chung, K. C., 2011. Current and future national costs to medicare for the treatment of distal radius fracture in the elderly. The Journal of Hand Surgery 36, 1282-1287.

Skahen, J. R., Palmer, A. K., Werner, F. W., Fortino, M. D., 1997. The interosseous membrane of the forearm: anatomy and function. The Journal of Hand Surgery 22, 981-985.

Spadaro, J., Werner, F., Brenner, R., Fortino, M., Fay, L., Edwards, W., 1994. Cortical and trabecular bone contribute strength to the osteopenic distal radius. Journal of Orthopaedic Research 12, 211-218.

Staebler, M., Moore, D., Akelman, E., Weiss, A., Fadale, P., Crisco, J., 1999. The Effect of Wrist Guards on Bone Strain in the Distal Forearm. The American Journal of Sports Medicine 27, 500-506.

Tilley, A. R., 2002. Angle Movements of Body Components. John Wiley & Sons, New York, pp. 16.

Troy, K. L., Donovan, S. J., Marone, J. R., Bareither, M. L., Grabiner, M. D., 2008. Modifiable performance domain risk-factors associated with slip-related falls. Gait & Posture 28, 461-465.

Troy, K. L., Grabiner, M. D., 2007a. Asymmetrical ground impact of the hands after a trip-induced fall: Experimental kinematics and kinetics. Clinical Biomechanics 22, 1088-1095.

Troy, K. L., Grabiner, M. D., 2007b. Off-axis loads cause failure of the distal radius at lower magnitudes than axial loads: A finite element analysis. Journal of Biomechanics 40, 1670-1675.

Van Staa, T., Dennison, E., Leufkens, H., Cooper, C., 2001. Epidemiology of fractures in England and Wales. Bone 29, 517-522.

Wheeler, A. J., Ganji, A. R., 2010a. Electrical Resistance Strain Gage. Prentice Hall, New Jersey, pp. 244- 250.

Wheeler, A. J., Ganji, A. R., 2010b. Load Cells. Prentice Hall, New Jersey, pp. 272-274.

Wigderowitz, C. A., Paterson, C. R., Dashti, H., McGurty, D., Rowley, D. I., 2000. Prediction of Bone Strength from Cancellous Structure of the Distal Radius: Can We Improve on DXA? Osteoporosis International 11, 840-846.

Wojcik, L. A., Thelen, D. G., Schultz, A. B., Ashton-Miller, J. A., Alexander, N. B., 1999. Age and gender differences in single-step recovery from a forward fall. The Journals of Gerontology.Series A, Biological Sciences and Medical Sciences 54, M44-50.

Workplace Safety Insurance Board, 2002. Statistical supplement.

Wu, C., Hans, D., He, Y., Fan, B., Njeh, C., Augat, P., Richards, J., Genant, H., 2000. Prediction of bone strength of distal forearm using radius bone mineral density and phalangeal speed of sound. Bone 26, 529- 533.

Yoganandan, N., Pintar, F. A., Boynton, M., Begeman, P., Prasad, P., Kuppa, S. M., Morgan, R. M., Eppinger, R. H., 1996. Dynamic axial tolerance of the human foot-ankle complex. SAE 962426, 207-218.

Yoganandan, N., Pintar, F. A., Kumaresan, S., Boynton, M., 1997. Axial impact biomechanics of the human foot-ankle complex. Journal of Biomechanical Engineering 119, 433-437.

CHAPTER 2

DESIGN AND ASSESSMENT OF AN IMPROVED IMPACT APPARATUS

2.1 INTRODUCTION

In order to conduct thorough and accurate distal radius fracture research, a reliable impact testing apparatus is required. Several methods have been used in the past (Table 1.4) to apply impacts indicative of forward falls to cadaveric forearm specimens, including the use of pneumatic pressure or ballasted pendulum systems. While these methods offer the advantage of repeatable load application, they have a greater potential to apply excessive loading rates and forces that could result in fracture patterns that are not clinically relevant.

A novel pneumatically controlled impact system was developed in the Jack McBain Biomechanics Laboratory at Western University in 2010 (Figure 2.1) (Quenneville *et al.*, 2010) and was used to apply systematic impact loading to isolated cadaveric tibia (Quenneville, 2009) and radius (Burkhart *et al.*, 2012b) specimens. Briefly, the original system (Quenneville *et al.*, 2010) consisted of a projectile ram that travelled through an acceleration tube, the velocity of which was controlled by adjusting the pressure within the tube. As the ram exited the acceleration tube, it struck an intermediate impact plate, and the load was transferred through a load cell (Denton femur load cell model: 1914A; Denton ATD, Inc. Rochester Hills, MI) onto the specimen, which was constrained to move on a linear rail. While this apparatus was used successfully to create clinically relevant fractures, it was not without its limitations (Table 2.1). For example, the method of specimen fixation created an excessive bending moment (transferred at impact) that resulted in damage over extended use (*i.e.*, broken linear bearings and rail). Additionally, certain aspects of the apparatus required disassembly and reassembly during regular operation (*e.g.* re-setting the ram distance or mass), significantly prolonging the testing protocol, and there were limited adjustments available to alter specimen orientation. Given these limitations (Table 2.1), an extensive redesign of the existing impact-loading apparatus was required to accommodate improved impact testing of intact cadaveric

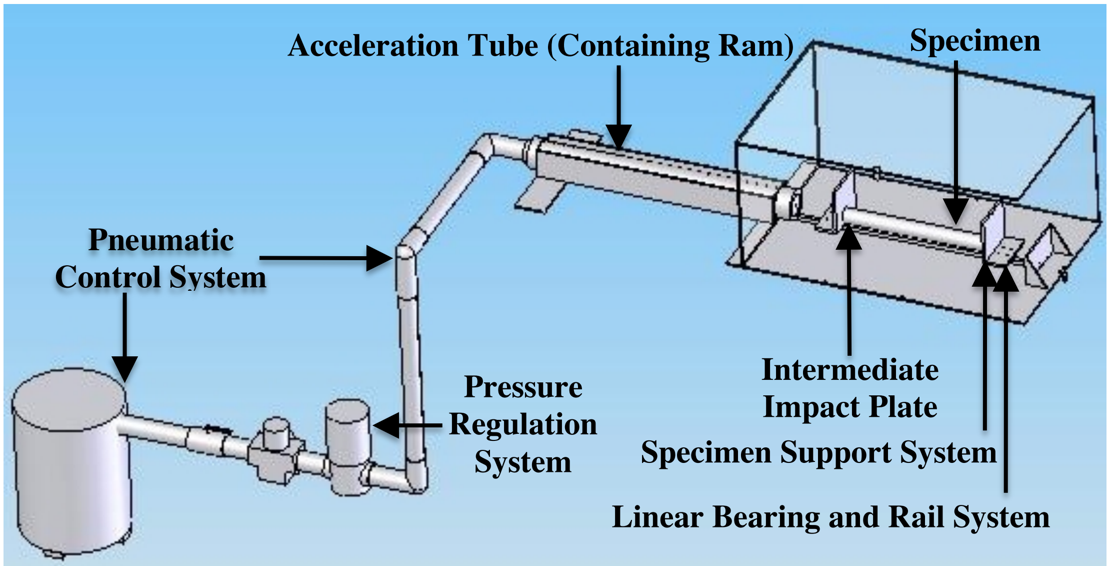

Figure 2.1: Existing impact apparatus

A schematic representation of the original (Quenneville *et al*., 2010) impact apparatus showing the key components. Due to damage incurred (*e.g.*, rail bending and bearing breaking) from excessing loading moments, and other limitations, the original apparatus required a redesign for use in further impact testing.

Table 2.1: A summary of the design challenges of the original impact apparatus and the subsequent requirements for a new apparatus.

Design Challenges	Existing Apparatus	Design Requirement for New Apparatus
Loading Moment	Restriction in the degrees of freedom of the specimen generates a damaging bending moment.	The specimen support system must not sustain damage arising from the potential impact moments.
Specimen Alignment	Positioning the specimen for off-axis loading is done during potting, and cannot be adjusted.	Maintain linear ram trajectory, while allowing for variation in specimen position and angulation.
Post-impact Energy	Energy not absorbed by the specimen is transferred to the apparatus, causing damage and wear.	Allow safe dampening of post-impact energy.
Pneumatic Pressure Control	The existing pressure regulator often over/under shoots the target pressure.	Establish reliable control over the pressure in the acceleration tube.
Ram Extraction	The ram is extracted through the front of acceleration tube, which requires significant disassembly.	Provide access to the ram to ensure ease of mass adjustment and repositioning.
Ram Distance Reference	A measuring tape is extended down the acceleration tube until contact is made with the ram.	Provide a measure for reliable ram reset distance.
Muscle Control	System designed for isolated bone testing (*i.e.*, no soft tissues).	Expand testing capabilities to intact cadaveric specimens (*i.e.*, bone + overlying tissue), and allow for muscle load application with anatomical line-of-action

specimens (Quenneville *et al*, 2010). Therefore, the purpose of the work described in this chapter was (1) to establish design requirements and implement necessary changes for the development of a new impact testing apparatus; and (2) to assess the reliability of the final design.

2.2 METHODS

2.2.1 APPROACH TO APPARATUS RE-DESIGN

The new apparatus design (drawings of which are provided in Appendix C) was based largely around overcoming the design challenges of the original impact apparatus (Table 2.1). After carefully reviewing the original design's performance, seven specific design requirements were developed to address the limitations observed (Table 2.1). While some of the impacting apparatus' existing features (*e.g.*, the pneumatic control and acceleration tube) were maintained, many new features were required to address the concerns of further impact testing.

The overall operation of the new apparatus is similar to that of the original, whereby pressurized air is released through a solenoid valve to move an impact ram of known mass that travels down the acceleration tube and strikes an impact plate following exit from the tube (Figure 2.2a). The velocity of the ram is calculated through the use of two LED sensors (HOA0149; Honeywell International Inc. Morristown, NJ) placed in series at the exit of the acceleration tube (Figure 2.2b) that trigger a square voltage pulse. Measuring the pulse duration, and knowing the distance between the sensors permits velocity calculation. To secure specimens in the impact apparatus, soft tissues are removed proximally, and the exposed bones cemented (Denstone Golden, Heraeus Dental; South Bend, IN) in short lengths (*e.g.*, 8 – 10 cm) of PVC tubing (diameter = 10 cm). The PVC mates with a cylindrical guide that is hung in the apparatus' potting mount (Figure 2.2b).

The major differences between the original and new apparatuses relate to the following improvements: a new pressure regulation system, wye-fitting acceleration tube, hydraulic damping pistons, specimen support and angle system, hanging cables and tendon

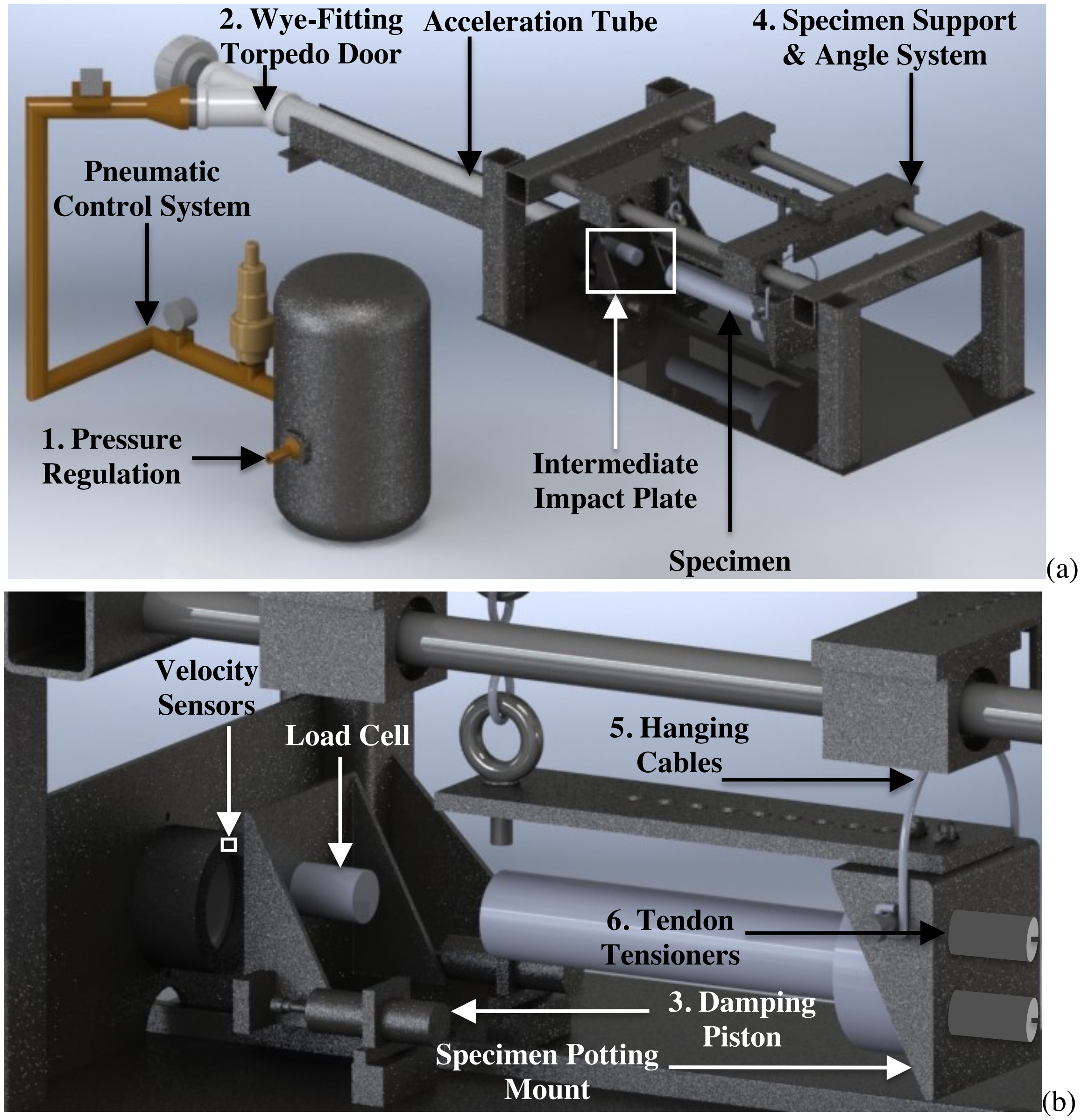

Figure 2.2: New impact apparatus

A schematic of the new impact apparatus (a) showing all six (numbered labels) re-designed components, and a close-up schematic of the impact apparatus chamber (b) showing the addition of the damping pistons and the specimen suspension system.

tensioning system (Figure 2.2).

2.2.1.1 PRESSURE REGULATION SYSTEM

The original system for pneumatic pressure regulation used a digital pressure regulator (T-500 Electropneumatic Transducer; ControlAir Inc., Amherst, NH) that would commonly overshoot the targeted pressure and was difficult to control. This resulted in variability of the set pressure for a given input voltage. To ensure more reliable pressures could be achieved, the digital pressure regulator was swapped for a proportional pressure controller (PPC) (PPC5C-AAA-AGCB-BBB-JD; MAC Valves Inc. Wixom, MI) (Figure 2.3). PPCs accurately moderate the pressure output (which can be displayed by a digital pressure gauge) as a percentage of the input pressure based on an electrical voltage. In addition, for an output pressure up to 30 psi, the input voltage range was 0 - 1.5 V for the original regulator compared to 0 - 3.5 V for the PPC, meaning improved resolution and output pressure control.

2.2.1.2 WYE-FITTING TORPEDO DOOR

In the original apparatus, when the mass of the ram required adjustment, the entire ram had to be removed through the discharge end of the acceleration tube. This also required removing the intermediate impact plate assembly, which was an inconvenient addition and time costing to the testing protocol. Additionally, to reset the ram distance a measuring tape was used to push the ram back down the acceleration tube, which proved challenging. To address both of these issues the new apparatus was designed with a 'torpedo-bay-door', allowing for the ram to be accessed through a new wye-fitting on the back end of the acceleration tube. The sealing cap of the new door is attached to a cable, which is tethered to the back-end of impacting ram. This allows the ram's distance to be reset by reeling it back to the appropriate distance. In addition, to quantify the ram's reset distance, an adhesive ruler is located on the top surface of the transparent acceleration tube. This allows the user to see through the tube and visually gauge the ram's alignment with respect to a desired distance (Figure 2.4).

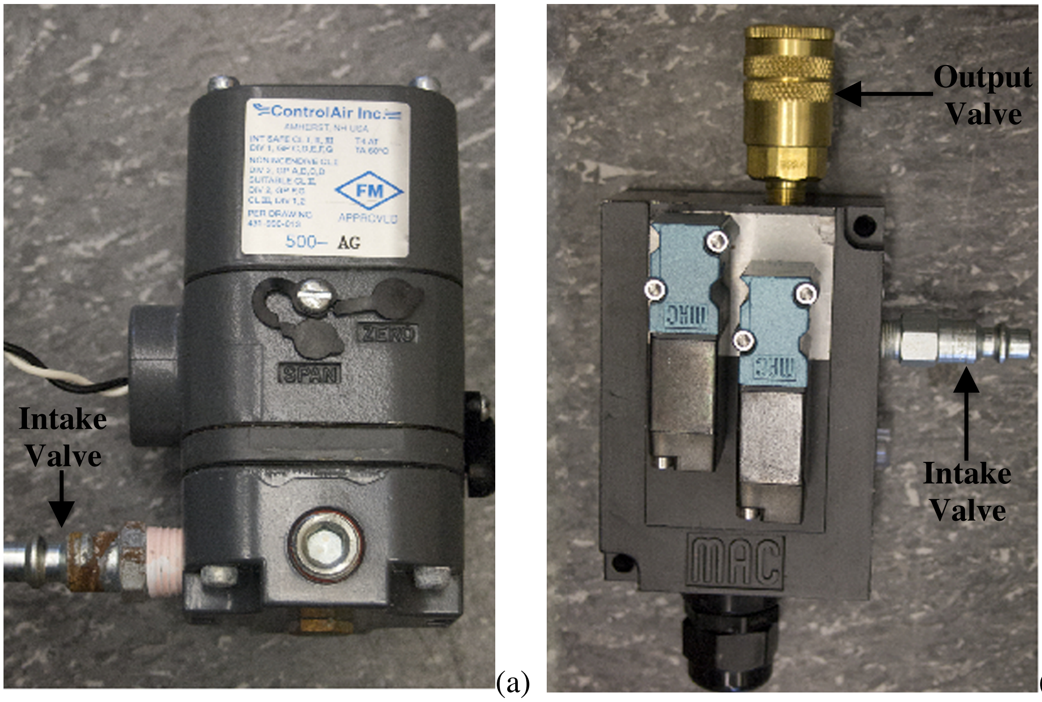

(a) (b)

Figure 2.3: Original and new pressure regulation systems
Comparison of the original pressure regulator (T-500 Electropneumatic Transducer; ControlAir Inc., Amherst, NH) (a) that would overshoot the desired pressure when supplied a voltage input; and the new proportional pressure controller (PPC5C-AAA-AGCB-BBB-JD; MAC Valves Inc. Wixom, MI) (b) that moderates the set pressure in a more precise manner with increased resolution.

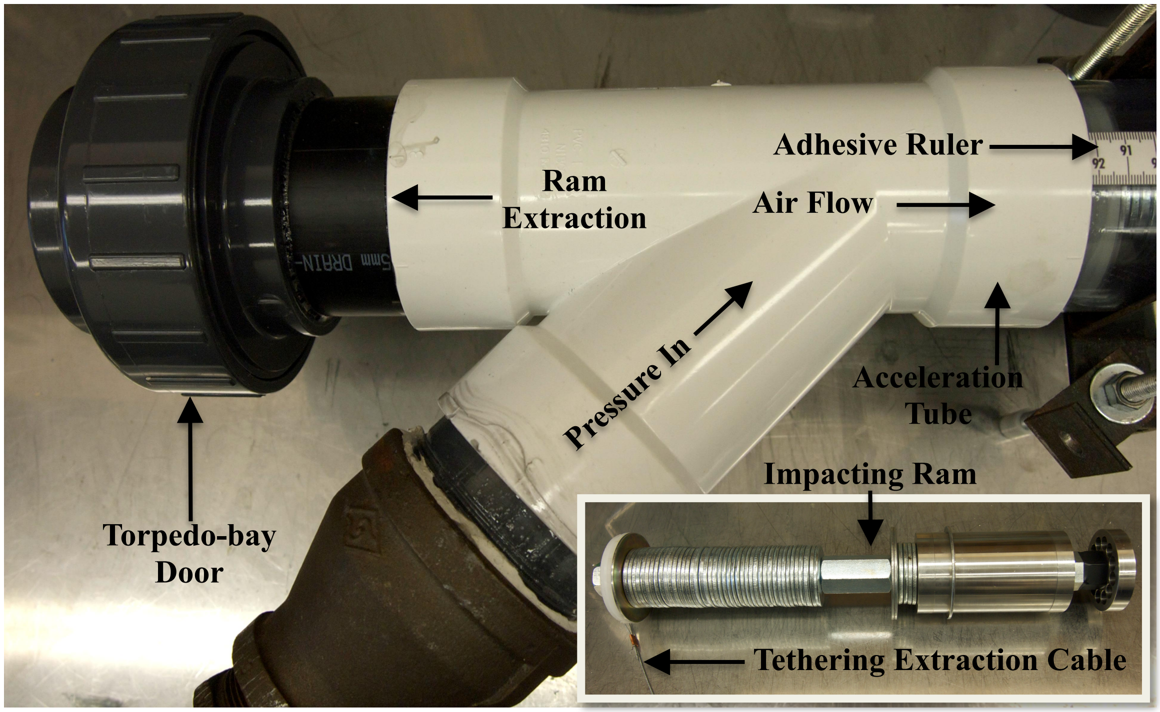

Figure 2.4: Wye-fitting torpedo door
A close-up view of the wye-fitting torpedo door system showing the direction of airflow into the acceleration tube (Wye-fitting supplied by McMaster-Carr; Robbinsville, NJ). When the ram requires extraction, the 'torpedo-bay door' is unthreaded and a tether connecting the door to the end of the ram is used to reel the ram out of the acceleration tube. To ensure pressure is maintained behind the ram, the door has a rubberized seal that is compressed when closed.

2.2.1.3 HYDRAULIC DAMPING PISTONS

During impact testing, the transfer of energy from the impact ram to the specimen is not 100% efficient, as some of the energy is lost through the intermediate impact plate leading to possible apparatus damage, as observed with the original design (*e.g.*, rail bending, bearing breaking). To mitigate these effects, a hydraulic damping system that consisted of a pair of hydraulic pistons (9530K52; McMaster-Carr Inc.; Aurora, OH) (Figure 2.5), was incorporated into the design to prevent excessive intermediate impact plate translation and to safely absorb excess energy. These damping pistons can be offset from the intermediate impact plate at the time of specimen impact, but engage once the plate has translated through a preset displacement (Figure 2.5), with the internal hydraulic fluid of the pistons contributing to the dissipation of plate energy and motion.

2.2.1.4 SUPPORT AND ANGLE SYSTEM

The original apparatus supported specimens using a linear ball-bearing and rail system that permitted only uni-axial translation. Due to this constraint, bending moments generated during impact caused damage to the rail and bearings. To reduce the constraint, a support and angle system was devised that allows specimen movement in multiple degrees-of-freedom over the duration of the impact, through a pendulum-style potting system suspended from a linear sleeve-bearing (9338T6, MacMaster-Carr Inc. Aurora, OH) rail system (Figure 2.6). This design permits the specimen to swing away from the impact plate following the initial impact while the low-friction linear sleeve-bearing rail system ensures that the specimen position can be adjusted with ease. The bearing system also provides the option of having the specimen translate away from the intermediate impact plate post-impact if desired. Adjustable ballasting weights can be added to the potting system to simulate a percentage body mass of the specimen being tested.

The original design did not allow for specimen orientation adjustments after the specimen had been potted. To address a lack of specimen alignment control with the original design, the specimen support incorporates an angle system that provides horizontal adjustments from -23° to 23° (Figure 2.6a) and vertical adjustments from 0° to 34° (Figure 2.6b). Together, these two adjustments can be combined to test acute fracture

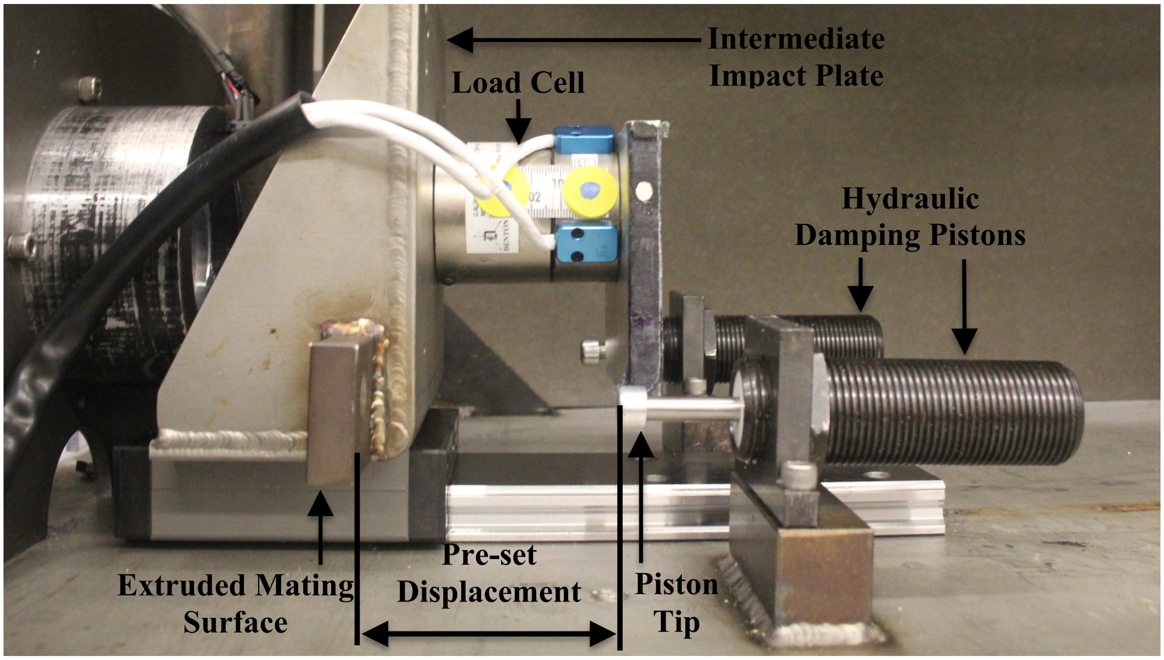

Figure 2.5: Energy damping system

A close-up view of the energy damping system consisting of the hydraulic pistons and the addition of extrusions to the intermediate impact plate. When the intermediate impact plate is struck by the impacting ram, it translates through the pre-set displacement (during which time it would impact the specimen). After the extruded mating surfaces contact the damping pistons, the plate begins to slow due to resistance afforded by the damping pistons' hydraulic fluid. This process safely dissipates any excess impact energy within the system.

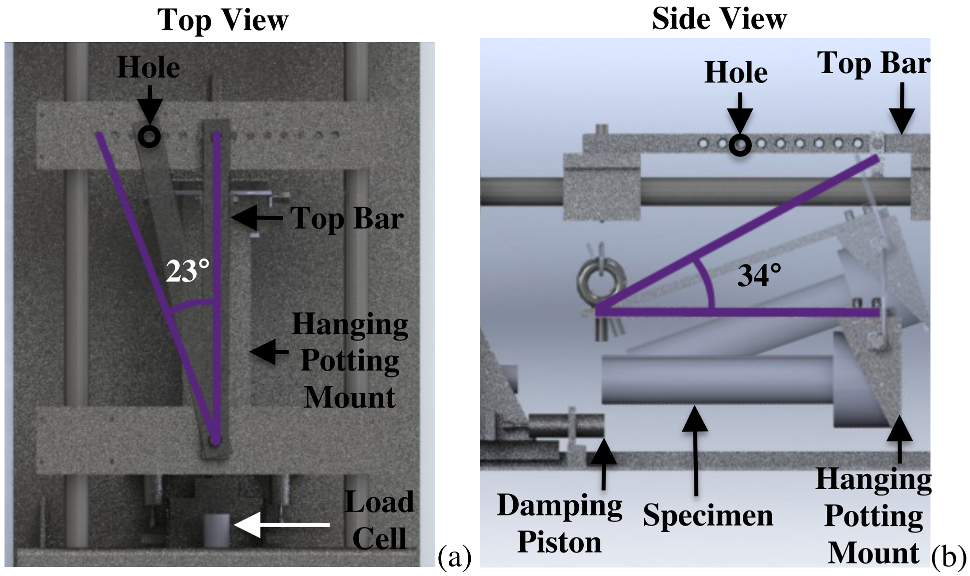

Figure 2.6: New support and angle system
The new apparatus allows for horizontal (a) and vertical (b) angle adjustments allowing the specimen to be offset from the impacting ram's trajectory. Horizontal adjustments are made by changing which hole the top bar is mated with (as shown in (a)), while vertical adjustments can be made by changing which hole the potting mount's hanging cables travel through (as shown in (b)).

modes in axial, planar (horizontal or vertical specimen angle), or 3-dimensional loading scenarios (horizontal and vertical specimen angle).

2.2.1.5 HANGING CABLES

To further assist with varying specimen orientation and suspension, the hanging potting mount was attached to the specimen support system by adjustable locking cables (8418D, Master Lock Company LLC, Oak Creek, WI) (Figure 2.7) that use a steel cable 'pinch-locking' system adjustable from 15 cm to 180 cm in length. While specimen vertical angle can be set using the new specimen support and angle system (by adjusting which holes the cables are positioned in), the use of hanging cables adds to the adjustability already incorporated, allowing a specimen's vertical angle and height to be adjusted by simply varying the cable length. Adjusting the length of the cable requires only pulling/pushing the cable through the lock (while the key is placed in the unlock position) and locking the position into place once the appropriate length is achieved (the key is turned into the lock position).

2.2.1.6 TENDON TENSION LOCKING SYSTEM

The original impactor design tested only isolated cadaveric bones (*i.e.*, no soft tissues). To incorporate the effect of soft tissues and simulate the loads that are present in the forearm musculature during a forward fall (Burkhart and Andrews, 2013), a cable system was developed that sets the tension applied through the tendon prior to impact. As noted in Section 1.3.3, the four key flexor-extensor muscles of the forearm are FCU, FCR, ECU and ECRL. Prior to testing, the tendons from these muscles can be surgically isolated and connected to galvanized steel cables via a Krackow locking suture (Krackow *et al.*, 1986). To control anatomical line-of-action for each muscle, tubes are placed in the cement at the time of specimen potting to create tunnels for the muscle cables to pass through (Figure 2.8). These tubes are aligned with holes drilled through the hanging potting mount, and cable tension is achieved and maintained by then passing the cables through 'line tighteners' (C78990V; Ben-Mor Cables Inc. Calgary, AB) buttressed against the back of the potting mount (Figure 2.9). Tension was set in each cable using a digital tension scale (78-0069-4; Matzuo America; South Sioux City, NE) attached to the loop on

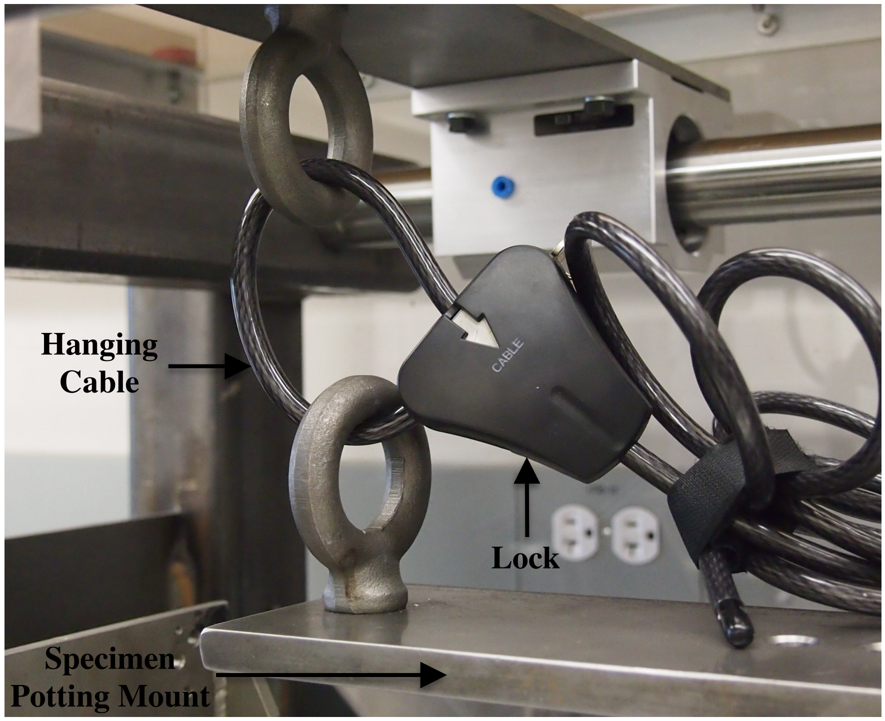

Figure 2.7: Adjustable locking cable system
Components of the locking cable system that assist in specimen vertical position adjustability. Changing the hanging cable length adds to the adjustment provided through the top bar holes (Figure 2.6b), and allows specimen height to be varied with ease.

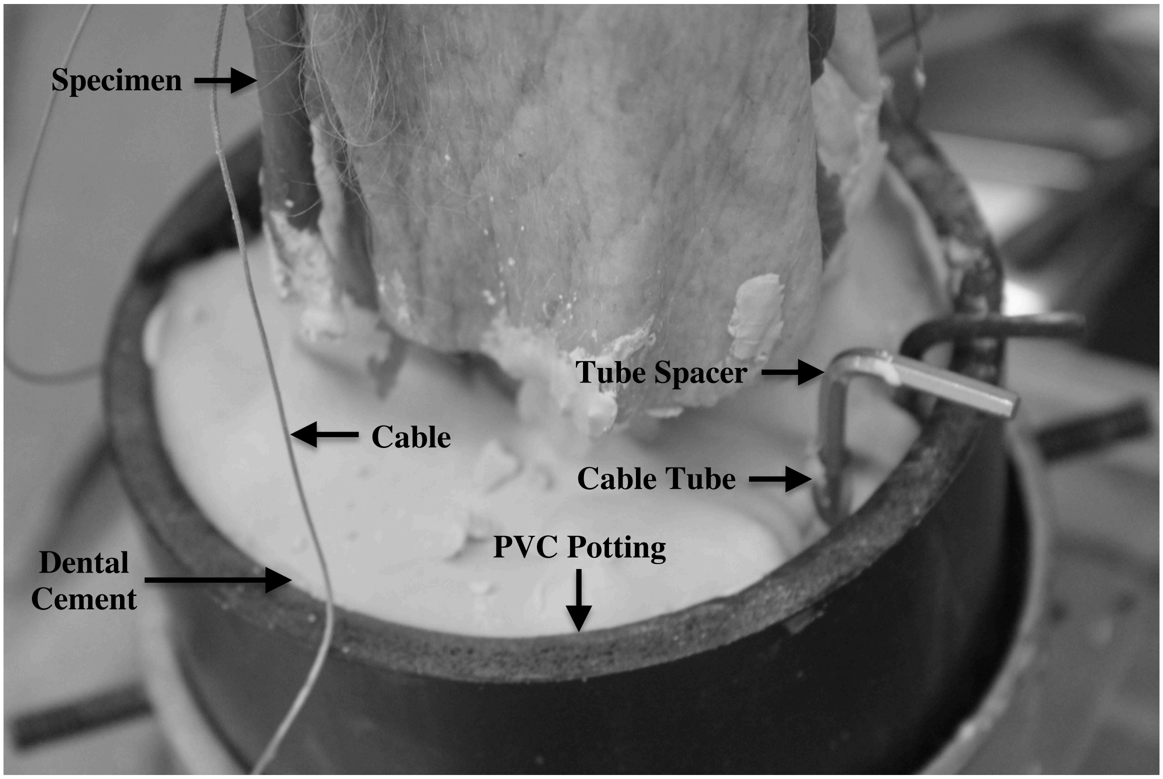

Figure 2.8: Potting tendon lead tubing
Cable tubes are cemented into the specimen potting to ensure that the tendon cables can travel through the cement, proving more anatomical alignment of muscle force lines of action. Allen keys are used as tube spacers to ensure that expansion during cement setting does not collapse the tubing.

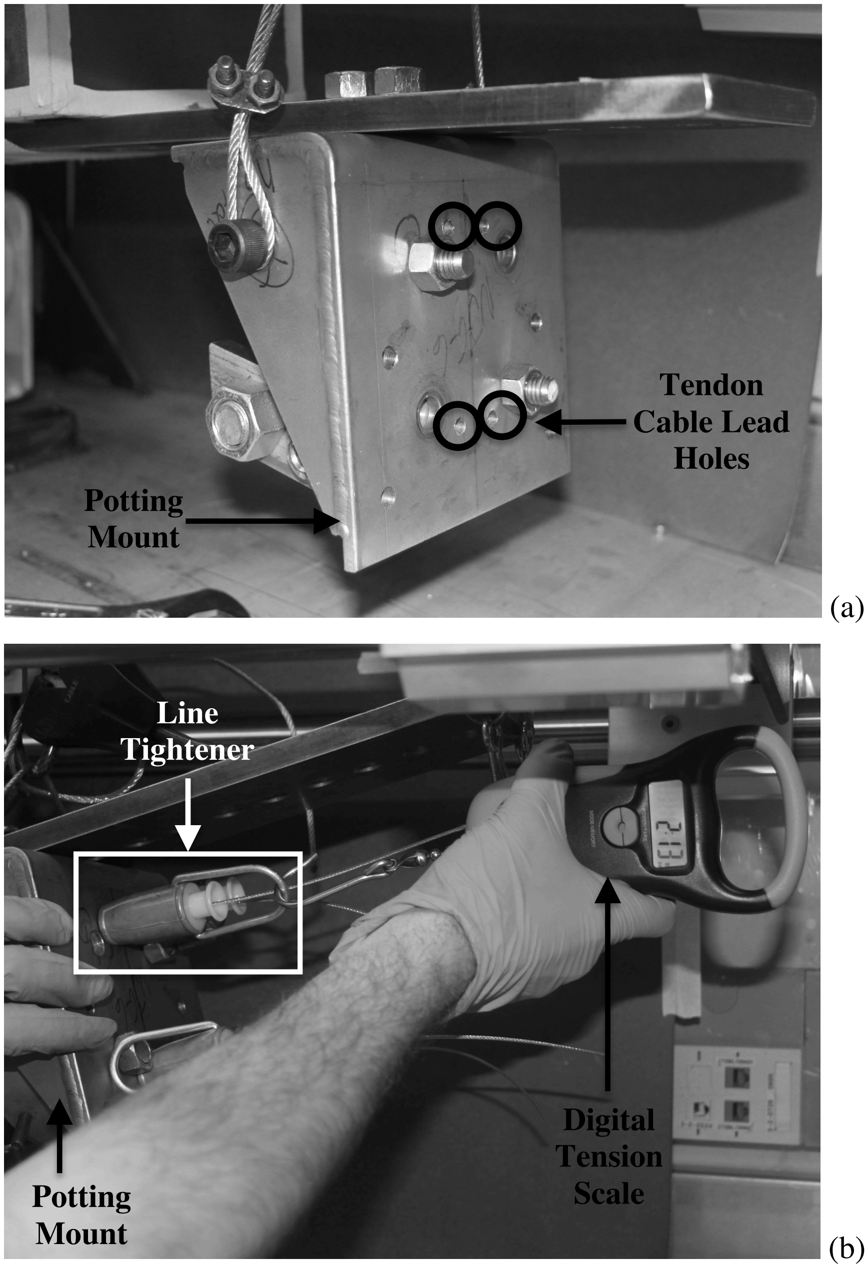

Figure 2.9: Tendon tension locking system
Components of the tendon tension locking system including the lead holes (a) allowing for anatomical alignment and the line tighteners (b) used to control the load applied through the selected tendons. A digital tension scale is used to measure the tension in a tendon. Line tighteners are adjusted such that they begin to lift off the back of the potting mount when the desired tensile force is applied.

the line tightener. The position of the line tightener was adjusted such that it just began to lift off the back of the potting mount when the load displayed on the tension scale equalled the desired load in the tendon.

2.2.2 APPARATUS ASSESSMENT

The second objective of this work was to assess the reliability of the new apparatus' operation. In doing so, functional guidelines were established that would act as a reference for future testing protocols.

2.2.2.1 PRESSURE REGULATION

To compare the performance between the original and new pressure regulation systems, plots were created of pressure output vs. input voltage. As the two systems work on separate voltage scales, pressure output was recorded at varying voltage increments for each system. First, the original pressure regulator was used, and the resulting output pressure was recorded at voltage increments of 0.05 V from 0 V to 1.5 V and back to 0 V. Testing was then repeated, substituting the existing pressure regulator for the new PPC, recording pressure from 0 V to 5 V and back to 0 V in 0.5 V increments.

2.2.2.2 IMPACT ASSESSMENT

A series of impacts were performed starting at 5 psi and increasing in 1 psi intervals up to 12 psi (full procedures are found in Appendix D). Three different ram masses were tested (1.28 kg, 3.31 kg and 6.66 kg) and a constant ram distance of 520 mm was used. Testing was conducted against the intermediate impact plate, with damping pistons absorbing all of the post-impact energy. No test specimen was used. Output variables of interest were the ram velocity, kinetic energy and peak impact force, which were recorded for each trial. The above procedures, at all three masses, were repeated three times to assess within-day repeatability while the 6.66 kg mass was tested between two days (k = 2) to assess between-day apparatus repeatability.

Each output parameter was plotted against input pressure (separate plots for each ram mass), with the coefficient of determination (R^2) used to quantify the relationships (linear regression was used for ram velocity and axial force, while quadratic was used for ram kinetic energy). Two-way random, absolute agreement, single measures ICC analyses (ICC 2,1) were conducted to determine the within-day repeatability (McGraw and Wong, 1996) while two-way random, absolute agreement, average measure ICC analysis (ICC 2, k) were used to assess between-day reliability (Burkhart *et al*., 2012c; Shrout and Fleiss, 1979). ICC values were categorized as follows: ICC < 0.4 = poor; 0.4 < ICC > 0.59 = fair; 0.6 < ICC > 0.74 = good; and ICC > 0.74 = excellent (Grove, 1981). ICCs were calculated using SPSS software (version 20; IBM; Armonk, NY).

2.3 RESULTS

2.3.1 APPARATUS ASSESSMENT

2.3.1.1 PRESSURE REGULATION ASSESSMENT

The original pressure regulation system exhibited hysteresis when transitioning between rising and falling pressures (Figure 2.10a), which was eliminated when the new PPC pressure regulation system was implemented (Figure 2.10b). Furthermore, the new PPC was found to have a linear relationship with voltage input, an improvement from the original system that showed an initial non-linear lead-in period (up to approximately 0.6 V).

2.3.1.2 WITHIN-DAY ASSESSMENT

Across all ram masses, the R^2 values fell between 0.97 – 1.00, demonstrating strong correlations between input pressure and the output variables (Figure 2.11). Additionally, with ICC's ranging from 0.98 – 1.00 there was excellent within-day repeatability (Table 2.2). Within-day specimen and summary data can be found in Appendices E.1 and E.2.

2.3.1.3 BETWEEN-DAY ASSESSMENT

Similar to the within-day findings, excellent correlations were found between the input pressure and the between-day output measures (0.98 – 0.99) (Figure 2.12). Furthermore, excellent reliability was found for between-day impactor operation, with ICCs of 0.99 for all measures (Table 2.2). Between-day specimen and summary data can be found in

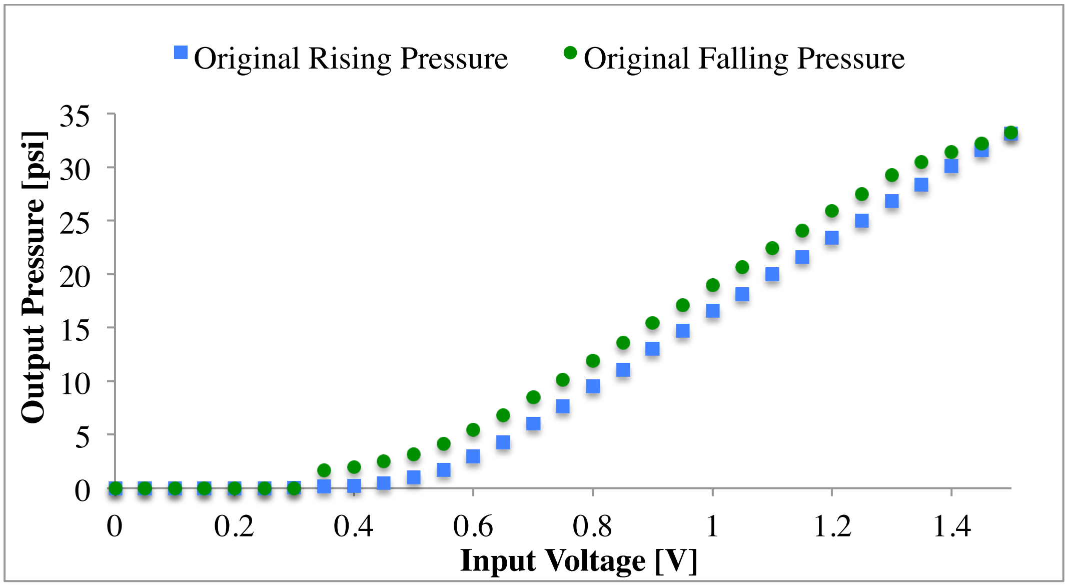

(a)

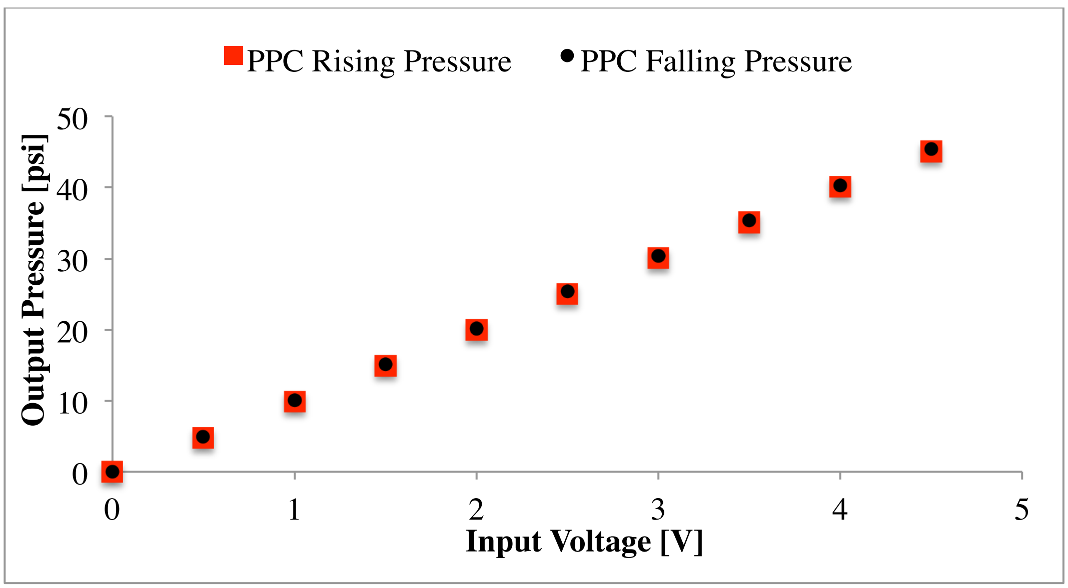

(b)

Figure 2.10: Pressure vs. voltage curves

Comparison of the relationships between the input voltage and output pressure for the original (a) and new (b) systems. When hysteresis was not detected in the PPC, the input voltage range was extended (increased range on x-axis) to investigate variation at higher pressure; however, PPC performance remained linear.

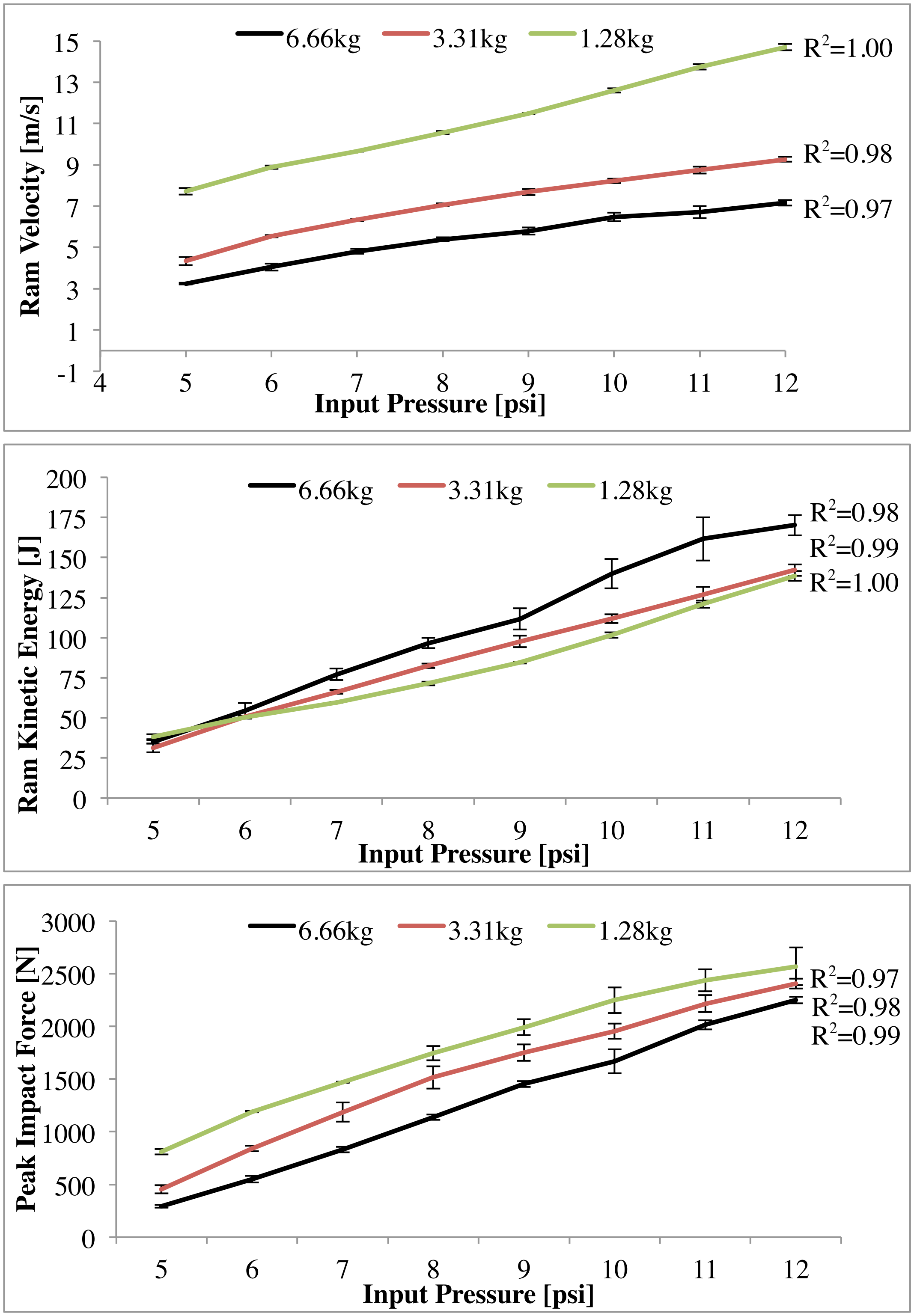

(a)

(b)

(c)

Figure 2.11: Within-day relationships

Within-day relationships between the input pressure and output measures of ram velocity (a), ram kinetic energy (b) and peak impacting force (c). Error bars indicate SD over three trials.

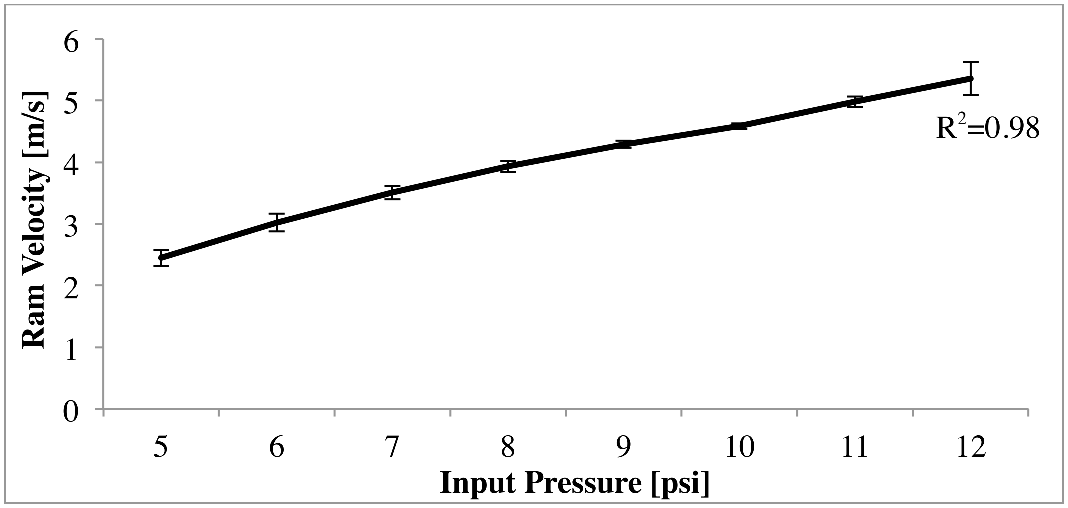

(a)

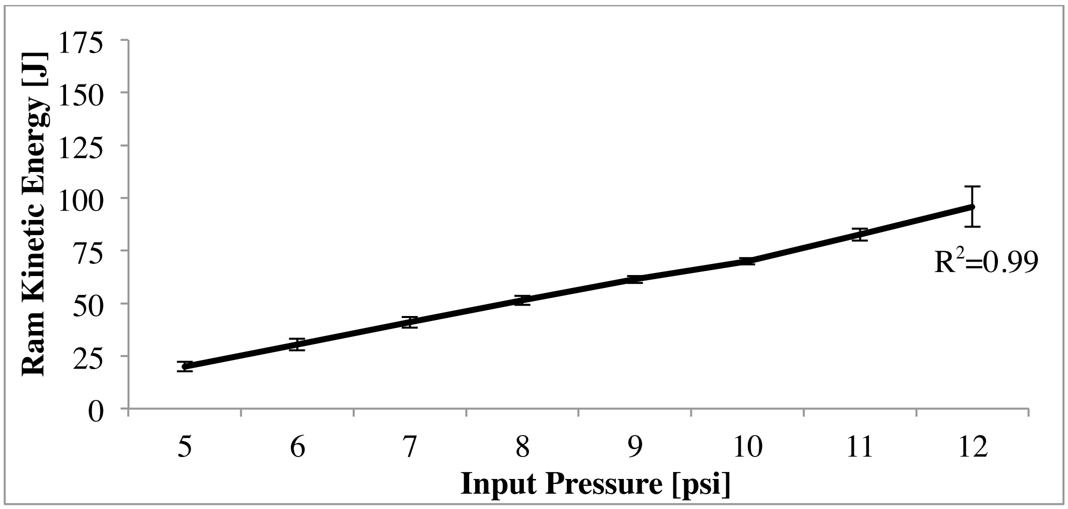

(b)

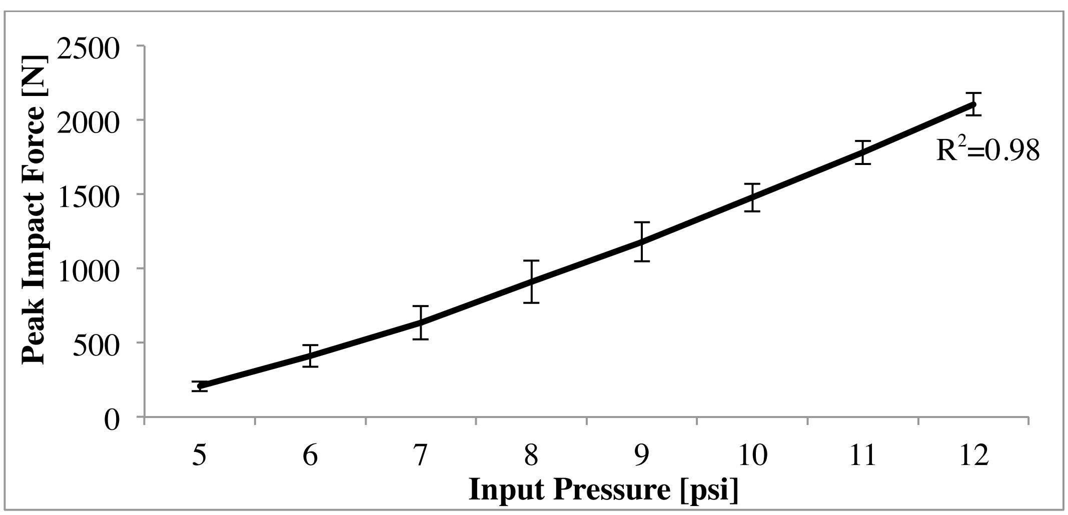

(c)

Figure 2.12: Between-day relationships

Between-day relationships between the input pressure and output measures of ram velocity (a), ram kinetic energy (b) and peak impacting force (c) using the 6.66 kg mass. Errors bars indicate SD over two trials.

Table 2.2: Summary of the ICCs for within- and between-day.

	Within-Day			Between-Day
Variable	1.28 kg	3.31 kg	6.66 kg	6.66 kg
Ram Velocity	0.99	0.99	0.98	0.99
Ram Kinetic Energy	1.00	0.99	0.98	0.99
Peak Impact Force	0.99	0.99	1.00	0.99

Appendices E.3 and E.4.

2.4 DISCUSSION

By implementing specific design improvements, key design challenges present in the original apparatus were addressed. The strong correlations between input pressure and output measures, coupled with the excellent within- and between-day reliability demonstrate the precise control of the new impact apparatus. Together, these measures suggest that the new impact apparatus is proficient in its desired function, and ready to conduct *in vitro* cadaveric fracture analysis.

2.4.1 APPARATUS DESIGN

To improve testing efficiency and expand apparatus capability, the design challenges identified (Table 2.1) were addressed through the fabrication of a new impactor. Hanging the specimen in a pendulum style support created extra degrees-of-freedom that were previously not available, eliminating the resulting moment and greatly reducing the likelihood of damaging the specimen support structure (*Requirement #1*). Additionally, the new locking cable system provides the user with fine control over height adjustment allowing for more accurate control over the vertical alignment between the specimen and load cell. Finally, these design improvements to specimen positioning allow for axial, planar or three-dimensional impact testing (*Requirement #2*).

In an attempt to safely dissipate the impact energy, two removable hydraulic damping pistons were attached to the new apparatus chamber and oriented to contact the intermediate impact plate post-impact. The addition of these pistons dampens out the post-impact energy, reducing the likelihood of structural damage and improving operator safety (*Requirement #3*).

Overall, the PPC was seen as a better system for pressure regulation as it resulted in a linear relationship between the input voltage and the resulting pressure for pneumatic control. This decreased the protocol times by allowing the user to more accurately set the pressure initially (*Requirement #4*). Furthermore, the reduction in hysteresis seen in the new system allows the user to easily correct the pressure if it is initially under or overset.

The new system implements a wye-fitting torpedo bay door, requiring the user to simply unthread the end-cap in order to gain access to the ram. This design removes interference with the testing chamber, provides convenient ram access and aids in controlling the ram-reset distance (*Requirement #5*). A tether that attaches the ram to the threaded seal of the torpedo door, combined with the addition of an adhesive ruler (affixed to the outer surface of the acceleration tube) improves the ability of the user to accurately reset the ram start distance (*Requirement #6*).

Finally, with the implementation of 'line tighteners', loads can be applied to four musculotendinous units. The tendon is sutured and attached to an aircraft cable that is threaded through holes in the potting cement and the specimen potting mount. This configuration allows for substantial muscle loads along anatomical lines-of-action characteristic of those found *in vivo* (Burkhart and Andrews, 2013; Holzbaur *et al*., 2005) (*Requirement #7*).

2.4.2 APPARATUS RELIABILITY ASSESSMENT

The regression analysis showed strong correlations between the input pressure and the dependent variables (ram velocity, ram kinetic energy and peak impact force) suggesting that these parameters can be accurately targeted across a range of masses. The results of the reliability analysis demonstrated excellent within- and between-day reliability for all variables. This ensures that the external loads that the impact apparatus applies to specimens are consistent between impacts and specimens.

Together, the pressure input curves and the reliability analysis confirmed the repeatable operation of the new impact-loading apparatus. As the two main variables used to determine the impact velocity and energy are the input pressure and the ram's mass, the data produced from this work (Figures 2.11 and 2.12) can be used to select an appropriate mass-pressure combination. With these improvements in place, the new impact loading apparatus has met the design requirements and overcome the design challenges of the original apparatus while maintaining operator safety. The new apparatus is operational and can be used to assess the effect of muscle load on the threshold of distal radius fractures in cadaveric subjects.

2.5 REFERENCES

Burkhart, T. A., Andrews, D. M., Dunning, C. E., 2012a. Failure characteristics of the isolated distal radius in response to dynamic impact loading. Journal of Orthopaedic Research: Official Publication of the Orthopaedic Research Society 30, 885-892.

Burkhart, T. A., Clarke, D., Andrews, D. M., 2012b. Reliability of impact forces, hip angles and velocities during simulated forward falls using a novel Propelled Upper Limb fall ARrest Impact System (PULARIS). Journal of Biomechanical Engineering 134, 011001-1 - 011001-8.

Burkhart, T. A., Andrews, D. M., 2013. Kinematics, kinetics and muscle activation patterns of the upper extremity during simulated forward falls. Journal of Electromyography and Kinesiology 23, 688-695.

Grove, W. A., 1981. Statistical Methods for Rates and Proportions. American Journal of Psychiatry 138, 1644-1645.

Holzbaur, K. R., Murray, W. M., Delp, S. L., 2005. A model of the upper extremity for simulating musculoskeletal surgery and analyzing neuromuscular control. Annals of Biomedical Engineering 33, 829- 840.

Krackow, K. A., Thomas, S. C., Jones, L. C., 1986. A new stitch for ligament-tendon fixation. Brief note. The Journal of Bone and Joint Surgery.American Volume 68, 764-766.

McGraw, K. O., Wong, S. P., 1996. Forming Inferences About Some Intraclass Correlation Coefficients. Psychological Methods 1, 30-46.

Quenneville, C. E., Fraser, G. S., Dunning, C. E., 2010. Development of an apparatus to produce fractures from short-duration high-impulse loading with an application in the lower leg. Journal of Biomechanical Engineering 132, 014502-1 - 014502-4.

Quenneville, C. E., 2009. Experimental and numerical assessments of injury criteria for short-duration, high-force impact loading of the tibia.

Shrout, P. E., Fleiss, J. L., 1979. Intraclass correlations: uses in assessing rater reliability. Psychological Bulletin 86, 420-428.

CHAPTER 3

DEVELOPMENT AND VALIDATION OF A COLOUR-THRESHOLDING TECHNIQUE TO QUANTIFY HIGH-SPEED PLANAR MOTION IN THE ISOLATED DISTAL RADIUS

3.1 INTRODUCTION

To develop appropriate strategies for decreasing the prevalence of distal radius fractures, it is important to first quantify the injury mechanisms (kinematics and kinetics) associated with these injuries through *in vitro* investigations (Section 1.4.2). While the kinetics (*e.g.*, forces) can be measured relatively easily through the use of load cells, the high load rates associated with impact events makes it more difficult to assess the kinematics (*e.g.*, velocity, acceleration). Optoelectronic motion tracking systems that use active or passive reflective markers (*e.g.*, Optotrak, Northern Digital Inc., Waterloo, ON; EvaRT, Motion Analysis Corporation, Santa Rosa, CA) are commonly used in biomechanical application; however, the low capture frequency (~30 - 100 Hz) of these systems, combined with the rapid nature of impact (*i.e.*, fracture load rates of 1029 kN/s, impulse durations of 31 ms) (Burkhart *et al.*, 2012b), makes their application less than ideal in impact scenarios. High-speed cameras (typically > 1000 fps) (Stockum and Gorenflo, 1994) have be used to document impacts and fracture (*e.g.*, determine region of crack onset) (Cristofolini *et al.*, 2007; de Bakker *et al.*, 2009), and regular frame-rate cameras have been used to quantify specimen kinematic parameters (*e.g.* segment position, velocity and angle) (Burrows and Morris, 2001; McLachlin *et al.*, 2011; Patterson *et al.*, 1998); however, kinematic measures have rarely been quantified from high speed video data simultaneously with fracture analysis.

Video analysis for kinematic parameters often occurs post-data collection and most commonly employs either feature recognition (Brydges *et al.*, 2012) or colour-thresholding techniques (McLachlin *et al.*, 2011) to isolate a marker from its surroundings. Once isolated, the *x*- and *y*-position coordinates of the marker's centroid can be determined with respect to the camera frame of reference. While this has traditionally required relatively expensive third-party software (*e.g.*, ~ $8000 for ProAnalyst Professional Edition, Xcitex; Cambridge, MA) (Brydges *et al.*, 2012; Patterson *et al.*, 1998), several data collection software programs (*e.g.,* LabVIEW version 10.0 (National Instruments; Austin, TX), MATLAB (Mathworks; Natick, MA)) now contain the required programming tools (Kolahi *et al.*, 2007). To the author's knowledge, however, programs such as these have not been validated for the analysis of impact kinematics. Therefore, the purpose of this study was to evaluate the efficacy of a motion tracking system incorporating a high-speed camera and colour-thresholding analysis techniques to quantify distal radius impact kinematics.

3.2 METHODS

3.2.1 CUSTOM OPTICAL TRACKING SYSTEM

A high speed camera (MotionScope M3, Red Lake Imaging, San Diego, CA; 2000 fps, 640 x 256 px at 0.000475 m/px) with factory image acquisition software (Redlake Imaging Studio 1.6.2; Red Lake Imaging, San Diego, CA) was used in combination with custom markers and the image analysis feature of LabVIEW (National Instruments; Austin, TX) to create an in-house motion analysis system. The markers were circular dots (approximately 0.01 m in diameter) whose colour could be varied. Colour was selected to be distinctive from the background colour of the image to be tracked, so as to provide the greatest contrast possible in the RGB spectrum (*e.g.*, a white marker on a black object). Appropriate marker size and colour were determined through pilot testing, and were chosen to ensure that the marker diameter was greater than resolution of the system (Muacevic *et al.*, 2000), as well as to differentiate the marker from other shapes in the camera frame. Marker size was also used as a calibration factor, converting camera pixels to SI units (*i.e.*, 0.000475 m/pixel).

The selected marker is placed on an object of interest and videoed during impact/motion. Each frame of a video is extracted using VirtualDub freeware (virtualdub.org), converted into a single picture (.jpeg), and each picture is then analyzed in sequence using a LabVIEW program adapted from a previously developed system (McLachlin *et al.*, 2011) (Figure 3.1). This program uses colour-thresholding (RGB spectrum), as well as area and perimeter constraints, to isolate the marker from the background image for each frame of the video, outputting the *x*- and *y*-coordinates of each marker's centroid in the camera's frame of reference based on the aforementioned calibration factor. Once the marker's position data are determined, velocity and acceleration are easily calculated as the first and second derivatives of the position with respect to time, respectively.

3.2.2 MOTION TRACKING VALIDATION

To validate this new marker tracking system, a white marker was placed on a black steel bar (0.02 m diameter, 0.065 m length) connected to the linear actuator of an Instron® materials testing machine (Instron® 8874, Instron; Canton, MA) (Figure 3.2) (see Appendix F for assessment procedures). The Instron® was programmed in displacement control to move through a triangular waveform with an amplitude of 0.02 m at a rate of 0.02 m/s. The high-speed camera was placed at 0.5 m from the actuator and used to record the motion of the steel bar for 3 seconds. A different LabVIEW program synchronized the outputs from the Instron® (axial position collected at 2000 Hz) and camera system (frames) through a triggering mechanism that initiated data collection from both systems simultaneously. Testing was repeated a total of four times.

Position data from both the Instron and marker tracking program were dual-pass filtered using a 4th order low-pass Butterworth filter at a cut-off frequency of 8.5 Hz, as determined through residual analysis conducted for each system separately (Burkhart *et al*., 2011; Winter, 1990) (sample in Appendix G). The filtered position data were then used to calculate the velocity and acceleration. Percent differences were calculated between the Instron® (acting as the expected (gold standard) values) and camera data for peak position, average positive velocity, and peak acceleration. Average positive velocity was calculated over the positive velocity plateau (~1.5 s), defined as the time over which velocity remains relatively constant. Finally, the time lag between the two systems was quantified at the time of peak position, zero velocity and peak acceleration.

3.2.3 ISOLATED RADIUS TESTING

The high-speed camera system (Section 3.2.1) was integrated with the new impact

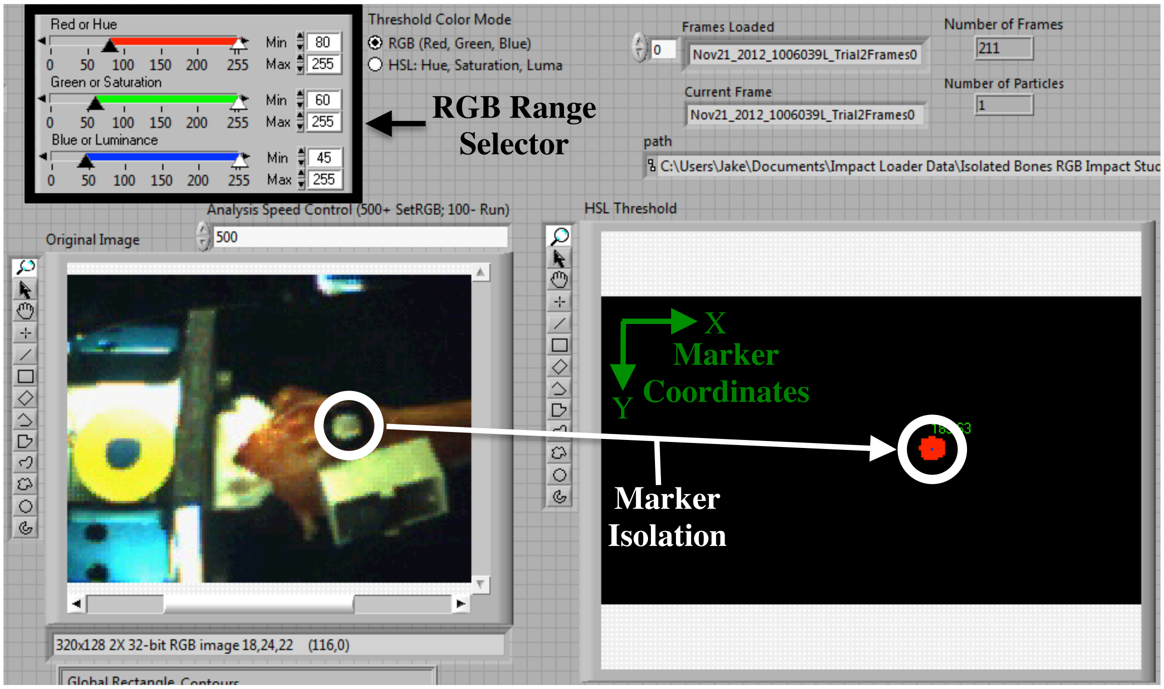

Figure 3.1: Custom colour-thresholding LabVIEW program front panel
A screenshot showing the user controls of the colour-thresholding system and the transformation from the video (left panel) to the measurement (right panel) views. The colour-thresholding technique operates by converting each pixel of the image into a Boolean function. For example, if the pixel's red, green and blue values all fall within the specified ranges (on scales of 0 - 255), the pixel is assigned a value of true. Therefore, all that remains in the processed frame are false pixels that corresponded to the background, and true pixels that correspond to the marker. The remaining markers are then screened to see which has an area and perimeter that are within the user-defined limits; only those that pass all stages remain as true (Boolean valued) markers in the program. Once the appropriate RGB settings are determined, a camera calibration factor (meters/pixel) is found by measuring an object of known length, visible in the same plane as the motion-tracking marker. As a result, the position (*x*- and *y*-coordinates) of the markers centroid (in the cameras frame of reference) can be determined, from which velocity and acceleration can be calculated.

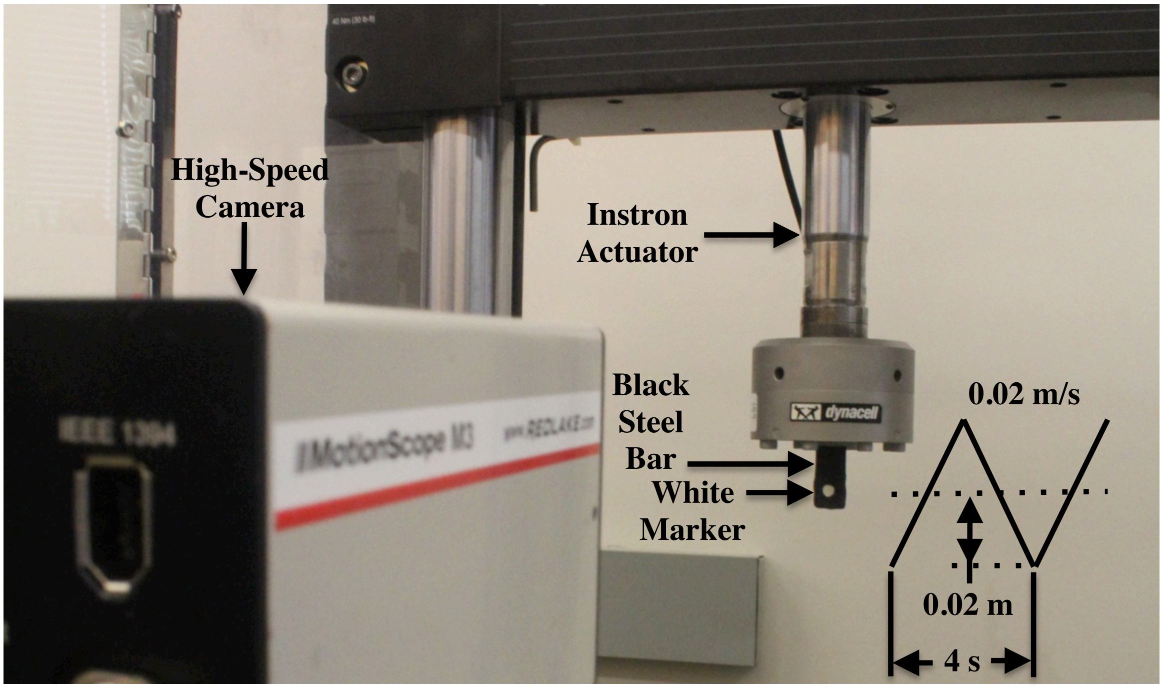

Figure 3.2: Motion tracking validation setup
Experimental set-up of the validation testing highlighting the magnitude and rate of the triangular waveform programmed into the materials testing machine, which served as the gold standard.

apparatus (Chapter 2) and its ability to track during impact testing was assessed using five fresh-frozen isolated cadaveric radii (*i.e.,* soft tissues removed) (see Appendix H for full assessment procedures). A custom marker was (0.01 m diameter; white with a black border to provide contrast) placed on the lateral surface of each radial styloid (Figure 3.3a). Using a custom designed potting jig, the specimens were cemented (Denstone Golden, Heraeus Dental; South Bend, IN) into 5 cm sections of 10 cm diameter PVC tubing, and then placed in the impactor. To simulate the position of the radius during a forward fall, specimens were positioned such that there was no frontal plane tilt, and the radius' longitudinal axis was at an angle of 75° in the sagittal plane (Burkhart *et al.*, 2012b; Burkhart *et al.*, 2011) (Figure 3.3b). In an attempt to recreate the anatomical radiocarpal interface, each specimen was buttressed against a high-density polyethylene model lunate-scaphoid (SawBones®, Pacific Research Labs, Vashon, WA) attached to a five degree-of-freedom load cell (Denton femur load cell model: 1914A; Denton ATD, Inc. Rochester Hills, MI) (Burkhart *et al.*, 2012b).

To determine an appropriate impact loading protocol that would minimize the number of impacts each specimen would be subjected to prior to fracture, one specimen was randomly selected for pilot testing. The pilot testing consisted of a ramped loading protocol beginning at an impact of 20 J (ram mass = 6.66 kg) and increasing in intervals of approximately 10 J until fracture was detected (fracture was defined as visual damage to the bone surface, which occurred at 80 J). As a result, the remaining four specimens were subjected to two initial pre-fracture impacts at 30 J to investigate intra-specimen variation, and a fracture impact of 80 J.

The resultant fracture force (calculated from the three orthogonal force values recorded by the impactor's load cell), resultant impulse, and ram velocity were recorded using a customized LabVIEW data acquisition program (Appendix I.1). The camera was used to record marker motion; however damage incurred to the specimens during fracture loading made it difficult to isolate the marker (*i.e.,* marker compression, fragments shadowing the marker). Therefore, only the two pre-fracture impacts were analyzed. The colour-thresholding marker tracking program (Section 3.2.1) (Appendix I.2) was used to extract the position data (*x*, *y*-coordinates) of the marker, and subsequently the specimen resultant

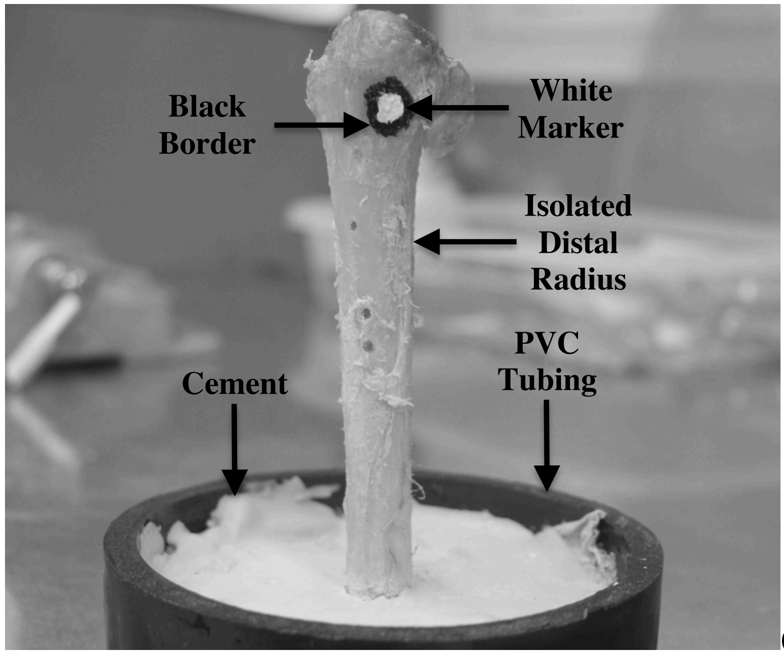

(a)

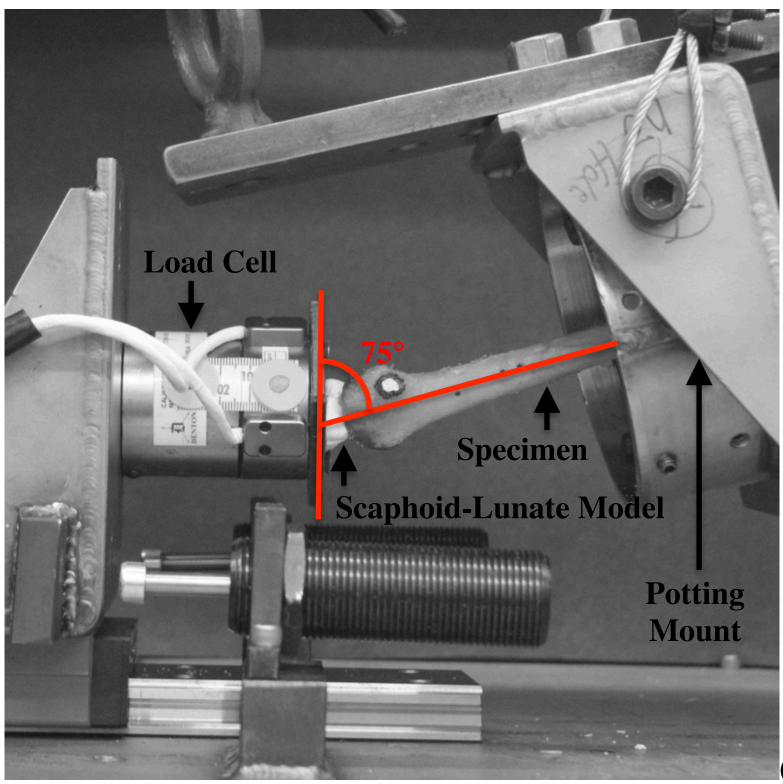

(b)

Figure 3.3: Isolated radius marker placement
To permit motion tracking, a custom white paint-based marker with a black border was applied to specimens (a), which were then hung in the impact apparatus (b) against a model scaphoid-lunate at an angle of 75° in the sagittal plane.

velocity and velocity angle were calculated. Together with their respective masses, the ram and specimen velocities were used to calculate ram and specimen kinetic energies.

3.3 RESULTS

3.3.1 MOTION TRACKING VALIDATION RESULTS

Overall, a relatively strong agreement was found between the custom motion tracking system and the Instron® data such that, the percent differences for the peak position, average positive velocity and peak acceleration were 1.4 (0.9) %, 1.0 (0.5) %, and 6.1 (3.3) %, respectively among the 4 repeated trials (Figure 3.4 shows a representative trial). Based on the offset of peak position, zero velocity and peak acceleration, between-system time lag was found to be 0.035 (0.014) s for all measures.

3.3.2 ISOLATED RADIUS FRACTURE RESULTS

Each specimen was subjected to a total of three impacts (two pre-fracture, one fracture), and fractured at an impacting energy of 80 J without having displayed visual signs of damage from pre-fracture impacts. To summarize, mean (SD) fracture force, impulse and ram energy were found to be 1746 (915) N, 9 (3) N·s and 79.2 (3.1) J, respectively (Table 3.1). Additionally, through the use of the colour-thresholding program, mean (SD) pre-fracture specimen velocity and kinetic energy were found to be 1.0 (0.1) m/s and 5.0 (1.2) J, respectively. This suggests that approximately 20 % of the ram's kinetic energy was transferred to specimen kinetic energy at impact (Table 3.1).

3.4 DISCUSSION

Given the prevalence and potential long-term effects of distal radius fractures, *in vitro* investigations have been launched to study the mechanisms surrounding this injury (Section 1.4.2). In an attempt to expand existing in-house impact testing capabilities to quantify impact kinematics (without the purchase of additional, expensive, third party software), a custom LabVIEW motion tracking data analysis program was designed. To the author's knowledge, custom programs have not been previously validated for impact

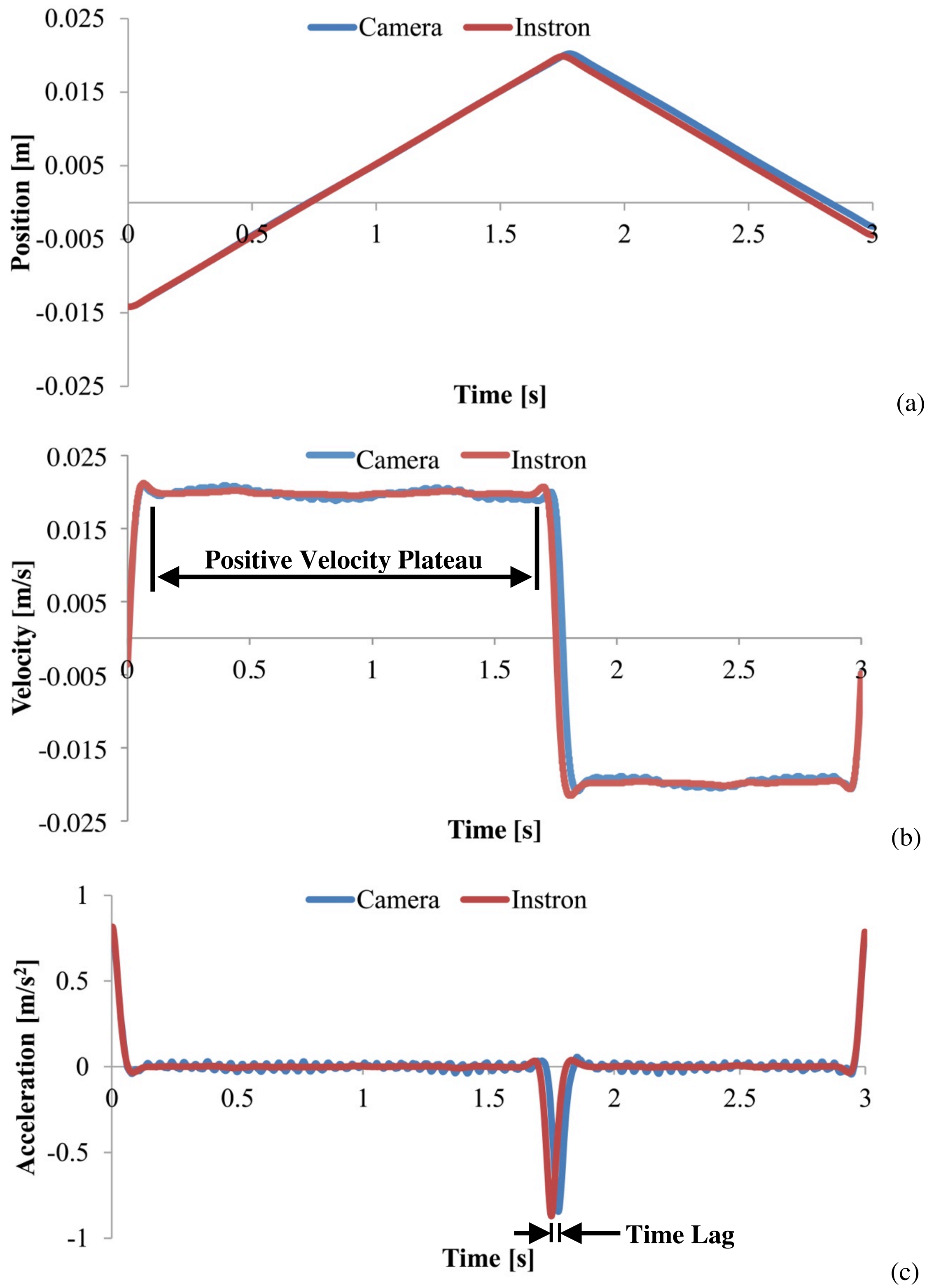

Figure 3.4: Camera and Instron motion data

Representative graphs comparing the Instron® and camera, position (a), velocity (b) and acceleration (c) measures.

Table 3.1: Pre-fracture and fracture measures for isolated radius impacts (Pre-Fracture n=8, Fracture n=4).

	Resultant Force		Velocity (m/s)			Energy (J)	
Condition	**Peak (N)**	**Impulse (N·s)**	**Ram[a]**	**Specimen Resultant**	**Specimen Resultant Angle (°)[b]**	**Ram[c]**	**Specimen[d]**
Pre-fracture 1							
1006039L	1671	9	3.0	1.0	26.6	30.4	4.3
1008004L	1515	14	3.0	1.2	11.0	29.4	6.4
1103022L	1568	8	2.9	1.0	23.8	27.8	4.5
1103026L	1323	8	2.9	0.9	32.1	28.4	3.8
Pre-fracture 2							
1006039L	1546	7	2.8	0.9	22.0	26.3	3.8
1008004L	1705	10	2.9	1.2	25.3	28.0	7.1
1103022L	1413	10	2.9	1.1	18.2	27.6	5.5
1103026L	908	6	3.1	1.0	36.5	31.6	4.4
Fracture							
1006039L	1183	6	5.0	-	-	81.6	-
1008004L	3107	13	5.0	-	-	81.9	-
1103022L	1456	10	4.8	-	-	75.4	-
1103026L	1238	6	4.8	-	-	78.0	-
Means (SD)							
Pre-fracture	1456 (254)	9 (2)	2.9 (0.1)	1.0 (0.1)	24.4 (7.9)	28.7 (1.7)	5.0 (1.2)
Fracture	1746 (915)	9 (3)	4.9 (0.1)	-	-	79.2 (3.1)	-

[a]As captured by velocity sensor on impactor

[b]Angle is clockwise from the horizontal axis

[c]Ram Energy = ½(Ram Mass)(Ram Velocity)^2, where ram mass = 6.66 kg

[d]Ram Energy = ½(Ram Mass)(Ram Velocity)^2, where mass is specimen specific

motion analysis. Therefore, it was necessary to evaluate the efficacy of this high-speed motion tracking system to quantify distal radius impact kinematics within the laboratory testing environment.

The initial phase of this study aimed to validate the proposed new custom motion-tracking system. The relatively low percent differences found when compared to an industry calibrated Instron® suggest that this high-speed system allows for accurate calculation of the position, and subsequently, velocity and acceleration of an object of interest. This is supported by the absolute error between the two systems' position data (0.289 (0.173) mm) being less than the resolution of the camera system (0.475 mm). Some noise amplification was evident in the velocity and acceleration outputs from the camera and Instron® systems, but this is most likely due to passing the data through successive derivatives (Antonsson and Mann, 1985). With maximum errors below 10 %, this was still considered acceptable.

While this is not the first custom motion-tracking system to be developed, most programs to date have focused on tracking participants through larger frames of reference, which understandably has resulted in greater error ranges associated with marker identification (position errors: 6 – 100 mm) (Corazza *et al.*, 2007; Lind *et al.*, 2005; Weinhandl *et al.*, 2010). Additionally, since the present system is focused on impact analysis, the capture frequency presently employed (2000 Hz) is well in excess of that reported for other systems (75 – 250 Hz) (Anderst *et al.*, 2009; Corazza *et al.*, 2006; Corazza *et al.*, 2007; Korstanje *et al.*, 2010; Weinhandl *et al.*, 2010). One study by Korstanje *et al.* (2010) focused their motion tracking, more specifically (using ultrasound) to track tendon motions at a rate of 120 Hz, and found tracking errors of 0.3 mm (1.6 %) that are comparable to the present investigation. Although the errors presented here are in agreement with the well-established Optotrack system (0.1 mm), Optotrack is only capable of sampling data between 30 Hz and 100 Hz, an inadequate capture rate for impact scenarios. A popular electromagnetic (EM) tracking system, The Flock of Birds (Ascension Technology; Milton, VT), has similar limitations on data collection rate (~60 Hz), with position error in the range of 0.25 mm (Milne *et al.*, 1996). Overall, the present system provides novel function by tracking high-speed motion with acceptable accuracy for impact analysis.

Presently, the colour-thresholding system requires initial manual input of the marker isolation constraints (*e.g.,* RGB and area ranges). While this is a relatively straight-forward process, standardizing the marker size (to maintain consistent area and perimeter ranges) and contrast (to maintain consistent RGB thresholds), as well as ensuring adequate lighting, would allow this step of the program to be automated, permitting real-time motion data analysis. Furthermore, additional lighting would also permit increases in the camera frame rate (max frame rate of the present camera is 32,000 Hz), allowing for finer sampling intervals that would better match the rate of bone fracture (0.08 – 0.50 ms) (Juszczyk *et al*., 2010; Juszczyk *et al*., 2012).

The presence of a time lag between the two systems could potentially result in errors if the timing between two variables (e.g., peak force and impact velocity) was of interest. The LabVIEW program that synchronized the collection of data (via triggering) uses computer memory to run, and the less memory that is available, the slower the program operates (National Instruments, 2011). While the camera uses on-board memory to store the collected images, the triggering of the camera and Instron® is controlled by a separate computer. Accordingly, it is speculated that this time lag arose because of execution delays within the computer program (a function of computer memory usage at the time the program ran). In the current investigation, since each output was analyzed independently through post processing, this time lag is unlikely to have significantly affected any of the findings reported here.

With the validated camera system in place, the second goal of this study was to incorporate motion analysis with the impact apparatus developed in Chapter 2. This was accomplished successfully, allowing kinematic measures to be quantified without purchasing additional third party software, expanding current testing capabilities. For example, previously, the impact system was only capable of quantifying ram velocity. While this provided insight into the impacting energy, direct measurement of the velocity of one of the impacted surfaces (*i.e*., the impacting plate or specimen) was unavailable. The addition of the new camera and colour-thresholding motion tracking system allows for post-impact specimen velocity to be calculated and compared to previously reported *in vivo* values of wrist velocity at impact. For example, the styloid process pre-impact velocity reported in the current investigation agrees relatively well with that of Burkhart, *et al*. (2013) who found an *in vivo* mean (SD) wrist impact velocity of 1.5 (0.4) m/s for sub-fracture 0.10 m forward falls. This agreement confirms that the impacts simulated in the present investigation were relevant to forward fall induced upper extremity impacts.

The ability to determine specimen velocity also permits the calculation of specimen kinetic energy, which can be compared to the ram's kinetic energy. This provides insight into the percentage of the ram's energy that is transferred to the specimen at impact, resulting in bone strain and post-impact specimen motion. A previous *in vitro* study of cadaveric forearm impacts by Kim *et al*. (2006) reported force transmission ratios by comparing forces detected on either side of an impact, and found that impacts to the bare palm (as opposed to wearing a wrist guard, gloves, *etc*.) typically have transmission ratios of 75 %. Previous *in vitro* forearm impact studies have also quantified energy absorption (39 %) and force attenuation factors (32 %) from force time curves, but have focused on differences between test conditions (*e.g*., wrist guard vs. bare palm) rather than across an impact (Hwang and Kim, 2004; Kim *et al*., 2006). As illustrated in the present investigation, specimen kinetic energy can be determined to provide insight into energy transfer throughout an impact. As *in vitro* studies have been shown (Section 1.5) to employ different methods of specimen fixation, the amount of impacting energy lost to specimen motion varies across studies. Accounting for reductions in impacting energy due to specimen motion would allow for a more direct comparison of impact energy thresholds when comparing the literature. Accordingly, future work should report not only the impacting kinetic energy, but also some measure of wrist velocity and kinetic energy.

Although it was not an initial aim of this study, the cadaveric impact data collected allowed for an initial assessment of the new impactor design. A similar study by Burkhart, *et al*. (2012) reported a mean (SD) fracture force of 2142 (1229) N and impulse of 14.2 (5.5) N·s that agree well with the values presented here. This provides further validation of the new impact-loading apparatus, demonstrating the relevance of study results produced with the new, more versatile apparatus.

The *in vitro* testing performed in this study is not without limitations. One potential shortcoming was the use of isolated specimens. To better recreate the native radiocarpal joint, a high-density polyethylene model lunate-scaphoid (SawBones®, Pacific Research Labs, Vashon, WA) was used for all impacts. While this ensured that the load passed through the radius, and that carpal fracture did not occur prior to radius fracture (Dennis *et al.*, 2011), the absence of soft tissues (*e.g.*, overlying muscles, the interosseous membrane) may have affected specimen alignment and support during impact (Berger, 1996). Additionally, the cadaveric nature of this study limited the sample size, which prevented a quantitative statistical analysis from being conducted (*e.g.*, ICCs could have been used to assess position and velocity measures) and in response, it was necessary to rely on qualitative measures. Despite this, the agreement of both the kinematic and kinetic measures with previous literature suggests that those reported here are accurate (Burkhart *et al.*, 2012b; Burkhart and Andrews, 2013). Specimen velocity and energy were only calculated for the pre-fracture impacts due to specimen destruction at fracture. On a positive note, the use of custom paint-based surface markers allows rigid body motions to be tracked without the use of bone pins (Patterson *et al.*, 1998), which have been shown to create stress concentrations that may alter a specimen's fracture threshold (Rogge *et al.*, 2002). However, to allow for the quantification of fracture impact velocities, future work should improve marker integrity (*e.g.*, use a rigid marker), improve lighting to avoid marker shadowing, and provide manual centroid selection on a frame-by-frame basis. By providing manual selection, even if the marker could not be isolated using the program, the user would be able to determine marker position data. To ensure the collection of impact velocity and energy data for both pre-fracture and fracture trials, a second marker should be placed on the rigid impact plate. By quantifying motion of the impact plate, the amount of energy that is lost between ram-strike and specimen-impact due to apparatus frictional losses could also be determined. Together, impact plate energy and specimen kinetic energy could then provide insight into how much of the impacting ram's energy is actually transmitted to specimens for the purpose of causing injury.

The validated colour-thresholding high-speed motion-tracking program presented in this chapter allows for the accurate calculation of pre-fracture specimen position, velocity and kinetic energy. Together this new information will further aid in characterizing high-speed cadaveric impact testing. Although LabVIEW was used specifically for this project, motion tracking can also be accomplished with other common data collection programs (*e.g.*, MATLAB (Kolahi *et al.*, 2007)) broadening the potential use of the approaches presented here. This system will allow future testing to not only report the magnitude of impact kinetic energy, but will also provide a measure of wrist velocity at impact that can be contrasted against *in vivo* upper extremity impact work to ensure that loading rates are appropriate. Furthermore, by knowing the impact plate and specimen kinetic energy at impact, energy losses can be quantified and clearer insight can be drawn into how much of the impacting energy is actually transferred to the specimen for the purpose of causing injury.

3.5 REFERENCES

Altissimi, M., Antenucci, R., Fiacca, C., Mancini, G. B., 1986. Long-term results of conservative treatment of fractures of the distal radius. Clinical Orthopaedics and Related Research 206, 202-210.

Anderst, W., Zauel, R., Bishop, J., Demps, E., Tashman, S., 2009. Validation of three-dimensional model- based tibio-femoral tracking during running. Medical Engineering & Physics 31, 10-16.

Antonsson, E. K., Mann, R. W., 1985. The frequency content of gait. Journal of Biomechanics 18, 39-47.

Berger, R. A., 1996. The anatomy and basic biomechanics of the wrist joint. Journal of Hand Therapy : Official Journal of the American Society of Hand Therapists 9, 84-93.

Brydges, E. A., Burkhart, T. A., Altenhof, W. J., Andrews, D. M., 2012. Reliability of Leg Soft Tissue Marker Motion Following Manual Digitization. In Canadian Society of Biomechanics/Societe Canadienne De Biomechanique, Simon Fraser University, Vancouver, BC.

Burkhart, T. A., Andrews, D. M., Dunning, C. E., 2012. Failure characteristics of the isolated distal radius in response to dynamic impact loading. Journal of Orthopaedic Research : Official Publication of the Orthopaedic Research Society 30, 885-892.

Burkhart, T. A., Andrews, D. M., 2013. Kinematics, kinetics and muscle activation patterns of the upper extremity during simulated forward falls. Journal of Electromyography and Kinesiology 23, 688-695.

Burkhart, T. A., Dunning, C. E., Andrews, D. M., 2011. Determining the optimal system-specific cut-off frequencies for filtering in-vitro upper extremity impact force and acceleration data by residual analysis. Journal of Biomechanics 44, 2728-2731.

Burrows, M., Morris, G., 2001. The kinematics and neural control of high-speed kicking movements in the locust. Journal of Experimental Biology 204, 3471-3481.

Corazza, S., Mündermann, L., Chaudhari, A., Demattio, T., Cobelli, C., Andriacchi, T., 2006. A markerless motion capture system to study musculoskeletal biomechanics: Visual hull and simulated annealing approach. Annals of Biomedical Engineering 34, 1019-1029.

Corazza, S., Mündermann, L., Andriacchi, T., 2007. A framework for the functional identification of joint centers using markerless motion capture, validation for the hip joint. Journal of Biomechanics 40, 3510- 3515.

Cristofolini, L., Juszczyk, M., Martelli, S., Taddei, F., Viceconti, M., 2007. In vitro replication of spontaneous fractures of the proximal human femur. Journal of Biomechanics 40, 2837-2845.

de Bakker, P. M., Manske, S. L., Ebacher, V., Oxland, T. R., Cripton, P. A., Guy, P., 2009. During sideways falls proximal femur fractures initiate in the superolateral cortex: Evidence from high-speed video of simulated fractures. Journal of Biomechanics 42, 1917-1925.

Dennis, H. H. W., Sze, A. C. K., Murphy, D., 2011. Prevalence of carpal fracture in Singapore. The Journal of Hand Surgery 36, 278-283.

Gabriel, S. E., Gabriel, S. E., Tosteson, A. N. A., Leibson, C. L., Crowson, C. S., Pond, G. R., Hammond, C. S., Melton, I.,L.J., 2002. Direct Medical Costs Attributable to Osteoporotic Fractures. Osteoporosis International 13, 323-330.

Hwang, I., Kim, K., 2004. Shock-absorbing effects of various padding conditions in improving efficacy of wrist guards. Journal of Sports Science and Medicine 3, 23-29.

Juszczyk, M., Cristofolini, L., Kaniuk, J., Schileo, E., Viceconti, M., 2010. A novel method for determining the time and location of abrupt fracture initiation in bones. The Journal of Strain Analysis for Engineering Design 45, 481-493.

Juszczyk, M. M., Cristofolini, L., Salvà, M., Zani, L., Schileo, E., Viceconti, M., 2012. Accurate in vitro identification of fracture onset in bones: Failure mechanism of the proximal human femur. Journal of Biomechanics 46, 158-164.

Kim, K., Alian, A. M., Morris, W. S., Lee, Y., 2006. Shock attenuation of various protective devices for prevention of fall-related injuries of the forearm/hand complex. The American Journal of Sports Medicine 34, 637-643.

Kolahi, A., Hoviattalab, M., Rezaeian, T., Alizadeh, M., Bostan, M., Mokhtarzadeh, H., 2007. Design of a marker-based human motion tracking system. Biomedical Signal Processing and Control 2, 59-67.

Korstanje, J. H., Selles, R. W., Stam, H. J., Hovius, S. E., Bosch, J. G., 2010. Development and validation of ultrasound speckle tracking to quantify tendon displacement. Journal of Biomechanics 43, 1373-1379.

Lind, N. M., Vinther, M., Hemmingsen, R. P., Hansen, A. K., 2005. Validation of a digital video tracking system for recording pig locomotor behaviour. Journal of Neuroscience Methods 143, 123-132.

MacDermid, J. C., Roth, J. H., Richards, R. S., 2003. Pain and disability reported in the year following a distal radius fracture: a cohort study. BMC Musculoskeletal Disorders; doi: 10.1186/1471-2474-4-24.

McLachlin, S. D., Al Saleh, K., Gurr, K. R., Bailey, S. I., Bailey, C. S., Dunning, C. E., 2011. Comparative assessment of sacral screw loosening augmented with PMMA versus a calcium triglyceride bone cement. Spine 36, E699-704.

Milne, A., Chess, D., Johnson, J., King, G., 1996. Accuracy of an electromagnetic tracking device: a study of the optimal operating range and metal interference. Journal of Biomechanics 29, 791-793.

National Instruments, 2011. Profiling VI Execution Time and Memory Usage. 2013, 1.

Patterson, R. M., Nicodemus, C. L., Viegas, S. F., Elder, K. W., Rosenblatt, J., 1998. High-speed, three- dimensional kinematic analysis of the normal wrist. The Journal of Hand Surgery 23, 446-453.

Rogge, R. D., Adams, B. D., Goel, V. K., 2002. An analysis of bone stresses and fixation stability using a finite element model of simulated distal radius fractures. The Journal of Hand Surgery 27, 86-92.

Shauver, M. J., Yin, H., Banerjee, M., Chung, K. C., 2011. Current and future national costs to medicare for the treatment of distal radius fracture in the elderly. The Journal of Hand Surgery 36, 1282-1287.

Stockum, L. A., Gorenflo, R. L., 1994. High-speed video instrumentation system. U.S. Patent and Trademark Office 5,301,240.

Van Staa, T., Dennison, E., Leufkens, H., Cooper, C., 2001. Epidemiology of fractures in England and Wales. Bone 29, 517-522.

Weinhandl, J. T., Armstrong, B. S., Kusik, T. P., Barrows, R. T., O'Connor, K. M., 2010. Validation of a single camera three-dimensional motion tracking system. Journal of Biomechanics 43, 1437-1440.

Winter, D.A., 1990. Biomechanics and Motor Control of Human Movement. John Wiley & Sons, Inc., Hoboken, New Jersey, 27-45.

CHAPTER 4

THE EFFECT OF STATIC MUSCLE LOADS ON FRACTURE THRESHOLD MEASURES FOR THE INTACT DISTAL RADIUS SUBJECTED TO IMPACT LOADING

4.1 INTRODUCTION

Several previous studies have aimed at quantifying the kinetics and kinematics of *in vivo* upper extremity ground impacts arising from forward falls (Burkhart and Andrews, 2010; Burkhart and Andrews, 2013; DeGoede *et al*., 2001; DeGoede and Ashton-Miller, 2002; Dietz *et al*., 1981; Grabiner *et al*., 2008; Groen *et al*., 2010; Hernandez *et al*., 2013; Hsiao and Robinovitch, 1998; Kim and Brunt, 2013; Kim and Ashton-Miller, 2003; Lo *et al*., 2003; Troy and Grabiner, 2007b; Troy *et al*., 2008; Wojcik *et al*., 1999). This work has provided a good understanding of how impact forces change when different fall strategies are employed (*e.g.,* highest forces during straight-arm falls) (Burkhart and Andrews, 2013; DeGoede and Ashton-Miller, 2002; Troy and Grabiner, 2007a). Importantly, these studies have also identified a preparatory muscle response in the forearm extensors and flexors that peak approximately130 ms to 250 ms prior to peak impact force (Burkhart and Andrews, 2013; Dietz *et al*., 1981). Despite the identification of this response, only one known study has simulated muscle loads during *in vitro* distal radius fracture testing; and this study failed to document the magnitude of the applied loads, as they were only simulated to position the wrist in extension (McGrady *et al*., 2001). As the muscle loads increase, it is suggested that the muscle stiffness increases, creating a stiffer segment that can ultimately result in greater force propagation through the soft tissues (Challis and Pain, 2008; Nigg and Liu, 1999; Pain and Challis, 2002; Pain and Challis, 2001); though muscle does not carry compressive loads, tension may effect shock propagation through the construct. This has the potential of increasing the risk of injury to the anatomical structures located proximal to the initial site of impact. Moreover, the application of joint reaction forces, arising from muscle insertion across joints, may also provide a more realistic strain distribution (Duda *et al*., 1998) in the radius and ulna, and it has been suggested that engagement of the musculature crossing a joint can improve the overall stability of the that joint (McGill *et al*., 2003; Santello, 2005).

In addition to potential muscle loading effects, the majority of *in vitro* studies to date have applied a single, quasi-static external load to induce fracture (Section1.5). These investigations have demonstrated variability in fracture measures, and identified a range of fracture forces (1104 N to 3986 N), impulses (14.2 N·s to 82 N·s) and energies (1.09 J to 362 J). The dynamic (impact) nature of a forward fall suggests that fracture testing should be conducted in a realistic manner to avoid applying fracture loads in excess of the injury threshold (Burkhart *et al*., 2012b; Lewis *et al*., 1997). Therefore the purpose of this work is to determine the significance of static forearm muscle loads on the fracture threshold measures of the *in vitro* distal radius in response to simulated forward fall impacts.

4.2 METHODS

4.2.1 SPECIMEN PREPARATION

A detailed description of the testing methods employed, complete with pictures, is presented in Appendix J; the following is a summary. Six pairs (3 male, 3 female; mean (SD) age 63 (11) years, height 171 (13) cm, weight 66 (31) kg, BMI 21.8 (7.0)) of intact, fresh-frozen human cadaveric forearms (*i.e*., disarticulated at the elbow with an intact wrist joint) were tested. Each specimen was screened for bone affecting disease (*e.g*., osteoporosis, osteopetrosis) prior to procurement to ensure that the sample was representative of a healthy population. Further, all specimens were CT scanned and examined under fluoroscopy to ensure no pre-existing bony injury (Establishing baseline images). The soft tissues were dissected 8 cm – 10 cm from the proximal end of the specimens to allow for potting, ensuring that no damage occurred to the interosseous membrane (IOM). The specimens were then fixed in full pronation by applying three screws through the proximal diaphysis of the radius and ulna, and were subsequently potted upright in 5 cm – 7 cm of PVC tubing using dental cement (Denstone Golden, Heraeus Dental; South Bend, IN). Specimen alignment during potting was maintained using a vertical laser level and potting jig to keep the specimen upright (sagittal plane – forearm longitudinal axis aligned with centered markings on the potting jig; frontal plane – wrist in a neutral posture, the long axis of the third phalange was aligned with a central marking on the potting jig in the same plane). During specimen potting, four plastic tubes were aligned with precut holes in the specimen potting mount to allow for passage of the tendon cables (Section 2.2.1.6). Following potting, incisions were made along the dorsal and palmar side of the forearm, exposing the tendons of extensor carpi ulnaris (ECU), extensor carpi radialis longus (ECRL), flexor carpi ulnaris (FCU), and flexor carpi radialis (FCR). Each of the tendons was isolated from the surrounding musculature and sutured with 0.5 mm thread (Spider Wire; Spirit Lake, IA; 100 lb capacity) using the Krackow technique (Krackow *et al.*, 1986). The thread's free end was then attached to an insulated galvanized steel cable, and the forearm skin was sutured closed to maintain the internal moisture of the specimens.

Two incisions were made on the dorsal aspect of the specimen, just proximal to the extensor retinaculum, exposing the underlying bone. Here, two rectangular 45° strain gauge rosettes (SGD-3/350-RY53, Omega Environmental; Laval, QC) were attached to the radius and ulna such that the central (45°) gauge was visually aligned with the long axis of the bone. To protect against moisture and abrasion from the overlying soft-tissues, the gauges were insulated using a fast-drying silicone sealant (Alex Fast Dry, DAP; Baltimore; MD). Finally, the phalanges were carefully removed prior to testing, to avoid interference between the specimen and the impact apparatus' base plate.

The specimens were placed in the impact apparatus (Figure 4.1) such that the forearm/impact-surface angle was 75° in the sagittal plane (Burkhart *et al.*, 2012b). A laser level aligned with a vertical marking on the hanging potting was used to ensure no axial rotation about the specimens long axis occurred. To set wrist extension, the specimen's palmar surface was buttressed against the impact plate, and a laser level was used to ensure that the radiocarpal joint (detected by palpation of the radial styloid) was aligned with the center of the load cell. To permit impact plate tracking, one custom white marker was placed on the edge of the plate in line with the load cell's z-axis. Three custom white markers (approximately 1 cm in diameter, with black borders) were placed on the visible side of each specimen (skin mounted); one on the outer ridge of the radial or ulnar diaphysis approximately 10 cm proximal to the radiocarpal joint, the second

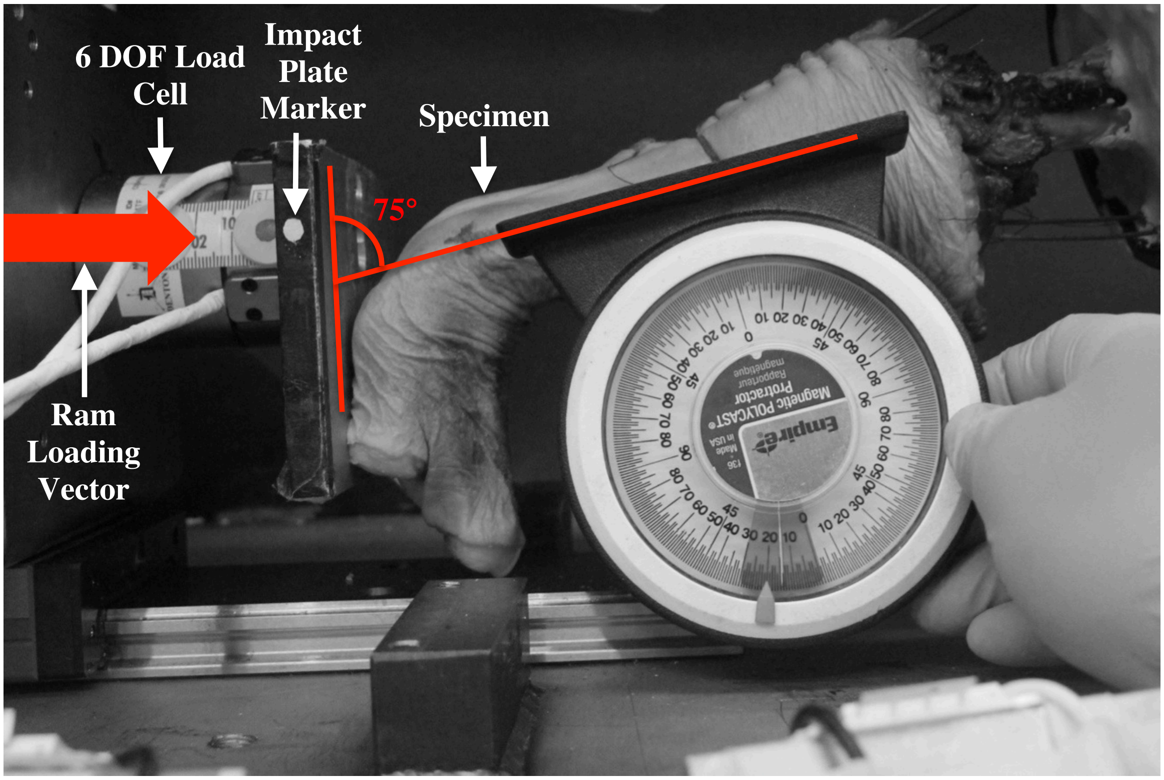

Figure 4.1: Testing configuration
Experimental set-up of the specimen orientation prior to impact highlighting the forearm/impact-surface interaction and angle. The apparatus was adjusted to ensure a specimen-impact plate angle of 75°.

located at the wrist joint center (found through repeated wrist flexion, extension and carpal palpation) and finally a third at the distal-most end of the first visible metacarpal (Figure 4.2). Finally, to simulate the effective mass acting on the wrist (Chiu and Robinovitch, 1998), additional masses were securely strapped to the top of the specimen's hanging potting mount. The ballasted mass was determined through pilot testing and targeted at a 40 % – 50 % of the donor's bodyweight.

To assess the effect of muscle load on the fracture strength of the distal radius, the six matched pairs were divided into two groups: muscle load (left arms) and no load (right arms). In the load group, using peak muscle forces (Holzbaur *et al*., 2005) and muscle activation patterns established for forward falls *in vivo* (Burkhart, 2011; Burkhart and Andrews, 2013), lower threshold targets of 19 N, 61 N, 9 N and 5 N were identified for ECU, ECRL, FCU and FCR, respectively. The tension was set in each muscle cable using a digital tension scale (78-0069-4; Matzuo America; South Sioux City, NE) attached to the loop on the line tightener (C78990V; Ben-Mor Cables Inc. Calgary, AB). The position of the line tightener was adjusted such that the desired tension was applied as it began to lift off the back of the specimen potting mount (Section 2.2.1.6). Each muscle force was measured three times, and specimens were impacted immediately following the final measurement.

4.2.2 IMPACT-LOADING PROTOCOL

Impacts were initiated when a weighted ram (6.66 kg) made contact with an intermediate impact plate subsequently transferring the impact force through a six degree-of-freedom load cell (Denton femur load cell model: 1914A; Denton ATD, Inc. Rochester Hills, MI) onto the palmar soft tissue of the specimen (Figure 4.1). Each specimen was subjected to an initial pre-fracture impact targeted at 25 J, followed by a 150 J fracture impact (the energy targets were determined through pilot testing). However, if a specimen did not fracture as a result of the second impact they were subsequently impacted in 20 J increments until fracture occurred (*i.e.,* 170 J, 190 J, *etc*.). All impacts were recorded using a high-speed camera (MotionScope M3, Red Lake Imaging, San Diego, CA; 2000 fps, 640 x 256 px at 0.000439 m/px) that was started simultaneously with the onset of data collection. Following each impact, anterior-posterior and lateral fluoroscopic images

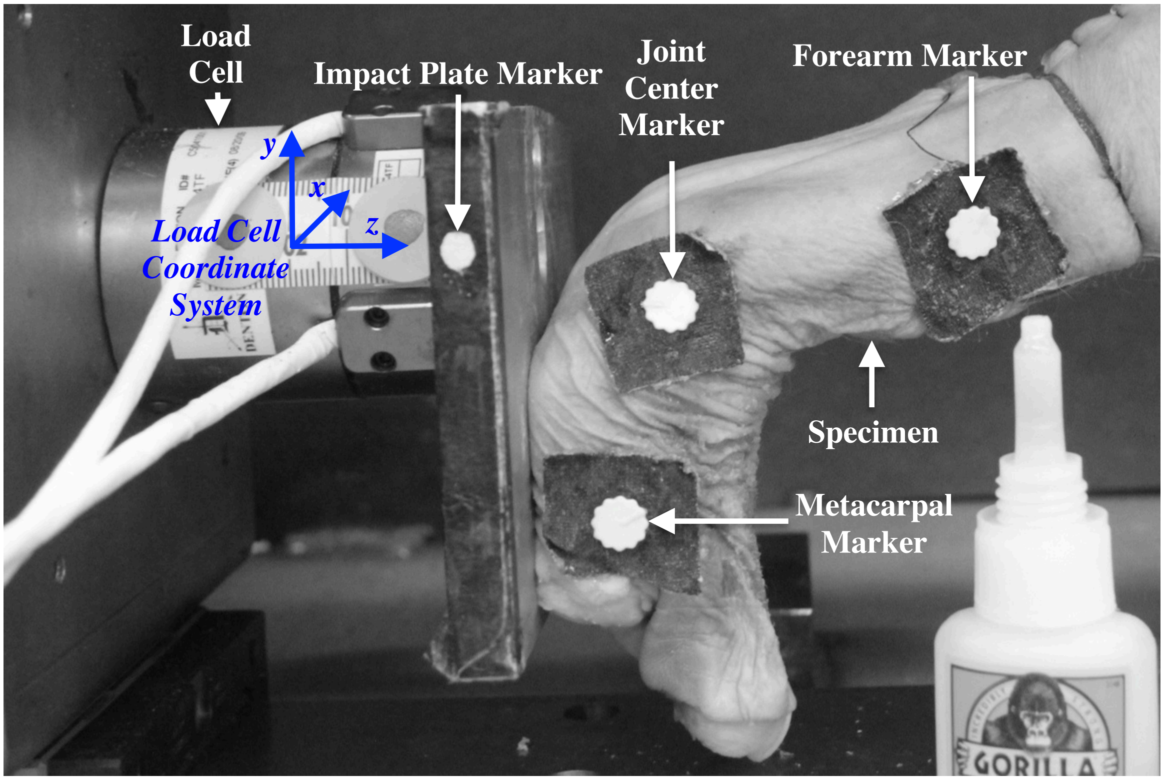

Figure 4.2: Wrist angle markers
The markers used to calculate the pre-impact wrist angle are shown, along with the marker used to track the motion of the intermediate impact plate. The load cell coordinate system (*x*-*y*-*z*) is shown, such that *z* is perpendicular to the impact plate, and *x* & *y* lie in a plane parallel to the palmar surface of the specimen.

were taken to determine if fracture occurred (compared to baseline images), as well as to ensure that there was no damage from the pre-fracture loading trials (images provided in Appendix K). Fracture was defined as the presentation of a break in the continuity of either the ulna or radius. Post-testing, an orthopedic surgeon examined the radiographs to classify fractures according to the AO Classification (Section 1.2.3) (Muller *et al*., 1990), and to determine the resulting volar tilt and radial inclination angles as per standardized guidelines (Kreder *et al*., 1996a).

4.2.3 DATA ANALYSIS AND STATISTICS

A custom designed LabVIEW program was used to collect all raw data at 15 kHz from which the peak forces (F_x, F_y, F_z, F_r), moments (M_x, M_y) and impulses (Im_x, Im_y, Im_z, Im_r) were determined (with respect to the load cell's reference frame). The load cell force data was transformed using trigonometric functions to orient the *x*- and *y*-axis as seen in Figure 4.2. Load rates (quantified as the slope taken between 30 % and 70 % of the peak force (Burkhart *et al*., 2012a; Duquette and Andrews, 2010)) and impulse durations were also calculated for all force components. The raw load cell data was low pass filtered using a 4th order dual-pass Butterworth filter and cutoffs were derived individually for each channel of data (F_x, F_y, F_z, M_x and M_y) from residual analyses conducted for pre-fracture and fracture trials separately (Table 4.1) (again, see Appendix G for sample residual analysis procedure).

Peak axial, and maximum/minimum principal strains, from both the radial and ulnar gauges, were collected and used to calculate load sharing as percentage of radial strain (Eq. 4.1). In addition, the strain rates were calculated using the same method described above (*i.e.,* from the slope taken between 30 % and 70% of the peak strain). As the purpose of this investigation was focused towards distal radius fractures, which were expected to occur at peak radial strain (McElhaney, 1966), radius-ulna load sharing at time points leading up to this event were of interest to investigate if radius-ulna load sharing would change en-route to injury. Peak axial (*i.e*., strain from the central 45° gauge of the applied rosette), and maximum and minimum principal radial strains were identified, and load sharing was determined

Table 4.1: Cutoff frequencies used for pre-fracture and fracture data analysis.

Data Channel	Pre-fracture [Hz]	Fracture [Hz]
F_x	510	355
F_y	540	425
F_z	335	680
M_x	600	600
M_y	595	590
Impact Plate Marker	60	60
Wrist Marker	40	-
Forearm Marker	40	-

at four time points corresponding to 25 %, 50 %, 75 % and 100 % of the peak radial strain according to Equation 4.1:

$$Radial\ Load\ Share = \frac{Radius\ Strain}{Radius\ Strain + Ulna\ Strain} \times 100\ \% \qquad (4.1)$$

The colour-thresholding program described in Section 3.2.1 was used to determine the *x*- and *y*-coordinates of the plate, wrist and forearm markers. The wrist-to-metacarpal and wrist-to-forearm vectors prior to impact were determined and the angle between them was found using the cross-product calculation. The wrist and forearm markers were also used to calculate the wrist and forearm velocity and kinetic energy (using total mass of specimen and ballast), as well as the peak change in distance between the wrist and forearm markers. All specimen marker position data was filtered using a 4^{th} order dual pass Butterworth filter and a cutoff frequency obtained from residual analysis performed on each specimen (Table 4.1). The change in the distance between the wrist and forearm markers was assumed to be related to skin motion artifact (see Taylor *et al*, 2005) and was therefore also quantified. Finally, the colour-thresholding program was used to quantify the intermediate impact plate velocity and kinetic energy (Figure 4.2).

One-way Repeated Measures ANOVAs were used to determine the statistical significance of muscle loading on the dependent variables for the pre-fracture and fracture trials separately where all directional measures (*i.e.*, forces, moments, strains) were analyzed as absolute values. To ensure that the muscle loads were applied in a repeatable manner, two-way random, absolute agreement, average measure ICCs were used (ICC 2, k) to assess between-impact (pre-fracture vs. fracture) muscle load reliability (Burkhart *et al.*, 2012c; Shrout and Fleiss, 1979); all ICCs were classified as presented in Section 2.2.2.2 (Grove, 1981). Furthermore, ensemble average plots (±1SD) from the beginning of marker motion were established for plate, wrist and forearm markers. All ANOVAs were conducted using SigmaStat software (version 3.5; Systat Software; San Jose, CA), while ICCs were analyzed using SPSS software (version 20; IBM; Armonk, NY), with alpha set at 0.05 for all statistical tests.

4.3 RESULTS

4.3.1 SPECIMEN POSITIONING AND STATIC MUSCLE LOADS

Specimens were oriented with a mean (SD) wrist angle of 59.4° (9.5°) and ballasted to 46.5 (1.6) % of the donor's body mass. Within each pair of specimens, static muscle loads were successfully applied to the left arm. Static fracture muscle loads of 26 (4) N, 59 (9) N, 15 (1) N and 12 (1) N were applied to ECU, ECRL, FCU and FCR, respectively and the ICC analysis determined that these loads were applied with excellent repeatability between pre-fracture and fracture trials (ICCs ranging from 0.78 to 1.00) (Table 4.2) (all specimen specific and mean measures for intact testing are found in Appendix L).

4.3.2 DISTAL RADIUS FRACTURES

Impacts at the targeted pre-fracture limit of 25 J, corresponding to a ram velocity of 2.7 (0.4) m/s and ram energy of 25.3 (7.7) J, did not induce damage to any of the specimens, as verified by fluoroscopy (Table 4.3). At higher impact energies, distal radius fractures were achieved in 10 specimens (*i.e.*, 5 pairs), while 1 pair experienced perilunate dislocations as opposed to fractures. The results that follow in this section include only the 5 pairs that fractured.

Overall, no differences were found between the load and no load conditions for any of the force (peak, impulse, load rate, duration) or energy variables for either the pre-fracture or fracture impacts ($p > 0.05$).

4.3.2.1 PRE-FRACTURE IMPACTS

Pre-fracture mean (SD) impact plate velocity and kinetic energy were found to be 1.4 (0.2) m/s and 4.3 (1.2) J, respectively and were not significantly different between the muscle loading groups ($p > 0.05$). These values agreed well with the wrist and forearm velocities found from the colour-thresholding program regardless of load condition (Table 4.3, Figure 4.3). It should be noted that the specimen velocities from a single pair was determined to be an outlier and was removed from the analysis. It was noted that the

Table 4.2: ICC results for muscle load force application reliability (n = 6 pairs).

Muscle	Between-Impact
ECU	0.96
ECRL	1.00
FCU	0.78
FCR	0.88

Table 4.3: Mean (SD) velocity and kinetic energy terms for pre-fracture and fracture of load and no load conditions (Pre-fracture: n = 5 pairs; Fracture: n = 5 pairs).

	Pre-fracture		Fracture	
	Load	**No Load**	**Load**	**No Load**
Resultant Velocity (m/s)				
Ram	2.7 (0.4)	2.8 (0.5)	6.7 (0.8)	6.5 (0.9)
Plate	1.4 (0.2)	1.4 (0.2)	3.9 (0.2)	3.9 (0.5)
Wrist[a]	0.9 (0.1)	1.0 (0.2)	-	-
Forearm[a]	1.0 (0.2)	1.1 (0.2)	-	-
Distance Change (mm) [a,b]				
Peak Wrist-Forearm	3.4 (1.8)	5.9 (2.2)	-	-
Kinetic Energy (J)				
Ram	24.0 (6.7)	26.4 (9.3)	151.8 (37.7)	143.6 (44.9)
Plate	4.4 (1.4)	4.3 (1.2)	35.6 (5.4)	35.6 (9.9)
Wrist[a]	10.2 (2.2)	13.8 (5.6)	-	-
Forearm[a]	13.5 (4.5)	16.2 (6.9)	-	-

[a]n = 4 pairs due to removal of an outlier.

[b]Load: 3/4 were contraction; no load: 4/4 were contraction.

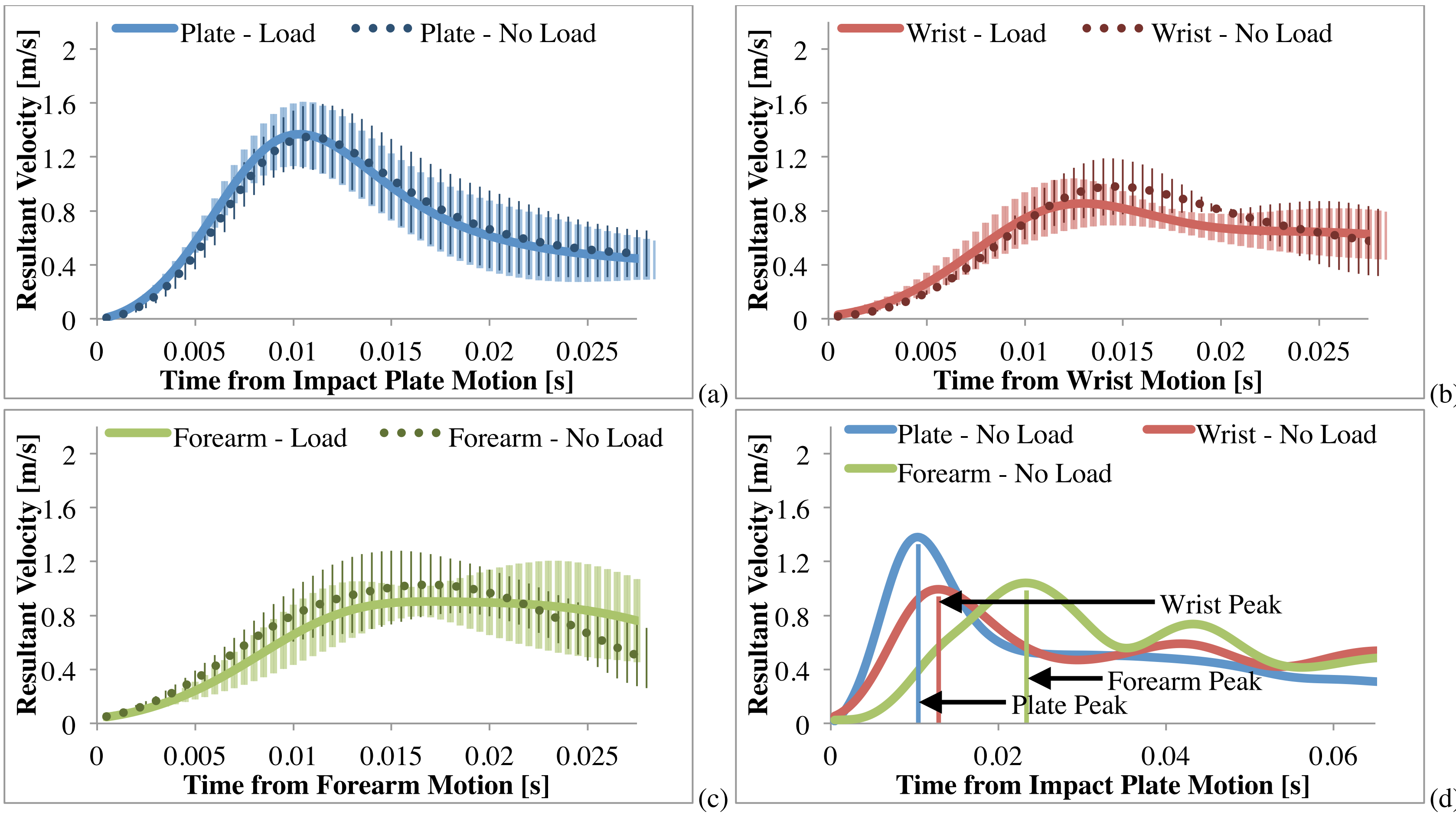

Figure 4.3: Plate, wrist and forearm resultant velocities

Ensemble average plots (±1 SD) for load and no load condition resultant plate (n = 5) (a), wrist (n = 4) (b), and forearm (n = 4) (c) markers, as well as a representative plot of plate, wrist and forearm marker resultant velocities as a function of time (d). The time scale in parts (a) through (c) was set to show marker velocity peaks in fine resolution, while part (d) demonstrates that the peaks did correspond to the first rise in velocity, and that velocity did not subsequently peak later in time.

plate resultant velocity peaked prior to wrist resultant velocity, which in turn peaked prior to forearm resultant velocity (Figure 4.3d). The change in distance between wrist and forearm markers occurred regardless of condition and had means (SD) ranging from 3.4 (1.8) mm to 5.9 (2.2) mm (Table 4.3).

4.3.2.2 FRACTURE IMPACTS

In the specimens with muscle loads applied, a mean (SD) of 2.2 (0.4) impacts (ranging from 2 – 3 impacts) were required to cause fracture, which corresponded to ram velocities of 6.7 (0.8) m/s and ram energies of 151.8 (37.7) J (Table 4.3). In the specimens without muscle loads applied, a mean (SD) of 2.0 (0.0) impacts were required to cause fracture, which corresponded to ram velocities of 6.5 (0.9) m/s and ram energies of 143.6 (44.9) J (Table 4.3). Statistical analysis revealed there was no difference in the ram velocities or energies between the load and no load conditions ($p > 0.05$)

Regardless of load condition, at fracture, the mean (SD) impact plate velocity was 3.9 (0.4) m/s, which corresponded to a kinetic energy of 35.6 (7.5) J, neither of which was significantly different between conditions ($p > 0.05$) (Table 4.3). Due to marker shadowing, it was not possible to calculate wrist and forearm velocity peaks at fracture. Resultant load/no load mean (SD) fracture forces of 6565 (866) N and 8665 (5133) N, as well as impulses of 47 (6) N·s and 57 (30) N·s were reported (Figure 4.4). Additionally, static muscle preloading did not have any appreciable effect on fracture force load rates, impulse duration or peak moments ($p > 0.05$) (Table 4.4).

4.3.2.3 STRAIN DATA

As a result of gauge failure and/or de-bonding during testing, axial strain data could only be recorded for four of the five fracture pairs for pre-fracture, and only one pair for fracture (Table 4.5). Additionally, principal strains could only be calculated for two pre-fracture pairs and one fracture pair. The only term to demonstrate significance was pre-fracture radius-ulna load sharing at 50 % of peak radius strain (means of 76 % vs. 61 %) ($p = 0.013$). Load and no load peak radial strain means (SD) ranged from 276 (140) $\mu\varepsilon$ – 1057 (505) $\mu\varepsilon$ (load) and 675 (568) $\mu\varepsilon$ – 2025 (1876) $\mu\varepsilon$ (no load) for pre-fracture and

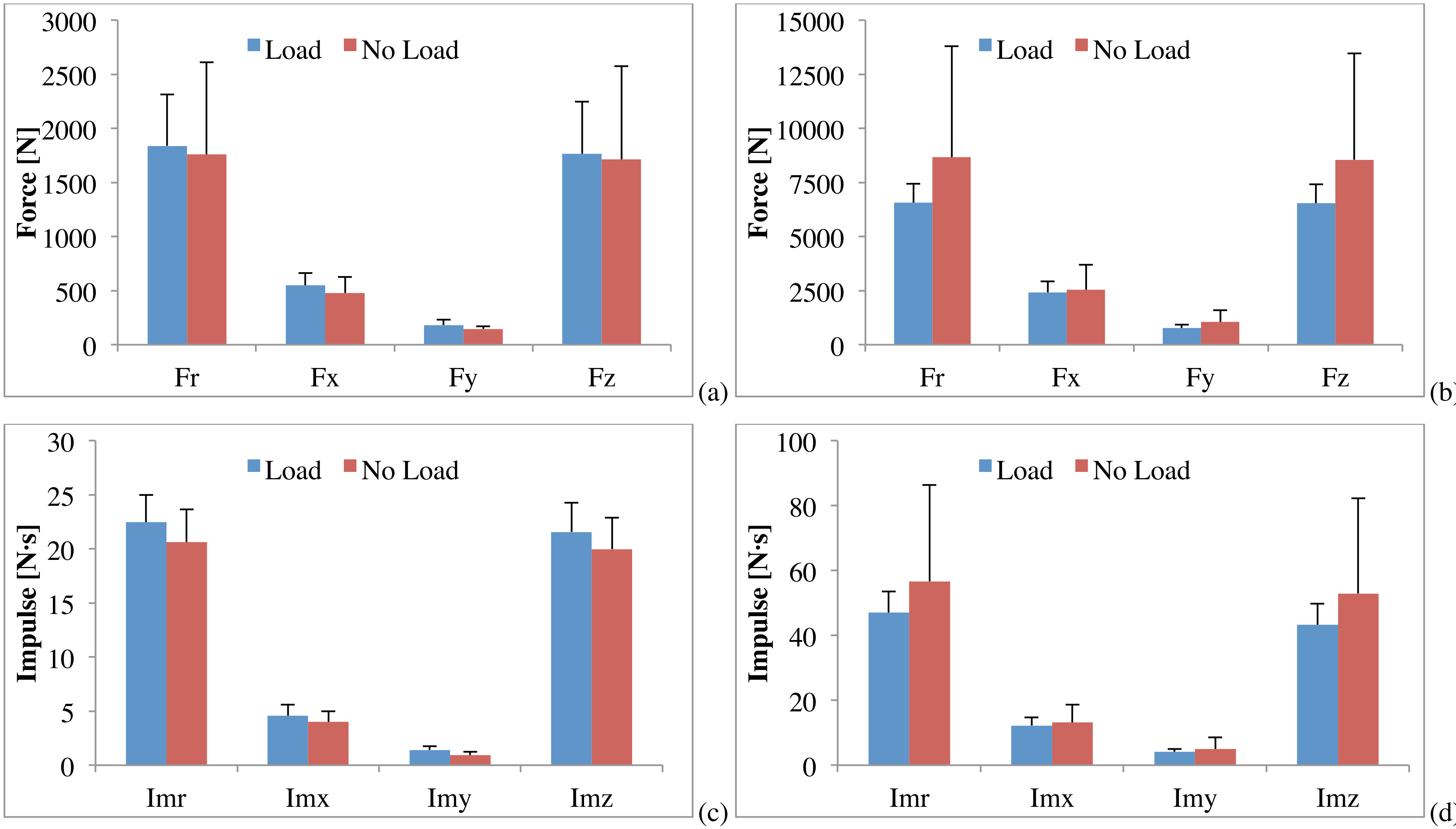

Figure 4.4: Peak pre-fracture and fracture forces and impulses

Comparison of the mean (SD) (n = 5) peak pre-fracture force (a) fracture force (b) pre-fracture impulse (c) and fracture impulse (d) between conditions.

Table 4.4: Mean (SD) Peak moments, load rates and impulse durations for pre-fracture and fracture between the muscle load and no muscle load conditions.

	Pre-fracture		Fracture	
	Load	**No Load**	**Load**	**No Load**
Peak Moment (N·m)				
M_x[a]	20 (12)	12 (9)	55 (23)	46 (10)
M_y[b]	44 (14)	48 (13)	161 (31)	148 (32)
Load Rate (kN/s)				
F_r	312 (128)	281 (258)	11118 (1771)	147844 (9226)
F_x[c]	134 (58)	231 (190)	3689 (876)	3339 (562)
F_y	79 (74)	73 (53)	1053 (332)	1611 (1150)
F_z[d]	276 (156)	245 (277)	11116 (1764)	14865 (9490)
Impulse Duration (ms)				
Im_r	41 (19)	40 (31)	36 (12)	37 (21)
Im_x	27 (7)	24 (13)	27 (10)	26 (9)
Im_y	32 (16)	23 (12)	33 (12)	25 (11)
Im_z	41 (19)	40 (31)	36 (12)	37 (21)

Note: all of the following directions are with respect to the load cell when viewed from the specimen side towards the acceleration tube:

[a]Pre-fracture: 4/5 no load directed to the left; Fracture: 1/5 load and 4/5 no load directed to the left.

[b]All pre-fracture directed downwards; Fracture: 4/5 load and 3/5 no load directed downwards.

[c]Fracture: 1/5 load and 1/5 no load directed to the left.

[d]All pre-fracture and fracture loads were directed into the load cell.

Table 4.5: Mean (SD) load sharing terms for pre-fracture and fracture of load and no load conditions (Pre-fracture: axial n = 4 pairs, principal n = 2 pairs; Fracture: n = 1 pair) (*p < 0.05).

	Pre-fracture		Fracture	
% of Peak Radial Strain	**Load**	**No Load**	**Load**	**No Load**
Axial Strain				
100%	72.4 (25.2)	62.8 (24.3)	95.5	15.4
75%	75.9 (25.6)	60.8 (26.2)	95.8	19.7
50%	75.9 (23.4)*	61.0 (24.8)*	91.3	22.9
25%	74.6 (18.2)	71.2 (7.5)	63.5	26.7
Maximum Principal Strain				
100%	67.9 (22.1)	71.3 (3.2)	94.6	36.6
75%	66.9 (25.6)	72.3 (25.6)	96.5	48.8
50%	68.0 (23.1)	59.6 (14.5)	89.6	14.6
25%	72.3 (18.1)	48.8 (8.7)	57.4	10.7
Minimum Principal Strain				
100%	59.1 (21.8)	54.9 (12.9)	95.5	18.8
75%	63.4 (25.1)	54.2 (14.0)	95.8	23.8
50%	63.3 (25.9)	53.1 (15.6)	91.2	29.9
25%	62.1 (26.9)	51.3 (17.7)	93.3	56.1

1495 $\mu\varepsilon$ – 1948 $\mu\varepsilon$ (load) and 209 $\mu\varepsilon$ – 1028 $\mu\varepsilon$ (no load) for fracture. With respect to load sharing, pre-fracture means (SD) demonstrate that the radius carries the majority of the load passing through the bones of the forearm during impact, with axial and maximum/minimum values ranging from 48.8 (8.7) % - 75.9 (25.6) % across all measures (Table 4.6). Finally, no differences were found between strain rates or magnitudes for load and no load conditions ($p > 0.05$) (Figure 4.5).

4.3.2.4 FRACTURE CLASSIFICATION

Of those specimens that experienced a fracture to the radius, four also had damage to the ulna, and one involved the carpals (Table 4.7). All fractured specimens inclined radially, resulting in a mean (SD) radial inclination of 9.9 (5.5)°. Additionally, an absolute mean (SD) post-fracture volar tilt angle 19.8 (15.1)° was found as with eight being directed dorsally, one volar and one neutral. Neither dorsal inclinations, nor volar tilts were found to vary significantly as a result of the applied static muscle loads. Fracture severity remained consistent across all specimens such that all were completely articular with seven reported as C3, two as C2 and one as C1 (Section 1.2.3).

4.3.3 PERILUNATE DISLOCATIONS

One pair of specimens did not fracture at the higher impact levels, but rather both specimens sustained a perilunate dislocation (*i.e.*, radius-lunate articulation is maintained, but the remaining carpals are dislocated posteriorly). Each of these specimens required four impacts before the injury presented and the ram velocity was found to differ by only 0.2 m/s between the 2 specimens (one with muscle load and one without). This resulted in load and no load impacting ram energies of 274.5 J and 284.9 J, respectively (Table 4.8). Additionally, the plate velocity was found to decrease by 1 m/s from the load to no load condition (Table 4.8), which translated to plate kinetic energies of 33.6 J and 18.8 J, respectively. The near doubling of impact plate kinetic energy for the load condition translated to the peak resultant dislocation force being 1.6 times greater (14 102 N vs. 8612 N) (Table 4.9). Interestingly, however, only a minor increase in resultant impulse was observed (65 N·s vs. 62 N·s). It should be noted that no statistical tests were performed on the specimens that experienced the dislocations ($n = 1$).

Table 4.6: Mean (SD) peak strains and strain rates for pre-fracture and fracture of load and no load conditions (Pre-fracture: axial n = 4 pairs, principal n = 2 pairs; Fracture: n = 1 pair).

	Pre-fracture		Fracture	
% of Peak Radial Strain	**Load**	**No Load**	**Load**	**No Load**
Axial Strain[a]				
Radius Peak (με)	706 (444)	1349 (716)	1895	848
Radius Strain Rate (με/s)	19288 (11160)	22221 (10236)	19650	15375
Ulna Peak (με)	338 (140)	1327 (1633)	4353	4842
Ulna Strain Rate (με/s)	10139 (7094)	27700 (37210)	64682	81910
Maximum Principal Strain[b]				
Radius Peak (με)	276 (140)	675 (568)	1495	209
Radius Strain Rate (με/s)	8129 (3025)	12040 (6998)	5480	2078
Ulna Peak (με)	206 (157)	442 (202)	2058	1577
Ulna Strain Rate (με/s)	6513 (8082)	11657 (4394)	32067	7245
Minimum Principal Strain[c]				
Radius Peak (με)	1057 (505)	2025 (1876)	1948	1028
Radius Strain Rate (με/s)	32428 (21797)	47351 (41564)	18751	18134
Ulna Peak (με)	1168 (1440)	2228 (2456)	4501	4541
Ulna Strain Rate (με/s)	35783 (48700)	47267 (53903)	67196	86726

[a]All radius and ulna pre-fracture and fracture are compressive.

[b]2/4 radius and 2/4 ulna pre-fracture, and 1/2 ulna fracture are compressive.

[c]All radius and ulna pre-fracture and fracture are compressive.

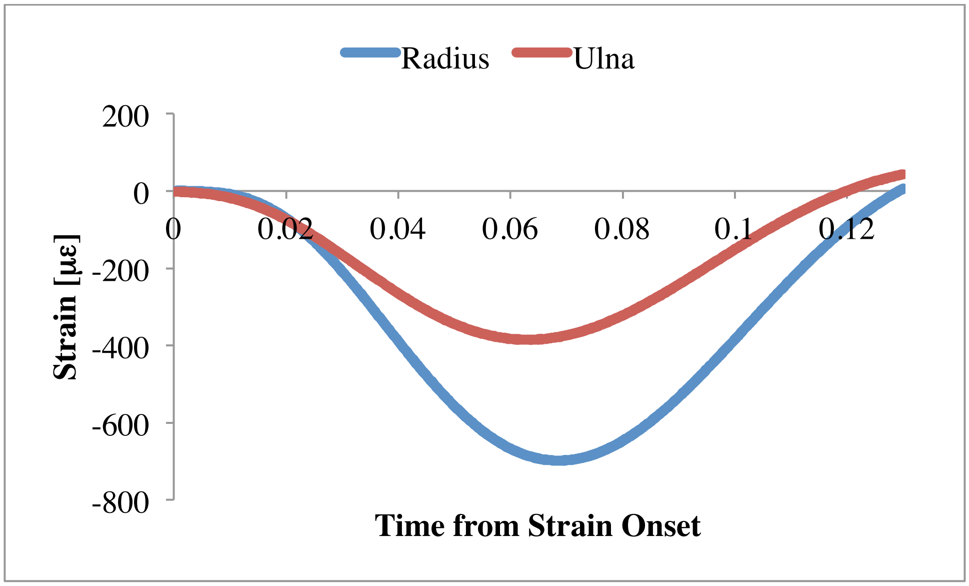

(a)

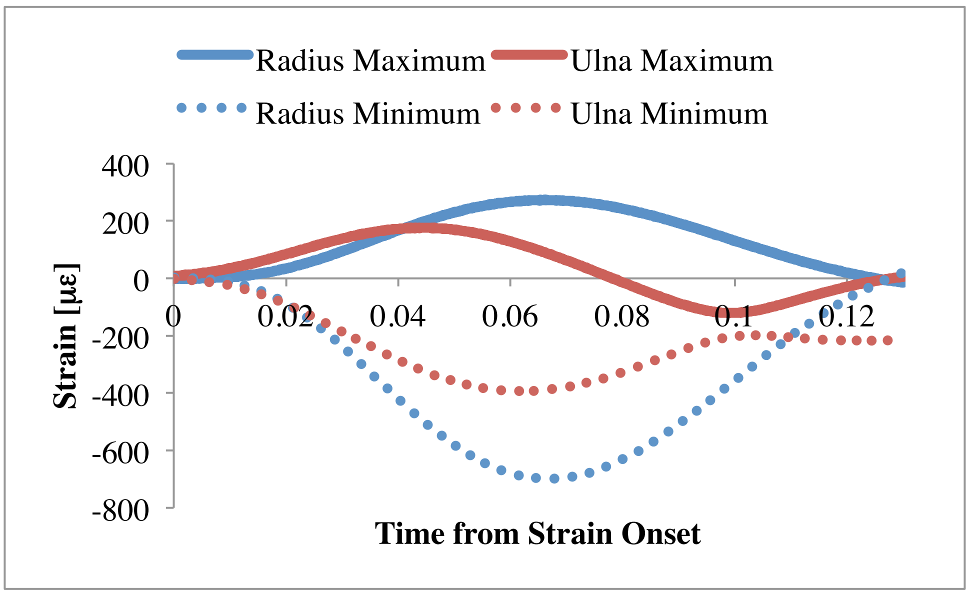

(b)

Figure 4.5: Representative plots of radius and ulna strain during radial strain peak

Axial (a) and maximum/minimum principal (b) strains during the rise and fall of the peak radial strain in a representative specimen.

Table 4.7: Injury classification of all specimens.

Specimen	Condition	AO	Involvement			Volar Tilt (°)	Radial Inclination (°)
			Radius	Ulna	Carpals		
1206066L	Load	C3	Yes	-	-	20	12
1206066R	No Load	C2	Yes	-	-	-50	5
1206067L	Load	C2	Yes	-	-	-5	11
1206067R	No Load	C1	Yes	-	-	-24	3
1207016L	Load	C3	Yes	Yes	Yes	-11	12
1207016R	No Load	C3	Yes	Yes	-	-9	17
1207036L	Load	C3	Yes	Yes	-	0	11
1207036R	No Load	C3	Yes	-	-	-15	16
1208016L	Load	C3	Yes	-	-	-32	0
1208016R	No Load	C3	Yes	Yes	-	-32	12
1207012L[a]	Load	-	-	-	Yes	-	-
1207012R[a]	No Load	-	-	-	Yes	-	-

[a]Perilunate dislocation.

Table 4.8: Mean (SD) velocity and kinetic energy terms for pre-injury and dislocation of load and no load conditions (n = 1 pair).

	Pre-injury		Dislocation	
	Load	**No Load**	**Load**	**No Load**
Velocity (m/s)				
Ram	3.2	3.0	9.1	9.3
Plate	1.5	1.3	3.8	2.8
Wrist	0.8	0.7	-	-
Forearm	0.5	0.6	-	-
Distance Change (mm)				
Peak Wrist-Forearm	-6.9	-6.0	-	-
Kinetic Energy (J)				
Ram	34.5	29.4	274.6	284.9
Plate	5.4	3.9	33.6	18.8
Wrist	16.4	7.6	-	-
Forearm	14.4	11.3	-	-

Table 4.9: Mean (SD) Peak forces, moments, load rates and impulse durations for pre-injury and dislocation load and no load conditions (n = 1 pair).

	Pre-injury		Dislocation	
	Load	**No Load**	**Load**	**No Load**
Peak Force (N)				
F_r	1818	1791	14102	8612
F_x	520	536	2868	2778
F_y	165	168	-2036	999
F_z	1799	1766	13717	8576
Peak Moment (N·m)				
M_x	-26	16	368	-41
M_y	-38	-29	335	183
Load Rate (kN/s)				
F_r	169	192	29718	3366
F_x	53	65	2310	4471
F_y	207	17	-4347	1085
F_z	166	191	29866	3122
Impulse (N·s)				
Im_r	25	24	65	62
Im_x	5	5	36	10
Im_y	1	2	10	3
Im_z	25	23	49	60
Impulse Duration (ms)				
F_r	41	33	21	12
F_x	23	27	30	11
F_y	35	23	16	11
F_z	41	33	21	12

4.4 DISCUSSION

To the author's knowledge, this is the first study to investigate the effect of static muscle loading on the fracture threshold of the distal radius. The results demonstrated a single significant difference between muscle load and no load conditions, suggesting that static muscle loads at the magnitudes applied in this study have only a minor effect on how the distal radius responds to forward fall like impacts. The muscle load levels presently applied were based on peak contraction forces established for each muscle by Holzbaur *et al*, 2005, and peak percent MVC EMG data provided during *in vivo* fall analysis (Burkhart and Andrews, 2013). It is important to note that while *in vivo* fall data provides real-world insight, the EMG data was limited to pre-fracture impacts.

The fractures created with the experimental set up were clinically-relevant in nature, as assessed by a fellowship trained orthopaedic surgeon who assigned their AO classifications. No significant differences were found between the load and no load test conditions for the resulting volar tilt or radial inclination. This result was not surprising given that the applied external loads were far greater in magnitude than the internal muscle forces, and had a much stronger influence on fracture fragment displacement and inclination.

Regardless of the muscle preload condition, it is noted that the mean fracture forces (6565 N and 8665 N) found in the current study are consistently higher than those previously reported in the literature (Section 1.4.2), but that impulse (47 N·s and 57 N·s) and energy (152 J and 144 J) means fit well within the expected ranges. When standard deviations are accounted for, the current grand mean (SD) (*i.e.*, mean across all fracture specimens) resultant force (7615 (3643) N) agrees well with the upper limit of many previous studies (Augat *et al*., 1996; Augat *et al*., 1998; Duma *et al*., 2003; Giacobetti *et al*., 1997; Greenwald *et al*., 1998; Horsman and Currey, 1983; Lubahn *et al*., 2005; Myers *et al*., 1991). It is likely that reductions in apparatus constraints have resulted in the increased resultant fracture forces, and may be more indicative of how injury would occur *in vivo*. Specifically, as discussed in Section 1.5, most previous studies have attempted to restrict post-impact specimen motion (*e.g.,* specimen confined to a linear rail), while the present apparatus allowed the specimen to move in six degrees of freedom. Furthermore, an effort was made in the current investigation to simulate the effective body mass (achieved through specimen-specific ballasting) seen by the upper extremity during a fall. Ballasting provides realistic inertial constraints on the specimen, and has been shown to affect the magnitude of impacting forces during forward falls (Chiu and Robinovitch, 1998). The percentage of ballast simulated in the present study (46.5 %) agrees well with that presented by Chiu and Robinovitch (1998) (49 %), and was determined through repeated pilot work aimed at increasing specimen-impact plate contact time and achieving fracture distally as opposed to proximally (which occurred when ballasting exceeded present levels). Also noted during pilot work, it was seen that extending the impact duration (through prolonged specimen impact plate contact) was necessary to initiate a fracture. This suggests that injury prevention techniques could potentially focus on reducing the time of hand-ground contact during forward falls.

Qualitatively, it was noted that the pair of specimens that experienced a dislocation were subjected to higher levels of impact energy compared to those that fractured, suggesting that dislocations may occur when bone strength is sufficient to prevent breakage. The two specimens that suffered dislocation came from a donor that had the largest BMI (weight: 124 kg; BMI: 35). As BMI has been shown to be related to bone mineral density (BMD) (Fawzy *et al*, 2011), and increases in BMD have been found to increase fracture thresholds (Augat *et al*, 1996), it is likely that the bone strength of these specimens was great enough to resist fracture. Furthermore, as both specimens were impacted four times, it is possible that repeated loading led to ligament weakening that would have resulted in a reduced threshold to dislocation (Trieb, 2008). Finally, although only one pair of specimens was in the dislocation group, the specimen with muscle loading produced a larger plate kinetic energy and generally greater dislocation parameters compared to the no load side. This may suggest that the inclusion of muscle loads could improve the stiffness and stability of the joint and ultimately the threshold of wrist dislocation.

To avoid altering the anatomy of the distal radius to measure load sharing (*i.e.*, by creating an osteotomy and implanting a load cell) (Markolf *et al.*, 1998), strain gauges were directly applied to the bone surface to determine radius-ulna load sharing in a nondestructive manner. The presentation of load sharing at increments building up to peak radial strain was done in an attempt to document a change in how the forearm carries load en-route to injury, and is an improvement over most studies that report load sharing at a single instance in time (Shepard *et al*, 2000). Although load sharing in response to dynamic loads has been reported in pilot testing of the spine (Yoganandan *et al*., 1986), this is the first time that it has been presented, dynamically, between the radius and ulna. The results presented here suggest, that for pre-fracture impact, the percent of load carried by the radius remains relatively constant both between conditions and across sampling intervals (*i.e*., 25 % - 100 % peak radial strain). The application of static muscle loads was seen to result in a significant increase in the load carried by the radius at 50 % of the peak radial strain during pre-fracture impacts. This increase in radial load share is possibly due to muscle loads providing additional compression across the wrist joint. Since the radiocarpal joint is the only direct connection between the carpals and the forearm, it is understandable that increases in applied load would have a more prominent effect on radial strain. Though not significant, increases in mean radial load share at 25 %, 75 % and 100 % of peak radial strain for the condition of muscle preload follow this trend. Regardless of whether load sharing was calculated using axial or principal strain, the results suggest that the distal radius carries more load than the ulna during pre-fracture impact. This may in part explain why the distal radius is so commonly fractured during forward fall initiated upper extremity impacts.

Many investigations into human motion require the use of skin-based marker tracking (*e.g.,* gait analysis) (Jenkyn *et al*, 2008). Unfortunately, this style of marker is prone to error due to soft tissue motion (Taylor *et al*, 2005). Ideally, forearm motion during impact could be tracked using markers pinned (Reinschmidt *et al*, 1997) into the radius or ulna, but as bone pinning has been shown to cause stress concentrations that could reduce fracture thresholds (Rogge *et al*., 2002), this was not an option for the present investigation. Alternate techniques for dealing with soft-tissue motion include redundant marker systems that use least squares or the eigenvalues of the inertia tensor (*i.e*., point cluster technique) to minimize errors (Chèze *et al*, 1995; Taylor *et al*, 2005), and the use of optimal filtering (although this cannot remove soft-tissue errors completely) (Burkhart and Andrews, 2013). Given the limited view of the high-speed camera used here, the only viable method for reducing soft tissue motion errors was filtering at an optimal cutoff frequency obtained through residual analysis. Despite filtering, some change in wrist-forearm marker distance was noted, and was attributed to soft tissue motion. Regardless of the presence of this motion, the wrist and forearm velocities reported at pre-fracture levels agree well with *in vivo* wrist velocities (1.5 (0.4) m/s) reported for forward falls (Burkhart and Andrews, 2013). Due to excessive marker shadowing that occurred during fracture impacts, wrist and forearm marker velocities could not be obtained; however, given the agreement between the plate and wrist velocities, plate velocities were used to quantify the peak impact velocity for fracture loading. As expected, the fracture plate velocity was found to be greater than *in vivo* wrist velocity, as *in vivo* studies have only reported pre-fracture level kinematics (to protect participants from injury).

Due to restrictions in apparatus design only static muscle loading was simulated in the present study, and was only replicated in four muscles. While the muscle loads applied in this study were low, they did satisfy the lower threshold of anatomically relevant *in vivo* muscle loads (outlined in Section 4.2.1) (Burkhart, 2011; Burkhart and Andrews, 2013; Holzbaur *et al*., 2005). Additionally, the muscles lines-of-action were not set on a specimen-specific basis. Rather, it was necessary to offset lines-of action at greater distances from the forearm’s longitudinal axis to ensure that loads could be applied to specimens of varying size. While the muscle load cable hole layout attempted to reflect tendon positioning across the wrist, future work should improve this system to allow for variation in hole positioning between specimens (Amis *et al*., 1979). Regardless, the present investigation generated wrist joint reaction forces, which are not expected to vary greatly due to changes in the present muscle lines-of-action.

During this investigation, loading was applied in an incremental fashion (*i.e*., pre-fracture and fracture) in order to reduce the cumulative effect of damage. However, pilot testing yielded a fairly large load gap and it is likely that if forces were applied in smaller increments, it may have been possible to detect fracture in a more sensitive nature, as well as the magnitude of external force at which the effect of muscle loading became negligible. This may be supported by the fact that four of five pairs incurred fracture at the same impact energy, while one pair required an additional impact to fracture under the muscle load condition; perhaps indicating an increase in fracture threshold due to the application of static muscle loads.

Unfortunately, strain gauge application in an intact cadaveric environment is inherently difficult, as it is necessary to insulate the gauge against moisture and the abrasion of overlying soft tissues. Accordingly, strain gauge application techniques were refined during pilot testing, but could not guarantee gauge integrity throughout impact (see Appendix J for strain gauge application procedures). Furthermore, while the distal placement of strain gauges provided insight into load sharing near the wrist joint, this positioning left gauges prone to destruction during fracture loading. Additionally, to provide bending compensation, strain gauges should be affixed to both the dorsal and volar aspects of the bone in the future.

The small sample size presented in this study is a common limitation of cadaveric testing. Coupled with the failure of some strain gauges, the small sample size prevented the statistical assessment of principal strain load sharing, and generally lowered statistical power. Moreover, cadaveric specimens are limited in that they often represent an elderly population, making it difficult to extrapolate findings beyond that demographic; however our specimen sample is classified by Health Canada as being at least-to-increased risk of developing health problems based on mean (SD) BMI (Health Canada, 2003). Additionally, our specimen sample agrees well with mean values of height (males: 172.6 cm – 174.9 cm; females: 158.0 cm – 161.9 cm), weight (males: 84.3 kg – 87.2 kg; females: 68.9 kg – 72.6 kg) and BMI (males: 28.3 – 28.5; females: 27.6 – 27.8) reported for Canadians 45 – 79 years of age (Shields *et al.*, 2008).

The fracture classifications of the present injuries suggest that the resulting injury thresholds (*i.e.*, fracture force, impulse, energy) are indicative of clinically relevant complete articular distal radius fractures. Furthermore, quantification of pre-fracture impact plate and specimen kinetic energies allowed for the removal of associated energy losses, providing insight into how much of the impacting ram's energy is applied to specimens for the purpose of causing bone strain. Overall, through the use of incremental dynamic loading, clinically relevant distal radius fractures were simulated in the presence and absence of static muscle loads. The results suggest that static muscle loads at the magnitudes applied in this study may have a negligible effect on the fracture threshold of the distal radius.

4.5 REFERENCES

Altissimi, M., Antenucci, R., Fiacca, C., Mancini, G. B., 1986. Long-term results of conservative treatment of fractures of the distal radius. Clinical Orthopaedics and Related Research 206, 202-210.

Amis, A., Dowson, D., Wright, V., 1979. Muscle strengths and musculoskeletal geometry of the upper limb. Engineering in Medicine 8, 41-48.

Augat, P., Reeb, H., Claes, L., 1996. Prediction of fracture load at different skeletal sites by geometric properties of the cortical shell. Journal of Bone and Mineral Research 11, 1356-1363.

Augat, P., Iida, H., Jiang, Y., Diao, E., Genant, H. K., 1998. Distal radius fractures: Mechanisms of injury and strength prediction by bone mineral assessment. Journal of Orthopaedic Research 16, 629-635.

Burkhart, T. A., 2011. Biomechanics of the Upper Extremity in Response to Dynamic Impact Loading Indicative of a Forward Fall: An Experimental and Numerical Investigation. Ph.D. University of Windsor.

Burkhart, T. A., Dunning, C. E., Andrews, D. M., 2012a. Predicting distal radius bone strains and injury in response to impacts using multi-axial accelerometers. Journal of Biomechanical Engineering 134, 101007-1 - 101007-7.

Burkhart, T. A., Andrews, D. M., Dunning, C. E., 2012b. Failure characteristics of the isolated distal radius in response to dynamic impact loading. Journal of Orthopaedic Research : Official Publication of the Orthopaedic Research Society 30, 885-892.

Burkhart, T. A., Clarke, D., Andrews, D. M., 2012c. Reliability of impact forces, hip angles and velocities during simulated forward falls using a novel Propelled Upper Limb fall ARrest Impact System (PULARIS). Journal of Biomechanical Engineering 134, 011001-1-011001-8.

Burkhart, T. A., Andrews, D. M., 2013. Kinematics, kinetics and muscle activation patterns of the upper extremity during simulated forward falls. Journal of Electromyography and Kinesiology 23, 688-695.

Challis, J. H., Pain, M. T., 2008. Soft tissue motion influences skeletal loads during impacts. Exercise and Sport Sciences Reviews 36, 71-75.

Cheze, L., Fregly, B., Dimnet, J., 1995. A solidification procedure to facilitate kinematic analyses based on video system data. Journal of Biomechanics 28, 879-884.

Chiu, J., Robinovitch, S. N., 1998. Prediction of upper extremity impact forces during falls on the outstretched hand. Journal of Biomechanics 31, 1169-1176.

Colles, A., 1814. On the Fracture of the Carpal extremity of the Radius. The Edinburgh Medical and Surgical Journal 10, 182-186.

DeGoede, K. M., Ashton-Miller, J. A., 2002. Fall arrest strategy affects peak hand impact force in a forward fall. Journal of Biomechanics 35, 843-848.

Dietz, V., Noth, J., Schmidtbleicher, D., 1981. Interaction between pre-activity and stretch reflex in human triceps brachii during landing from forward falls. The Journal of Physiology 311, 113-125.

Duda, G. N., Heller, M., Albinger, J., Schulz, O., Schneider, E., Claes, L., 1998. Influence of muscle forces on femoral strain distribution. Journal of Biomechanics 31, 841-846.

Duma, S. M., Boggess, B. M., Crandall, J. R., MacMahon, C. B., 2003. Injury risk function for the small female wrist in axial loading. Accident Analysis and Prevention 35, 869-875.

Duquette, A., Andrews, D. M., 2010. Comparing methods of quantifying tibial acceleration slope. Journal of Applied Biomechanics 2, 229-233.

Fawzy, T., Muttappallymyalil, J., Sreedharan, J., Ahmed, A., Alshamsi, S. O. S., Al Ali, Mariyam Saif Salim Humaid, Bader, B., Al Balsooshi, K. A., 2011. Association between body mass index and bone mineral density in patients referred for dual-energy x-ray absorptiometry scan in Ajman, UAE. Journal of Osteoporosis 2011, 876307-1-876309-4.

Gabriel, S. E., Gabriel, S. E., Tosteson, A. N. A., Leibson, C. L., Crowson, C. S., Pond, G. R., Hammond, C. S., Melton, I.,L.J., 2002. Direct Medical Costs Attributable to Osteoporotic Fractures. Osteoporosis International 13, 323-330.

Giacobetti, F., Sharkey, P., Bos-Giacobetti, M., Hume, E., Taras, J., 1997. Biomechanical Analysis of the Effectiveness of In-Line Skating Wrist Guards for Preventing Wrist Fractures. The American Journal of Sports Medicine 25, 223-225.

Greenwald, R., Janes, P., Swanson, S., McDonald, T., 1998. Dynamic Impact Response of Human Cadaveric Forearms Using a Wrist Brace. The American Journal of Sports Medicine 26, 825-830.

Grove, W. A., 1981. Statistical Methods for Rates and Proportions. American Journal of Psychiatry 138, 1644-1645.

Health Canada, 2003. Health Risk Classification According to Body Mass Index. 2013, 1.

Holzbaur, K. R., Murray, W. M., Delp, S. L., 2005. A model of the upper extremity for simulating musculoskeletal surgery and analyzing neuromuscular control. Annals of Biomedical Engineering 33, 829- 840.

Horsman, A., Currey, J., 1983. Estimation of mechanical properties of the distal radius from bone mineral content and cortical width. Clinical Orthopaedics and Related Research 176, 298-304.

Jenkyn, T. R., Hunt, M. A., Jones, I. C., Giffin, J. R., Birmingham, T. B., 2008. Toe-out gait in patients with knee osteoarthritis partially transforms external knee adduction moment into flexion moment during early stance phase of gait: a tri-planar kinetic mechanism. Journal of Biomechanics 41, 276-283.

Krackow, K. A., Thomas, S. C., Jones, L. C., 1986. A new stitch for ligament-tendon fixation. Brief note. The Journal of Bone and Joint Surgery.American Volume 68, 764-766.

Kreder, H. J., Hanel, D. P., McKee, M., Jupiter, J., McGillivary, G., Swiontkowski, M. F., 1996. X-ray film measurements for healed distal radius fractures. The Journal of Hand Surgery 21, 31-39.

Lewis, L. M., West, O. C., Standeven, J., Jarvis, H. E., 1997. Do wrist guards protect against fractures? Annals of Emergency Medicine 29, 766-769.

Lubahn, J., Englund, R., Trinidad, G., Lyons, J., Ivance, D., Buczek, F. L., 2005. Adequacy of laboratory simulation of in-line skater falls. The Journal of Hand Surgery 30, 283-288.

MacDermid, J. C., Roth, J. H., Richards, R. S., 2003. Pain and disability reported in the year following a distal radius fracture: a cohort study. BMC Musculoskeletal Disorders 4, 24.

Markolf, K. L., Lamey, D., Yang, S., Meals, R., Hotchkiss, R., 1998. Radioulnar Load-Sharing in the Forearm. A Study in Cadavera*. The Journal of Bone & Joint Surgery 80, 879-888.

McElhaney, J. H., 1966. Dynamic response of bone and muscle tissue. Journal of Applied Physiology 21, 1231-1236.

McGill, S. M., Grenier, S., Kavcic, N., Cholewicki, J., 2003. Coordination of muscle activity to assure stability of the lumbar spine. Journal of Electromyography and Kinesiology 13, 353-359.

McGrady, L., Hoepfner, P., Young, C., Raasch, W., Lim, T., Han, J., 2001. Biomechanical effect of in-line skating wrist guards on the prevention of wrist fracture. Journal of Mechanical Science and Technology 15, 1072-1076.

Muller, M., Nazarian, S., Koch, P., Schatzker, J., 1990. The AO classification of long bones. Berlin etc: Springer–Verlag, 74-84.

Myers, E. R., Sebeny, E. A., Hecker, A. T., Corcoran, T. A., Hipp, J. A., Greenspan, S. L., Hayes, W. C., 1991. Correlations between photon absorption properties and failure load of the distal radiusin vitro. Calcified Tissue International 49, 292-297.

Nevitt, M. C., Cummings, S. R., 1993. Type of fall and risk of hip and wrist fractures: the study of osteoporotic fractures. The Study of Osteoporotic Fractures Research Group. Journal of the American Geriatrics Society 41, 1226-1234.

Nigg, B. M., Liu, W., 1999. The effect of muscle stiffness and damping on simulated impact force peaks during running. Journal of Biomechanics 32, 849-856.

Pain, M. T., Challis, J. H., 2002. Soft tissue motion during impacts: their potential contributions to energy dissipation. Journal of Applied Biomechanics 18, 231-242.

Pain, M. T., Challis, J. H., 2001. The role of the heel pad and shank soft tissue during impacts: a further resolution of a paradox. Journal of Biomechanics 34, 327-333.

Reinschmidt, C., Van Den Bogert, A., Nigg, B., Lundberg, A., Murphy, N., 1997. Effect of skin movement on the analysis of skeletal knee joint motion during running. Journal of Biomechanics 30, 729-732.

Rogge, R. D., Adams, B. D., Goel, V. K., 2002. An analysis of bone stresses and fixation stability using a finite element model of simulated distal radius fractures. The Journal of Hand Surgery 27, 86-92.

Santello, M., 2005. Review of motor control mechanisms underlying impact absorption from falls. Gait & Posture 21, 85-94.

Shauver, M. J., Yin, H., Banerjee, M., Chung, K. C., 2011. Current and future national costs to medicare for the treatment of distal radius fracture in the elderly. The Journal of Hand Surgery 36, 1282-1287.

Shepard, M. F., Markolf, K. L., Dunbar, A. M., 2001. The effects of partial and total interosseous membrane transection on load sharing in the cadaver forearm. Journal of Orthopaedic Research 19, 587- 592.

Shields, M., Gorber, S. C., Tremblay, M. S., 2008. Estimates of obesity based on self-report versus direct measures. HEALTH REPORTS-STATISTICS CANADA 19, 61.

Shrout, P. E., Fleiss, J. L., 1979. Intraclass correlations: uses in assessing rater reliability. Psychol Bull 86, 420-428.

Taylor, W. R., Ehrig, R. M., Duda, G. N., Schell, H., Seebeck, P., Heller, M. O., 2005. On the influence of soft tissue coverage in the determination of bone kinematics using skin markers. Journal of Orthopaedic Research 23, 726-734.

Trieb, K., 2008. Treatment of the wrist in rheumatoid arthritis. The Journal of Hand Surgery 33, 113-123.

Troy, K. L., Grabiner, M. D., 2007. Asymmetrical ground impact of the hands after a trip-induced fall: Experimental kinematics and kinetics. Clinical Biomechanics 22, 1088-1095.

Van Staa, T., Dennison, E., Leufkens, H., Cooper, C., 2001. Epidemiology of fractures in England and Wales. Bone 29, 517-522.

Yoganandan, N., Sances Jr, A., Maiman, D. J., Myklebust, J. B., Pech, P., Larson, S. J., 1986. Experimental spinal injuries with vertical impact. Spine 11, 855-860.

CHAPTER 5

GENERAL DISCUSSION

5.1 SUMMARY

Distal radius fractures are among the most prevalent fractures in society today (Shauver *et al*., 2011; Van Staa *et al*., 2001), costly to the health care system (Gabriel *et al*., 2002; Shauver *et al*., 2011) and associated with complications including long-term pain and deformity (Altissimi *et al*., 1986; MacDermid *et al*., 2003). Reducing the incidence of these injuries and improving outcomes requires dedicated biomechanical research, using both *in vivo* and *in vitro* models. Despite the *in vivo* identification of fall induced preparatory muscle responses (Burkhart and Andrews, 2013; Dietz *et al*., 1981), the effect that this has on distal radius fracture thresholds has not been investigated. Accordingly, the overall purpose of the work described in this thesis was to quantify the effect of static forearm muscle loads on fractures to the distal radius following forward fall initiated impact loading.

In Chapter 2, a re-vamped impact apparatus was designed and constructed to permit intact cadaveric fracture testing (*i.e.,* Objective #1). Specifically, six apparatus improvements were implemented, including: a new pressure regulation system, wye-fitting acceleration tube, hydraulic damping pistons, specimen support and angle system, hanging cables and tendon tensioning system. Strong correlations between the input pressure and the specified output measures (R^2 = 0.97 - 1.00), demonstrated that combinations of input pressure and ram mass could be chosen to target the required impacting loads in an attempt to reduce the number of impacts-to-fracture. Additionally, through the assessment of interclass correlation coefficients (ICCs), excellent within- (ICC's of 0.98 – 1.00) and between-day (ICC's of 0.99) reliability was demonstrated (*i.e.,* Hypothesis #1 is accepted). This work also resulted in the development of curves for pressure input vs. axial force, ram velocity and loading energy, allowing for standard operating guidelines to be established for the input parameters of pressure and ram mass.

In Chapter 3, a custom colour-thresholding program was developed and validated for the analysis of high-speed camera video data using LabVIEW (National Instruments; Austin, TX) software (*i.e.,* Objective #2). This program allowed the user to isolate custom markers based on colour, area and perimeter, and was then capable of sequentially tracking and recording the *x*- and *y*-position of the marker's centroid. Kinematic parameters such as velocity and acceleration could then be calculated.

Comparisons between the high-speed camera (MotionScope M3; Red Lake Imaging, San Diego, CA) and Instron® (Instron 8874; Canton, MA) position, velocity and acceleration outputs were made and the colour-thresholding program's performance was deemed acceptable (percent errors: position = 1.4 (0.9) %; velocity = 1.0 (0.5) %; acceleration = 6.1 (3.3) %) (*i.e.,* Hypothesis #2 is accepted). The program was then implemented in combination with the impact apparatus to quantify specimen velocity and kinetic energy during isolated bone testing. These terms provided insight into how energy was transferred during impact by quantifying the amount of impacting ram energy that becomes specimen kinetic energy. The importance of marker contrast consistency was highlighted during this testing as it was found that fracture-induced shadowing prevented marker isolation. This led to changing the marker location to the impacting plate for subsequent intact testing, which allowed for the quantification of impact plate kinetic energy. Alternatively, future work may choose to additionally incorporate feature recognition algorithms to improve system capabilities.

In Chapter 4, the new impact apparatus (Objective # 1) and the high-speed camera's colour-thresholding program (Objective # 2) were used to perform impact analyses on six pairs of intact cadaveric forearm specimens. To quantify the effect of preparatory muscle contraction on distal radius fracture threshold, the pairs were separated into two conditions: static muscle loads and no loads (*i.e.*, Objective #3). Five of the six pairs resulted in complete articular distal radius fractures (C1 - C3 on the AO classification scale) (Muller *et al.*, 1990), and one pair resulted in perilunate dislocations. While a single load sharing term (at 50 % of peak radial strain) was significant between conditions, the application of static muscle loads did not have a significant effect on any of the typical fracture measures of the distal radius (*i.e.*, fracture force, impulse and energy), and as such, Hypothesis #3 is also accepted.

5.2 OVERALL STRENGTHS AND LIMITATIONS

The strengths and limitations of each study have been addressed in their respective chapters. In general, however, the design of an improved impact apparatus with the implementation of a high-speed camera based kinematics measurement system provided valuable insight into distal radius fractures, specifically that at present magnitudes, fracture was unaffected by muscle loading. Impact kinematic measures of velocity and kinetic energy were reported for the impact plate and specimen at frame rates of 2000 frames per second. These measures provide insight into how energy is transferred within the present apparatus, and expand the previous in-house impact testing system. With the quantification of energy losses, a more direct comparison between impact studies can be drawn that accounts for variation in specimen constraint.

Through the use of intact (*i.e.*, fresh-frozen) test specimens, the native wrist articular surfaces and forearm soft tissues were maintained, which permitted the application of static muscle loads. This ensured that the applied external loads were transferred through native tissues, as they would in the case of an *in vivo* forward fall. This is an improvement over some previous distal radius fracture studies that have used isolated specimens (Augat *et al.*, 1996; Burkhart *et al.*, 2012b; Horsman and Currey, 1983). Additionally, the simulation of specimen specific ballasting that agreed with a previous investigation (Chiu and Robinovitch, 1998) ensured that an appropriate effective mass was simulated across all specimens during impact. Furthermore, to mitigate the effects of small sample size, testing was conducted using paired specimens. By placing one specimen from each pair in the muscle load condition, measures could be repeated across donors. In this manner, variations seen in fracture threshold were more likely to be the result of the applied muscle forces rather than inter-specimen variations (*i.e.*, bone quality, cortical thickness, lifestyle).

Finally, the incremental nature with which loads were applied during pilot work allowed for the identification of a fracture threshold that would require only two impacts-to-fracture (with the exception of a single specimen that required three impacts-to-fracture). By minimizing the number of impacts required to induce injury, a lowering of the reported threshold due to cumulative bone damage was avoided. Furthermore, to ensure that no specimens suffered fracture that went undiagnosed due to overlying soft tissues, lateral and anterior-posterior radiographs were taken prior to beginning testing and following each subsequent impact.

Despite the strengths of this work, it also important to discuss the limitations in an attempt to improve future work. The simulation of muscle loads presented is limited in that it was applied in a static nature and only for two flexor and two extensor muscles. *In vivo*, preparatory muscle loading during forward falls is a dynamic response that involves more than four muscles (Burkhart and Andrews, 2013; Dietz *et al*., 1981). In addition, the muscle loads applied here, though anatomically relevant, represent the lower bound of the loads that are seen *in vivo*, and muscle lines-of-action were not set on a specimen specific basis. Rather, to accommodate variation in specimen size, muscle lines-of-action were offset at greater distances from the forearm's longitudinal axis than would be expected *in vivo* (Amis *et al*., 1979). Despite these limitations this investigation was successful in applying a load across the wrist joint, potentially increasing the stiffness and stability of this joint in a way that was not expected to have varied greatly from natural forms.

Small sample sizes coupled with damage to the strain gauges, due to the destructive nature of fracture testing, prevented the determination of statistical significance for all forms of fracture load sharing, as well as pre-fracture load sharing calculated from principal strain. Moreover, a small sample size resulted in lower power during statistical assessment that may have yielded a type-two error. Working with cadaveric subjects also typically limits the tested population to elderly donors, which makes it difficult to extrapolate findings to a younger healthier population. While this does limit the applicability of findings, the fact that bone quality decreases with age means that *in vitro* cadaveric fracture testing provides conservative estimates of general population fracture thresholds, which are better for injury prevention.

While the present study focussed on injuries to the bone, and digital radiographs are appropriate in identifying bone damage, they fail to capture the soft tissue damage that may accompany fracture. As a consequence, variations due to muscle loading with respect to soft tissue injuries (*e.g.*, articular cartilage damage, ligament tears, *etc.*) could be missed. Future classification of these injuries would require direct visual assessment. Regardless, the use of digital radiographs after each impact ensured that boney injury was identified and that fractures were documented with the inciting loads.

5.3 FUTURE DIRECTIONS

It is recommended that a future distal radius fracture study should attempt to simulate greater magnitudes of muscle loading, which would require the design of a more robust tendon tensioning system. Through the continued use of paired specimens, future work should attempt to isolate fracture thresholds in two parts. First, one of the specimens should be impacted with minor increases in loads until fracture to identify the donor's fracture threshold (*i.e.*, target fracture energy). Then, the paired specimen could be subjected to a single impact at the specimen specific fracture level. In this manner, injury thresholds could be targeted more precisely, and in a way that would be more specific to an individual donor. Additionally, this form of paired testing would account for variation in donor bone strength, allowing fracture thresholds to be classified with finer precision and according to more specific demographics (*e.g.*, older women, younger men, those with osteoporosis).

If the colour-thresholding system is to be used to quantify impact kinematics in the future, testing should attempt to improve marker durability and contrast consistency to allow for the quantification of specimen velocity and kinetic energy during fracture. In this way, the reported energy terms will be able to better demonstrate how much of the impacting energy is transformed into post-impact specimen motion. Additionally, the identification of kinematic impact terms such as specimen velocity, wrist extension during impact, *etc.* should be quantified to provide further understanding of how the wrist is positioned when it fractures; as such terms may offer insight into fracture prevention techniques.

5.4 CONCLUSIONS

Overall, the present work has demonstrated the effectiveness of integrating a new impact apparatus and high-speed video based impact kinematic measurement system. With a new impact apparatus designed, external loads can be applied to cadaveric specimens in a repeatable and controlled incremental manner through the selection of appropriate ram mass and input pressure combinations. The implementation of a valid high speed camera and colour thresholding marker tracking system allows for the accurate quantification of important specimen kinematics, providing insight into how the distal upper extremity responds to a forward fall induced impact. Finally, through the pairing of intact cadaveric specimens it was found that the application of muscle loads had no appreciable effect on the *in vitro* distal radius fracture thresholds, suggesting that small anatomically relevant muscle loads need not be simulated in the fracture testing of the distal radius.

5.5 REFERENCES

Amis, A., Dowson, D., Wright, V., 1979. Muscle strengths and musculoskeletal geometry of the upper limb. Engineering in Medicine 8, 41-48.

Augat, P., Reeb, H., Claes, L., 1996. Prediction of fracture load at different skeletal sites by geometric properties of the cortical shell. Journal of Bone and Mineral Research 11, 1356-1363.

Burkhart, T. A., Andrews, D. M., Dunning, C. E., 2012. Failure characteristics of the isolated distal radius in response to dynamic impact loading. Journal of Orthopaedic Research : Official Publication of the Orthopaedic Research Society 30, 885-892.

Burkhart, T. A., Andrews, D. M., 2013. Kinematics, kinetics and muscle activation patterns of the upper extremity during simulated forward falls. Journal of Electromyography and Kinesiology 23, 688-695.

Dietz, V., Noth, J., Schmidtbleicher, D., 1981. Interaction between pre-activity and stretch reflex in human triceps brachii during landing from forward falls. The Journal of Physiology 311, 113-125.

Horsman, A., Currey, J., 1983. Estimation of mechanical properties of the distal radius from bone mineral content and cortical width. Clinical Orthopaedics and Related Research 176, 298-304.

Muller, M., Nazarian, S., Koch, P., Schatzker, J., 1990. The AO classification of long bones. Berlin etc: Springer–Verlag, 74-84.

Van Staa, T., Dennison, E., Leufkens, H., Cooper, C., 2001. Epidemiology of fractures in England and Wales. Bone 29, 517-522.

APPENDIX

APPENDIX A: GLOSSARY

Anterior: Referring to the front of the body.

Arthritis: Medical condition causing inflammation of joints due to infectious or metabolic causes.

Arthroscopy: Visual examination of a joint using a camera scope.

Articular: Of or pertaining to joints or their structural components.

Cadaver: Of or pertaining to a dead body, corpse.

Carpal: The classification of small bones found in the wrist, located between the forearm bones and the metacarpals.

Cartilage: A firm, but flexible tissue found in the articular surface of joints, but also throughout the body (*e.g.*, ears, nose).

Comminution: To be reduced into several small fragments.

Coronal Plane: Plane in the body moving from anterior to posterior.

Diaphysis: The shaft-like region of a long, slender bone.

Dislocation: Injury caused by part of a joint being displaced from its natural position.

Distal: Situated away from the point of attachment to the body.

Dorsal: Of or pertaining to the back side (*i.e.*, of the hand).

Dorsiflexion: Extension of the wrist.

Epidemiology: The science and study of the causes and effects of health and disease.

Extension: Movement around a joint that increases the angle between the bones of the limb at the joint.

Flexion: Movement around a joint that reduces the angle between the bones of the limb at the joint.

Fracture: Break found in an otherwise continuous structure such as bone.

Immobilization: Restraint from moving a body part, to promote healing.

Impaction: In the state of being struck rapidly by a force.

***In vitro*:** In reference to events taking place outside of a living organism.

***In vivo*:** In reference to events taking place within a living organism.

Interosseous Membrane: Thin sheet of fibrous tissue connecting the shafts of the radius and ulna, which begins near the radius' dorsal insertion of abductor pollicis longus and is approximately 10.6 cm long.

Intramedullary: Occurring within the channel in the bone that houses marrow.

Intraoperatively: Refers to an action that occurs during a surgery.

Lateral: Of or relating to the side lying away from the median axis of the body.

Ligament: Tough band of fibrous tissue that connects the articular extremities of bone.

Medial: Of or relating to the side lying towards the median axis of the body.

Metacarpal: Intermediate bones of the hand, located between the carpals and phalanges.

Metaphysis: Transitional zone in a long bone where the shaft like region and end of the bone meet.

Osteoporosis: A systemic skeletal condition characterized by low bone mass and micro-architectural deterioration of bone tissue, resulting in fragility and increased incidence of fracture.

Percutaneous: Performed through the skin.

Periosteum: Membrane of tissue that closely surrounds all bones, except at the articular surfaces.

Person-years: Unit of time referring to how long a group of people is monitored, exposed, etc; the sum total of the exposed time.

Phalanges: Bones of the human skeleton forming the fingers and toes.

Posterior: Referring to the back of the body.

Principal Axis: Axis along which the linear components of stress (principal stresses) are orthogonal and the shear stress is zero.

Principal Strains: The maximum and minimum normal strains, which occur when a strain element is rotated such that the shear strains equal zero.

Proximal: Situated closer to the midline of the body.

Radius: Of the two bones within the human forearm, the bone located on the thumb side.

Sagittal Plane: Plane in the body moving from medial to lateral.

Subchondral: Situated beneath cartilage.

Tendon: Dense fibrous tissue connecting muscle to bone.

Traction: The state of tension or pulling force exerted on a skeletal structure by external means.

Transverse Plane: Plane in the body moving from inferior to superior.

Trunk: The human torso.

Ulna: The bone located on the little finger side of the human forearm.

Volar: Of or pertaining to the palm of the hand or the sole of the foot.

APPENDIX B: PERMISSIONS

Campbell, Brenton - Hoboken

From: Goldweber, Paulette - Hoboken on behalf of Permissions - US
Sent: Monday, October 01, 2012 4:00 PM
To: Campbell, Brenton - Hoboken
Subject: FW: Permission Request Form Canada

Categories: Permissions

Thesis.

-----Original Message-----
From: [redacted] on ca.wiley.com [redacted]
Sent: Monday, October 01, 2012 11:44 AM
To: Permissions - US
Subject: Permission Request Form Canada

A01_First_Name: Jacob
A02_Last_Name: Reeves
A03_Company: The University of Western Ontario
A04_Address: 1151 Richmond Street
A05_City: London
A06_Province: Ontario
A07_Zip: N6A3K7
A08_Country: Canada
A09_Phone: 519-661-2111, ex. 88306
A10_Fax:
A11_Email: [redacted]
A12_Reference_Number:
A13_Requestor_Name:
A14_Requestor_Phone:
A15_Requestor_Fax:
A16_Product_Title: Principles of Human Anatomy
A17_ISBN: 0-471-36686-2
A18_Author_Name: Gerard J. Tortora
A19_Page_Number: pha12e_fig_01_05.jpg, pha12e_tabfig_06_02_06.jpg, pha12e_fig_08_05h.jpg, pha12e_fig_08_06ab_01.jpg, pha12e_fig_08_06ab.jpg, pha12e_fig_09_06d.jpg, pha12e_fig_09_07b.jpg, pha12e_fig_09_10h.jpg
A20_Number_of_Copies: 5
A21_Semesters: 3
A22_Professor_Name: Dr. Cynthia Dunning
A23_Course_Name: n/a
A24_Organization_Name: The University of Western Ontario
A25_Purpose_Reproduction: Masters Thesis
A26_Title_Your_Work: Comparison of Axial and Off-Axis Dynamic Loading of the Distal Radius
A26A_Resale: No
A27_Print_Run: n/a
A28_Publication_Date: April-May 2013
A29_World_Rights: Right to Reproduce Figures

PERMISSION GRANTED
BY: [redacted]
Global Rights Dept., John Wiley & Sons, Inc.

NOTE: No rights are granted to use content that appears in the work with credit to another source

1

Figure B.1: Permission (Part 1) for figures from Tortora: Principles of Human Anatomy

A30_Medium:
A31_Password:
32_Users:
A33_Duration_Posted_Web:
A34_CD_Print_Run: ,

2

Figure B.2: Permission (Part 2) for figures from Tortora: Principles of Human Anatomy

APPENDIX C: APPARATUS COMPONENT DRAWINGS

Note: All drawing units are imperial, as per the request of University Machine Services.

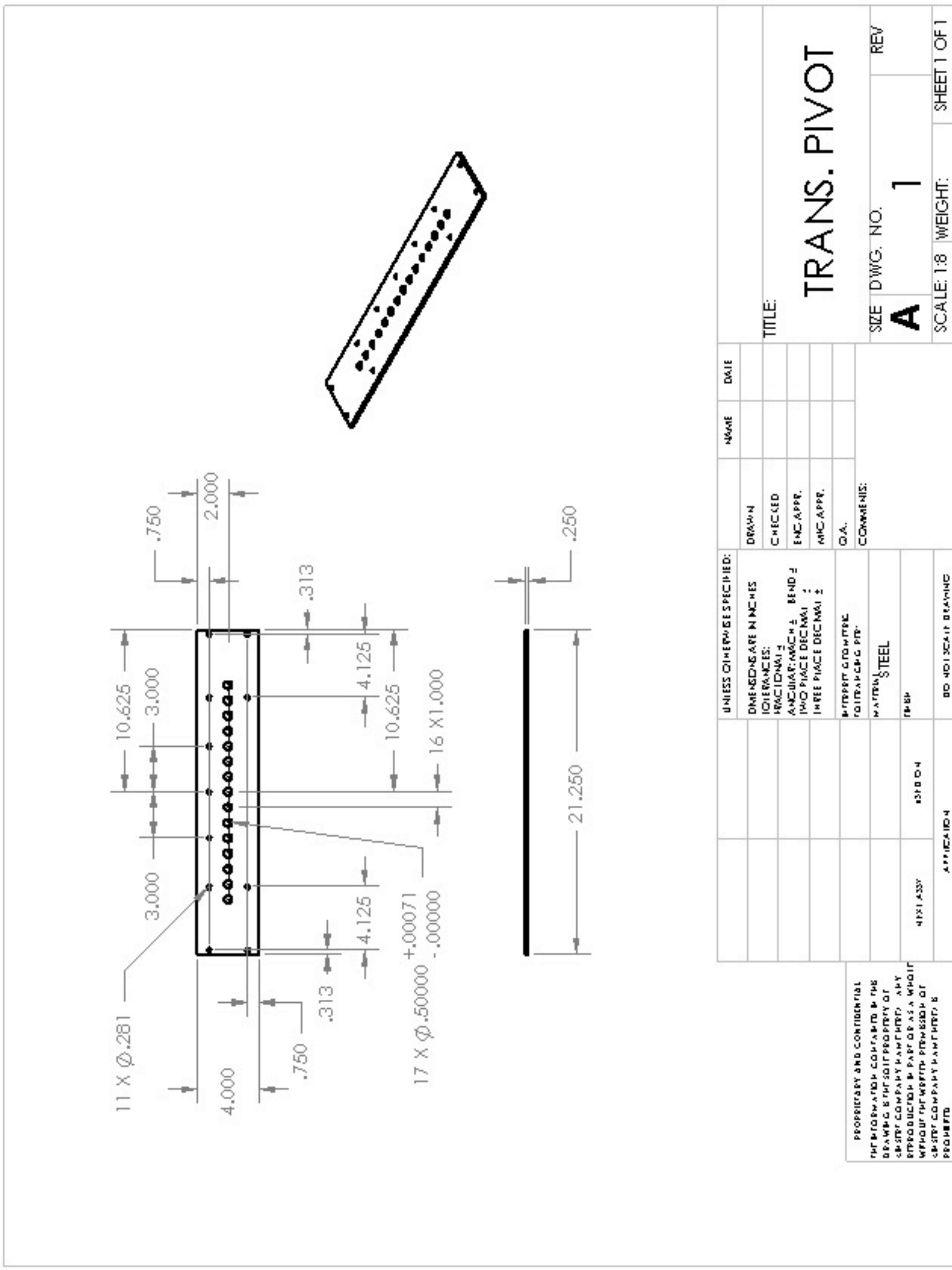

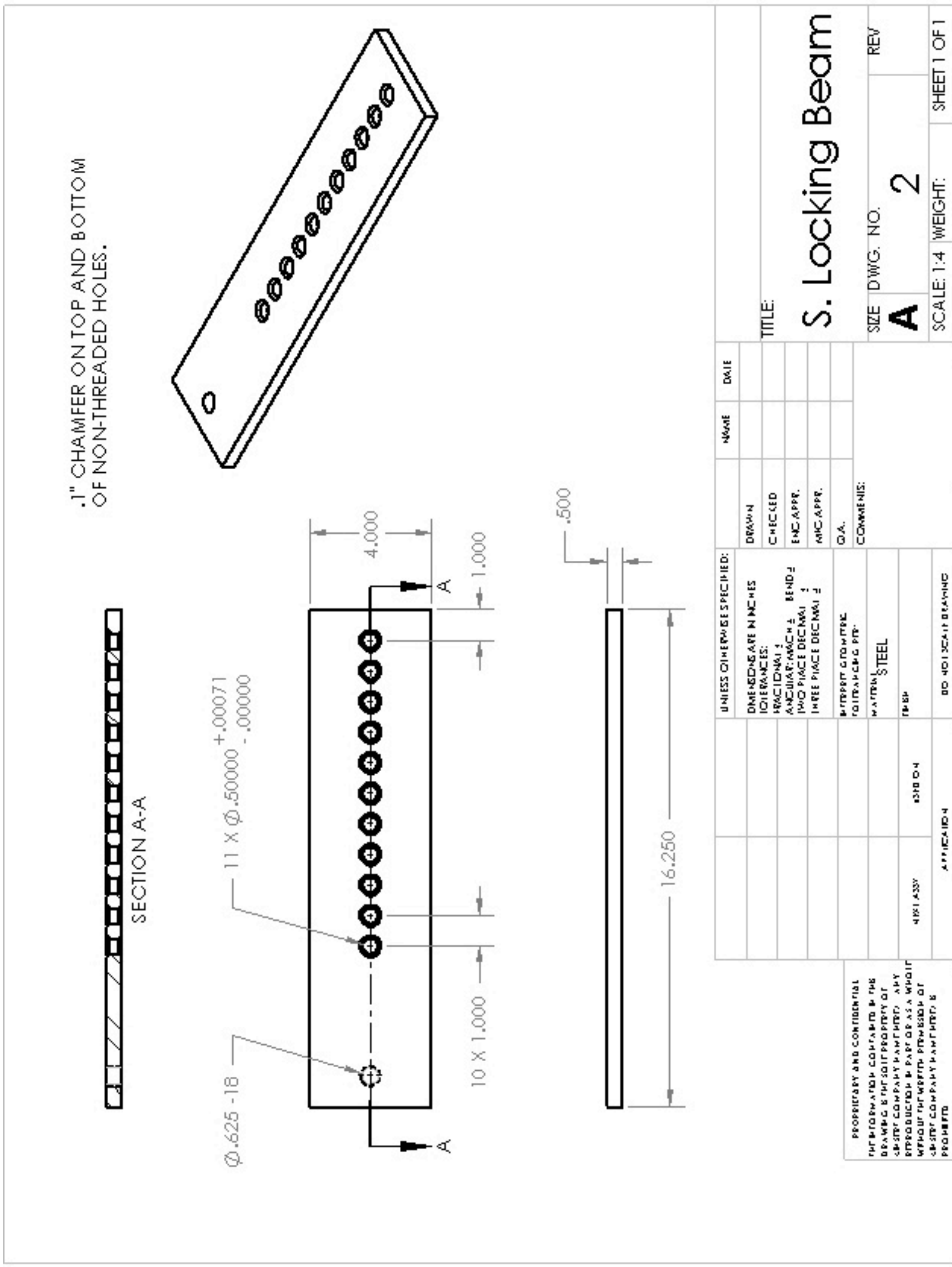

.1" CHAMFER ON TOP AND BOTTOM OF NON-THREADED HOLES.
SECTION A-A
11 X Ø.50000 +.00071 -.00000
Ø.625 -18
10 X 1.000
4.000
1.000
.500
16.250
A
A
UNLESS OTHERWISE SPECIFIED:
DIMENSIONS ARE IN INCHES
NAME
DATE
DRAWN
CHECKED
ENG APPR.
MFG APPR.
Q.A.
COMMENTS:
MATERIAL
STEEL
FINISH
NEXT ASSY
USED ON
APPLICATION
DO NOT SCALE DRAWING
TITLE:
S. Locking Beam
SIZE
A
DWG. NO.
2
REV
SCALE: 1:4
WEIGHT:
SHEET 1 OF 1

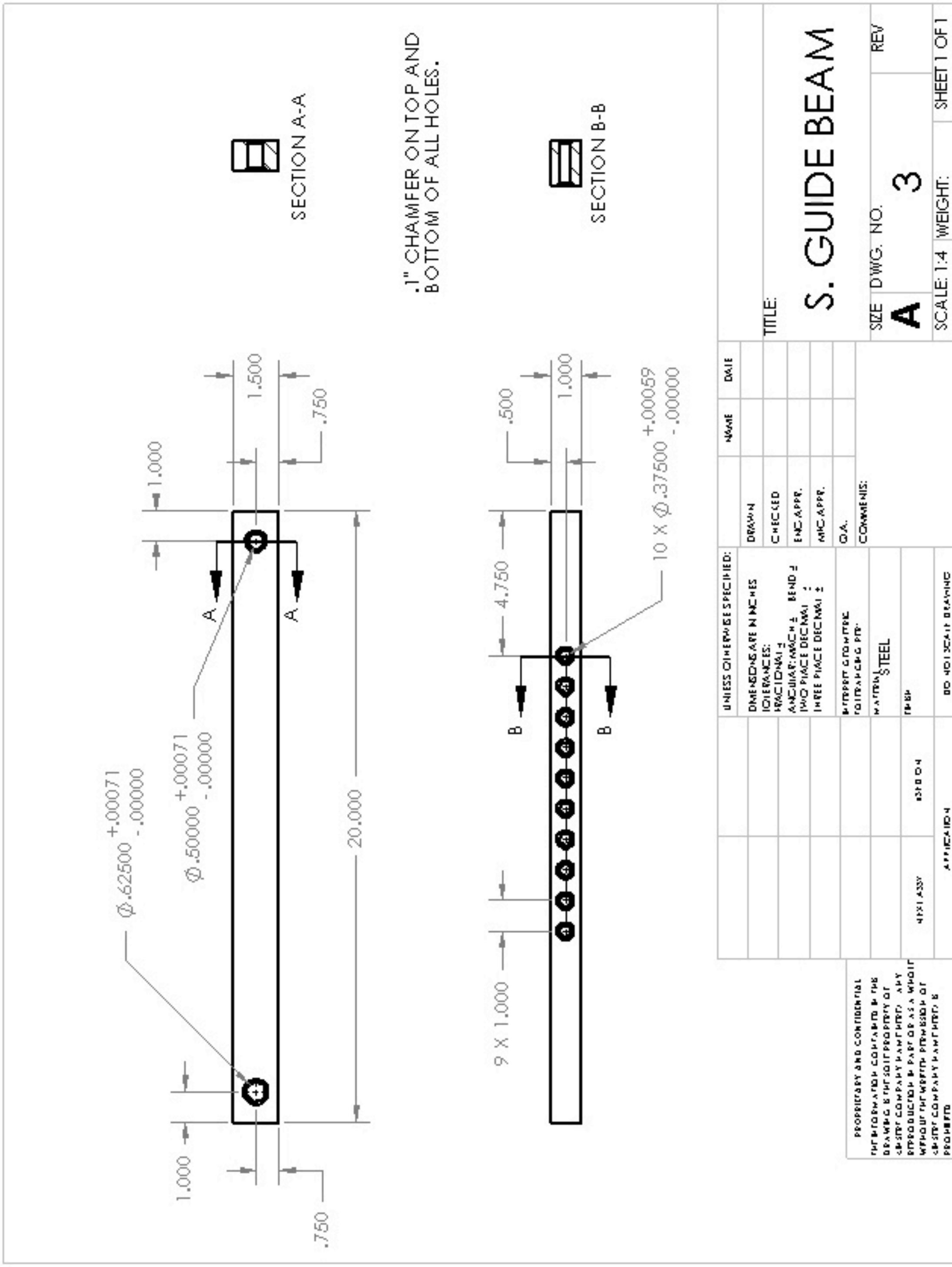

.1" CHAMFER ON TOP AND BOTTOM OF ALL HOLES.
SECTION A-A
SECTION B-B
A
A
B
B
Ø.62500 +.00071 -.00000
Ø.50000 +.00071 -.00000
1.000
1.000
1.500
.750
.750
20.000
9 X 1.000
4.750
.500
1.000
10 X Ø.37500 +.00059 -.00000
UNLESS OTHERWISE SPECIFIED:
NAME
DATE
DRAWN
CHECKED
ENG APPR.
MFG APPR.
Q.A.
COMMENTS:
STEEL
TITLE:
S. GUIDE BEAM
SIZE
A
DWG. NO.
3
REV
SCALE: 1:4
WEIGHT:
SHEET 1 OF 1

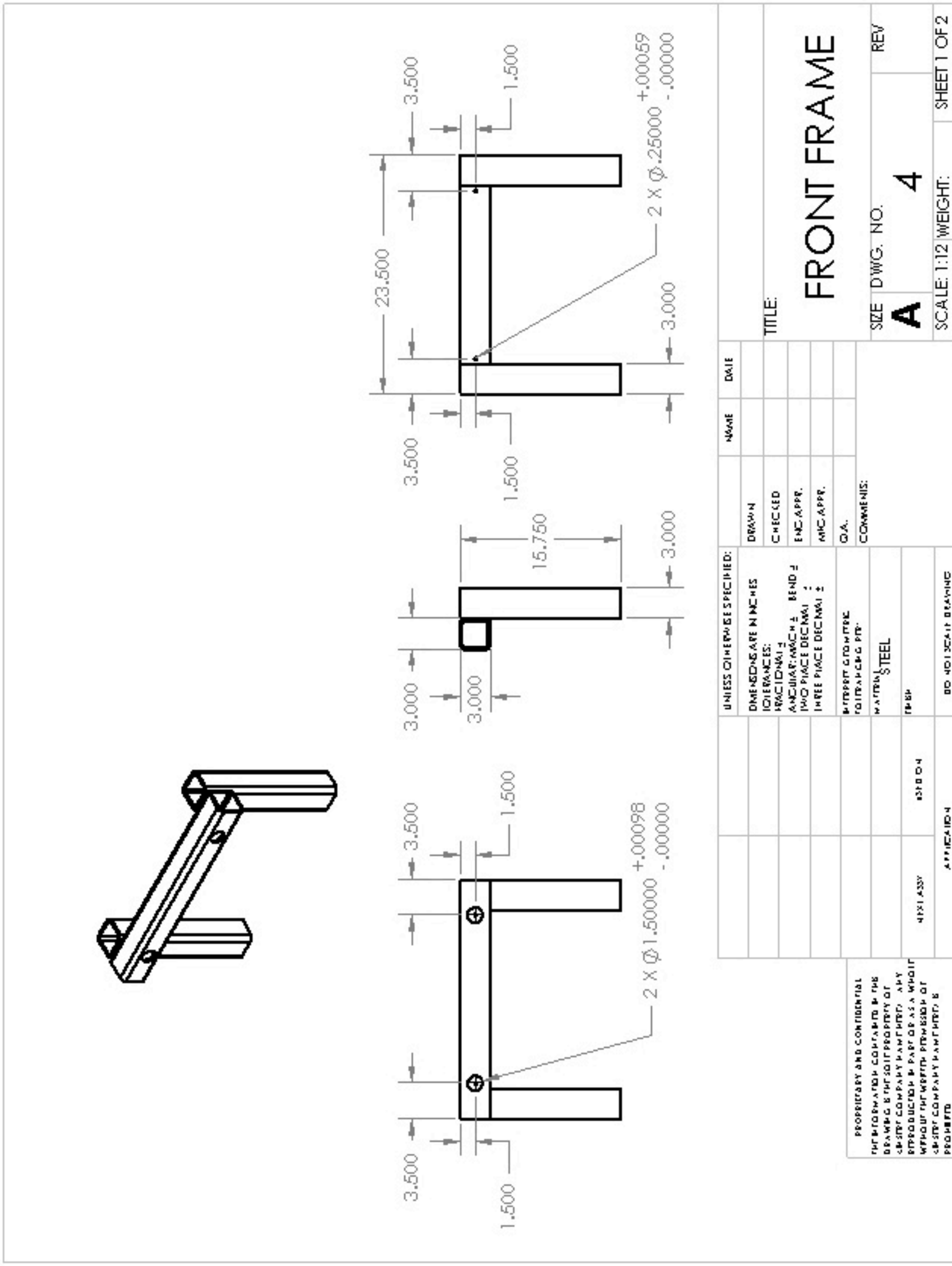
3.500
23.500
3.500
1.500
1.500
3.000
2 X ∅.25000 +.00059 -.00000
15.750
3.000
3.000
3.000
1.500
2 X ∅1.50000 +.00098 -.00000
UNLESS OTHERWISE SPECIFIED:
DRAWN
CHECKED
ENG APPR.
MFG APPR.
Q.A.
COMMENTS:
NAME
DATE
STEEL
DO NOT SCALE DRAWING
TITLE:
FRONT FRAME
SIZE
A
DWG. NO.
4
REV
SCALE: 1:12
WEIGHT:
SHEET 1 OF 2

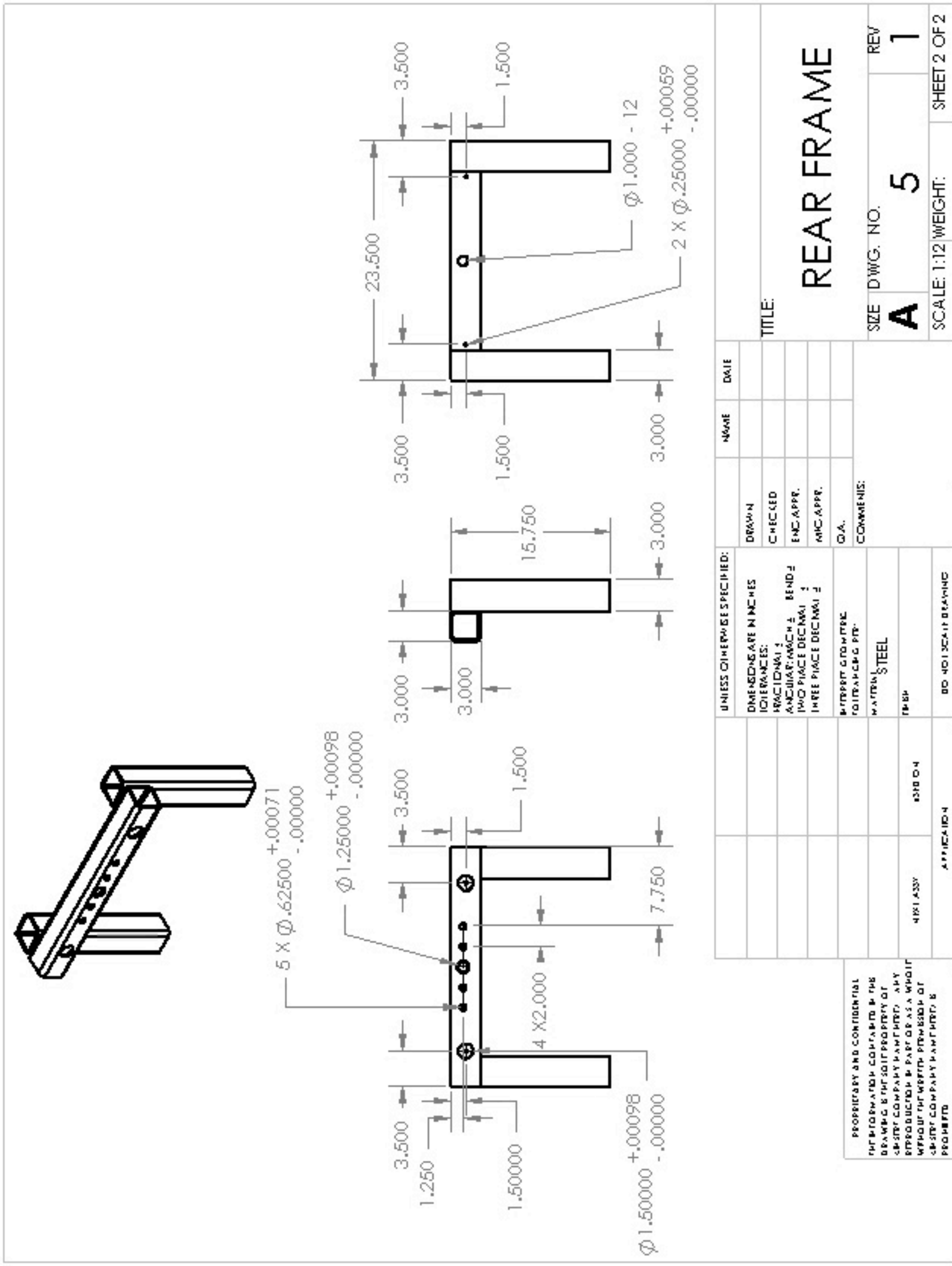

3.500
1.500
23.500
Ø1.000 - 12
2 X Ø.25000 +.00059 -.00000
3.500
1.500
3.000
15.750
3.000
3.000
3.000
5 X Ø.62500 +.00071 -.00000
Ø1.25000 +.00098 -.00000
3.500
1.500
7.750
4 X 2.000
3.500
1.250
1.50000
Ø1.50000 +.00098 -.00000
UNLESS OTHERWISE SPECIFIED:
NAME
DATE
DRAWN
CHECKED
ENG APPR.
MFG APPR.
Q.A.
COMMENTS:
MATERIAL STEEL
FINISH
DO NOT SCALE DRAWING
NEXT ASSY
USED ON
APPLICATION
TITLE:
REAR FRAME
SIZE A
DWG. NO. 5
REV 1
SCALE: 1:12
WEIGHT:
SHEET 2 OF 2

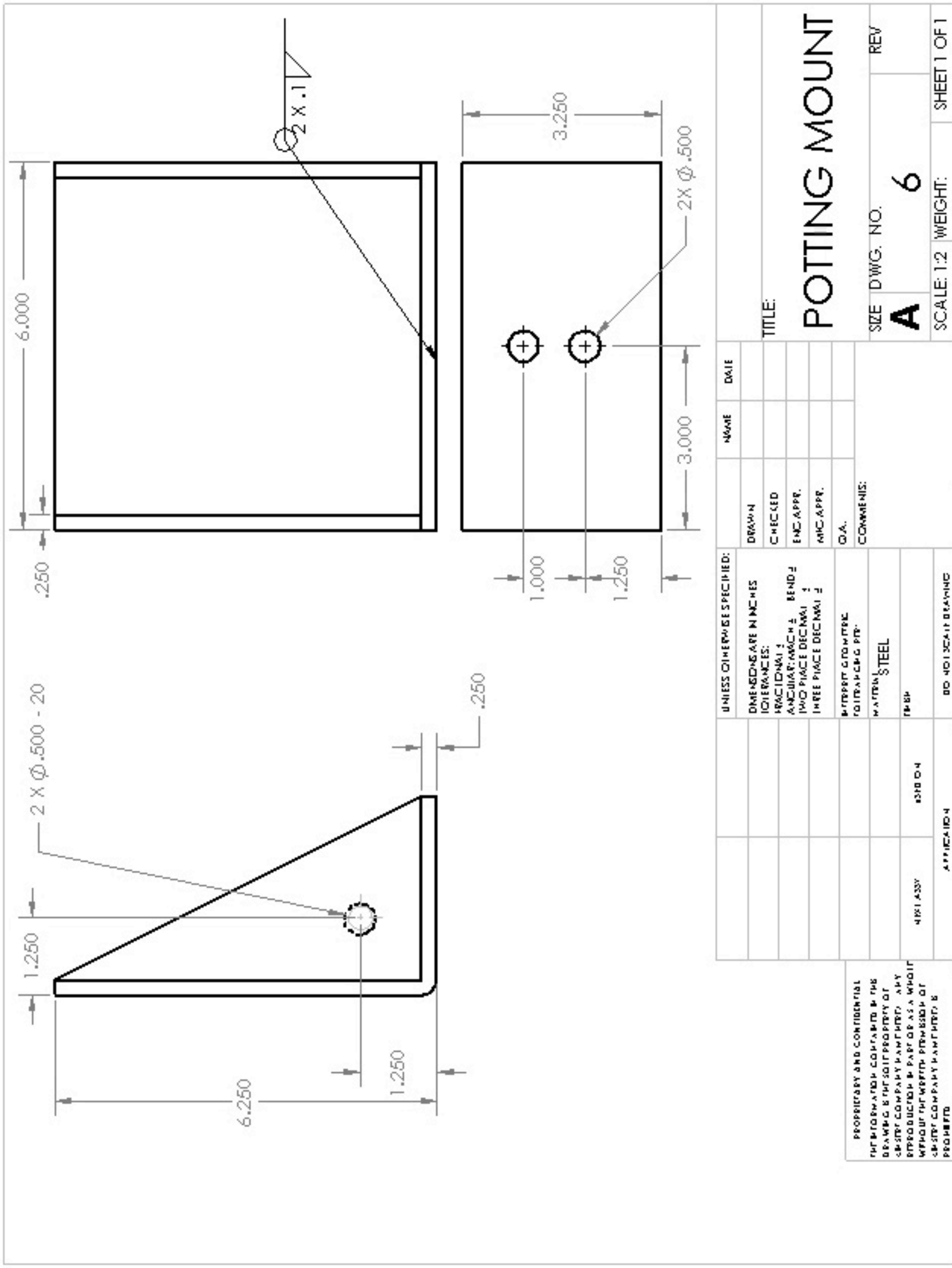

2 X .1
3.250
6.000
2X Ø.500
.250
3.000
1.000
1.250
2 X Ø.500 - 20
.250
1.250
6.250
1.250
UNLESS OTHERWISE SPECIFIED:
DRAWN
CHECKED
ENG APPR.
MFG APPR.
Q.A.
COMMENTS:
NAME
DATE
STEEL
NEXT ASSY
USED ON
APPLICATION
DO NOT SCALE DRAWING
PROPRIETARY AND CONFIDENTIAL
TITLE:
POTTING MOUNT
SIZE
A
DWG. NO.
6
REV
SCALE: 1:2
WEIGHT:
SHEET 1 OF 1
1
2
3
4
5

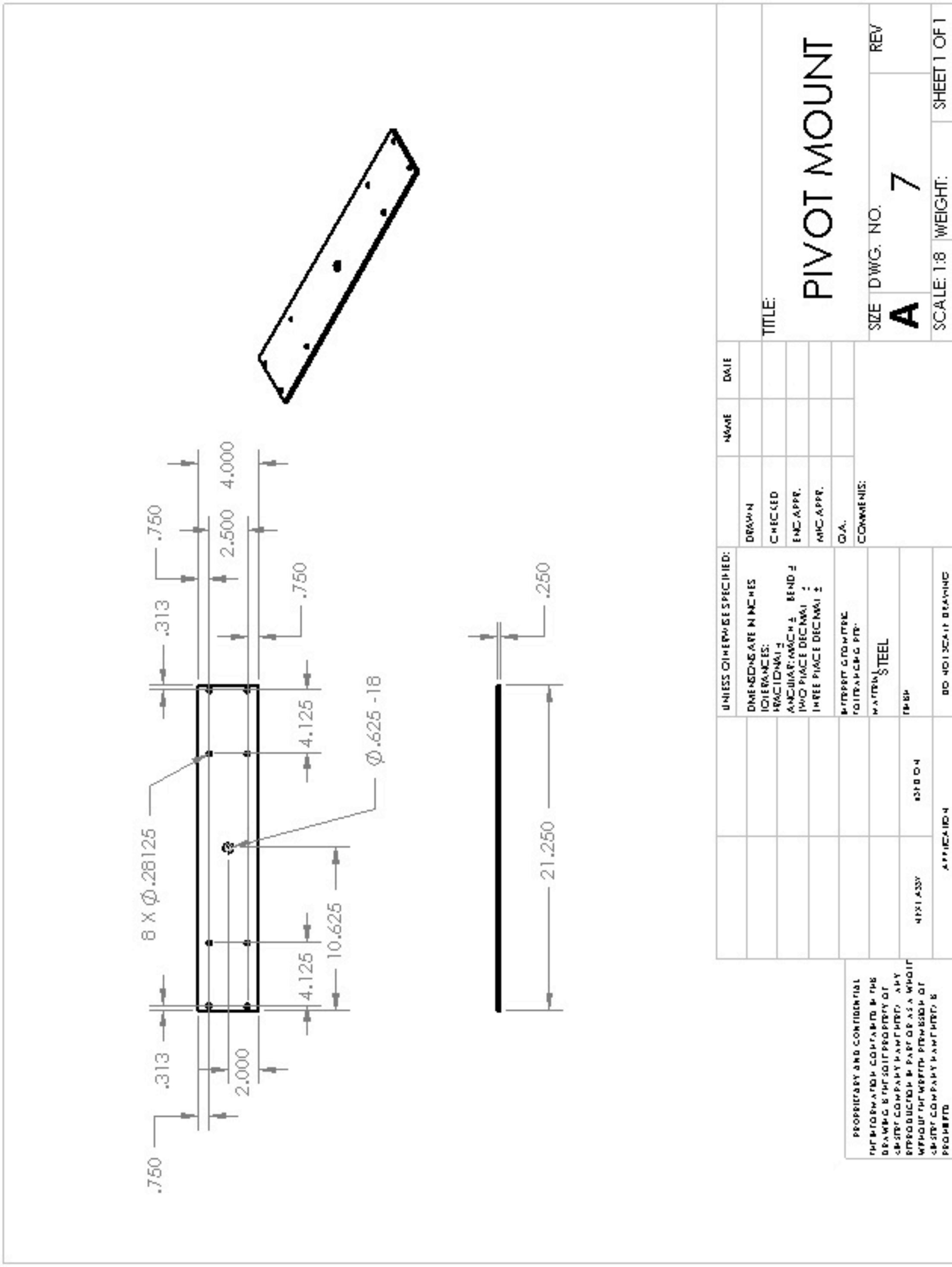

TITLE:
PIVOT MOUNT
SIZE
A
DWG. NO.
7
REV
SCALE: 1:8
WEIGHT:
SHEET 1 OF 1
UNLESS OTHERWISE SPECIFIED:
DIMENSIONS ARE IN INCHES
MATERIAL
STEEL
DO NOT SCALE DRAWING
NAME
DATE
DRAWN
CHECKED
ENG APPR.
MFG APPR.
Q.A.
COMMENTS:
NEXT ASSY
USED ON
APPLICATION
PROPRIETARY AND CONFIDENTIAL
8 X Ø.28125
Ø.625 - 18
.750
.313
2.500
4.000
2.000
4.125
10.625
21.250
.250

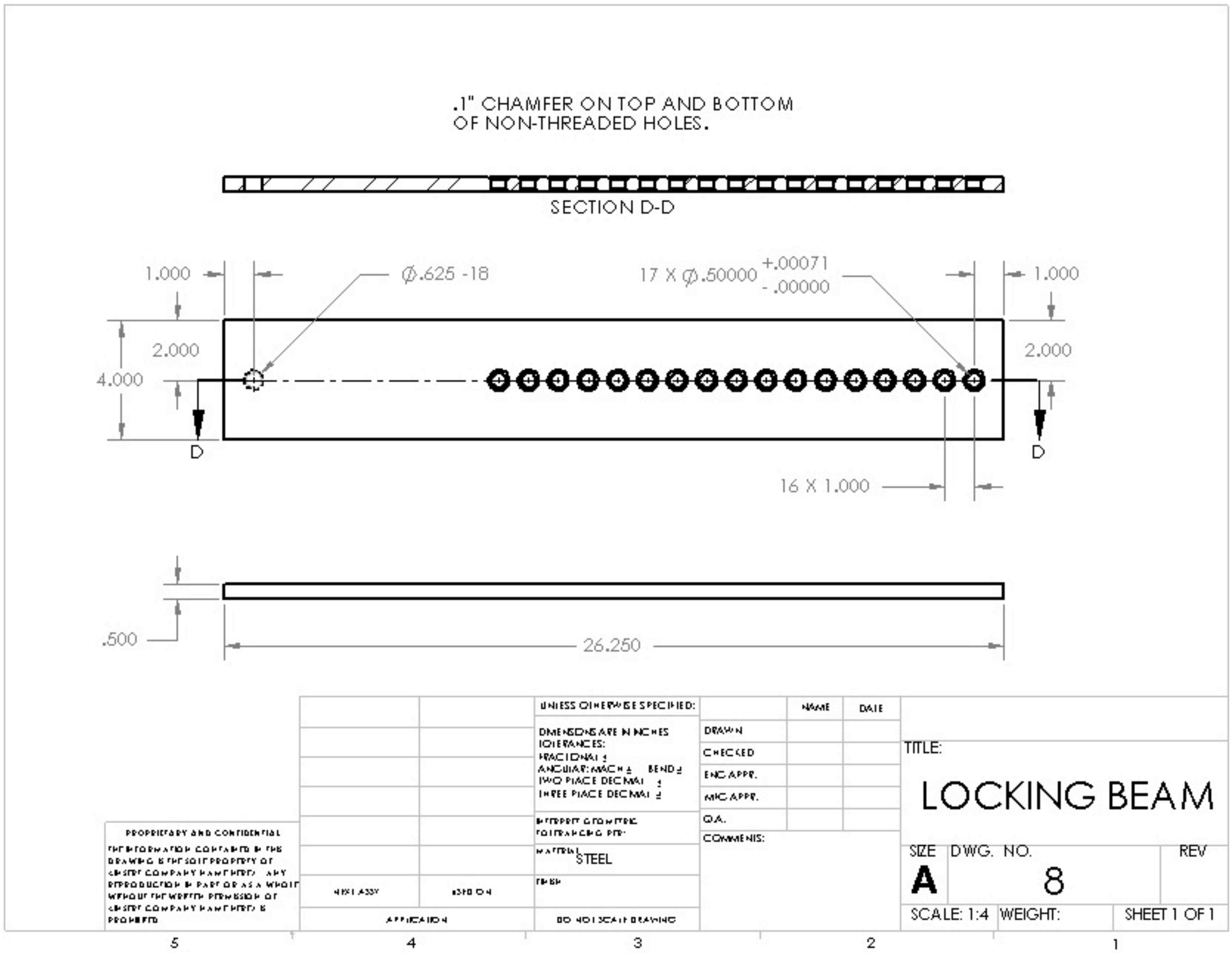
.1" CHAMFER ON TOP AND BOTTOM
OF NON-THREADED HOLES.
SECTION D-D
1.000
Ø.625 -18
17 X Ø.50000 +.00071 -.00000
1.000
2.000
4.000
2.000
D
D
16 X 1.000
.500
26.250
UNLESS OTHERWISE SPECIFIED:
DIMENSIONS ARE IN INCHES
NAME
DATE
DRAWN
CHECKED
ENG APPR.
MFG APPR.
Q.A.
COMMENTS:
MATERIAL
STEEL
FINISH
NEXT ASSY
USED ON
APPLICATION
DO NOT SCALE DRAWING
PROPRIETARY AND CONFIDENTIAL
TITLE:
LOCKING BEAM
SIZE
A
DWG. NO.
8
REV
SCALE: 1:4
WEIGHT:
SHEET 1 OF 1
5
4
3
2
1

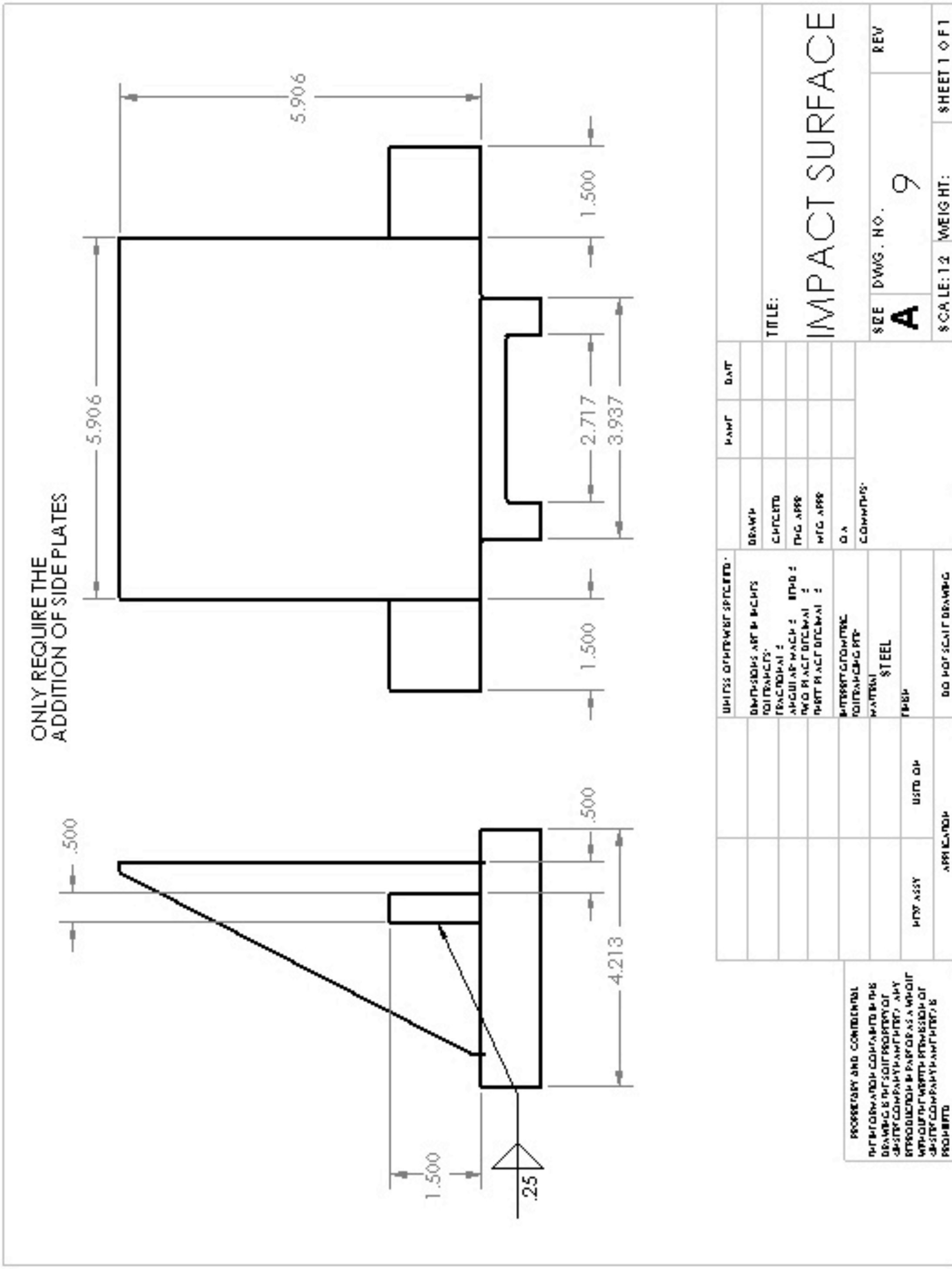
ONLY REQUIRE THE
ADDITION OF SIDE PLATES
5.906
5.906
1.500
1.500
2.717
3.937
.500
.500
4.213
1.500
.25
TITLE:
IMPACT SURFACE
SIZE
A
DWG. NO.
9
REV
SCALE: 1:2
WEIGHT:
SHEET 1 OF 1
STEEL
DO NOT SCALE DRAWING
PROPRIETARY AND CONFIDENTIAL

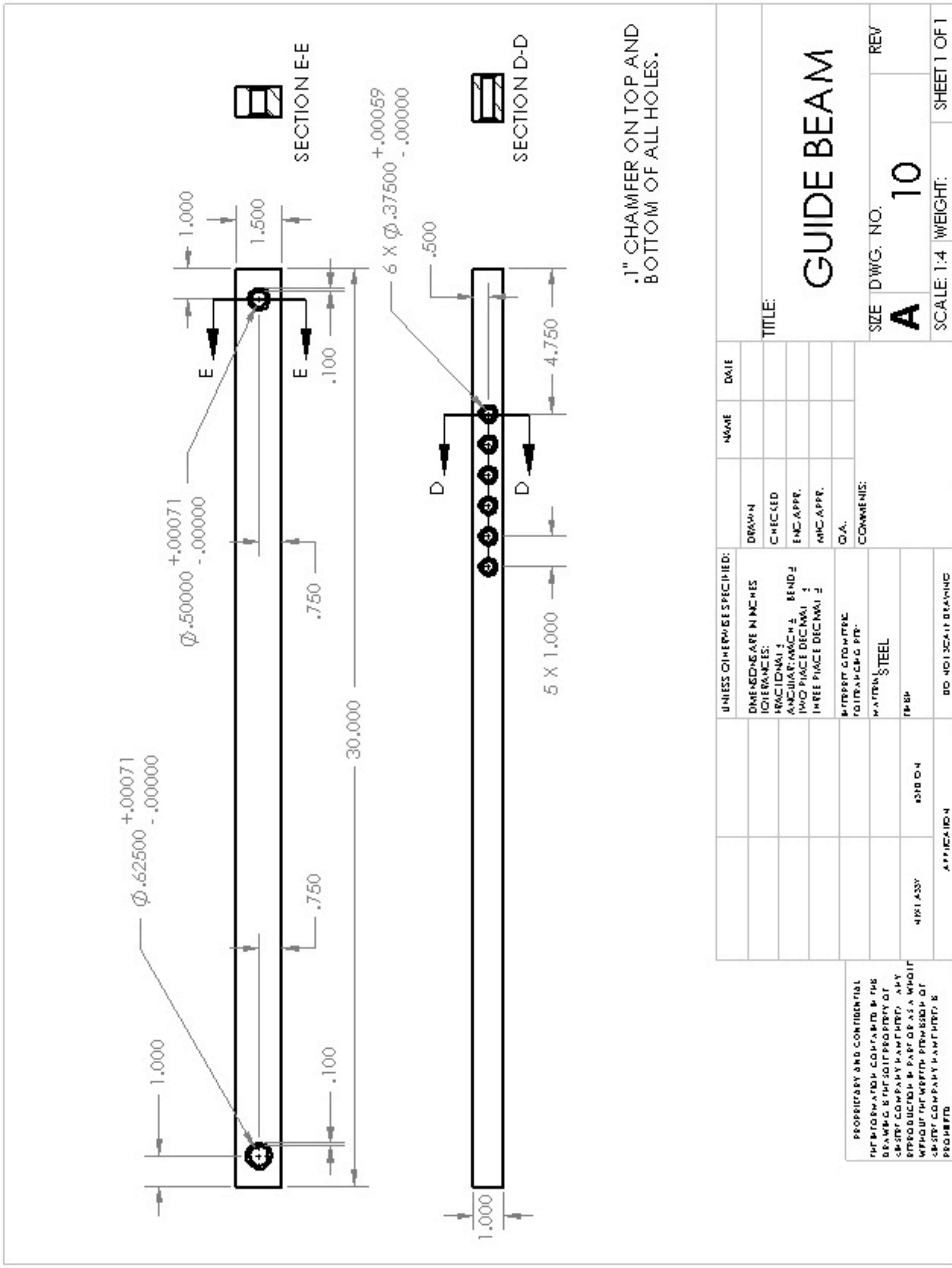

GUIDE BEAM
TITLE:
SIZE
A
DWG. NO.
10
REV
SCALE: 1:4
WEIGHT:
SHEET 1 OF 1
SECTION E-E
SECTION D-D
.1" CHAMFER ON TOP AND BOTTOM OF ALL HOLES.
6 X Ø.37500 +.00059 -.00000
Ø.50000 +.00071 -.00000
Ø.62500 +.00071 -.00000
1.000
1.500
.100
.750
30.000
.500
4.750
5 X 1.000
E
D
UNLESS OTHERWISE SPECIFIED:
DRAWN
CHECKED
ENG APPR.
MFG APPR.
Q.A.
COMMENTS:
NAME
DATE
MATERIAL
STEEL
FINISH
DO NOT SCALE DRAWING
NEXT ASSY
USED ON
APPLICATION

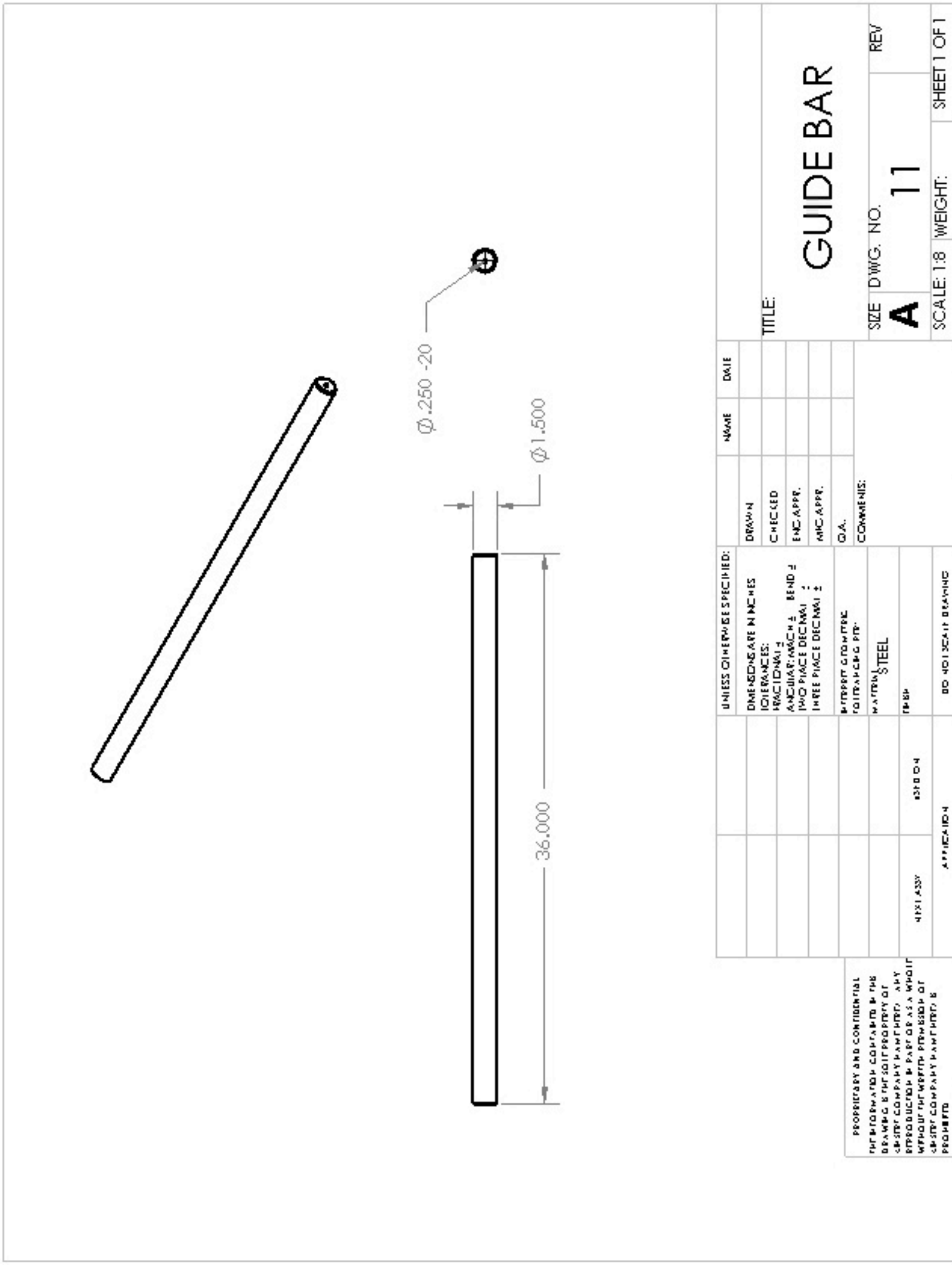
GUIDE BAR
TITLE:
SIZE
A
DWG. NO.
11
REV
SCALE: 1:8
WEIGHT:
SHEET 1 OF 1
Ø.250 -20
Ø1.500
36.000
STEEL
UNLESS OTHERWISE SPECIFIED:
NAME
DATE
DRAWN
CHECKED
COMMENTS:
Q.A.
1
2
3
4
5

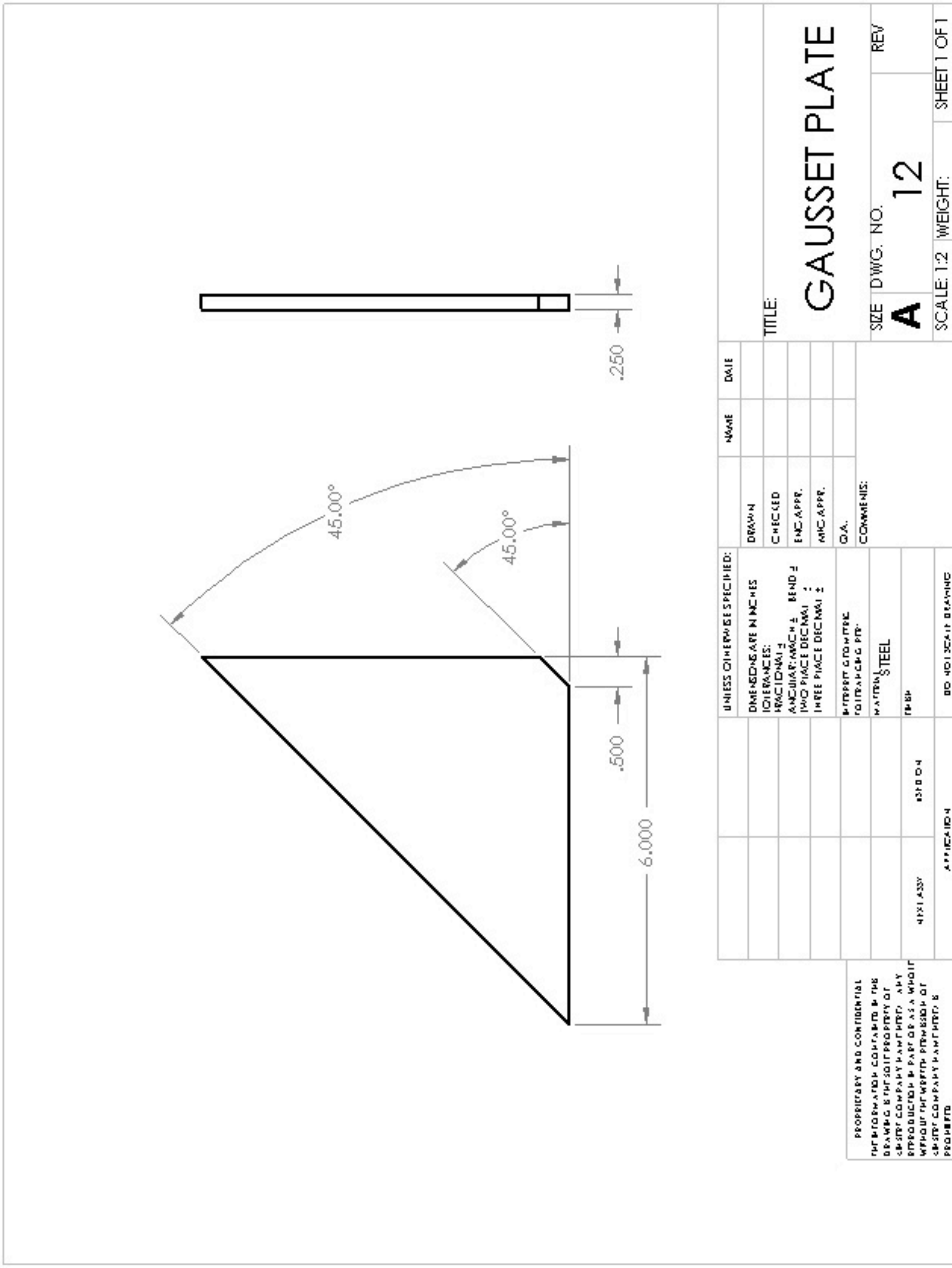

GAUSSET PLATE
TITLE:
SIZE
A
DWG. NO.
12
REV
SCALE: 1:2
WEIGHT:
SHEET 1 OF 1
6.000
.500
.250
45.00°
45.00°
STEEL
UNLESS OTHERWISE SPECIFIED:
DRAWN
CHECKED
ENG APPR.
MFG APPR.
Q.A.
COMMENTS:
NAME
DATE
NEXT ASSY
USED ON
APPLICATION
DO NOT SCALE DRAWING
PROPRIETARY AND CONFIDENTIAL

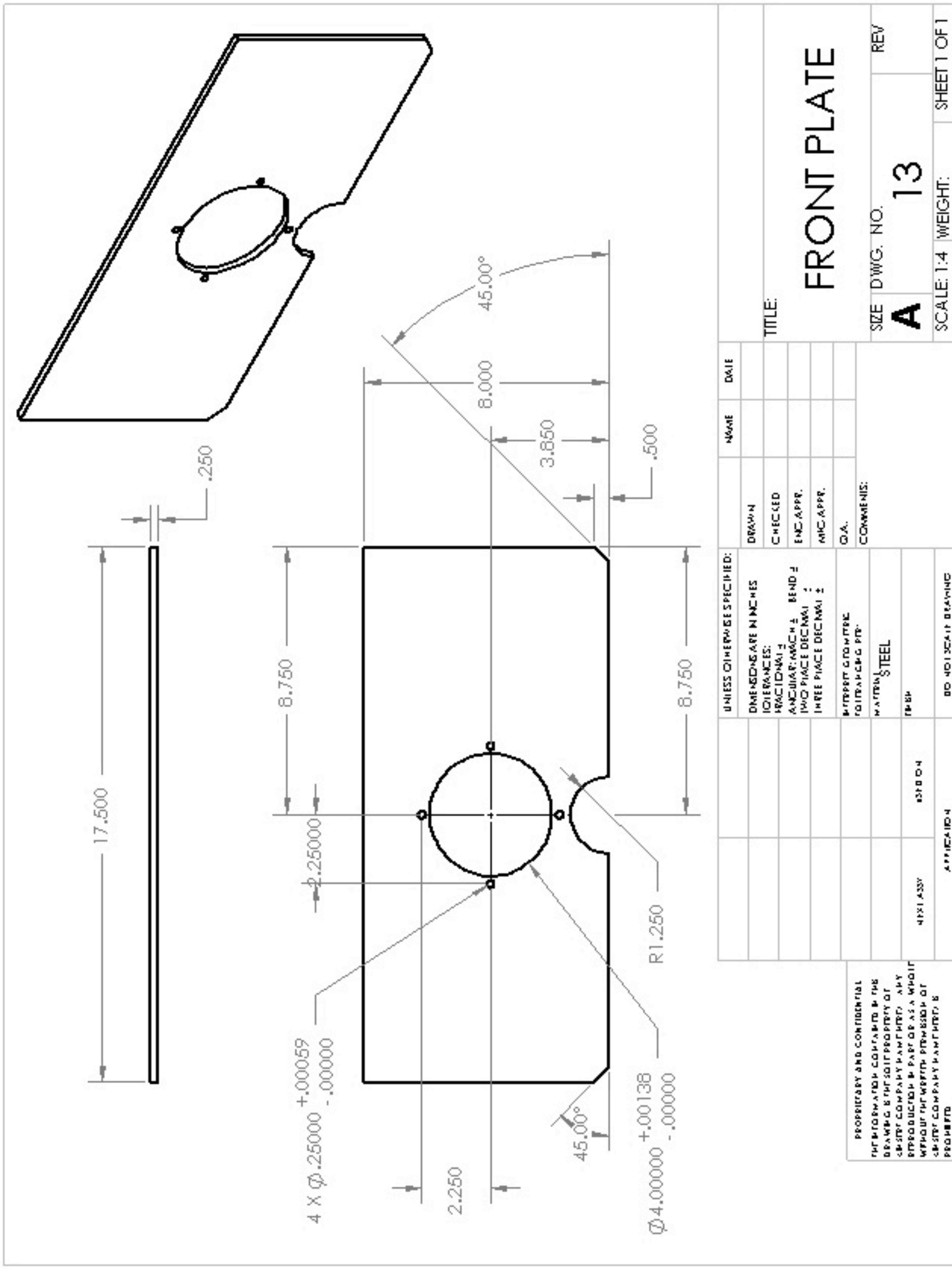

17.500
.250
8.750
8.750
8.000
3.850
.500
45.00°
45.00°
2.25000
2.250
R1.250
4 X Ø.25000 +.00059 -.00000
Ø4.00000 +.00138 -.00000
UNLESS OTHERWISE SPECIFIED:
DIMENSIONS ARE IN INCHES
DRAWN
CHECKED
ENG APPR.
MFG APPR.
Q.A.
COMMENTS:
NAME
DATE
MATERIAL
STEEL
FINISH
NEXT ASSY
USED ON
APPLICATION
DO NOT SCALE DRAWING
TITLE:
FRONT PLATE
SIZE
A
DWG. NO.
13
REV
SCALE: 1:4
WEIGHT:
SHEET 1 OF 1
1
2
3
4
5

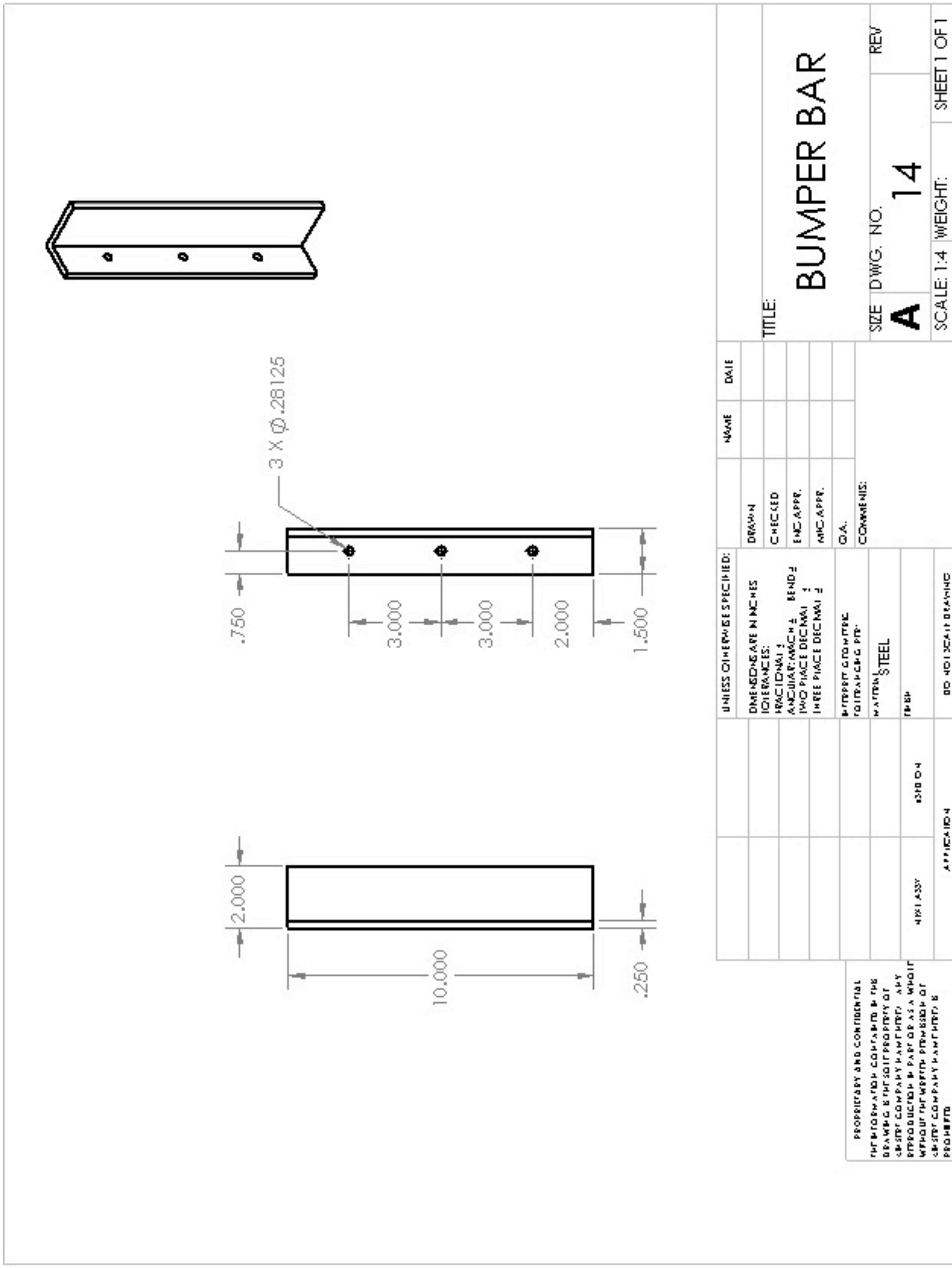

TITLE:
BUMPER BAR
SIZE
A
DWG. NO.
14
REV
SCALE: 1:4
WEIGHT:
SHEET 1 OF 1
3 X Ø.28125
.750
3.000
3.000
2.000
1.500
2.000
10.000
.250
UNLESS OTHERWISE SPECIFIED:
NAME
DATE
DRAWN
CHECKED
ENG APPR.
MFG APPR.
Q.A.
COMMENTS:
MATERIAL
STEEL

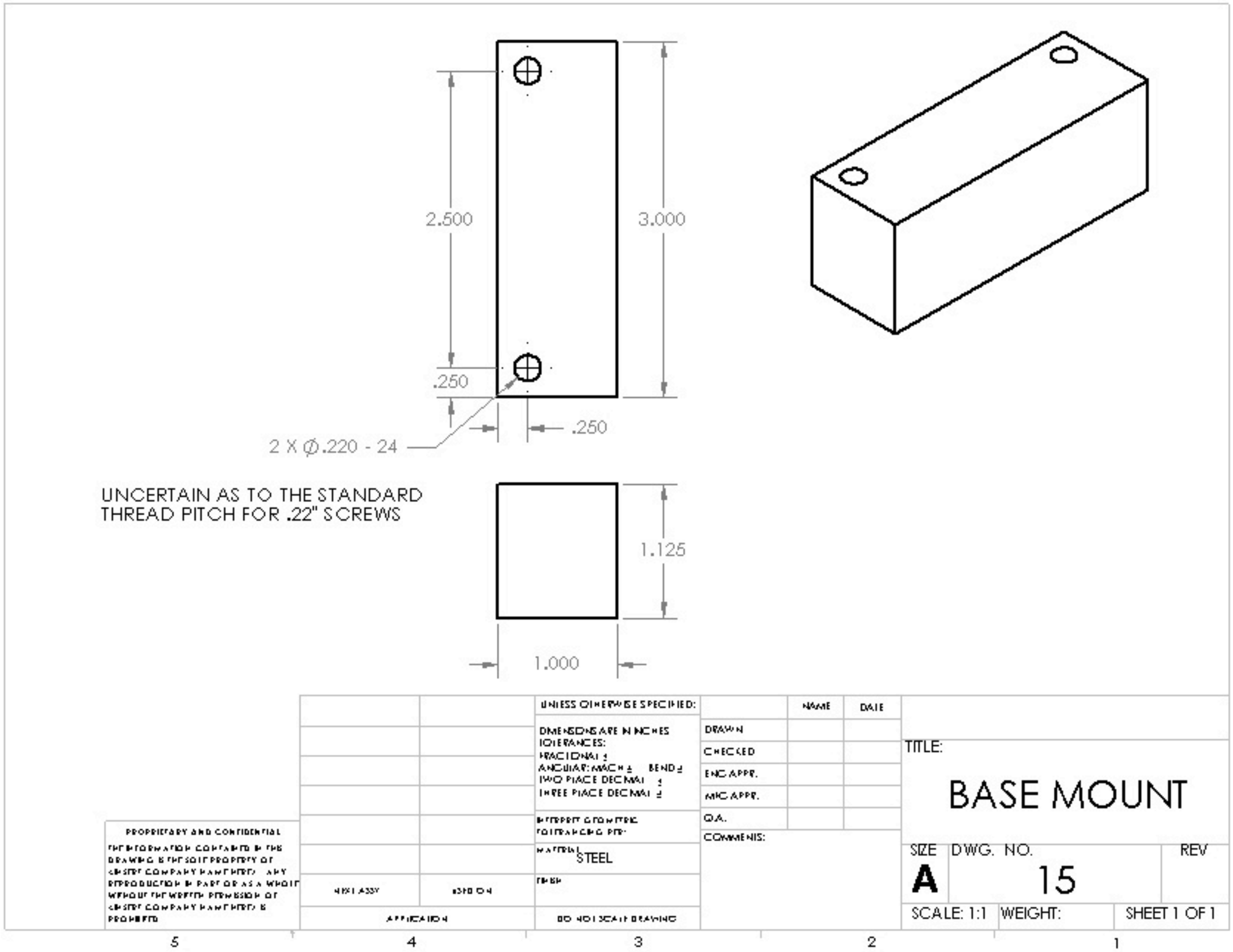
2.500
3.000
.250
.250
2 X Ø.220 - 24
UNCERTAIN AS TO THE STANDARD
THREAD PITCH FOR .22" SCREWS
1.125
1.000
UNLESS OTHERWISE SPECIFIED:
DIMENSIONS ARE IN INCHES
TOLERANCES:
NAME
DATE
DRAWN
CHECKED
ENG APPR.
MFG APPR.
Q.A.
COMMENTS:
MATERIAL
STEEL
FINISH
NEXT ASSY
USED ON
APPLICATION
DO NOT SCALE DRAWING
PROPRIETARY AND CONFIDENTIAL
TITLE:
BASE MOUNT
SIZE
A
DWG. NO.
15
REV
SCALE: 1:1
WEIGHT:
SHEET 1 OF 1
5
4
3
2
1

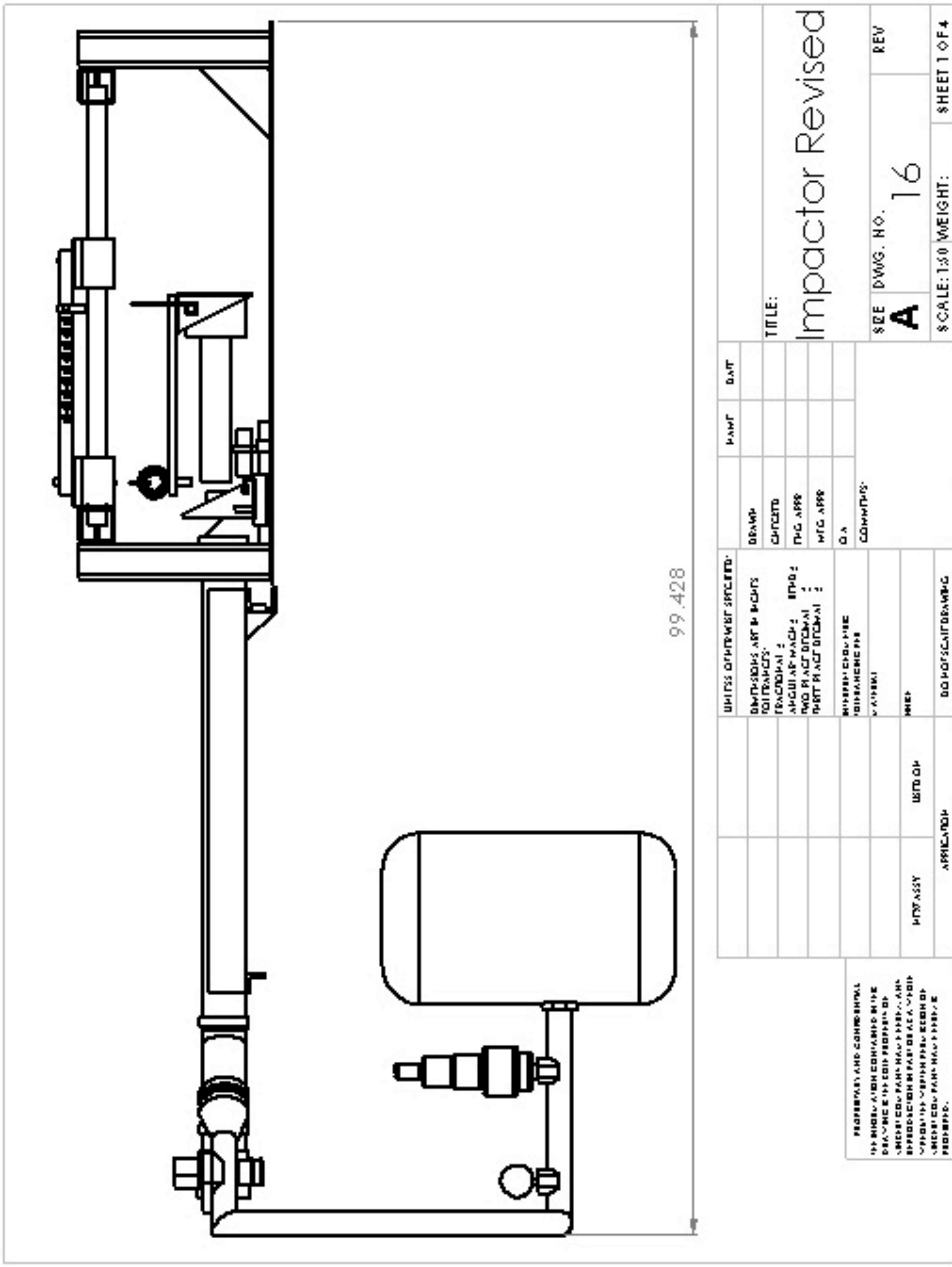
99.428
TITLE:
Impactor Revised
SIZE
A
DWG. NO.
16
REV
SCALE: 1:50
WEIGHT:
SHEET 1 OF 4
NAME
DATE
DRAWN
CHECKED
ENG APPR.
MFG APPR.
Q.A.
COMMENTS:
UNLESS OTHERWISE SPECIFIED:
DO NOT SCALE DRAWING
APPLICATION
USED ON
NEXT ASSY
PROPRIETARY AND CONFIDENTIAL

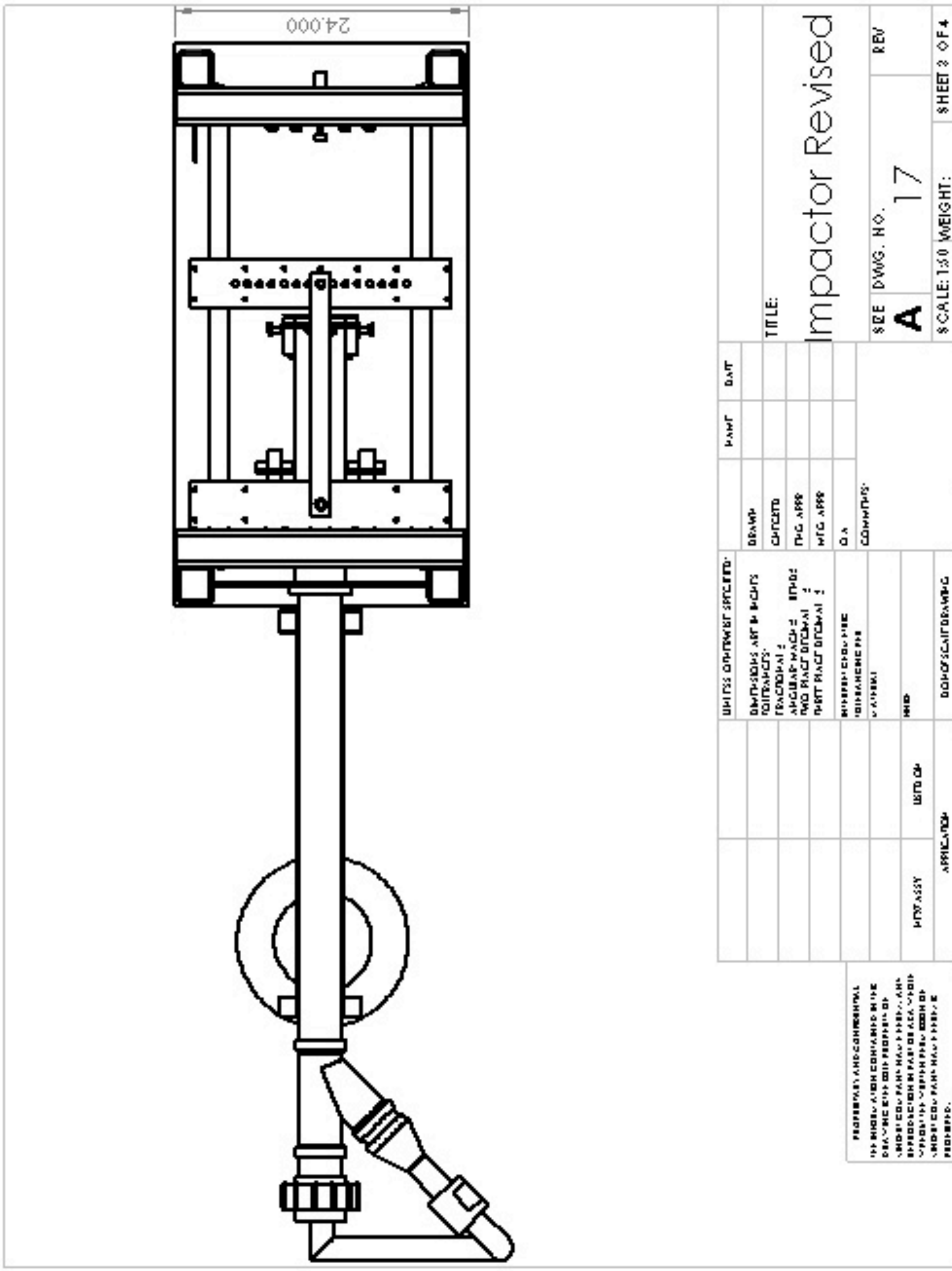
24.000
TITLE:
Impactor Revised
SIZE
A
DWG. NO.
17
REV
SCALE: 1:50
WEIGHT:
SHEET 3 OF 4

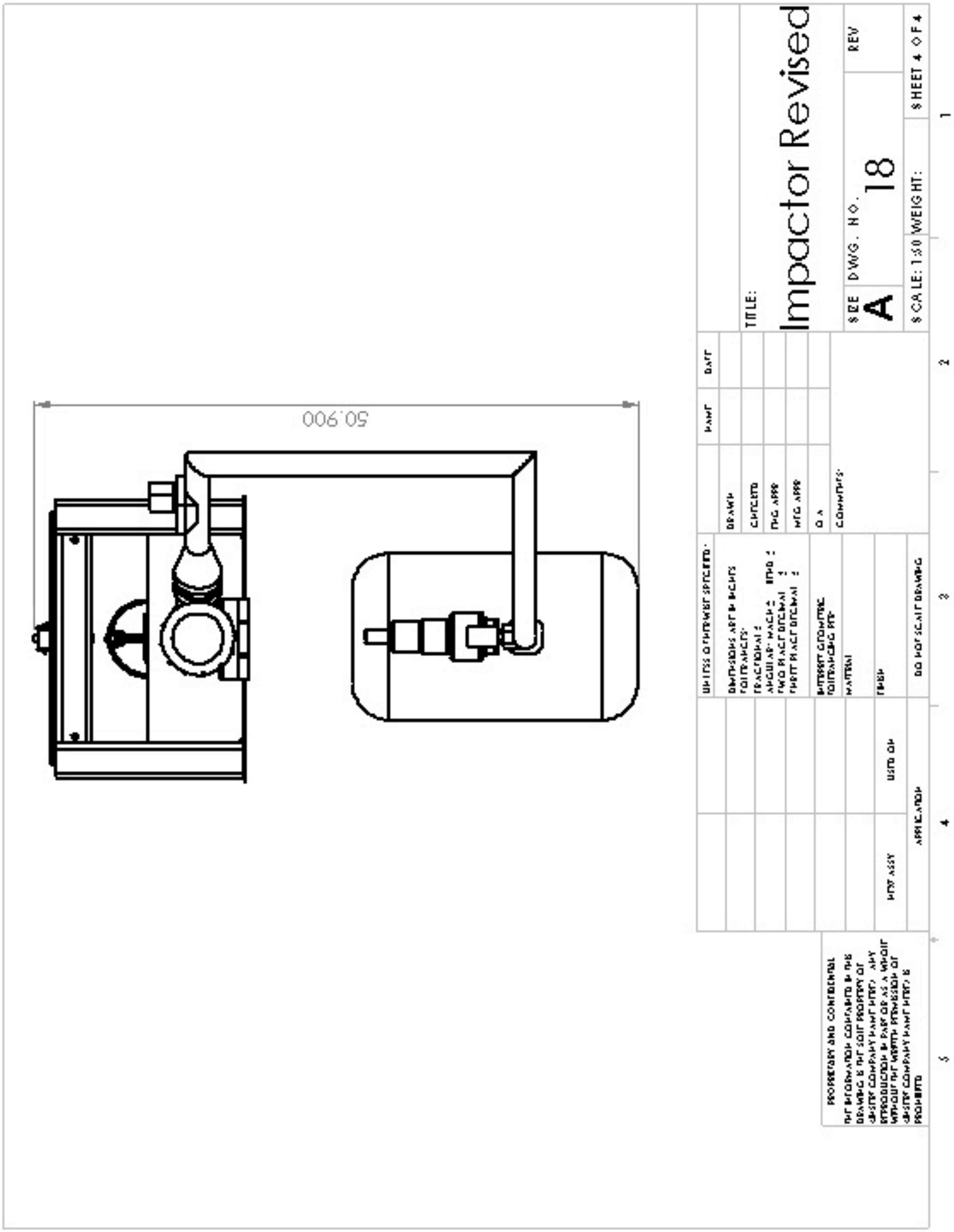
50.900
TITLE:
Impactor Revised
SIZE
A
DWG. NO.
18
REV
SCALE: 1:50
WEIGHT:
SHEET 4 OF 4

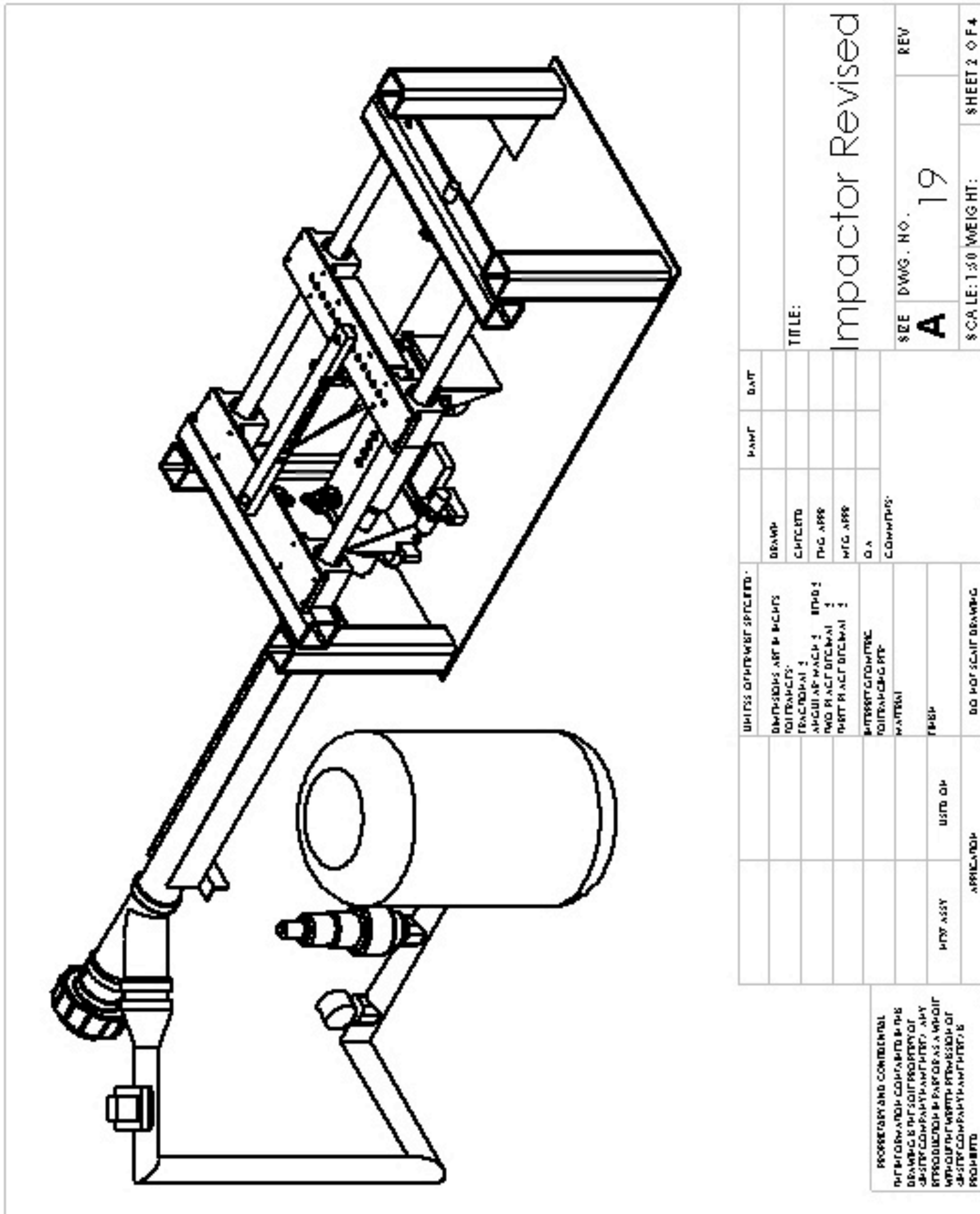
TITLE:
Impactor Revised
SIZE
A
DWG. NO.
19
REV
SCALE: 1:50
WEIGHT:
SHEET 2 OF 4
DO NOT SCALE DRAWING

APPENDIX D: APPARATUS VALIDATION PROCEDURE

1. The testing chamber is emptied, and the protective encasement is secured.
2. The impacting ram is removed from the accelerator tube and set to a mass of 6.66 kg.
3. The impacting ram is then placed back in the accelerator tube with its leading edge set to a distance of 0.52 m from the exit of the accelerator tube (Figure D.1).
4. The pressure in the tank is set to 5 psi using *PPC-Voltage_Set.vi*.
5. Using *IsolatedRadius_2012.vi* the solenoid is triggered, and resulting loads (from the load cell; Denton (maker, place) and ram velocity (from the optical sensors) are recorded and saved.
6. Impacting energy is calculated as the kinetic energy of the ram exiting the accelerator tube (Eq. D.1).

$$Impacting\ Energy = \frac{1}{2}(mass_{Ram})\times(velocity_{Ram})^2 \tag{D.1}$$

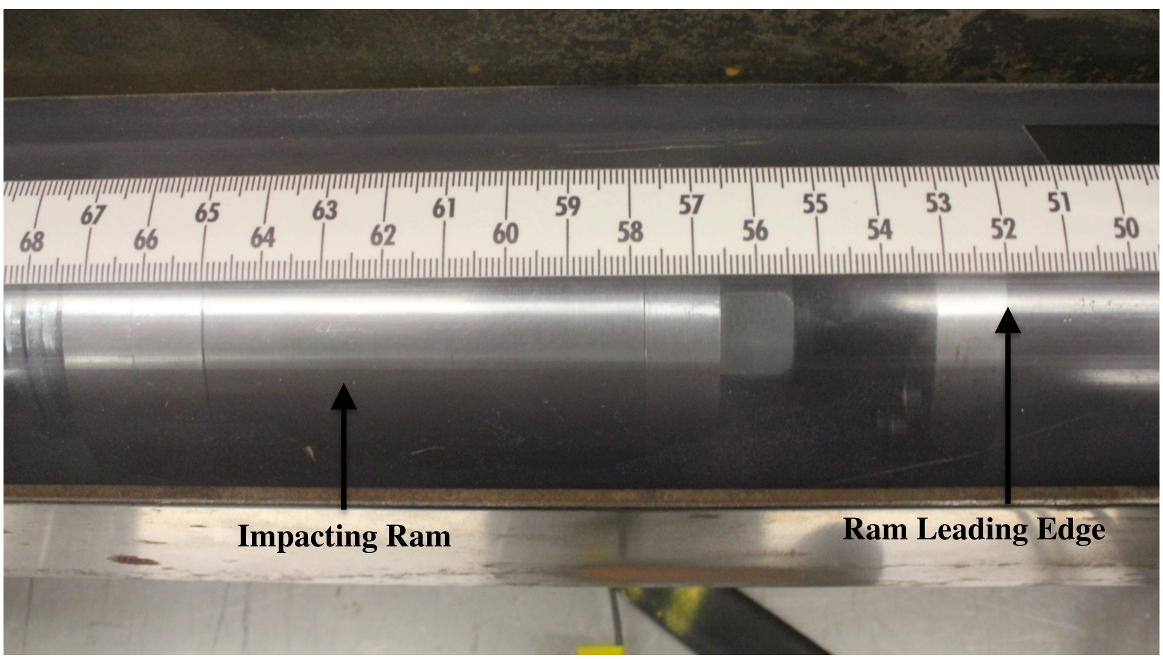

Figure D.1: Ram reset distance

The above procedure is repeated with increasing pressure from 5 psi to 14 psi in 1 psi increments. Following this, the impacting ram's mass is changed from 6.66 kg to 3.2 kg and finally to 1.27 kg (repeating the above procedure for each mass). By manipulating the impacting ram's mass and firing pressure, trends are developed showing how each affects impacting force, ram velocity and kinetic energy.

APPENDIX E: APPARATUS ASSESSMENT MEASURES SUMMARY

E.1: WITHIN-DAY IMPACT DATA

Table E.1: Peak force, ram velocity and kinetic energy data for the 6.66 kg mass.

Pressure [psi]	Ram Velocity [m/s]	Ram Kinetic Energy [J]	Force [N]
Trial 1			
5	3.3	36	310
6	4.2	58	570
7	4.9	81	851
8	5.5	99	1144
9	6.0	118	1432
10	6.5	142	1711
11	7.1	166	1999
12	7.2	172	2266
Trial 2			
5	3.2	35	287
6	4.1	57	569
7	4.8	77	841
8	5.4	97	1163
9	5.6	105	1485
10	6.3	130	1754
11	6.6	146	2063
12	7	163	2270
Trial 3			
5	3	34	281
6	4	49	514
7	5	74	800
8	5	93	1111
9	6	112	1442
10	7	148	1540
11	7	172	1981
12	7	176	2214

Table E.2: Peak force, ram velocity and kinetic energy data for the 3.31 kg mass.

Pressure [psi]	Ram Velocity [m/s]	Ram Kinetic Energy [J]	Force [N]
Trial 1			
5	4.1	28	410
6	5.6	52	811
7	6.3	65	1121
8	7.0	81	1394
9	7.8	101	1658
10	8.3	114	1873
11	8.8	128	2123
12	9.3	143	2356
Trial 2			
5	4.5	33	469
6	5.5	50	849
7	6.4	68	1252
8	7.1	84	1563
9	7.7	99	1797
10	8.3	113	1984
11	8.9	131	2273
12	9.4	145	2410
Trial 3			
5	4.5	33	482
6	5.5	50	864
7	6.3	66	
8	7.1	83	1586
9	7.5	94	1797
10	8.1	109	2007
11	8.6	121	2250
12	9.1	138	2448

Table E.3: Peak force, ram velocity and kinetic energy data for the 1.28 kg mass.

Pressure [psi]	Ram Velocity [m/s]	Ram Kinetic Energy [J]	Force [N]
Trial 1			
5	7.9	40	813
6	9.0	51	1198
7	9.7	60	1463
8	10.5	70	1707
9	11.5	84	1960
10	12.7	104	-
11	13.9	123	2382
12	14.8	141	2443
Trial 2			
5	7.6	37	783
6	8.9	50	1181
7	9.7	60	1472
8	10.6	71	1707
9	11.5	85	1938
10	12.6	101	2162
11	13.8	122	2369
12	14.8	140	-
Trial 3			
5	7.6	37	832
6	8.8	50	1192
7	9.6	59	1475
8	10.7	73	1826
9	11.5	84	2077
10	12.5	100	2336
11	13.6	118	2559
12	14.5	135	2695

E.2: WITHIN-DAY IMPACT SUMMARY DATA

Table E.4: Mean (SD) peak force, ram velocity and kinetic energy data for all masses (n = 3).

Pressure [psi]	Ram Velocity [m/s]	Ram Kinetic Energy [J]	Force [N]
6.66 [kg]			
5	3.2 (0.0)	35 (1)	293 (15
6	4.0 (0.2)	55 (5)	552 (32)
7	4.8 (0.2)	77 (4)	831 (27)
8	5.4 (0.1)	97 (3)	1139 (26)
9	5.8 (0.2)	112 (7)	1453 (28)
10	6.5 (0.2)	140 (9)	1668 (113)
11	7.0 (0.3)	162 (14)	2014 (43)
12	7.1 (0.1)	170 (6)	2250 (31)
3.33 [kg]			
5	4.3 (0.2)	31 (3)	454 (38)
6	5.5 (0.1)	51 (1)	841 (27)
7	6.3 (0.1)	66 (1)	1187 (93)
8	7.1 (0.1)	82 (2)	1514 (105)
9	7.7 (0.1)	98 (4)	1751 (80)
10	8.2 (0.1)	112 (3)	1954 (72)
11	8.8 (0.2)	127 (5)	2215 (81)
12	9.3 (0.1)	142 (4)	2405 (46)
1.28 [kg]			
5	7.7 (0.2)	38 (2)	809 (24)
6	8.9 (0.1)	50 (1)	1190 (8)
7	9.7 (0.0)	60 (0)	1470 (6)
8	10.6 (0.1)	71 (1)	1747 (69)
9	11.5 (0.0)	84 (0)	1992 (75)
10	12.6 (0.1)	102 (2)	2249 (123)
11	13.7 (0.1)	121 (2)	2437 (106)
12	14.7 (0.2)	138 (3)	2569 (178)

E.3: BETWEEN-DAY IMPACT DATA

Table E.5: Peak force, ram velocity and kinetic energy data for the 6.66 kg mass.

Pressure [psi]	Ram Velocity [m/s]	Ram Kinetic Energy [J]	Force [N]
Day 1			
5	2.5	21	229
6	3.1	32	463
7	3.6	43	715
8	4.0	53	1010
9	4.3	62	1272
10	4.6	71	1545
11	5.0	85	1835
12	5.6	103	2158
Day 2			
5	2.4	18	184
6	2.9	28	360
7	3.4	39	555
8	3.9	50	810
9	4.3	60	1087
10	4.6	69	1412
11	4.9	81	1726
12	5.2	89	2052

E.4: BETWEEN-DAY IMPACT SUMMARY DATA

Table E.6: Mean (SD) peak force, ram velocity and kinetic energy data for the 6.66 kg mass (n = 2).

Pressure [psi]	Ram Velocity [m/s]	Ram Kinetic Energy [J]	Force [N]
5	2.4 (0.1)	20 (2)	206 (32)
6	3.0 (0.1)	30 (3)	411 (73)
7	3.5 (0.1)	41 (2)	635 (113)
8	3.9 (0.1)	51 (2)	910 (142)
9	4.3 (0.1)	61 (2)	1180 (131)
10	4.6 (0.0)	70 (2)	1478 (94)
11	5.0 (0.1)	83 (3)	1781 (78)
12	5.4 (0.3)	96 (10)	2105 (75)

APPENDIX F: CAMERA COLOUR-THRESHOLDING VALIDATION PROCEDURE

1. A custom marker (approximately 1 cm in diameter) is constructed using white cotton hockey stick tape.
    a. Using a black extra fine tip Sharpie Paint marker, draw the outline of a circle, approximately 1 cm in diameter.
    b. Again, using the black marker, colour in the negative marker space such that what remains on the tape is a single white circle surrounded by black. (Note: The use of black and white provides the greatest contract for distinguishing between marker and peripheral space).
2. A threaded metal rod is then wrapped in the cotton tape, allowing the white marker to remain visible and in-line with the long axis of the rod.
3. The rod is screwed into the bottom of the Instron® materials testing machine actuator to ensure the two will translate together rigidly.
4. Using WaveMaker™ software on the Instron-controlling computer, a program is created to translate the marker up & down in position control:
    a. Triangular wave
    b. 2 cm in amplitude
    c. Translation rate of 2 cm/s
    d. Duration of 10 seconds (exceeding the capture duration of 3 seconds)
5. Position the camera parallel to the marker, approximately 50 cm away, ensuring the marker can be seen through its full range of motion (Figure F.1).
6. Synchronize the Instron and camera outputs for triggering through *IsolatedRadius_2012.vi* in LabVIEW.
7. Set the camera to capture at 4000 frames per second and clear the camera buffer prior to triggering.
8. Load the WaveMaker™ program in WaveRunner™ and begin running the program.
9. While the marker is translating, using *IsolatedRadius_2012.vi*, trigger the capture of camera and Instron data for a predefined duration of 3 seconds.

10. In *Jake's RGB Colour-Thresholding.vi*, determine the required RGB, area and perimeter settings to isolate the marker (See Appendix H.2 for more detailed program operation). A calibration factor (m/pixel) is determined using a known length present in the video frame.
11. Perform residual analysis and subsequent filtering on the camera and Instron position data (Lowpass Butterworth filter, yielded a cut-off frequency of 8.5 Hz for both systems).
12. Using the capture frequency of each system, calculate marker velocity and acceleration, to permit direct system comparison (using Instron outputs as the gold standard or ground truth).

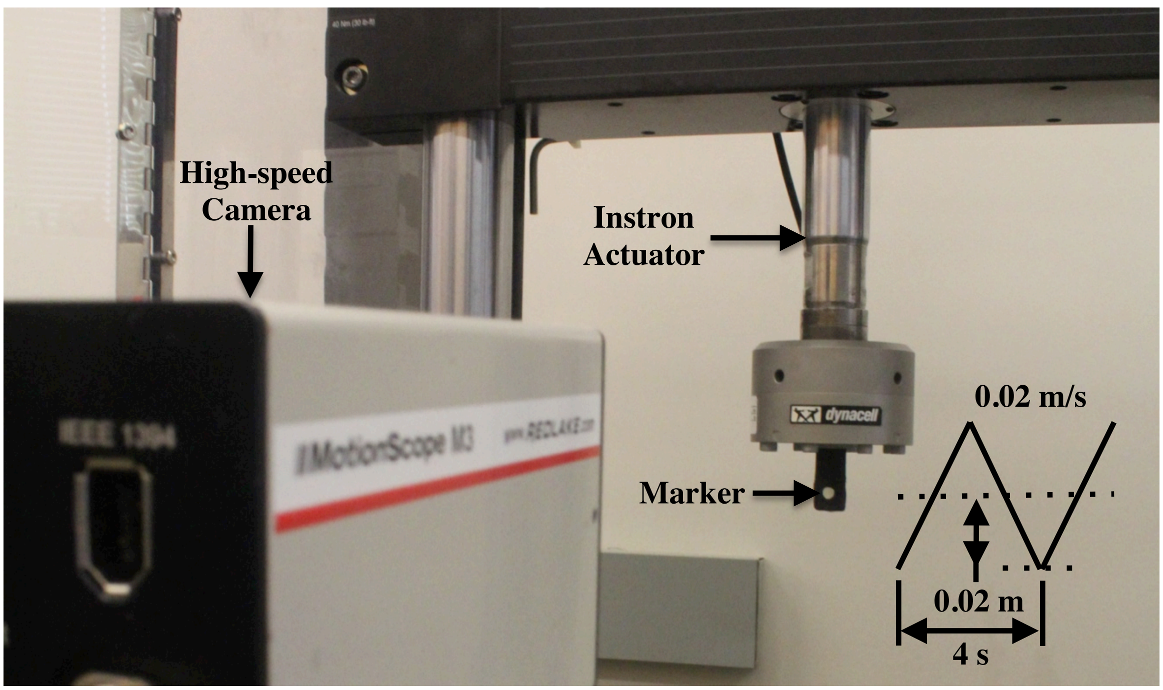

Figure F.1: Camera validation setup in Instron

APPENDIX G: RESIDUAL ANALYSIS

Residual analysis was conducted for various measures reported throughout this thesis (*e.g.*, load cell forces and moments, and camera *x* and *y* position data). The following is an example of how the optimal cutoff frequencies were determined. First, the raw data was filtered at varying cutoff frequencies (*e.g.*, 1 – 18 Hz at 1 Hz intervals). Then, the filtered data and raw data were used to calculate the residual (Eq. G.1) for each cutoff used. The resulting residuals were then plotted along the vertical axis against their corresponding cutoff frequencies (horizontal axis) to form a curve (Figure G.1). A tangential line was then drawn from the lower linear portion of the curve, and extended to intersect the vertical axis of the plot (A-B). From the vertical axis intersection point (B), a horizontal line was drawn until it intersected the curve (B-C). The curve intersection point (C) was then extended down vertically to intersect the *x*-axis (C-D). The horizontal axis intersection point (D) corresponded to the optimal cutoff frequency for the data.

$$Residual = \sqrt{\frac{1}{N}\sum_{n=1}^{N}(x_1 - x_1')^2} \quad \text{(G.1)}$$

Where *N* is the total number of data points, *x* is the original data point, and *x'* is the corresponding filtered data point.

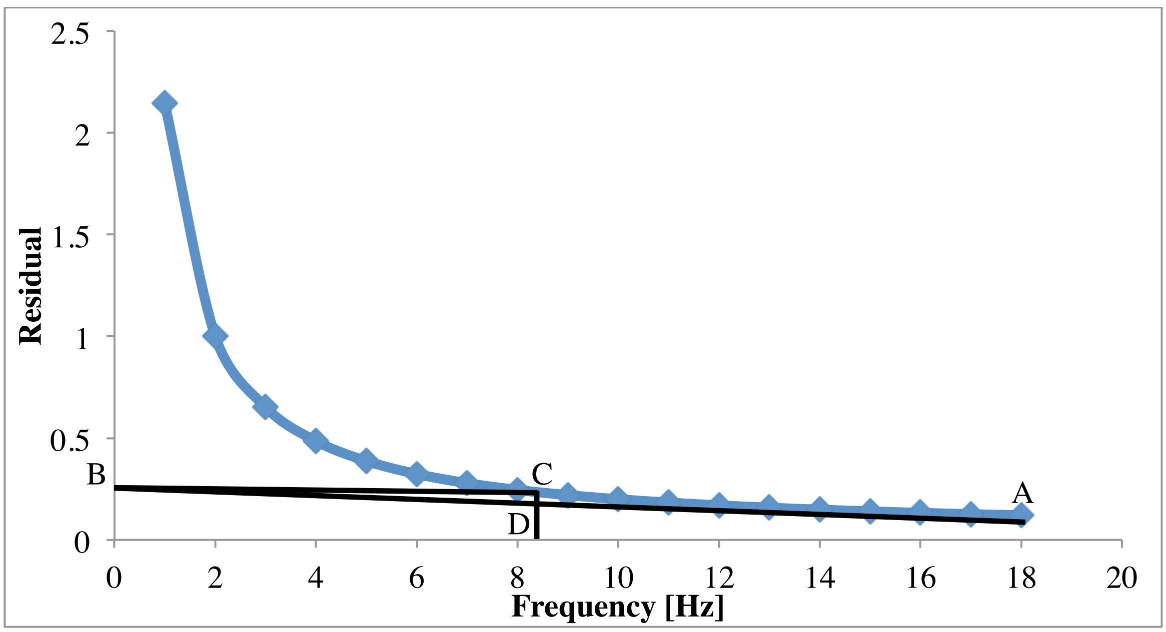

Figure G.1: Representative residual plot for determining the optimal cutoff frequency

APPENDIX H: ISOLATED RADIUS FRACTURE TESTING PROCEDURE

1. The frozen isolated radius specimen is thawed for 12 – 16 hours prior to testing.
2. Two screws are placed in the proximal diaphysis of the specimen to act as anchors during potting.
3. Using a laser level to ensure concentric alignment between the radial diaphysis and the potting tube, the specimen is proximally potted in a 0.08 – 0.1 m PVC tube using dental cement (Denstone Golden, Heraeus Dental; South Bend, IN) to interface with the impactor's potting mount (Figure H.1).

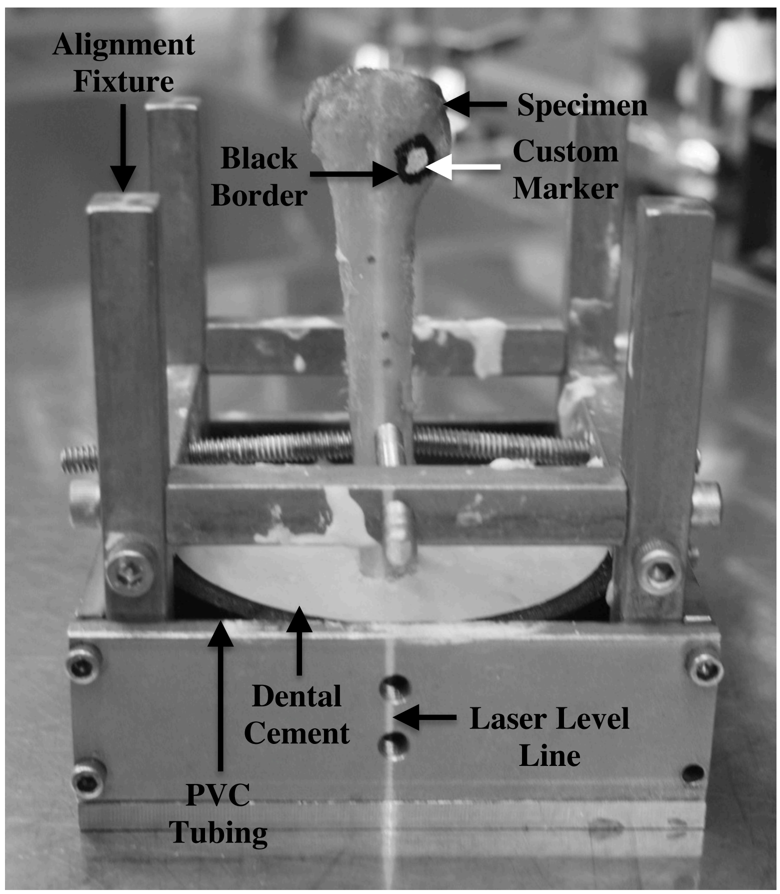

Figure H.1: Laser levelling used for specimen potting alignment

4. Specimens are instrumented with a paint based white marker (0.01m in diameter) surrounded by a black ring to provide maximum contrast (Figure H.1). The

marker is placed on the radial styloid to allow for line of sight with the high-speed camera (MotionScope M3, Red Lake Imaging, San Diego, CA).

5. The specimen is hung in the potting mount of the impactor at an angle of 75° in the sagittal plane with no frontal plane tilt and buttressed against a high-density polyethylene lunate-scaphoid model (SawBones®, Pacific Research Labs, Vashon, WA) attached to the impacting load cell (Figure H.2) (Burkhart *et al*., 2012b; Burkhart *et al*., 2011).

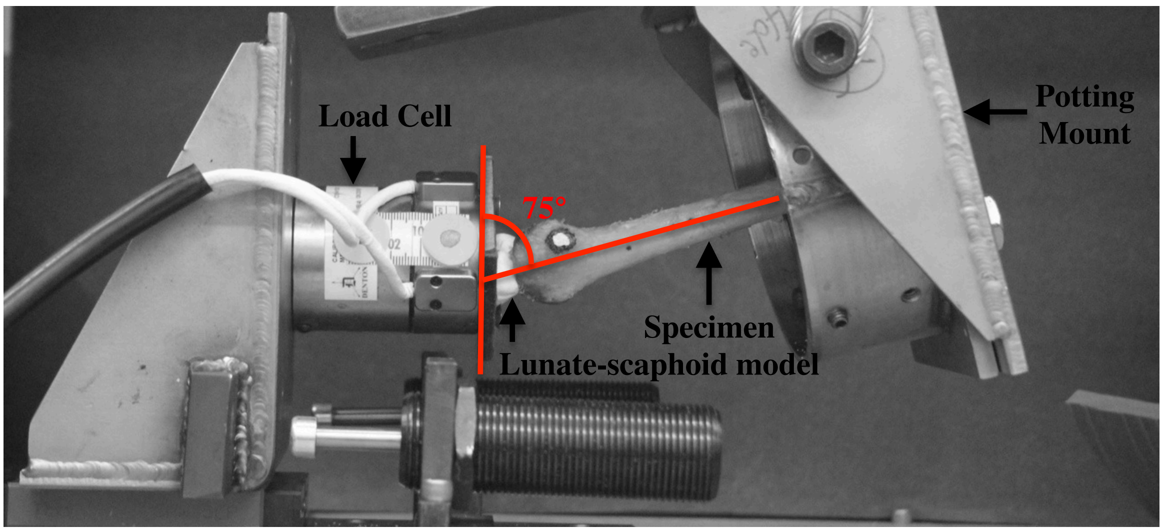

Figure H.2: Isolated bone impact apparatus setup

6. The impacting ram is removed from the accelerator tube and set to a mass of 6.66 kg (Figure H.3).

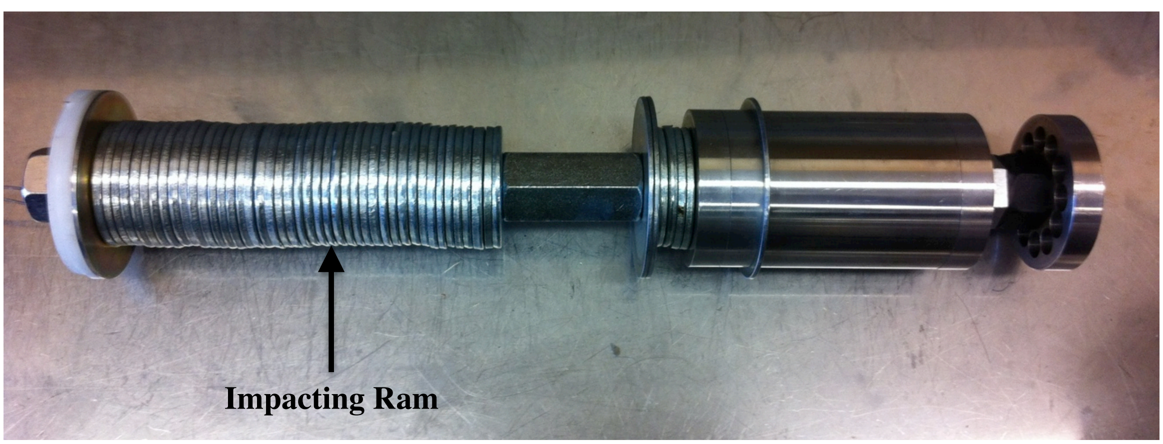

Figure H.3: 6.66 kg impacting ram

7. The impacting ram is then placed back in the accelerator tube with its leading edge set to a distance of 0.52 m from the exit of the accelerator tubing (Figure D.1).
8. The pressure in the tank is set to 5 psi using *PPC-Voltage_Set.vi* (Figure H.4) to correspond to a 30 J impact.

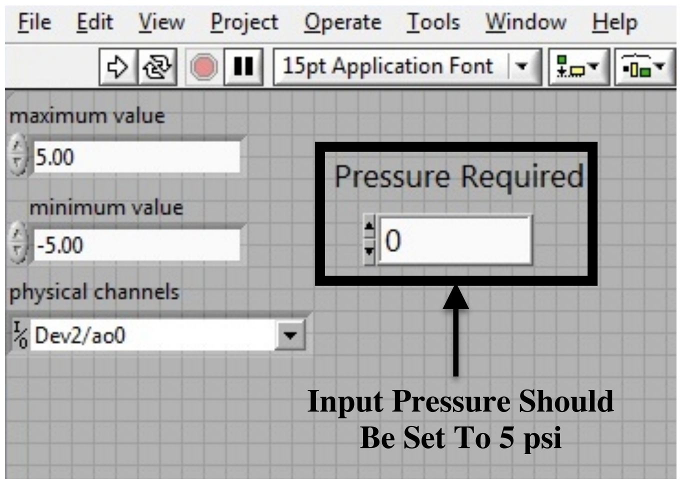

Figure H.4: Front panel of PPC-Voltage_Set.vi

9. Using *IsolatedRadius_2012.vi* the solenoid is triggered, and resulting loads and velocities are recorded and saved.

The above procedure is repeated at a ram kinetic energy of 30 J, to constitute two pre-fracture impacts. Following this, testing is again repeated targeting a ram kinetic energy of 80 J to cause fracture. These pre-fracture and fracture ram kinetic energy values are based on pilot testing that was conducted on a single specimen loaded sequentially in increments of 10 J until fracture, beginning at a ram kinetic energy of 20 J.

APPENDIX I: LabVIEW PROGRAM OPERATIONS

I.1: IMPACT APPARATUS OPERATIONAL PROCEDURE

1. Once the specimen is setup properly in the impacting chamber, the pressure must be set to the targeted value. To do this, use the LabVIEW program: *PPC-Voltage_Set.vi*.
    a. In *PPC-Voltage_Set.vi*, type the pressure that you are targeting in the 'Pressure Required' control box. Then, to send the targeted voltage signal, click the 'Run vi' button (arrow in top left corner of the program) (Figure I.1).
    b. Should the pressure set be over- or under-shot, repeat step 1.a. above varying the targeted pressure accordingly.

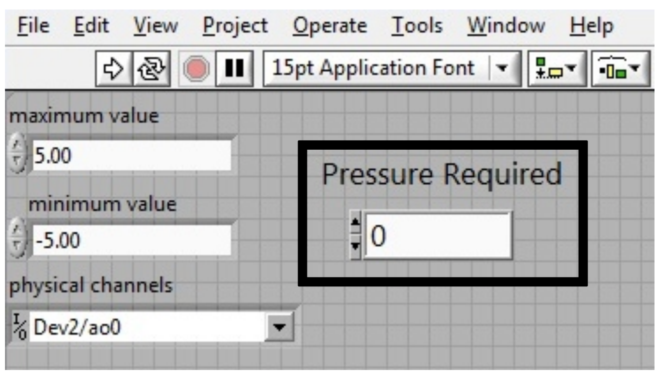

Figure I.1: Front panel of the PPC-Voltage_Set.vi program used to set pneumatic impacting pressure

2. Once the pressure is set to the desired value, triggering of the impactor is conducted using *IsolatedRadius_2012.vi* (Figure I.2).
    a. First, in the 'Save to Folder' control box, specify the path to which the generated data will be saved.
    b. Next, assign a file save name in the 'File Name' control box. This name must be changed for each subsequent test to avoid overwriting your previously saved files.

c. Leave the 'Pulse' and 'Collection Time' as the defaulted values of 1 and 3 seconds, respectively.

d. Once the specimen, pressure and inputs are set, the impactor can be triggered as follows:

    i. Click the 'Run vi' button to start the program.

    ii. Click the 'Start' button to begin collecting data and launch the ram.

e. The program collects data for the set duration (see step 2c, default of 3 seconds).

f. Once the data collection has stopped, click the 'Save' button to save the collected data to a file with the previously designated name and path (steps 2a, b).

g. Ram velocity is not saved to this file as a single number, so it is best to record this in a lab book for each impact.

h. Click the 'Stop vi' button to end the program (small stop sign in the top left corner of the front panel).

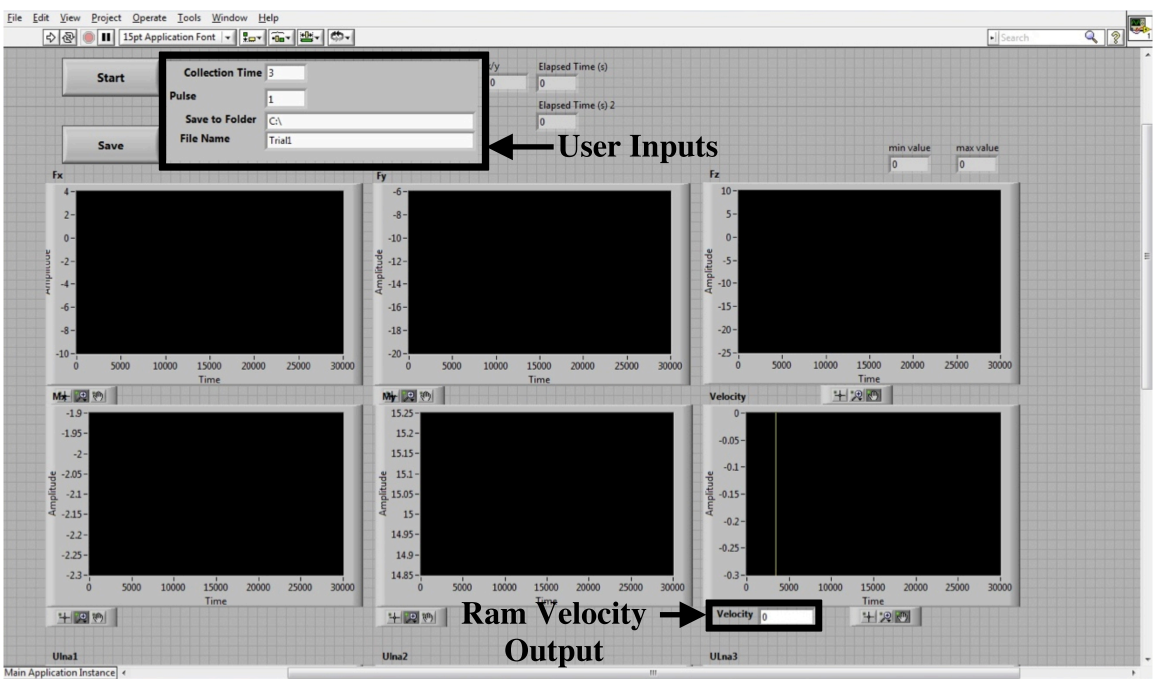

Figure I.2: Front panel of the IsolatedRadius_2012.vi program used for triggering and data collection

I.2: COLOUR-THRESHOLDING PROGRAM OPERATIONAL PROCEDURE

See Figure I.3 for reference to specific program components.

1. Prior to video capture, ensure that the camera's firewire cable is connected to the desired computer and that it is recognized in RedLake Imaging Studio E.2.1.6.2 video collection software (Red Lake Imaging, San Diego, CA). Furthermore, ensure that the camera settings are as you wish (*i.e.*, correct frame rate and size, triggering is enabled, the camera buffer is cleared by pressing the green circular button).
2. The camera will record automatically with the triggering of the impact apparatus, as the data collection (LabVIEW) program sends a triggering voltage to the camera.
3. Once the video is captured save it as a RAW file in folder on the computer hard-drive for that day's testing, then crop the video file to the desired start and end frames and save it as a separate file.
4. Load the Raw format video back into the RedLake software, and re-export it in AVI format (choosing Microsft Video 1 sub-format).
5. Create a folder on your computer called: *nameofvideo-frames*.
6. Using VirtualDub freeware available online (virtualdub.org), load your AVI file and export the frame sequence to the folder you just created.
7. Switching now to LabVIEW, and open *Jake's Image Colour-Thresholding.vi* (Figure I.3).
8. Adjust the Red, Green and Blue colour sliders to capture the desired range of values corresponding to your marker.
9. Adjust the area and perimeter upper and lower bound parameters shown on the front panel to match the range of your marker. (Note: By default, the program will launch with two area filters; you can change one of the filters to 'perimeter' by clicking on one of the dropdown menus that has 'area' selected on the front panel).
10. Additionally, if it is required, you may set a region of interest that will essentially crop the program analysis to a specified region.

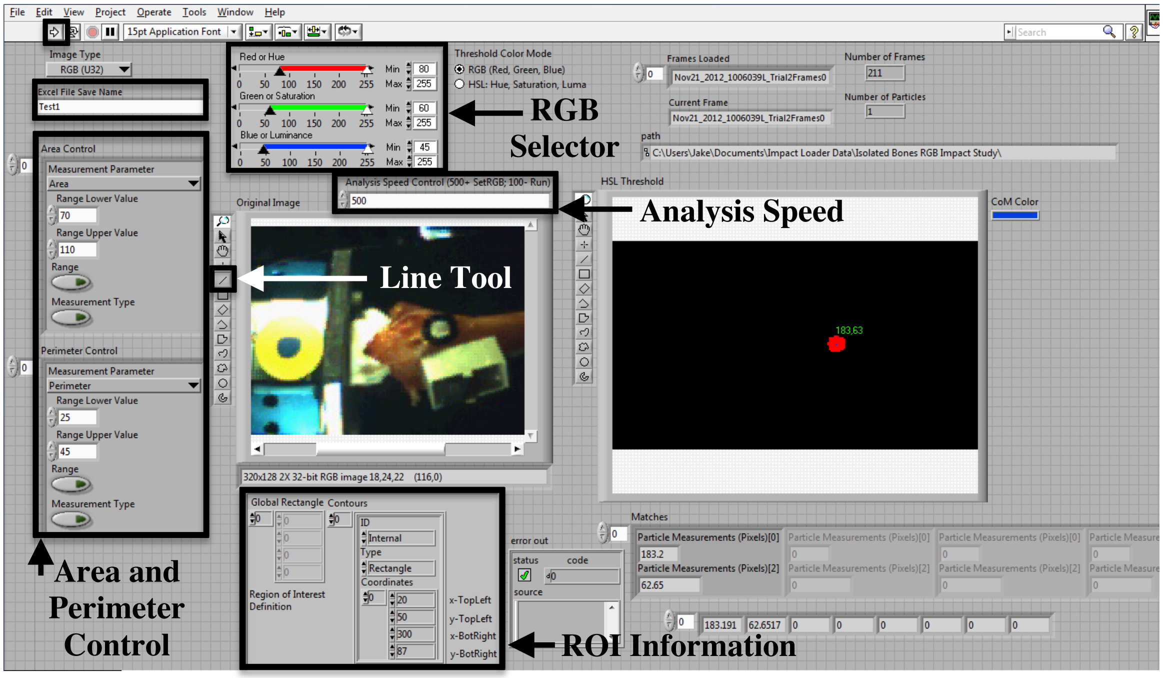

Figure I.3: Colour-thresholding program front panel with specific controls labeled

<u>Note:</u> To determine what RGB values and position values are present for your marker, aiding you in setting ranges of input parameters, you can run the program and stop it quickly to keep one frame visible. When you wave your cursor over a pixel in the video, you will see values of: (Red, Green, Blue) and (Position X, Position Y) along the video's bottom border.

Furthermore, to determine the area and perimeter values of your marker (once you have your RGB ranges set), you can change the Y-center of mass coordinate displayed (little green numbers) on the isolated marker screen (black and red screen) to either area or perimeter. To do so, you will have to make changes to the program's back panel. Don't forget to change it back to the Y-center of mass before you run the program to capture position data for real.

Additionally, you can slow or speed up the program's operational speed as desired by adjusting the analysis speed value on the front panel (Typically: 500 = Figuring out parameters, 100 = Running the program).

11. Once you have inputs selected that isolate your marker properly, provide a desired file name on the front panel, and ensure an adequate save path on the back panel.

Note that file names must be changed for each test or the program will overwrite old files.

12. You will want to determine a calibration factor (m/pixel) at this stage by using the line option on the left sidebar of the video display window to draw a line on the video, determining a known length in pixels. To make sure you are calibrating in the appropriate plane, use the height of your marker as the known distance (or some other feature with an established dimension that is easily visible).
13. To run the program: click the run-vi button (horizontal arrow in the top left corner of the program window).
14. Enter the folder containing the video frames and click the ‘Current Folder’ button.
15. Let the program run all the way through the video, it will stop and automatically save your data file to the specified path (found at the end of the code on the back panel).

APPENDIX J: INTACT FRACTURE TESTING PROCEDURE

J.1: SPECIMEN PREPARATION

1. All specimens (*i.e.*, intact forearms, disarticulated at the elbow) are both CT-scanned and fluoroscoped prior to beginning testing to ensure no pre-existing damage is present. Specimens are kept frozen.
2. Twenty-four hours prior to testing, a specimen is removed from the freezer to thaw (Figure J.1).

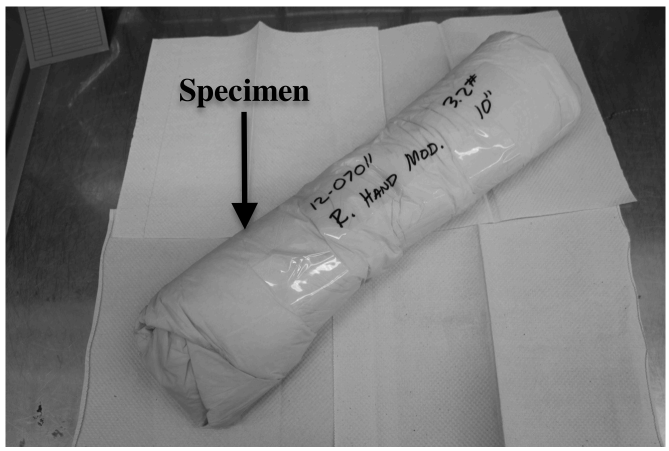

Figure J.1: Forearm specimen wrapped and thawing

3. Dissect the soft tissues on the forearm to expose the proximal radius and ulna for potting in dental cement, making sure that the integrity of the interosseous membrane is maintained (Figure J.2).

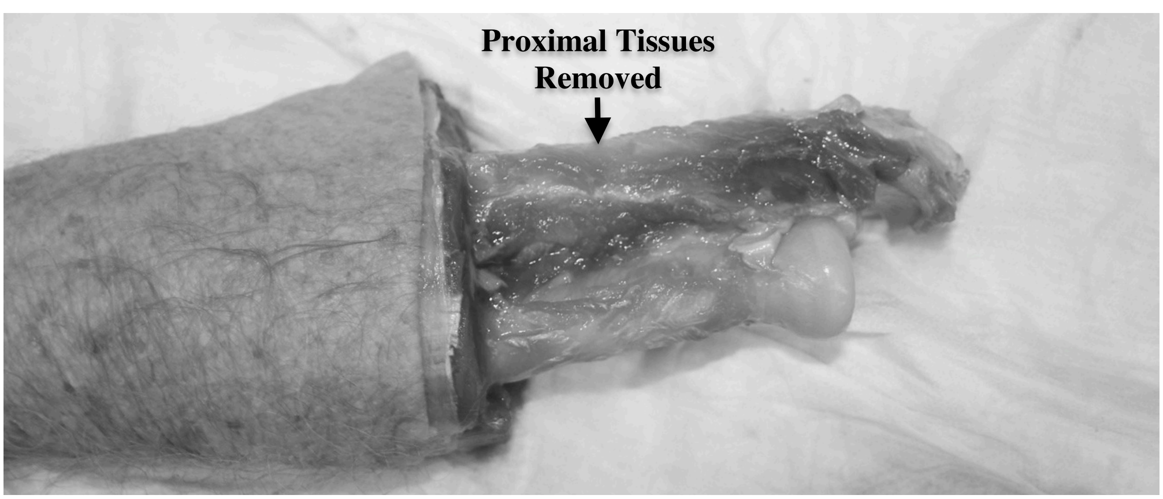

Figure J.2: Specimen with proximal soft tissues removed to permit potting

4. Make an incision longitudinally on the dorsal side of the forearm (distal to proximal) through the skin and fat. Then, use a scalpel to separate the skin from the muscle and tendon tissues (Figure J.3).

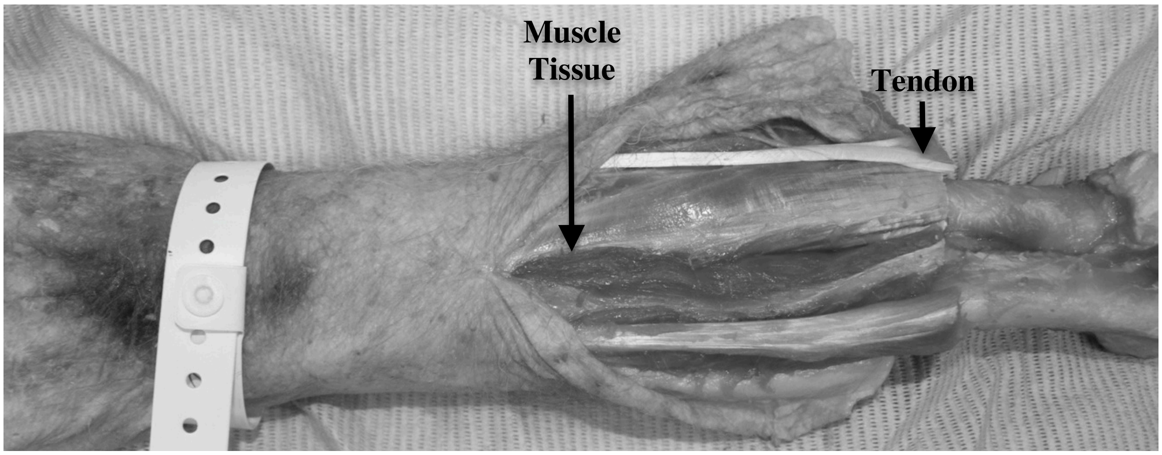

Figure J.3: Specimen with longitudinal dorsal incision, where skin and fat have been separated to expose forearm muscle and tendon

5. Isolate the extensor carpi ulnaris (ECU), and extensor carpi radialis longus (ECRL) tendons; then apply Krackow locking sutures to each (Figure J.4) (Krackow *et al*., 1986).

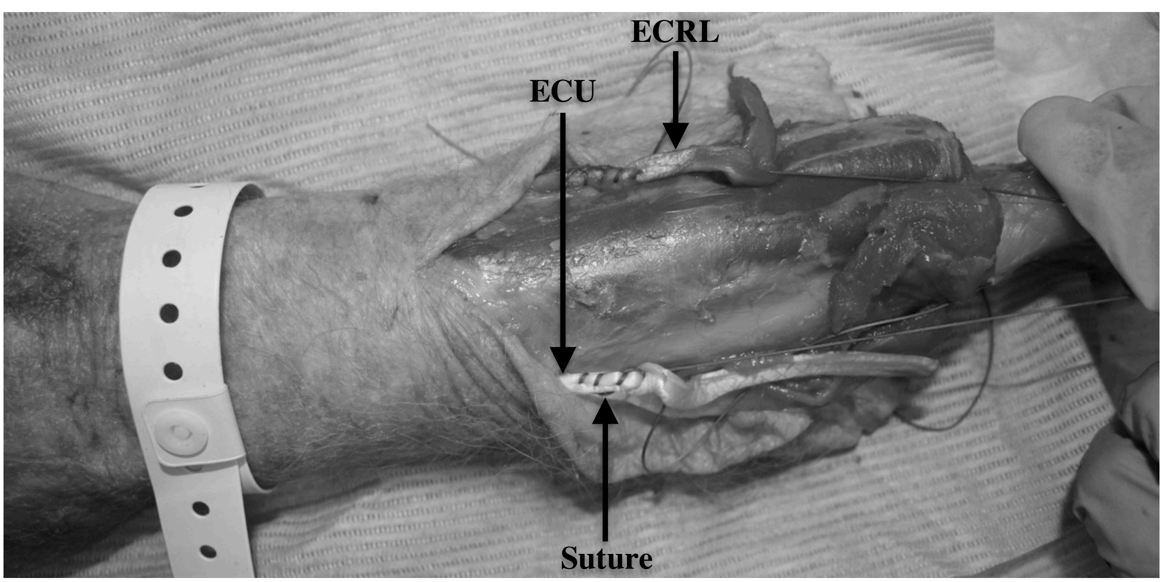

Figure J.4: Tendons ECU and ECRL isolated and sutured to using a Krackow locking suture

6. For the muscle-load specimens, tie the suture to the looped and crimped end of a braided galvanized steel cable approximately 20cm in length. These lines will act as tensioning cables that transmit the tendon loads (Figure J.5).

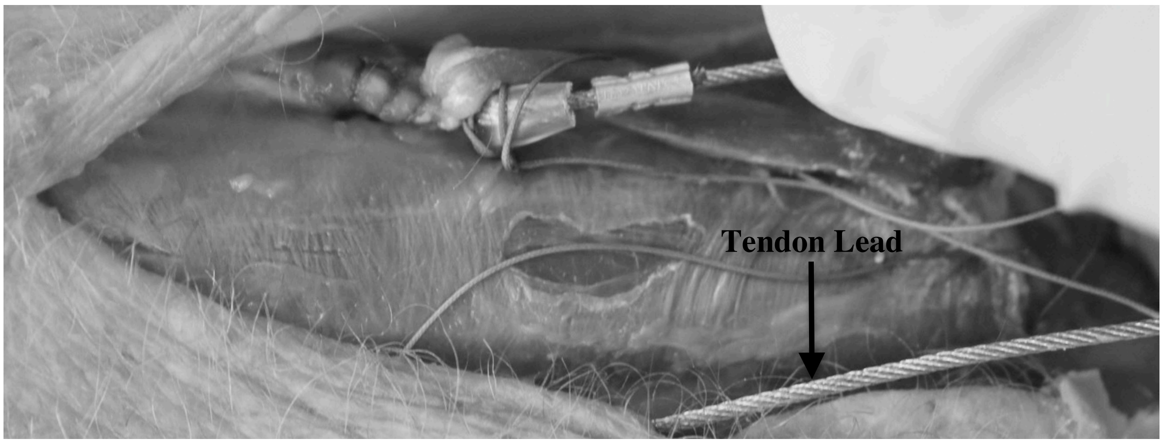

Figure J.5: Attachment of galvanized steel aircraft cable to the Krackow locking suture

7. Repeat steps 4-6 for the palmar side of the forearm, isolating the flexor carpi radialis (FCR), and flexor carpi ulnaris (FCU) tendons.
8. Make two small incisions on the dorsal side of the forearm (approximately 5cm in length) that will later allow for strain gauge application to the most distal and dorsal surfaces of the radial and ulnar diaphysis (Figure J.6).

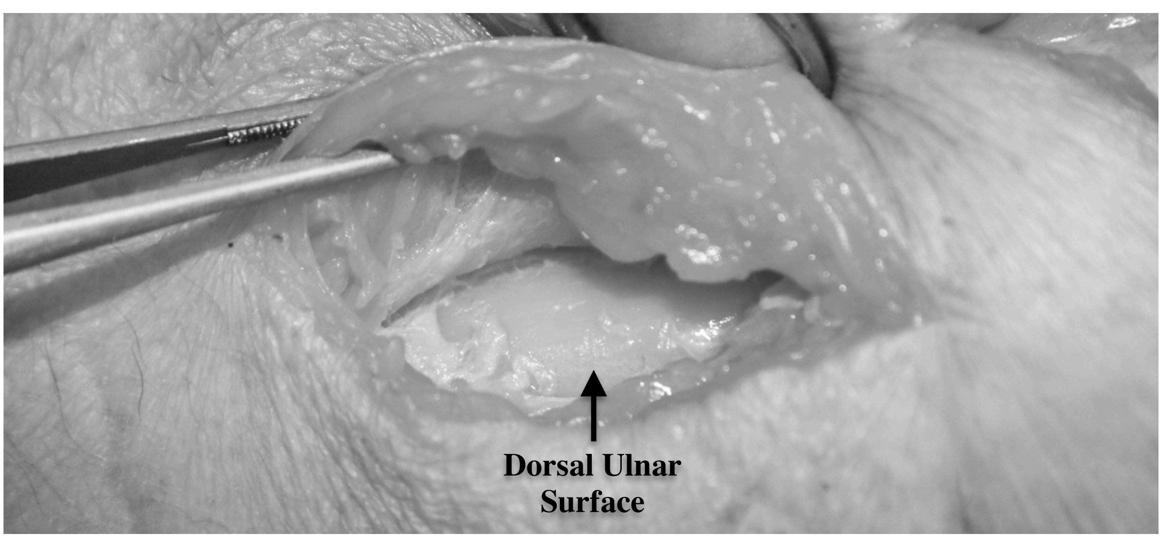

Figure J.6: One of two dorsal incisions made to permit strain gauge attachment to the radius and ulna

9. To provide additional stability of the specimen when potted, three wood screws are implanted in the proximal 3 – 5 cm of the radius and ulna. One screw passes through both the radius and ulna to hold the forearm in a pronated position (representative of the *in-vivo* orientation found during a fall on an outstretched hand), while the two remaining screws pass through either the radius or ulna and protrude to act as anchors in the cement (Figure J.7).

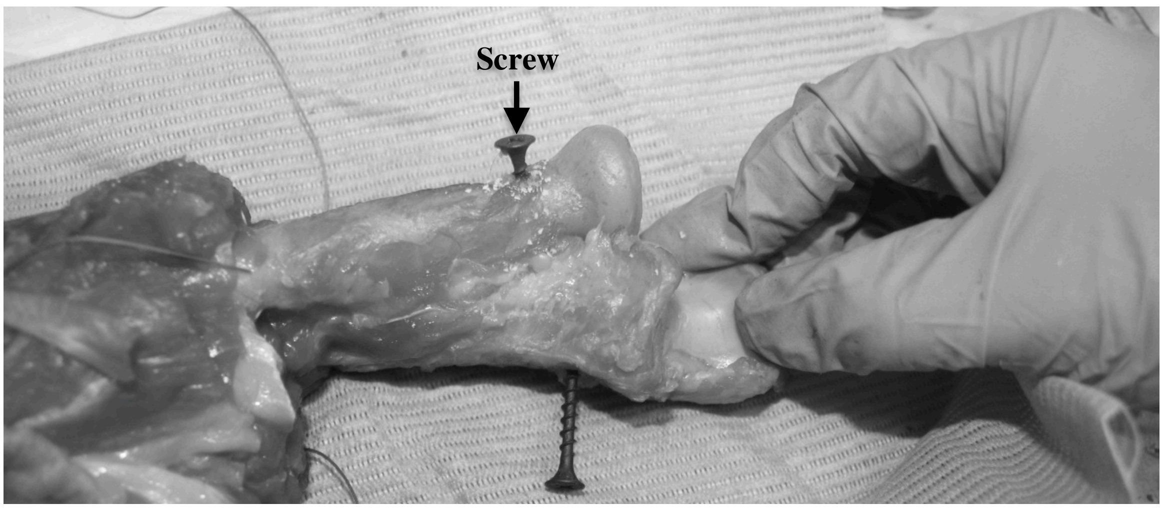

Figure J.7: Screws placed through the proximal end of the forearm to secure pronated positioning

10. Four catheter tubes are cut to size and aligned with holes in the specimen mount to ensure that the tendon leads will be able to pass through the dental cement and specimen mount unhindered. To prevent collapse of these tubes during cement expansion, hex-keys fill the hollow tubes while the cement sets (Figure J.8).

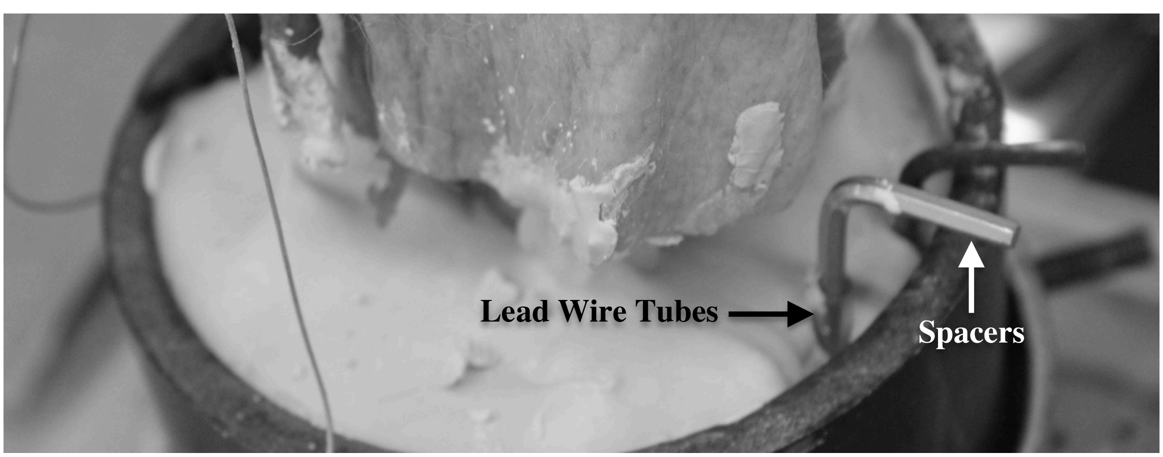

Figure J.8: Cable tubes positioned during potting to ensure proper muscle load alignment

11. The specimen is potted in a 5 – 7 cm PVC tube using Denstone dental cement, such that the forearm should fall along the internal axis of the tube. (Note: Angular positioning of 15° is done by moving the entire potting mount, not via specimen potting angle). Alignment within the PVC is ensured using a laser level highlighting the longitudinal axis of the forearm in both the coronal and sagittal planes (Figure J.9).

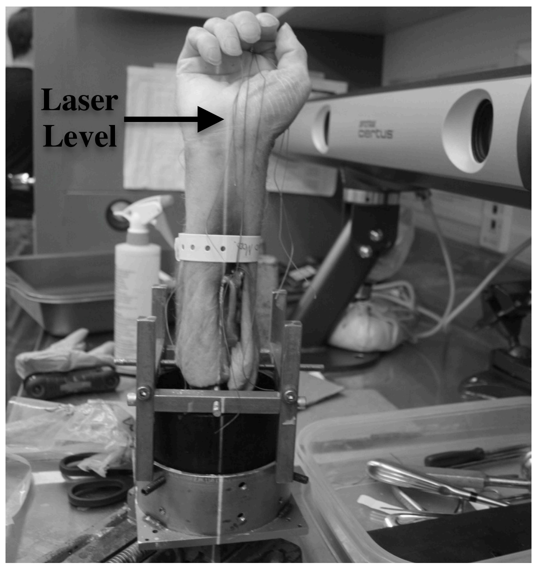

Figure J.9: Specimen orienting using a laser level during potting

12. Suture the initial longitudinal incision closed to contain the soft tissues of the forearm; ensuring that the strain gauge leads protrude through the skin to allow for integration into the data acquisition system, and that the suture leads protrude proximally under the skin (Figure J.10).

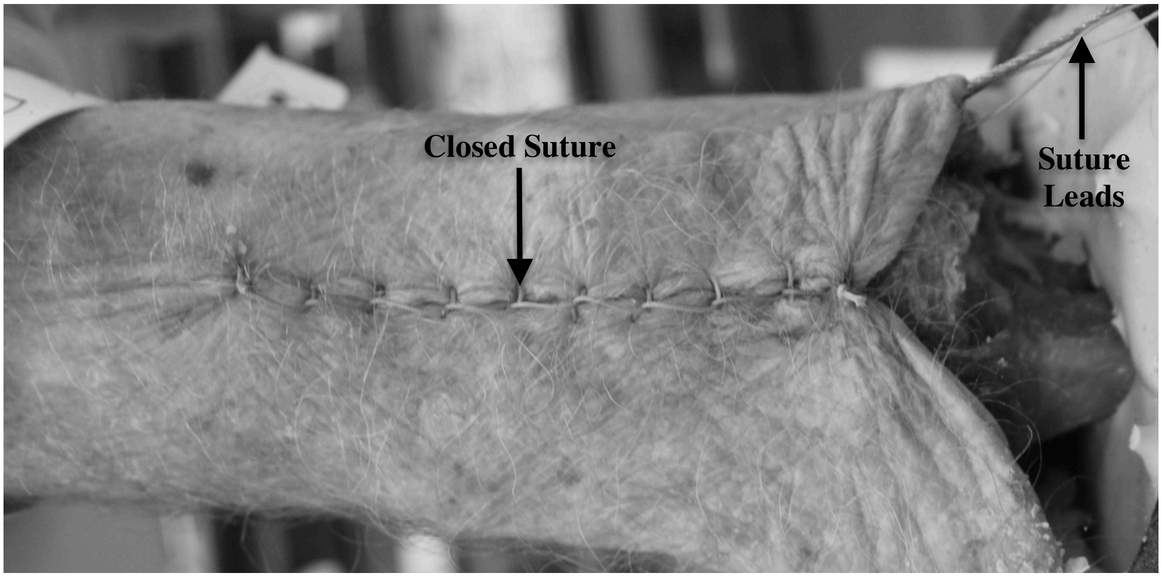

Figure J.10: Specimen with longitudinal incision closed to ensure the moisture and integrity of the soft tissues of the forearm

13. Using a scalpel, remove the phalanges from the metacarpals. This allows the specimen to be placed in the impact-loading machine without interference (*i.e.*, contact between the phalanges and the base of the impactor).
14. Insert a screw into the specimen's PVC pot (taking care not to pierce a bone) and hang the specimen from the materials testing machine to determine and record the specimen and cement weight for ballasting purposes (Figure J.11).

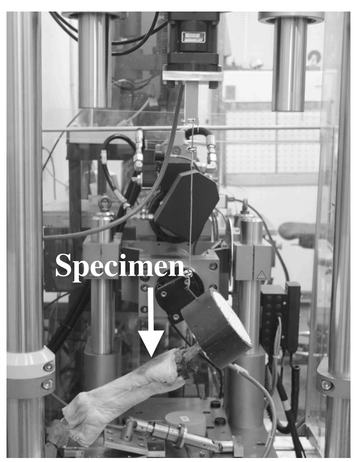

Figure E.11: Specimens are hung from a materials testing machine to quantify arm and cement weight

15. Apply strain gauges to the distal diaphysis of both the radius and ulna through the incisions created above (Figure J.12) (see the *Strain Gauge Application Procedure J.3* below for full details).

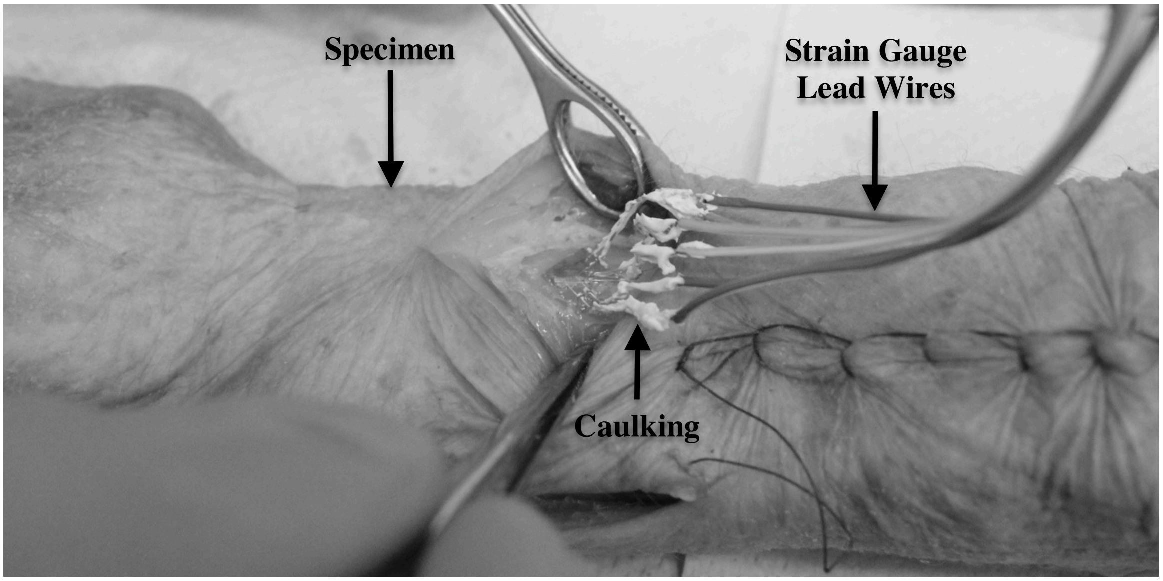

Figure J.12: Strain gauge applied to the dorsal, ulnar surface. With moisture resistant caulking shown in white overlying the gauge leads

16. Place the specimen in the specimen potting-mount and adjust the vertical height so that the center of the radiocarpal articulation is in line with the impacting load cell. A blue pen is used to mark the center of the radiocarpal articulation based on palpation to detect the radial styloid. Alignment is assessed using a laser level (Figure J.13).

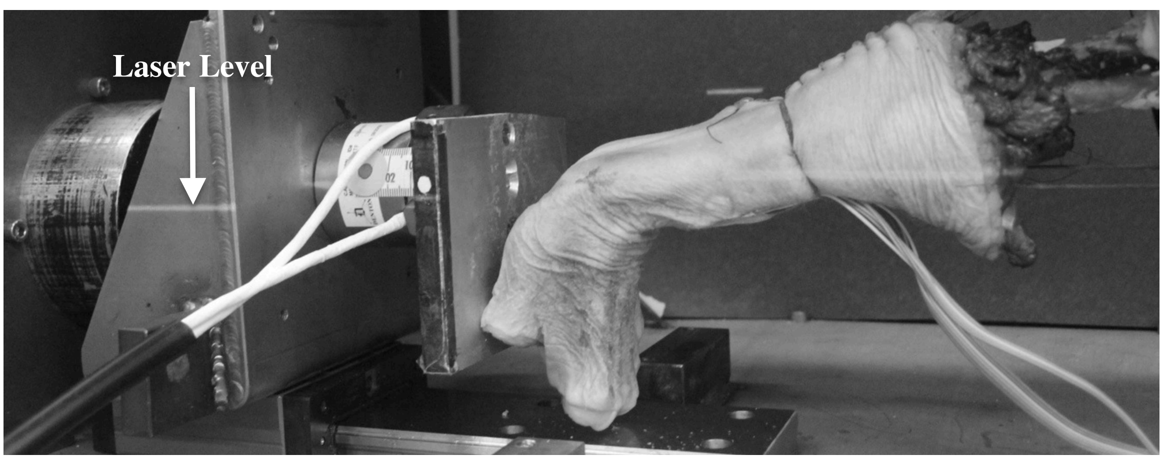

Figure J.13: Laser level assessment of radiocarpal alignment

17. Hang the specimen at the desired angle (15° to the horizontal) in the impact-loading machine (Figure J.14).

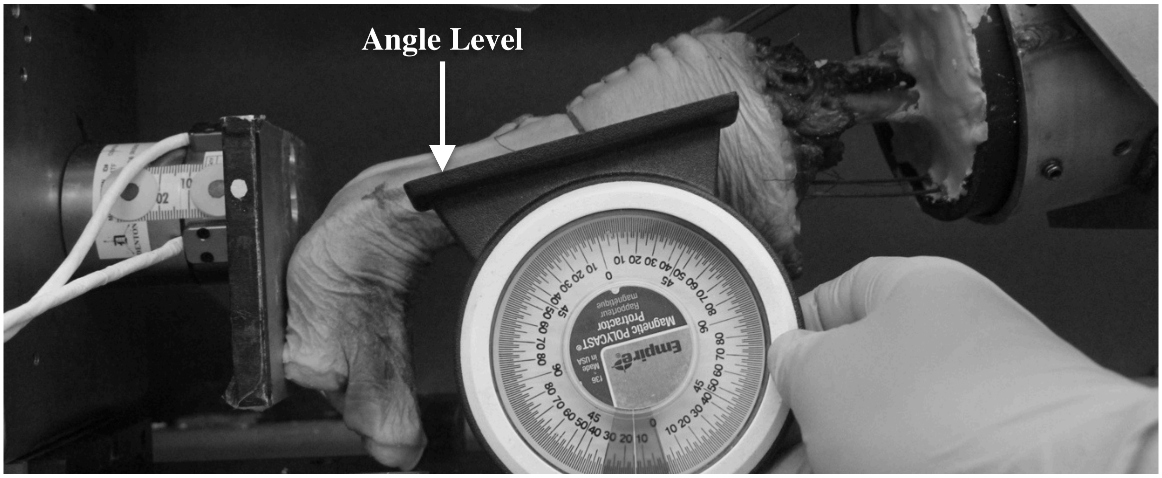

Figure J.14: Specimen orientation prior to impact

18. Apply three custom rigid markers (approximately 1cm in diameter) to the skin of the specimen using a gel-based adhesive: one at the center of wrist rotation, one on the medial (or lateral depending on whether right or left arm) surface of the forearm, in line with the forearms longitudinal axis, and one on the medial (or lateral depending on camera orientation) surface of the distal end of the first row of metacarpals. These markers allow for video tracking of the specimen to quantify post-impact velocity, as well as initial dorsiflexion angle (Figure J.15).

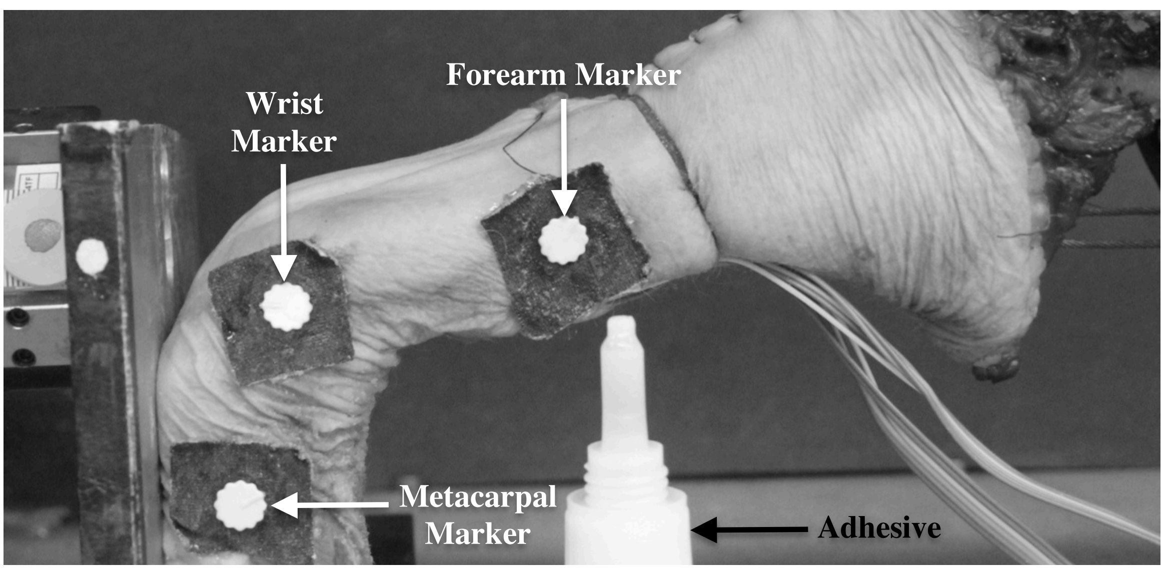

Figure J.15: Specimen wrist angle markers adhered to specimen soft tissues

19. Balance and record the agonist and antagonist tension to the extensor and flexor tendons, respectively, to position the wrist in such a way that the palm is flush with the palm-plate mounted to the load cell (Figure J.16). Individual tendon

loads are set to exceed the lower bound ranges shown in Table J.1 below (Burkhart and Andrews, 2013; Holzbaur *et al*., 2005). The specimen is then ready for impact loading.

Table J.1: Tendon load range representative of anatomical contractile loads during a forward, straight-armed fall. Based on % EMG activation and maximum reported muscle loads.

Tendon	Lower Bound [N]	Upper Bound [N]
ECU	19	56
ECRL	61	183
FCU	9	35
FCR	5	20

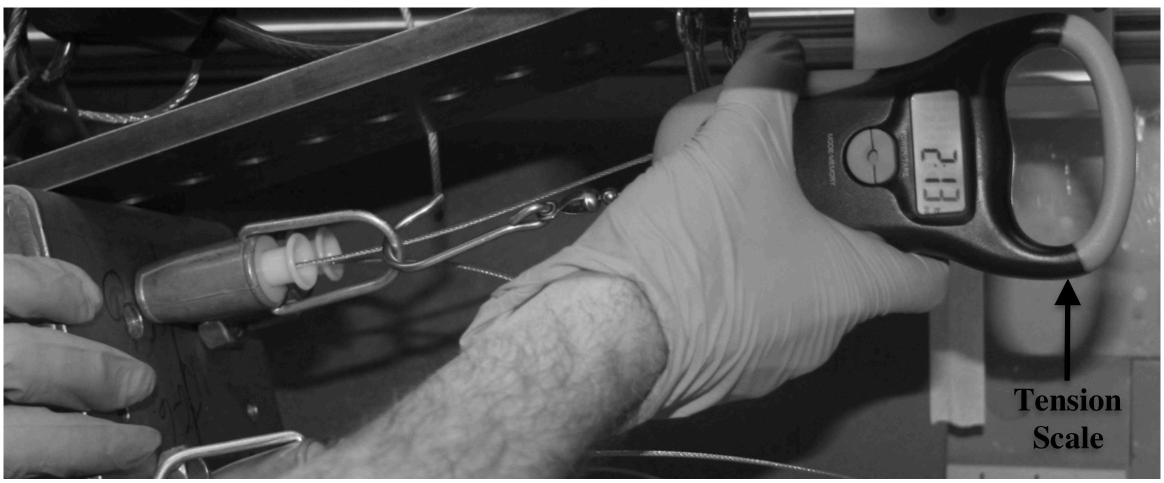

Figure J.16: Tendon load measurement

J.2: SPECIMEN LOADING

1. Once the specimen is placed in the impact-loading machine, attach a piece of 2 cm thick urethane foam to the loading side of the intermediate-impact-plate to ensure proper impact duration (Figure J.17).

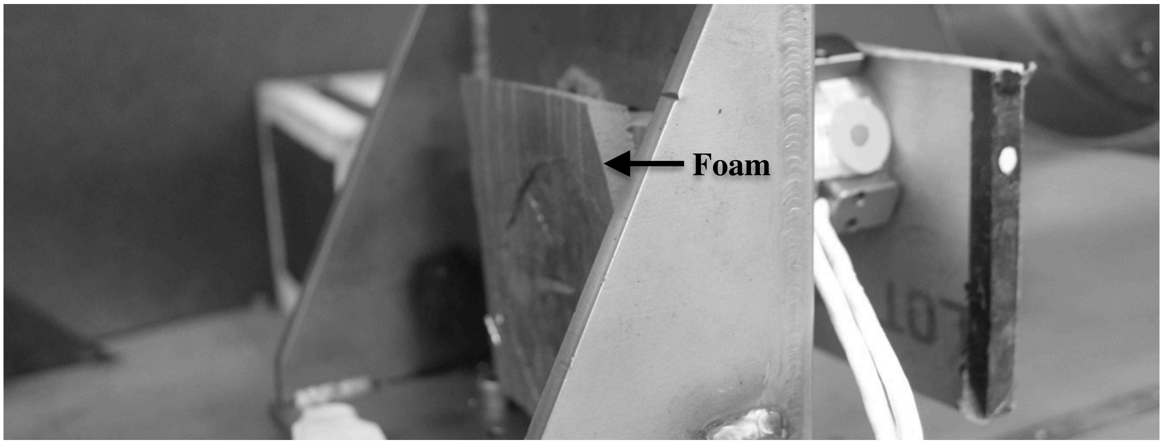

Figure J.17: Foam on the intermediate impact plate aids in prolonging the impact duration by reducing the coefficient of restitution between the impacting ram and the intermediate impact plate

2. Set the impacting ram mass to 6.66 kg (in accordance with apparatus validation data) (Figure G.3).
3. Set ram distance to be 520 mm from the intermediate impact plate (Figure D.1).
4. Using the ram kinetic energy as the target control (Figure J.18), two impacts will be applied to the specimen: one sub-fracture (5.5 psi) and one at expected fracture load (16.0 psi)

(Note: A pilot study was conducted, under low-level tendon loads, to determine the approximate fracture energy via gradually increasing loading energy).

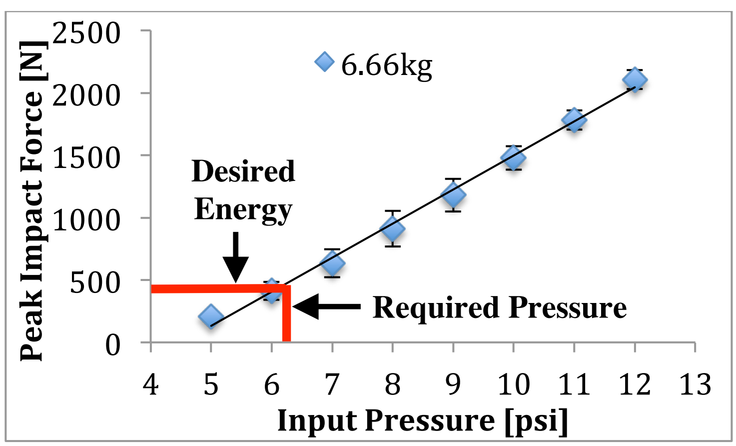

Figure J.18: Energy graph used to determine the targeted pressure input from the desired ram kinetic energy (as shown in red)

5. Fluoroscope (digital radiograph) scans are taken prior to the first impact and after each subsequent impact to detect any damage that may incur during each impact (Figure J.19).

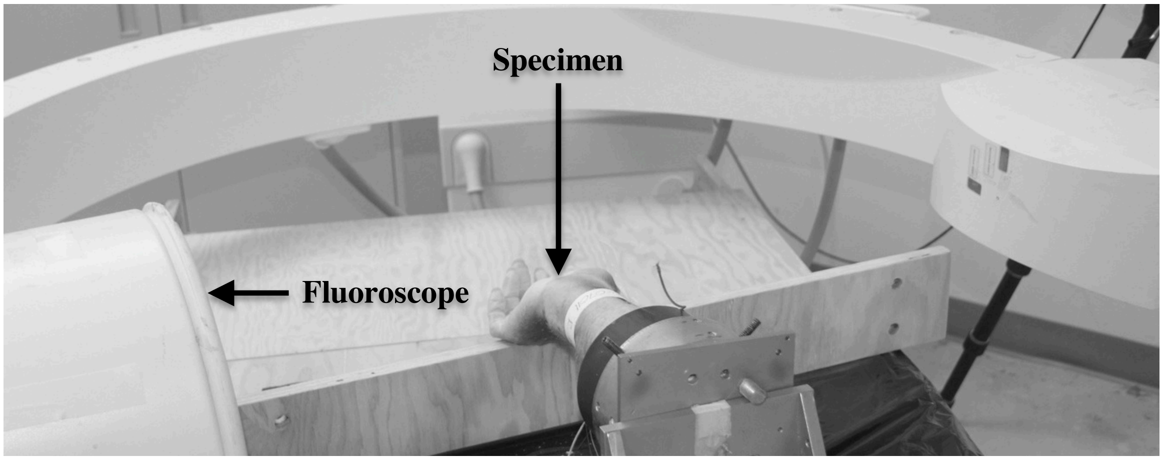

Figure J.19: Setup used to capture lateral digital radiographic images of the specimen pre- and post-fracture

6. The load, acceleration, strain and high-speed camera data are collected and saved for further analysis.
    a. Determine the peak loads developed in all axis from the 5-axis load cell attached to the intermediate impact plate.
    b. Calculate impulse by integrating the force-time data in all axis, then combining to form a resultant impulse.
    c. Calculate impact duration using the duration of axial load.
    d. Calculate specimen velocity at impact via the high-speed camera video and a custom LabVIEW program (captured at 2000Hz).
    e. Calculate the wrist dorsiflexion set angle prior to impact via the high-speed camera video and a custom LabVIEW program (captured at 2000Hz).

J.3: STRAIN GAUGE PREPARATION AND APPLICATION

1. The day prior to testing, preparation of the strain gauges is necessary to guard the gauges in the moist environment of the forearm. Begin by removing the strain gauge from the protective plastic and obtaining a 6 wire ribbon lead (Figure J.20).

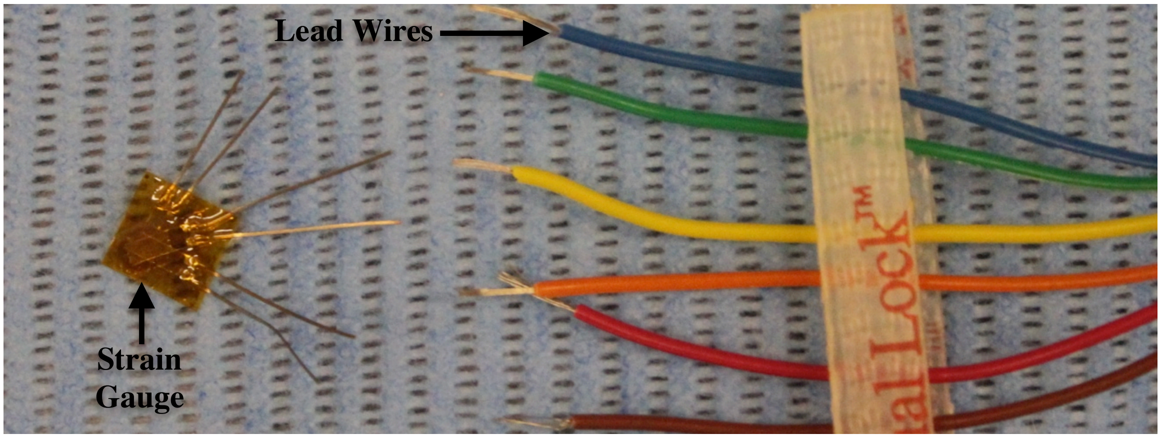

Figure J.20: Gauge leads must be connected to lead wires to permit integration into the data collection system

2. Solder each of the lead wires from the gauge to the corresponding wire ribbon (Figure J.21).

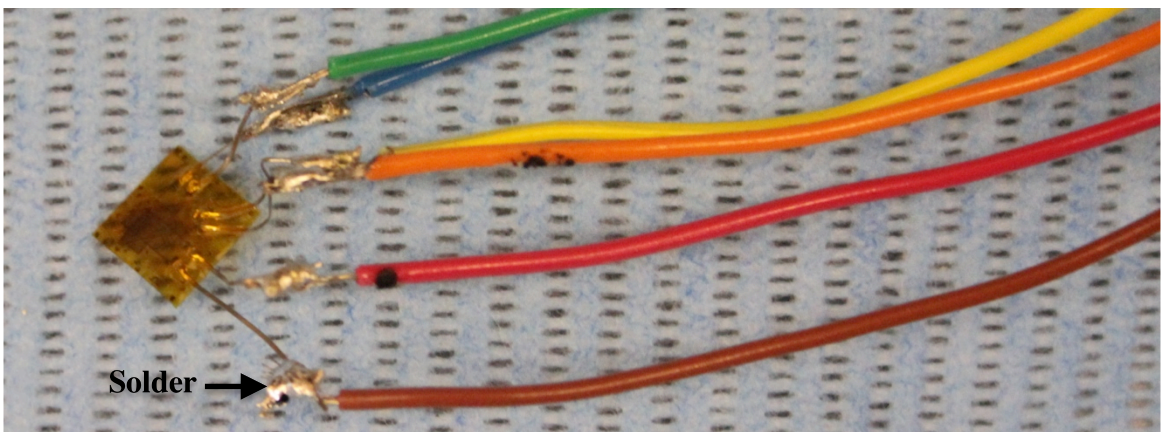

Figure J.21: Solder connects the strain gauge to wire leads, allowing the electrical signal to be transferred from the gauge into the data acquisition system

3. Using a thin tipped paintbrush, apply a coat of caulking over the ribbon leads from the edge of the strain gauge up to the rubber seal. This seals the lead wires from moisture (Figure J.22).

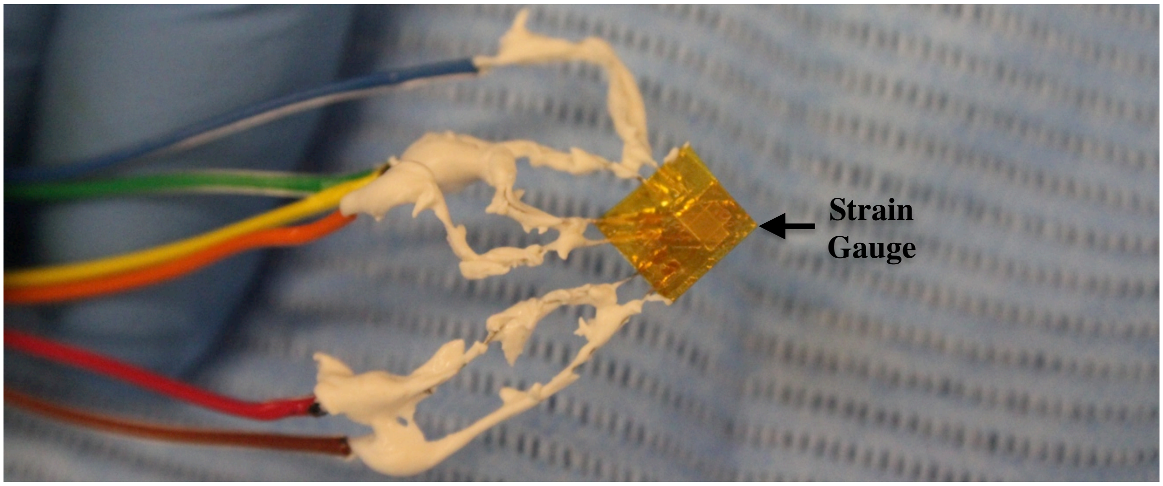

Figure J.22: Caulking acts as a moisture sealant and prevents wire leads from crossing and shorting out

4. Using a multi-meter, check the gauge resistances to make sure that they are still functioning properly (Figure J.23).

Figure J.23: The multi-meter resistance should match the number on the gauge packaging. A higher number implies that there is not a good connection, while a lower number implies that the gauge is shorting out

5. Let gauges dry over night to ensure the caulking sets properly.
6. Use a scalpel to remove the periosteum from the bone in the area of interest for strain gauge application (Figure J.6).
7. Use sandpaper (400 grit) on the area of interest to provide a good surface for adherence (Figure J.24).

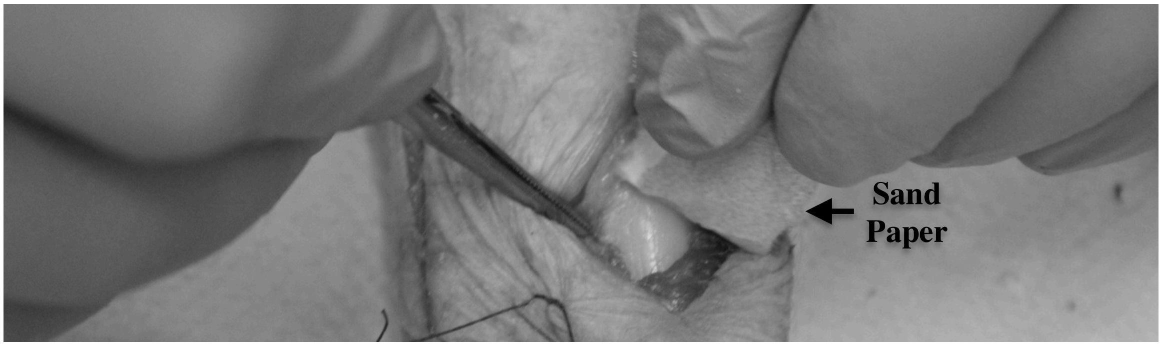

Figure J.24: Sand paper smooth's the bone surface and prepares it for the mating gauge

8. Apply alcohol to clean and degrease the area of interest. Let air dry for 30 seconds.
9. Apply neutralizer to the bone and spread using a Q-tip to degrease the bone surface (Figure J.25).

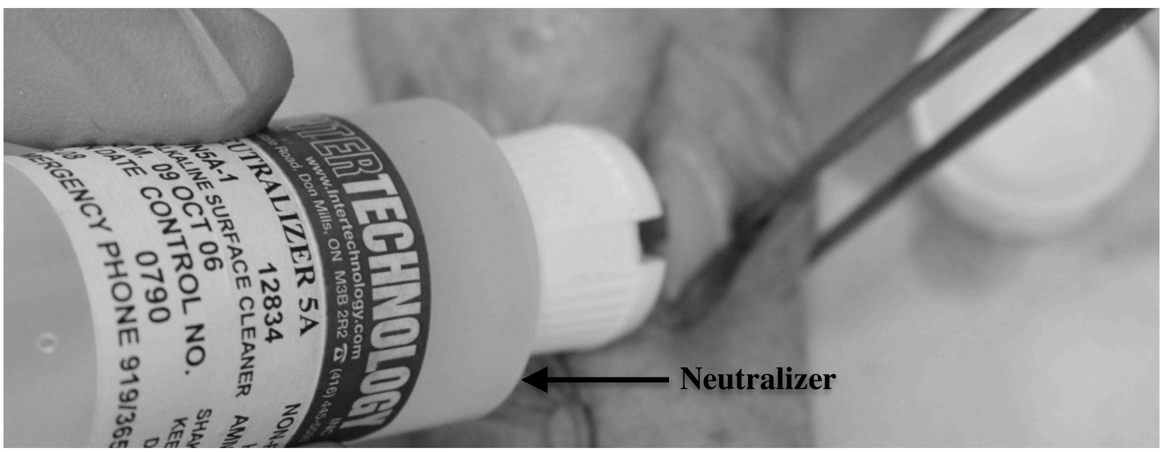

Figure J.25: The neutralizer degreases the bone surface, allowing for better adherence

10. Apply layer of M-bond 200 catalyst, sparingly (Figure J.26). Let air dry for 1 minute.

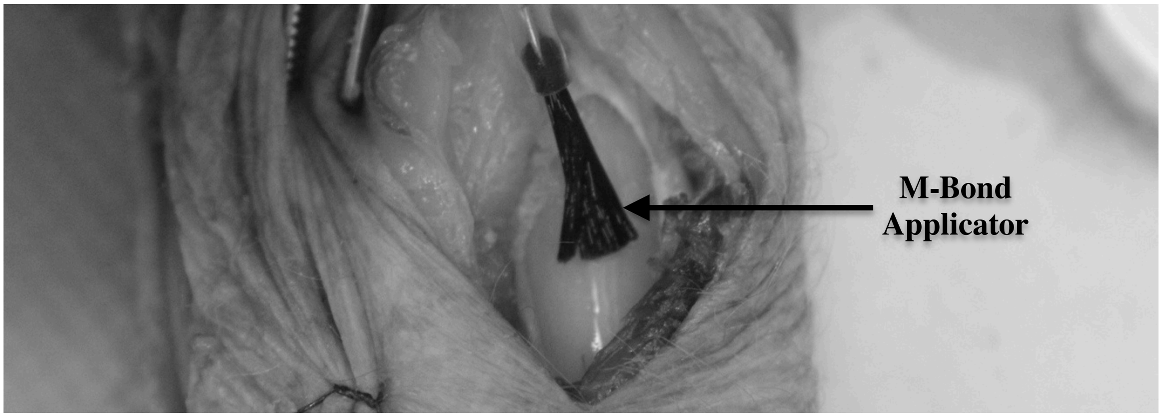

Figure J.26: The M-bone 200 catalyst ensures proper bonding between the bone and the M-bond adhesive

11. Apply 2 drops of M-bond to intended gauge area on bone. Using Q-tip swabs, press and spread drops on bone surface. Let dry for 5 minute.
12. Repeat the above steps 7-10 to prepare the bone surface to receive the strain gauge.
13. Apply M-bond 200 catalyst to back of strain gauge (Figure J.27).

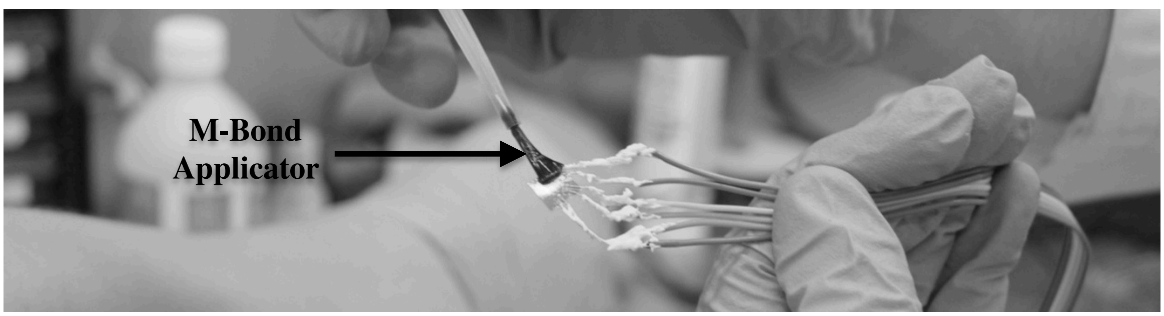

Figure J.27: The M-bond 200 catalyst activates the adhesive, and a thin coat should be applied to both of the surfaces being bonded

14. Apply a single drop of M-bond adhesive to the back of the strain gauge (Figure J.28).

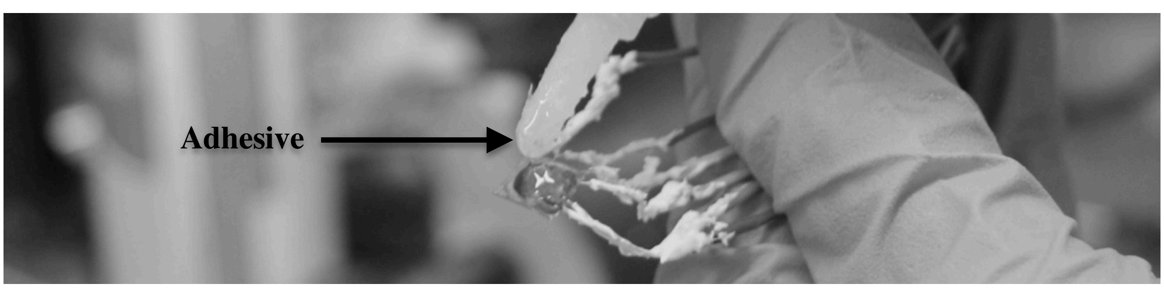

Figure J.28: Once the adhesive is applied to the gauge surface, it must be spread out to cover all corners. Act fast; it cures quickly

15. Align gauge to bone in the desired orientation, and apply gauge, pressing evenly & holding for 1 minute (Figure J.29).

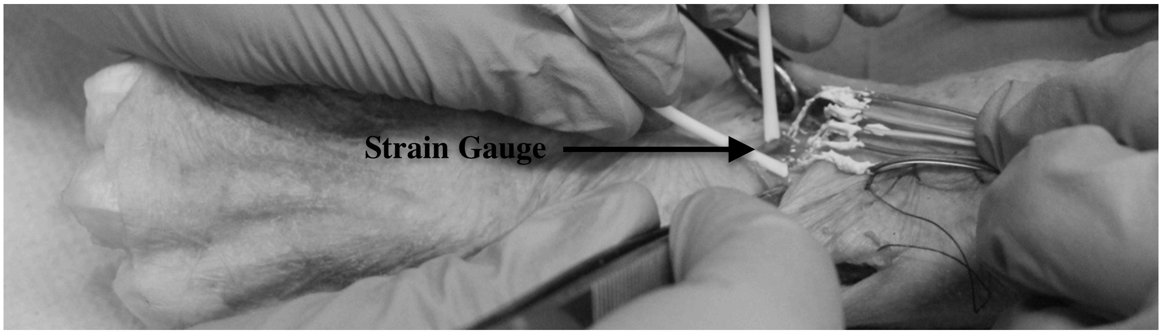

Figure J.29: Strain gauge orientation should be made such that the middle gauge is aligned with the longitudinal axis of the bone

16. Release pressure and let sit for 5 minutes.
17. Apply M-coat to strain gauge to secure the surface of the gauge and isolate it from the moist environment. Let stand for 5 minutes (Figure J.30).

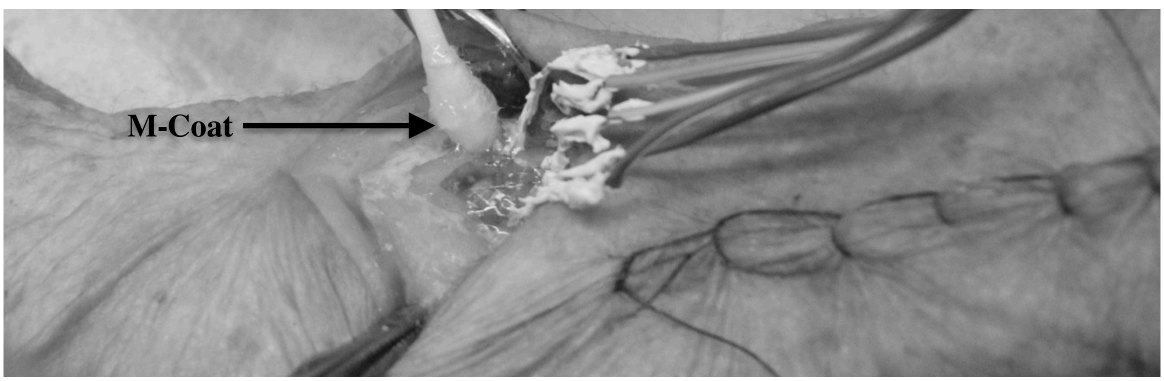

Figure J.30: The top gauge surface has minimal protective coating, so it is best to additionally apply a thin layer of M-coat due to the damp nature of the intact forearm

18. Check that the multi-meter is reading the correct resistance across each terminal of the strain gauges (Figure J.23).

APPENDIX K: DIGITAL RADIOGRAPHS

K.1: FRACTURE DIGITAL RADIOGRAPHS

(a)

(b)

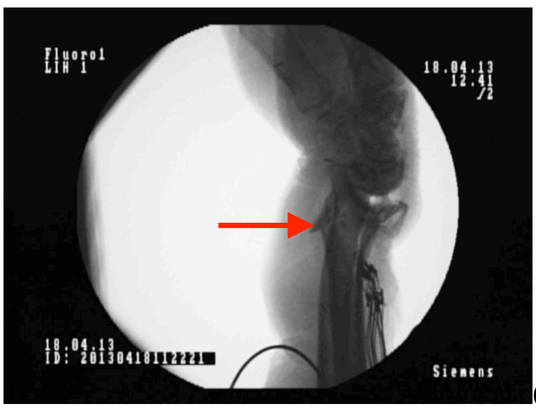

(c)

(d)

Figure K.1: Pre-fracture lateral (a) and anterior-posterior (b) digital radiographs, and fracture lateral (c) and anterior-posterior (d) digital radiographs for specimen 12-06066L

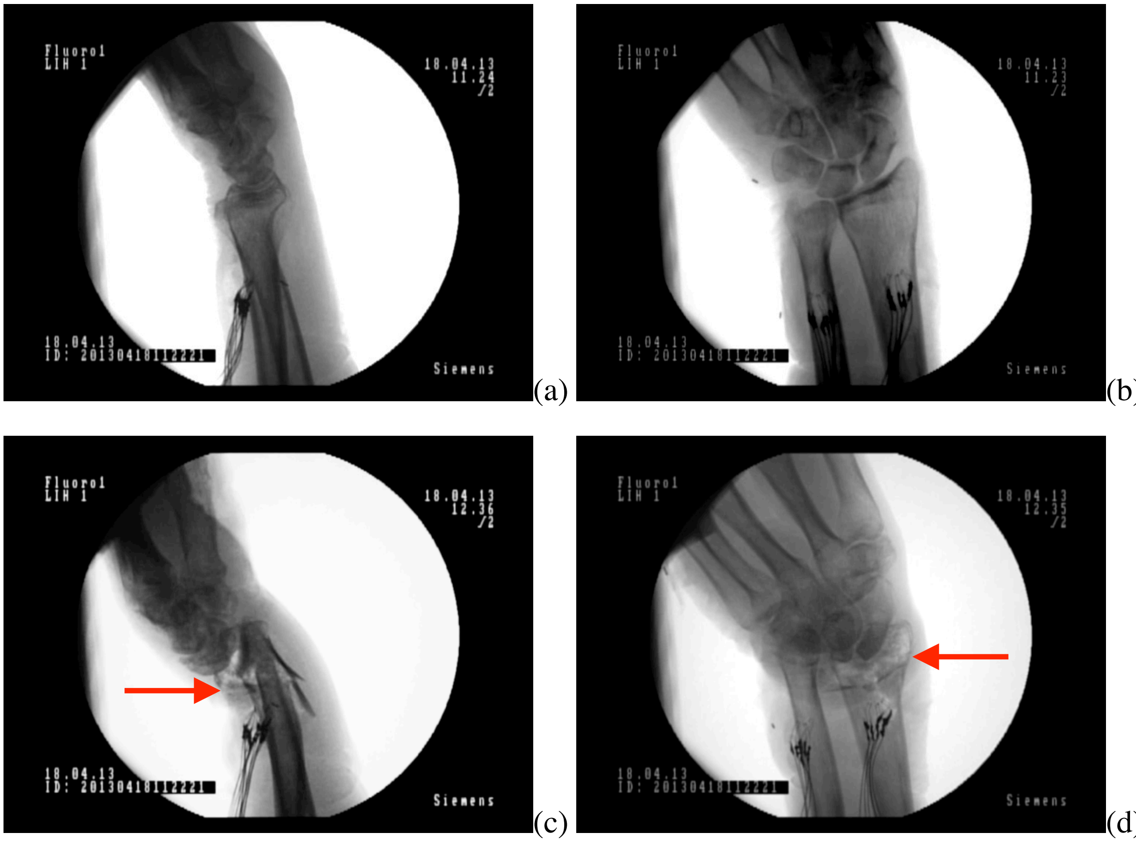

Figure K.2: Pre-fracture lateral (a) and anterior-posterior (b) digital radiographs, and fracture lateral (c) and anterior-posterior (d) digital radiographs for specimen 12-06066R

(a)

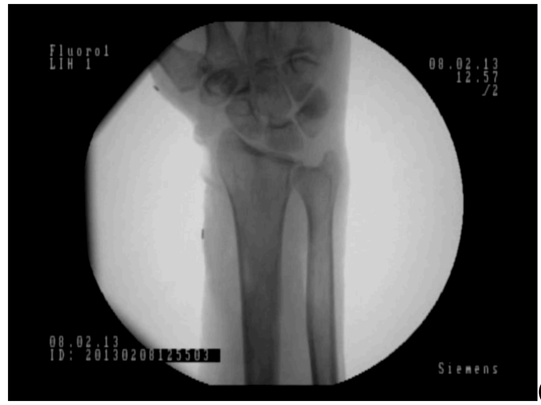

(b)

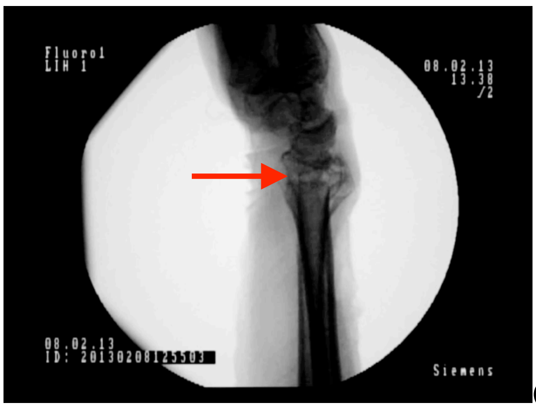

(c)

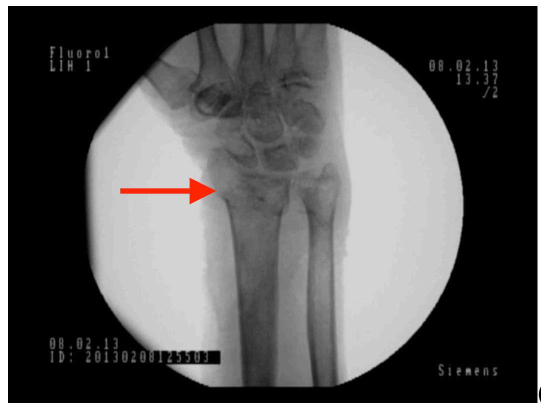

(d)

Figure K.3: Pre-fracture lateral (a) and anterior-posterior (b) digital radiographs, and fracture lateral (c) and anterior-posterior (d) digital radiographs for specimen 12-06067L

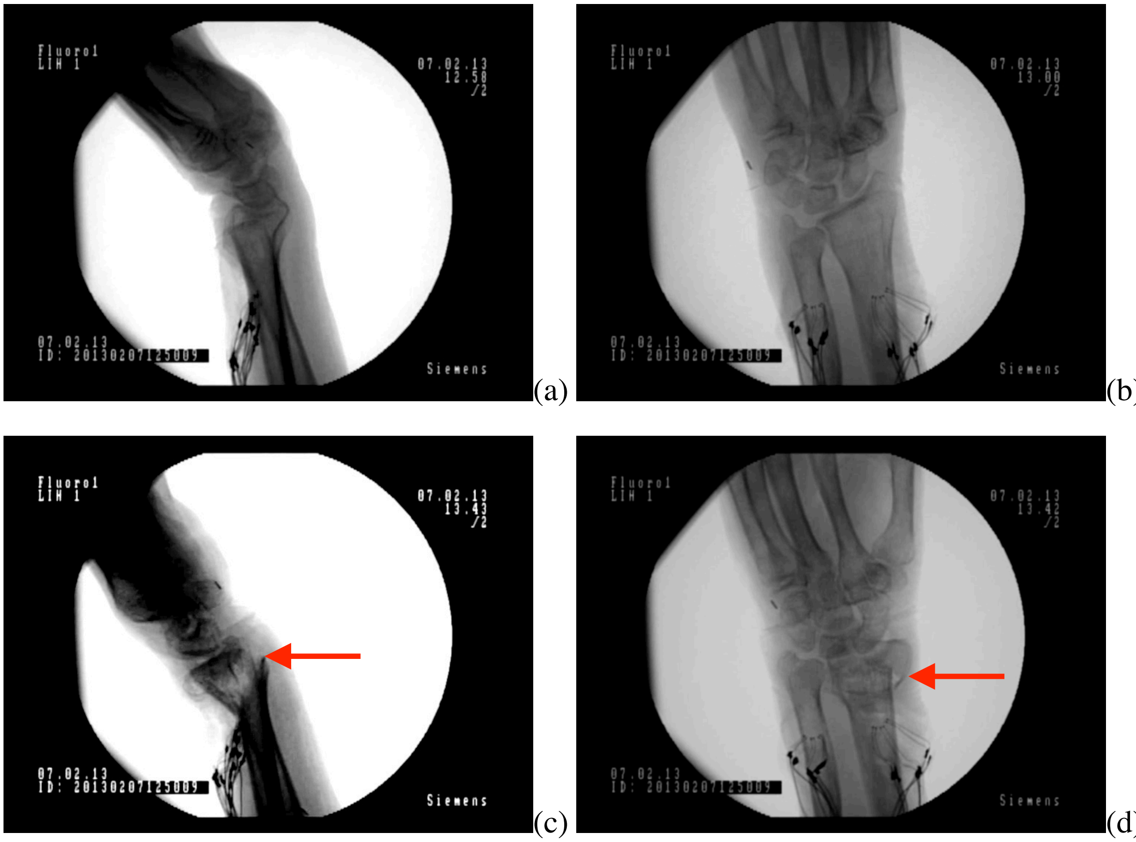

Figure K.4: Pre-fracture lateral (a) and anterior-posterior (b) digital radiographs, and fracture lateral (c) and anterior-posterior (d) digital radiographs for specimen 12-06067R

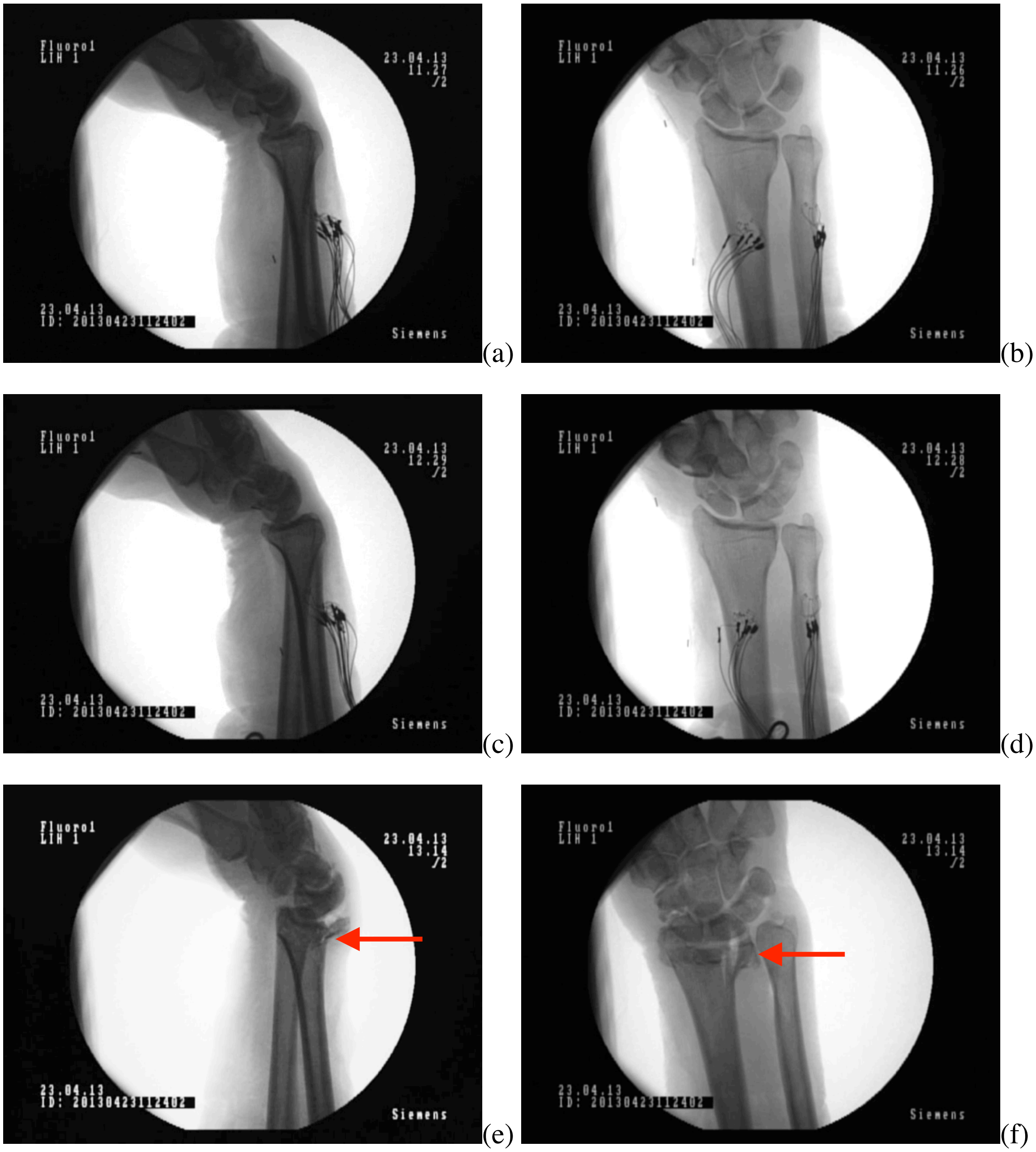

Figure K.5: Pre-fracture lateral (a) and anterior-posterior (b) digital radiographs, Intermediate lateral (c) and anterior-posterior (d) digital radiographs, and fracture lateral (e) and anterior-posterior (f) digital radiographs for specimen 12-07016L

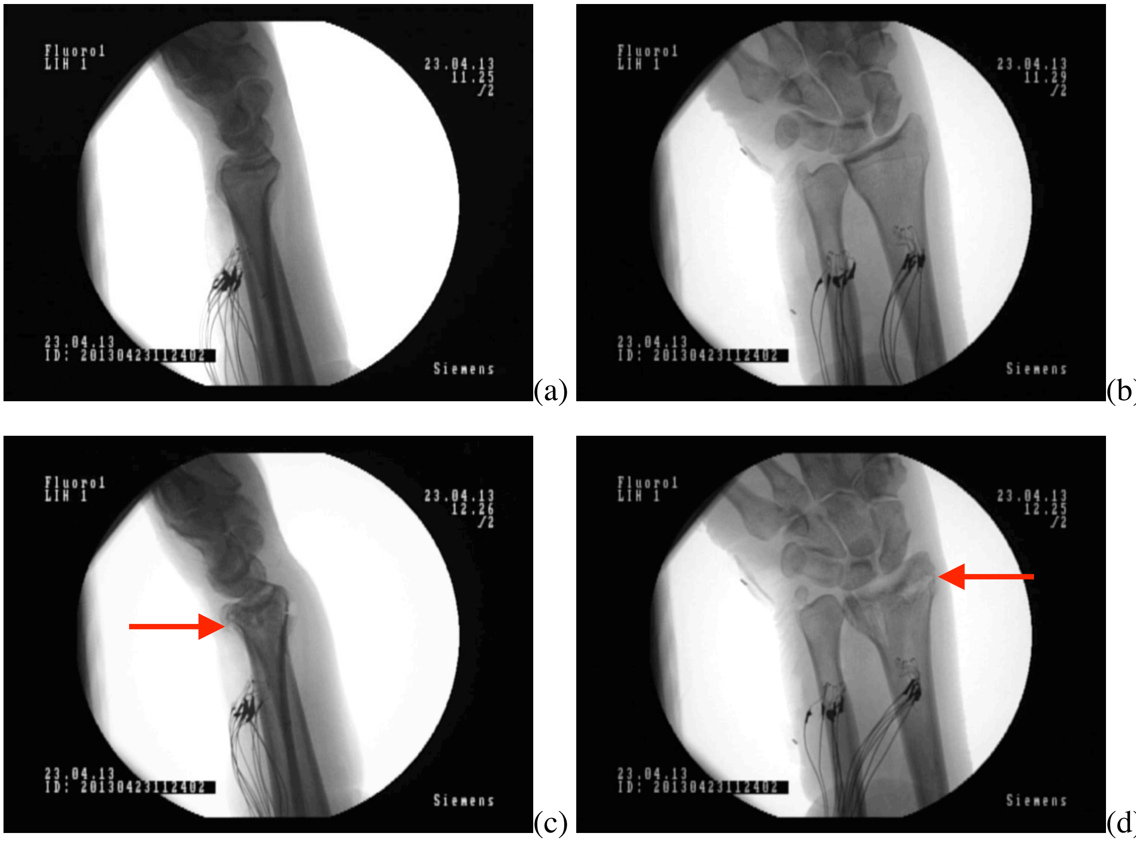

Figure K.6: Pre-fracture lateral (a) and anterior-posterior (b) digital radiographs, and fracture lateral (c) and anterior-posterior (d) digital radiographs for specimen 12-07016R

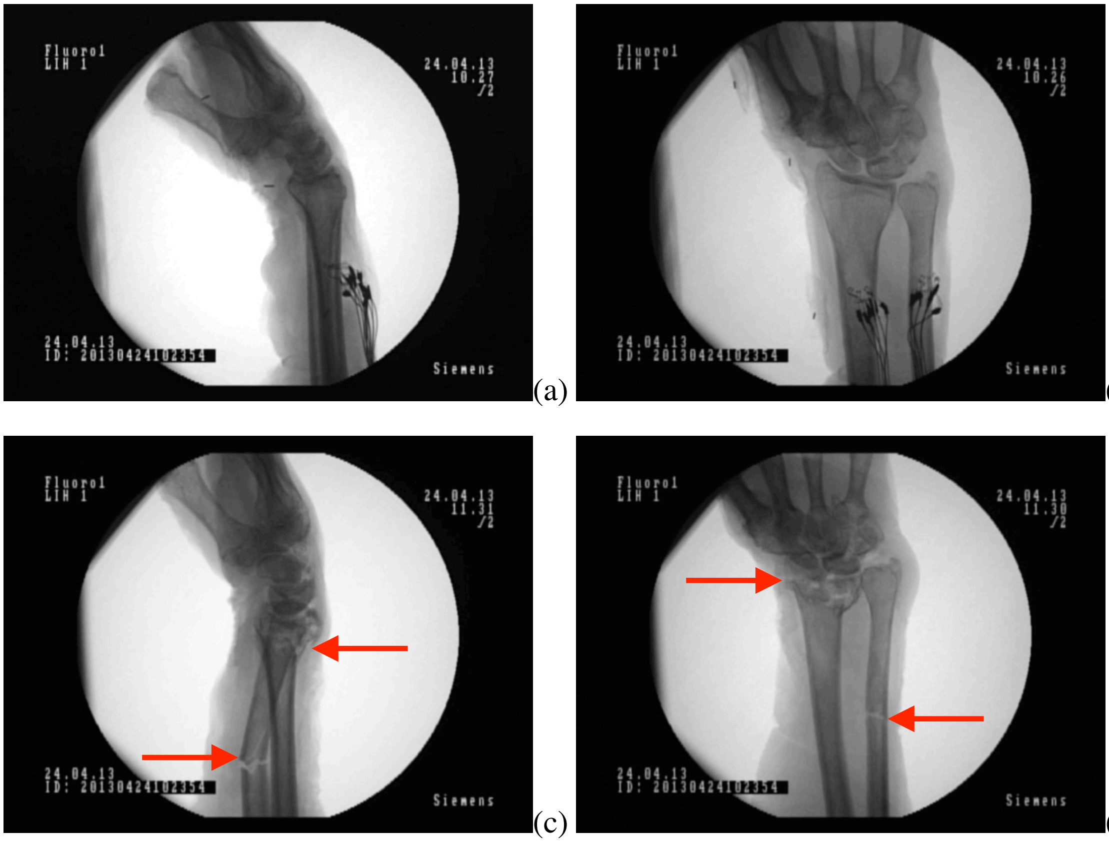

Figure K.7: Pre-fracture lateral (a) and anterior-posterior (b) digital radiographs, and fracture lateral (c) and anterior-posterior (d) digital radiographs for specimen 12-07036L

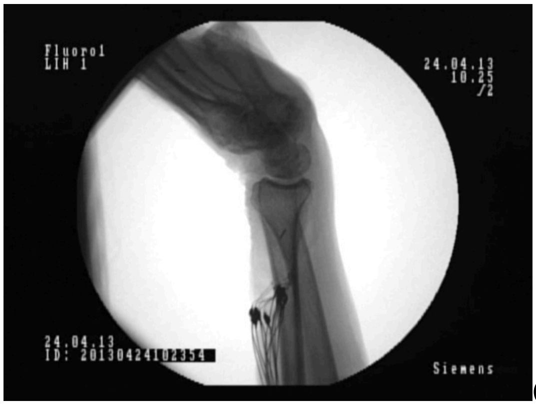

(a)

(b)

(c)

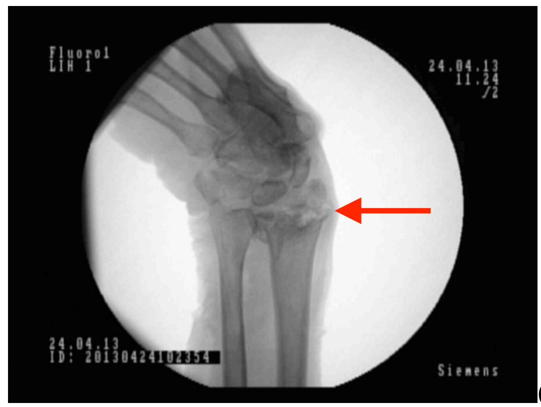

(d)

Figure K.8: Pre-fracture lateral (a) and anterior-posterior (b) digital radiographs, and fracture lateral (c) and anterior-posterior (d) digital radiographs for specimen 12-07036R

(a)

(b)

(c)

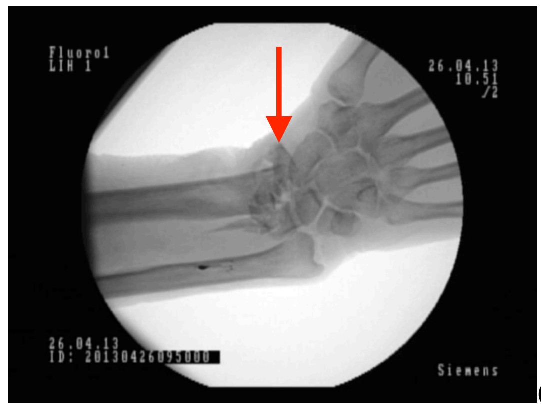

(d)

Figure K.9: Pre-fracture lateral (a) and anterior-posterior (b) digital radiographs, and fracture lateral (c) and anterior-posterior (d) digital radiographs for specimen 12-08016L

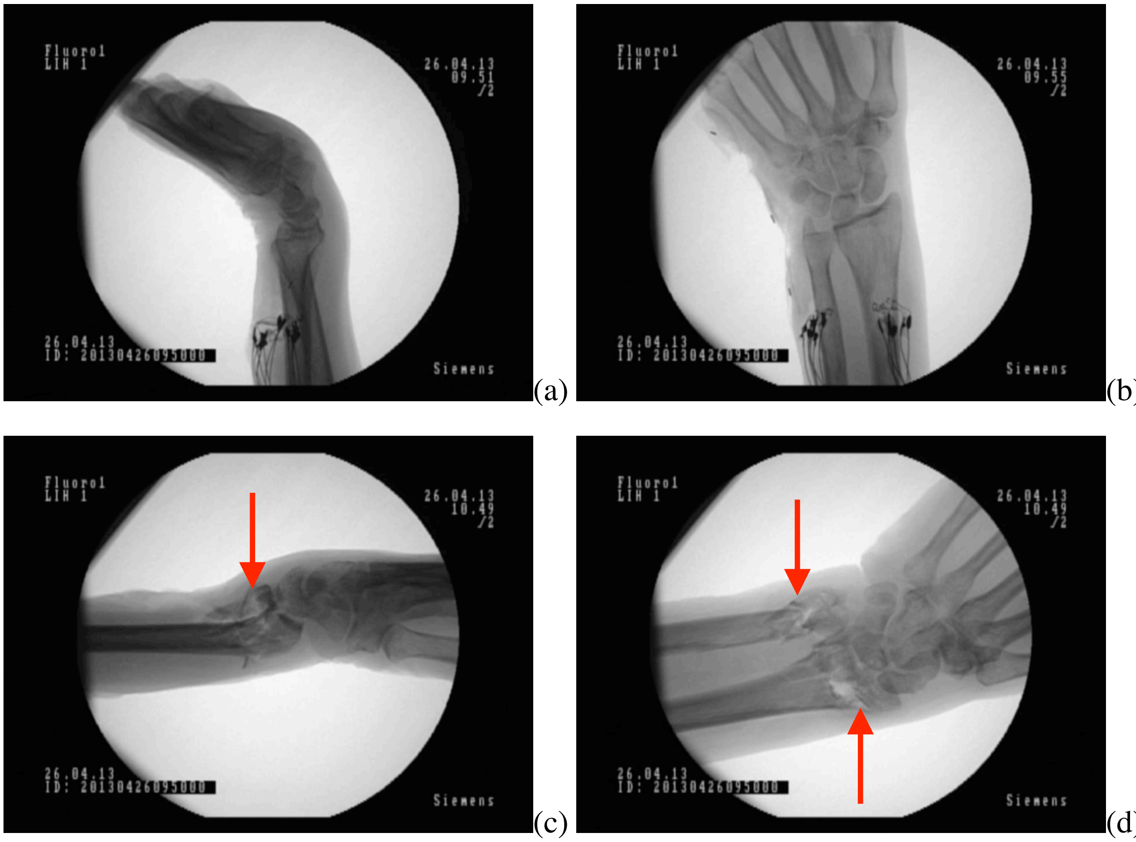

Figure K.10: Pre-fracture lateral (a) and anterior-posterior (b) digital radiographs, and fracture lateral (c) and anterior-posterior (d) digital radiographs for specimen 12-08016R

K.2: DISLOCATION DIGITAL RADIOGRAPHS

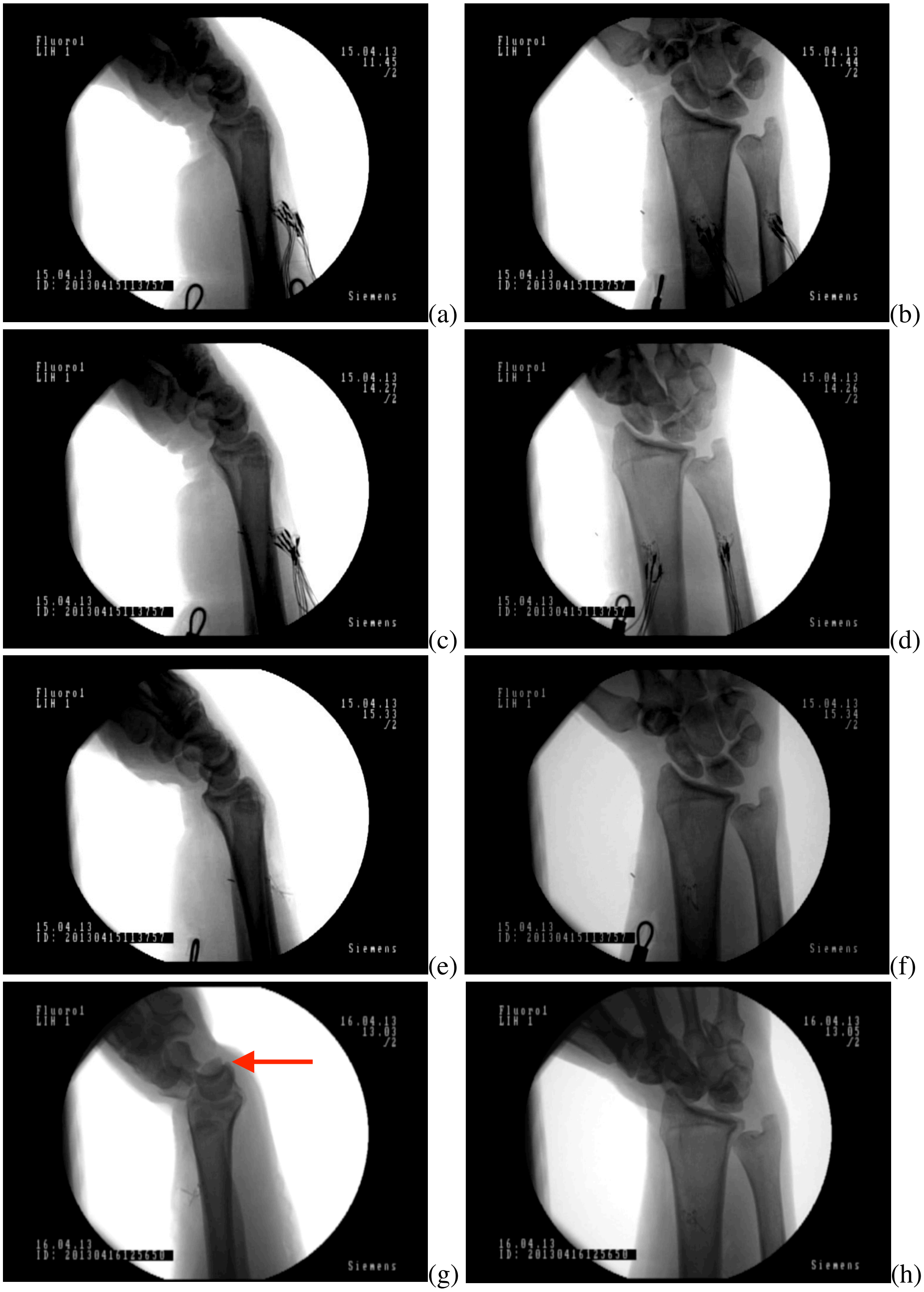

Figure K.11: Pre-injury lateral (a) and anterior-posterior (b) digital radiographs, Intermediate lateral (c, e) and anterior-posterior (d, f) digital radiographs, and dislocation medial (g) and anterior-posterior (h) digital radiographs for specimen 12-07012L

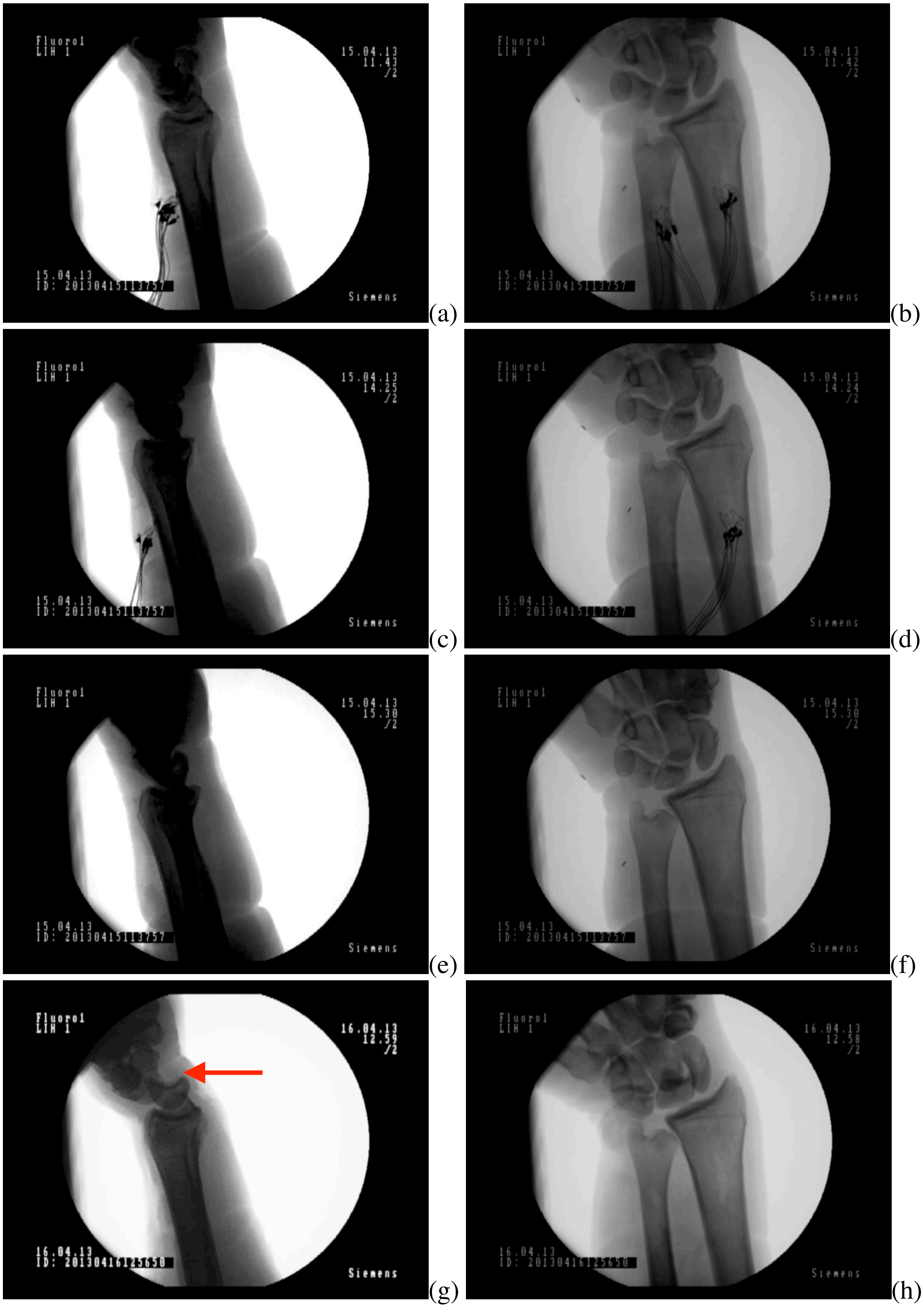

Figure K.12: Pre-injury lateral (a) and anterior-posterior (b) digital radiographs, Intermediate lateral (c, e) and anterior-posterior (d, f) digital radiographs, and dislocation lateral (g) and anterior-posterior (h) digital radiographs for specimen 12-07012R

APPENDIX L: INTACT TESTING MEASURES SUMMARY

L.1: FRACTURE SUMMARY DATA

Table L.1: Mean (SD) specimen information for pre-fracture and fracture trials (n = 5 pairs).

	Load	No Load	Grand Mean	P-value	Power	Significance
Pre-fracture						
Pressure [psi]	5.48 (0.04)	5.48 (0.04)	5.48 (0.04)			No
Frequency [Hz]	11108 (713)	10773 (923)	10940 (797)	0.362	0.054	No
Ballast [% BW]	46.3 (1.9)	46.4 (2.0)	46.4 (1.8)	0.374	0.05	No
Wrist Angle [°]	55.3 (13.6)	62.8 (7.5)	59.1 (11.1)	0.187	0.158	No
Fracture						
	Load	**No Load**	**Grand Mean**	**P-value**	**Power**	**Significance**
Pressure [psi]	16.82 (1.78)	16.02 (0.04)	16.42 (1.26)	0.374	0.05	No
Frequency [Hz]	11112 (760)	11074 (707)	11093 (692)	0.384	0.05	No
Ballast [% BW]	46.3 (1.9)	46.4 (2.0)	46.4 (1.8)	0.374	0.05	No
Wrist Angle [°]	57.2 (9.2)	63.7 (9.2)	60.4 (9.4)	0.268	0.096	No
Volar Tilt [°]	13.6 (12.7)	26.0 (16.0)	19.8 (15.1)	0.108	0.281	No
Radial Inclination [°]	9.2 (5.2)	10.6 (6.3)	9.9 (5.5)	0.735	0.05	No

Table L.2: Mean (SD) velocity and energy information for pre-fracture and fracture trials (n = 5).

Pre-fracture						
	Load	**No Load**	**Grand Mean**	**P-value**	**Power**	**Significance**
Plate Kinetic Energy [J]	4.4 (1.4)	4.3 (1.1)	4.3 (1.2)	0.859	0.050	No
Ram Velocity [m/s]	2.7 (0.3)	2.8 (0.5)	2.7 (0.4)	0.456	0.050	No
Plate Velocity [m/s]	1.4 (0.2)	1.4 (0.2)	1.4 (0.2)	0.899	0.050	No
Ram Kinetic Energy [J]	24.0 (6.7)	26.4 (9.3)	25.2 (7.7)	0.413	0.050	No
Wrist Velocity [m/s]	0.9 (0.1)	1.0 (0.2)	0.9 (0.2)	0.175	0.179	No
Wrist Velocity Angle [°]	22.2 (19.9)	21.8 (3.5)	22.0 (13.2)	0.970	0.052	No
Forearm Velocity [m/s]	1.0 (0.2)	1.1 (0.2)	1.0 (0.2)	0.256	0.109	No
Forearm Velocity Angle [°]	22.5 (35.2)	11.9 (16.0)	17.2 (25.9)	0.633	0.052	No
Wrist Kinetic Energy [J]	10.2 (2.2)	13.8 (5.6)	12.0 (4.4)	0.170	0.185	No
Forearm Kinetic Energy [J]	13.5 (5.5)	16.2 (6.9)	14.9 (5.6)	0.203	0.149	No
Peak Motion Between Specimen Markers [mm]	3.4 (1.8)	5.9 (2.2)	4.7 (2.3)	0.229	0.127	No
Fracture						
	Load	**No Load**	**Grand Mean**	**P-value**	**Power**	**Significance**
Plate Kinetic Energy [J]	35.6 (5.4)	35.6 (9.9)	35.6 (7.5)	0.997	0.05	No
Ram Velocity [m/s]	6.7 (0.8)	6.5 (0.9)	6.6 (0.8)	0.377	0.05	No
Plate Velocity [m/s]	3.9 (0.2)	3.9 (0.52)	3.9 (0.4)	0.916	0.05	No
Ram Kinetic Energy [J]	151.8 (37.7)	143.6 (44.9)	147.7 (39.3)	0.426	0.05	No

Table L.3: Mean (SD) force and impulse information for pre-fracture trials (n = 5pairs).

Pre-fracture						
	Load	**No Load**	**Grand Mean**	**P-value**	**Power**	**Significance**
Fr - Peak [N]	1839 (475)	1757 (852)	1798 (652)	0.701	0.050	No
Fr - Impulse Duration [ms]	41 (19)	40 (31)	41 (24)	0.900	0.050	No
Fr - Impulse [Ns]	22 (3)	21 (3)	22 (3)	0.176	0.170	No
Fr - Load Rate [kN/s]	312 (128)	281 (258)	296 (193)	0.706	0.050	No
Fx - Peak [N]	548 (114)	479 (149)	514 (130)	0.111	0.273	No
Fx - Impulse Duration [ms]	27 (7)	24 (14)	25 (11)	0.624	0.05	No
Fx - Impulse [Ns]	5 (1)	4 (1)	5 (1)	0.169	0.178	No
Fx - Load Rate [kN/s]	134 (58)	231 (190)	183 (142)	0.347	0.06	No
Fy - Peak [N]	182 (51)	146 (25)	164 (42)	0.057	0.464	No
Fy - Impulse Duration [ms]	32 (16)	23 (12)	28 (14)	0.221	0.127	No
Fy - Impulse [Ns]	1 (0)	1 (0)	1 (0)	0.091	0.325	No
Fy - Load Rate [kN/s]	79 (74)	73 (53)	76 (60)	0.872	0.050	No
Fz - Peak [N]	1765 (483)	1714 (858)	1739 (657)	0.813	0.050	No
Fz - Impulse Duration [ms]	41 (19)	40 (31)	41 (24)	0.900	0.050	No
Fz - Impulse [Ns]	22 (3)	20 (3)	21 (3)	0.225	0.124	No
Fz - Load Rate [kN/s]	276 (156)	278 (245)	277 (194)	0.976	0.050	No
Mx - Peak [Nm]	22 (12)	12 (9)	16 (11)	0.052	0.488	No
My - Peak [Nm]	44 (14)	48 (13)	46 (13)	0.180	0.165	No

Table L.4: Mean (SD) force and impulse information for fracture trials (n = 5 pairs).

Fracture						
	Load	**No Load**	**Grand Mean**	**P-value**	**Power**	**Significance**
Fr - Peak [N]	6565 (866)	8665 (5133)	7615 (3643)	0.353	0.057	No
Fr - Impulse Duration [ms]	36 (12)	37 (21)	37 (16)	0.862	0.05	No
Fr - Impulse [Ns]	47 (6)	57 (30)	52 (21)	0.517	0.05	No
Fr - Load Rate [kN/s]	11118 (1771)	14744 (9226)	12931 (6548)	0.344	0.061	No
Fx - Peak [N]	2420 (516)	2532 (1153)	2476 (844)	0.741	0.05	No
Fx - Impulse Duration [ms]	27 (10)	26 (9)	27 (9)	0.572	0.05	No
Fx - Impulse [Ns]	12 (2)	13 (5)	13 (4)	0.642	0.05	No
Fx - Load Rate [kN/s]	3689 (876)	3339 (562)	3514 (718)	0.213	0.133	No
Fy - Peak [N]	768 (171)	1045 (541)	906 (405)	0.191	0.153	No
Fy - Impulse Duration [ms]	33 (12)	25 (11)	29 (12)	0.138	0.221	No
Fy - Impulse [Ns]	4 (1)	5 (4)	5 (3)	0.676	0.05	No
Fy - Load Rate [kN/s]	1053 (332)	1611 (1150)	1332 (851)	0.22	0.127	No
Fz - Peak [N]	6543 (871)	8548 (4908)	7545 (3487)	0.35	0.058	No
Fz - Impulse Duration [ms]	36 (12)	37 (21)	37 (16)	0.862	0.05	No
Fz - Impulse [Ns]	43 (7)	53 (29)	49 (21)	0.52	0.05	No
Fz - Load Rate [kN/s]	11116 (1764)	14865 (9490)	12991 (6731)	0.345	0.06	No
Mx - Peak [Nm]	55 (23)	46 (10)	50 (17)	0.541	0.05	No
My - Peak [Nm]	161 (31)	148 (32)	155 (31)	0.552	0.05	No

Table L.5: Mean (SD) strain information for pre-fracture trials (axial: n = 4 pairs, Principals: n = 2 pairs).

Pre-fracture						
	Load	**No Load**	**Grand Mean**	**P-value**	**Power**	**Significance**
Rad Axial Strain Rate [με/s]	19288 (11160)	22221 (10236)	20754 (10037)	0.723	0.052	No
Rad Axial Strain – Peak [με]	706 (444)	1349 (716)	1027 (650)	0.288	0.091	No
Rad Axial Strain @ Fr Peak [με]	2 (1)	1 (1)	2 (1)	0.334	0.071	No
Ulna Axial Strain Rate [με/s]	10139 (7094)	27700 (37210)	18920 (26516)	0.34	0.069	No
Ulna Axial Strain – Peak [με]	338 (140)	1327 (1633)	833 (1196)	0.282	0.094	No
Ulna Axial Strain @ Fr Peak [με]	1 (1)	4 (3)	2 (2)	0.112	0.286	No
Rad LS Axial - 100%	72.4 (25.2)	62.8 (24.3)	67.6 (23.5)	0.412	0.052	No
Rad LS Axial - 75%	75.9 (26.6)	60.8 (26.2)	68.4 (25.3)	0.052	0.527	No
Rad LS Axial - 50%	75.9 (23.4)	61.0 (24.8)	68.5 (23.7)	0.013	0.922	Yes
Rad LS Axial - 25%	74.6 (18.2)	71.2 (7.5)	72.9 (13.0)	0.696	0.052	No
Rad Max Princ. Strain Rate [με/s]	8129 (3025)	12040 (6998)	10294 (4618)	-	-	-
Rad Max Princ – Peak [με]	276 (140)	675 (568)	419 (316)	-	-	-
Rad Max Princ@ Fr Peak [με]	5 (3)	1 (1)	10 (19)	-	-	-
Ulna Max Princ Strain Rate [με/s]	6513 (8082)	11657 (4394)	7685 (6620)	-	-	-
Ulna Max Princ Strain – Peak [με]	206 (157)	442 (202)	262 (188)	-	-	-
Ulna Max Princ Strain @ Fr Peak [με]	1 (1)	5 (6)	2 (3)	-	-	-
Rad LS Max Princ - 100%	67.9 (22.1)	71.3 (3.2)	70.7 (16.4)	-	-	-
Rad LS Max Princ - 75%	66.9 (25.6)	72.3 (25.6)	70.8 (21.8)	-	-	-
Rad LS Max Princ - 50%	68.0 (23.1)	59.6 (14.5)	68.2 (19.5)	-	-	-

Rad LS Max Princ - 25%	72.3 (18.1)	48.8 (8.7)	68.4 (20.1)	-	-	-
Rad Min Princ Strain Rate [με/s]	32428 (21797)	47351 (41564)	32200 (27648)	-	-	-
Rad Min Princ – Peak [με]	1057 (505)	2025 (1876)	1299 (984)	-	-	-
Rad Min Princ @ Fr Peak [με]	6 (4)	5 (1)	20 (37)	-	-	-
Ulna Min Princ Strain Rate [με/s]	35783 (48700)	47267 (53903)	34103 (43724)	-	-	-
Ulna Min Princ Strain – Peak [με]	1168 (1440)	2228 (2456)	1332 (1595)	-	-	-
Ulna Min Princ Strain @ Fr Peak [με]	2 (2)	4 (0)	3 (2)	-	-	-
Rad LS Min Princ - 100%	59.1 (21.8)	54.9 (12.9)	61.1 (18.6)	-	-	-
Rad LS Min Princ - 75%	63.4 (25.1)	54.2 (14.0)	64.2 (21.7)	-	-	-
Rad LS Min Princ - 50%	63.3 (25.9)	53.1 (15.6)	62.8 (21.4)	-	-	-
Rad LS Min Princ - 25%	62.1 (26.9)	51.3 (17.7)	63.8 (25.1)	-	-	-

Table L.6: Mean (SD) strain information for fracture trials (n = 1 pair).

Fracture						
	Load	No Load	Grand Mean	P-value	Power	Significance
Rad Axial Strain Rate [με/s]	19650	15375	17513 (3023)	-	-	-
Rad Axial Strain – Peak [με]	1895	848	1372 (740)	-	-	-
Rad Axial Strain @ Fr Peak [με]	12	2	7 (7)	-	-	-
Ulna Axial Strain Rate [με/s]	64682	81910	73296 (12182)	-	-	-
Ulna Axial Strain – Peak [με]	4353	4842	4597 (345)	-	-	-
Ulna Axial Strain @ Fr Peak [με]	2	2	2 (0)	-	-	-
Rad LS Axial - 100%	95.5	15.4	55.4 (56.6)	-	-	-
Rad LS Axial - 75%	95.8	19.7	57.8 (53.8)	-	-	-
Rad LS Axial - 50%	91.3	22.9	57.1 (48.4)	-	-	-
Rad LS Axial - 25%	63.5	26.7	45.1 (26.0)	-	-	-
Rad Max Princ. Strain Rate [με/s]	5480	2078	3779 (2406)	-	-	-
Rad Max Princ – Peak [με]	1495	209	852 (909)	-	-	-
Rad Max Princ@ Fr Peak [με]	1	7	4 (4)	-	-	-
Ulna Max Princ Strain Rate [με/s]	32068	7245	19656 (17552)	-	-	-
Ulna Max Princ Strain – Peak [με]	2058	1577	1818 (340)	-	-	-
Ulna Max Princ Strain @ Fr Peak [με]	0	1	1 (1)	-	-	-
Rad LS Max Princ - 100%	94.6	36.6	65.6 (41.0)	-	-	-
Rad LS Max Princ - 75%	96.5	48.8	72.6 (33.8)	-	-	-
Rad LS Max Princ - 50%	89.6	14.6	52.1 (53.0)	-	-	-
Rad LS Max Princ - 25%	57.4	10.7	34.1 (33.1)	-	-	-

Rad Min Princ Strain Rate [με/s]	18751	18134	18443 (437)	-	-	-
Rad Min Princ – Peak [με]	1948	1028	1488 (651)	-	-	-
Rad Min Princ @ Fr Peak [με]	11	5	8 (5)	-	-	-
Ulna Min Princ Strain Rate [με/s]	67196	86726	76961 (13810)	-	-	-
Ulna Min Princ Strain – Peak [με]	4501	4541	4521 (27.9)	-	-	-
Ulna Min Princ Strain @ Fr Peak [με]	2	6	4 (3)	-	-	-
Rad LS Min Princ - 100%	95.5	18.8	57.1 (54.2)	-	-	-
Rad LS Min Princ - 75%	95.8	23.8	59.8 (50.9)	-	-	-
Rad LS Min Princ - 50%	91.2	29.9	60.5 (43.4)	-	-	-
Rad LS Min Princ - 25%	93.3	56.1	74.7 (26.3)	-	-	-

L.2: DISLOCATION SUMMARY DATA

Table L.7: Mean data summary for dislocation trials (n = 1 pair).

	Pre-injury		Dislocation	
	Load	**No Load**	**Load**	**No Load**
Specimen #	1207012	1207012	1207012	1207012
Pressure [psi]	5.6	5.4	20.1	20.1
Frequency [Hz]	9765	9759	9775	9747
Ram Velocity [m/s]	3.2	3.0	9.1	9.3
Plate Velocity [m/s]	1.5	1.3	3.8	2.8
Ram Kinetic Energy [J]	34.5	29.4	274.5	284.9
Plate Kinetic Energy [J]	5.4	3.9	33.6	18.8
Wrist Velocity [m/s]	0.8	0.7	-	-
Wrist Velocity Angle [°]	-0.7	15.0	-	-
Forearm Velocity [m/s]	0.5	0.6	-	-
Wrist Kinetic Energy [J]	16.4	14.4	-	-
Forearm Kinetic Energy [J]	7.6	11.3	-	-
Forearm Velocity Angle [°]	-0.8	82.9	-	-
Peak Wrist-Forearm Distance Change [mm]	-6.9	-6.0	-	-
Ballast [% BW]	47.0	47.0	47.0	47.0
Wrist Angle [°]	46.5	60.1	60.9	62.1
Fr - Peak [N]	1818	1791	14102	8612
Fr - Impulse Duration [ms]	41	33	21	12
Fr - Impulse [Ns]	25	24	65	62
Fr - Load Rate [kN/s]	169456	192174	29717695	3366230
Fx - Peak [N]	520	536	2868	2778
Fx - Impulse Duration [ms]	23	27	30	11
Fx - Impulse [Ns]	5	5	36	10
Fx - Load Rate [kN/s]	53271	65185	2310263	4471430
Fy - Peak [N]	165	168	-2036	999
Fy - Impulse Duration [ms]	35	23	16	11
Fy - Impulse [Ns]	1	2	10	3
Fy - Load Rate [kN/s]	20734	17342	-4346971	1084572
Fz - Peak [N]	1799	1766	13717	8576
Fz - Impulse Duration [ms]	41	33	21	12
Fz - Impulse [Ns]	25	23	49	60
Fz - Load Rate [kN/s]	166153	191279	29865643	3121735
Mx - Peak [Nm]	-26	16	368	-41
My - Peak [Nm]	-38	-29	335	183

L.3: PRE-INJURY DATA FOR ALL LOAD-CONDITION SPECIMENS

Note: Specimens 12-07012R and 12-07012L dislocated.

Table L.8: Pre-injury specimen, velocity and energy data for load-condition specimens.

Specimen #	1206066	1206067	1207012	1207016	1207036	1208016
Pressure [psi]	5.5	5.5	5.6	5.5	5.4	5.5
Frequency [Hz]	9835	11407	9765	11375	11442	11478
Ballast [% BW]	46.0	43.2	47.0	48.0	47.0	47.4
Wrist Angle [°]	34.9	66.4	46.5	48.0	66.1	61.1
Ram Velocity [m/s]	3.3	2.5	3.2	2.5	2.6	2.4
Plate Velocity [m/s]	1.6	1.5	1.5	1.2	1.5	1.1
Ram Kinetic Energy [J]	36	21	35	21	23	20
Plate Kinetic Energy [J]	6	5	5	3	5	3
Wrist Velocity [m/s]	0.8	2.4	0.8	0.8	1.0	1.0
Wrist Velocity Angle [°]	-0.7	-49.5	-0.7	-10.7	-43.2	-34.4
Forearm Velocity [m/s]	1.2	1.8	0.5	0.9	0.8	1.1
Forearm Velocity Angle [°]	-0.3	-48.1	-0.8	-10.4	4.2	74.9
Wrist Energy [J]	7.3	54.1	16.4	10.5	12.6	10.3
Forearm Energy [J]	19.0	31.2	7.6	14.8	8.5	11.8
Peak Wrist-Forearm Distance Change [mm]	-6.1	-5.5	-6.9	-2.8	-2.2	2.5

Table L.9: Pre-injury force, impulse and moment data for load-condition specimens.

Specimen #	1206066	1206067	1207016	1207036	1208016	1207012
Fr - Peak [N]	1792	1306	2575	1583	1937	1818
Fr - Impulse Duration [ms]	41	73	30	38	24	41
Fr - Impulse [Ns]	19	22	24	26	21	25
Fr - Load Rate [kN/s]	313	245	495	150	354	169
Fx - Peak [N]	663	388	493	551	648	520
Fx - Impulse Duration [ms]	34	33	20	28	19	23
Fx - Impulse [Ns]	5	3	4	6	5	5
Fx - Load Rate [kN/s]	91	97	197	198	88	53
Fy - Peak [N]	154	139	267	187	162	165
Fy - Impulse Duration [ms]	41	55	20	29	16	35
Fy - Impulse [Ns]	1	2	2	1	1	1
Fy - Load Rate [kN/s]	92	36	35	202	28	21
Fz - Peak [N]	1674	1266	2527	1476	1882	1799
Fz - Impulse Duration [ms]	41	73	30	38	24	41
Fz - Impulse [Ns]	18	21	24	25	20	25
Fz - Load Rate [kN/s]	130	245	504	148	353	166
Mx - Peak [Nm]	10	10	37	16	27	-26
My - Peak [Nm]	-48	-20	-54	-55	-41	-38

Table L.10: Pre-injury strain and load-sharing data for load-condition specimens.

Specimen #	1206066	1206067	1207012	1207016	1207036	1208016
Rad Axial Strain Rate [µε/s]	-10509	-	-16624	-12951	-35277	-18416
Rad Axial Strain - Peak [µε]	-339	-	-521	-498	-1346	-641
Rad Axial Strain @ Fr Peak [µε]	1	-	-6	3	-3	-1
Ulna Axial Strain Rate [µε/s]	-20371	-	3943	-9033	-6883	-4270
Ulna Axial Strain - Peak [µε]	-537	-	107	-327	-265	-222
Ulna Axial Strain @ Fr Peak [µε]	2	-	-1	1	0	1
Rad LS Axial - 100%	38.9	-	83.7	69.2	83.6	97.8
Rad LS Axial - 75%	38.3	-	81.5	86.3	83.5	95.5
Rad LS Axial - 50%	41.1	-	81.5	88.1	83.5	90.9
Rad LS Axial - 25%	47.9	-	82.1	87.9	83.4	79.4
Rad Max Princ Strain Rate [µε/s]	-8432	-	-15460	6925	12149	5008
Rad Max Princ - Peak [µε]	-281	-	-478	203	470	151
Rad Max Princ@ Fr Peak [µε]	-2	-	-54	-2	8	-6
Ulna Max Princ Strain Rate [µε/s]	-18479	-	4429	3531	3349	692
Ulna Max Princ Strain - Peak [µε]	-442	-	122	122	145	116
Ulna Max Princ Strain @ Fr Peak [µε]	3	-	-1	0	-1	1
Rad LS Max Princ - 100%	41.1	-	80.6	91.7	78.8	59.9
Rad LS Max Princ - 75%	37.8	-	83.3	96.0	78.6	55.2
Rad LS Max Princ - 50%	42.7	-	85.9	94.7	78.5	56.3
Rad LS Max Princ - 25%	54.9	-	91.9	94.2	79.8	60.4
Rad Min Princ Strain Rate [µε/s]	-61862	-	-985	-12995	-35531	-19323
Rad Min Princ - Peak [µε]	-1594	-	-816	-499	-1357	-780
Rad Min Princ @ Fr Peak [µε]	-12	-	-104	3	-4	-5
Ulna Min Princ Strain Rate [µε/s]	-108431	-	-1056	-9023	-6986	-18692

Ulna Min Princ Strain - Peak [με]	-3302	-	-193	-329	-270	-773
Ulna Min Princ Strain @ Fr Peak [με]	4	-	-3	0	0	-4
Rad LS Min Princ - 100%	33.7	-	81.3	69.2	83.5	50.2
Rad LS Min Princ - 75%	36.5	-	87.3	86.0	83.5	47.7
Rad LS Min Princ - 50%	37.2	-	79.8	87.6	83.5	45.0
Rad LS Min Princ - 25%	37.3	-	95.2	87.3	83.4	40.6

L.4: PRE-INJURY DATA FOR NO LOAD-CONDITION SPECIMENS

Table L.11: Pre-injury specimen, velocity and energy data for no load-condition specimens.

Specimen #	**1206066**	**1206067**	**1207012**	**1207016**	**1207036**	**1208016**
Pressure [psi]	5.5	5.5	5.4	5.5	5.4	5.5
Frequency [Hz]	9786	11415	9759	9738	11477	11447
Ballast [% BW]	46.0	43.2	47.0	48.0	47.0	47.9
Wrist Angle [°]	51.2	61.8	60.1	68.7	70.4	62.1
Ram Velocity [m/s]	3.4	2.4	3.0	3.2	2.5	2.4
Plate Velocity [m/s]	1.3	1.6	1.3	1.0	1.5	1.4
Ram Kinetic Energy [J]	39	19	29	33	21	19
Plate Kinetic Energy [J]	4	5	4	2	5	5
Wrist Velocity [m/s]	0.9	1.8	0.7	0.9	1.3	1.0
Wrist Velocity Angle [°]	-25.0	-48.2	15.0	-24.0	-17.2	-20.8
Forearm Velocity [m/s]	1.4	1.1	0.6	1.1	0.9	1.0
Forearm Velocity Angle [°]	1.3	-43.9	82.9	-1.1	35.0	10.2
Wrist Energy [J]	9.9	31.1	14.4	14.4	21.4	9.4
Forearm Energy [J]	23.4	10.7	11.3	20.9	10.2	10.4
Peak Wrist-Forearm Distance Change [mm]	-5.0	-5.2	-6.0	-3.8	-8.8	-6.1

Table L.12: Pre-injury force, moment and impulse data for no load-condition specimens.

Specimen #	1206066	1206067	1207016	1207036	1208016	1207012
Fr - Peak [N]	2007	769	3064	1491	1455	1791
Fr - Impulse Duration [ms]	23	94	16	37	33	33
Fr - Impulse [Ns]	18	22	18	25	20	24
Fr - Load Rate [kN/s]	264	106	730	151	154	192
Fx - Peak [N]	644	236	509	506	498	536
Fx - Impulse Duration [ms]	17	47	10	24	22	27
Fx - Impulse [Ns]	4	4	3	5	5	5
Fx - Load Rate [kN/s]	536	54	284	150	130	65
Fy - Peak [N]	125	126	178	168	131	168
Fy - Impulse Duration [ms]	11	39	11	28	25	23
Fy - Impulse [Ns]	1	1	1	1	1	2
Fy - Load Rate [kN/s]	141	14	107	69	32	17
Fz - Peak [N]	1930	757	3056	1431	1393	1766
Fz - Impulse Duration [ms]	23	94	16	37	33	33
Fz - Impulse [Ns]	17	21	18	24	19	23
Fz - Load Rate [kN/s]	260	131	707	147	147	191
Mx - Peak [Nm]	7	-7	-29	-9	-7	16
My - Peak [Nm]	-51	-26	-62	-50	-49	-29

Table L.13: Pre-injury strain and load-sharing data for no load-condition specimens.

Specimen #	1206066	1206067	1207012	1207016	1207036	1208016
Rad Axial Strain Rate [με/s]	-12153	-274699	-	-22652	-17919	-36159
Rad Axial Strain - Peak [με]	-1445	-1224	-	-936	-699	-2316
Rad Axial Strain @ Fr Peak [με]	0	-1046	-	1	-3	1
Ulna Axial Strain Rate [με/s]	-82629	-320466	-	-1066	-9880	-17224
Ulna Axial Strain - Peak [με]	-3722	-1415	-	-198	-386	-1004
Ulna Axial Strain @ Fr Peak [με]	-7	-829	-	0	-3	5
Rad LS Axial - 100%	29.5	46.8	-	87.6	64.5	69.8
Rad LS Axial - 75%	23.5	42.7	-	84.3	64.4	71.1
Rad LS Axial - 50%	25.3	39.8	-	81.4	64.4	73.0
Rad LS Axial - 25%	65.5	36.9	-	77.7	64.1	77.7
Rad Max Princ Strain Rate [με/s]	-16988	-	-	-	7092	-
Rad Max Princ - Peak [με]	-1077	-	-	-	274	-
Rad Max Princ@ Fr Peak [με]	1	-	-	-	0	-
Ulna Max Princ Strain Rate [με/s]	-14765	-	-	-	8550	-
Ulna Max Princ Strain - Peak [με]	-585	-	-	-	299	-
Ulna Max Princ Strain @ Fr Peak [με]	-1	-	-	-	10	-
Rad LS Max Princ - 100%	73.6	-	-	-	69.1	-
Rad LS Max Princ - 75%	90.3	-	-	-	54.2	-
Rad LS Max Princ - 50%	69.8	-	-	-	49.3	-
Rad LS Max Princ - 25%	54.9	-	-	-	42.7	-
Rad Min Princ Strain Rate [με/s]	-76741	-	-	-	-17961	-
Rad Min Princ - Peak [με]	-3351	-	-	-	-699	-
Rad Min Princ @ Fr Peak [με]	-6	-	-	-	-4	-
Ulna Min Princ Strain Rate [με/s]	-85382	-	-	-	-9151	-

Ulna Min Princ Strain - Peak [με]	-3964	-	-	-	-492	-
Ulna Min Princ Strain @ Fr Peak [με]	-4	-	-	-	-4	-
Rad LS Min Princ - 100%	45.8	-	-	-	64.0	-
Rad LS Min Princ - 75%	44.3	-	-	-	64.1	-
Rad LS Min Princ - 50%	42.1	-	-	-	64.1	-
Rad LS Min Princ - 25%	38.7	-	-	-	63.8	-

L.5: INJURY DATA FOR ALL LOAD-CONDITION SPECIMENS

Table L.14: Injury specimen, velocity and energy data for load-condition specimens.

Specimen #	1206066	1206067	1207012	1207016	1207036	1208016
Pressure [psi]	16	16.1	20.1	20	16	16
Frequency [Hz]	9752	11437	9775	11444	11458	11471
Ballast [% BW]	46.0	43.2	47.0	48.0	47.0	47.4
Wrist Angle [°]	49.1	62.4	60.9	45.9	67.6	60.9
Ram Velocity [m/s]	7.9	6.1	9.1	7.2	6.3	6.1
Plate Velocity [m/s]	3.9	4.0	3.8	3.8	3.7	4.3
Ram Kinetic Energy [J]	209	124	275	172	132	122
Plate Kinetic Energy [J]	36	30	34	35	32	44

Table L.15: Injury force, moment and impulse data for load-condition specimens.

Specimen #	1206066	1206067	1207016	1207036	1208016	1207012
Fr - Peak [N]	5585	6933	7770	5895	6644	14102
Fr - Impulse Duration [ms]	42	42	23	24	48	21
Fr - Impulse [Ns]	50	43	43	42	57	65
Fr - Load Rate [kN/s]	10046	10964	14157	9714	10710	29718
Fx - Peak [N]	2077	-2008	3295	2403	2315	2868
Fx - Impulse Duration [ms]	39	16	21	25	36	30
Fx - Impulse [Ns]	15	8	14	11	12	36
Fx - Load Rate [kN/s]	3585	-2580	5038	3605	3634	2310
Fy - Peak [N]	708	568	1035	792	737	-2036
Fy - Impulse Duration [ms]	40	37	18	24	46	16
Fy - Impulse [Ns]	5	4	3	4	5	10
Fy - Load Rate [kN/s]	992	767	1576	1147	782	-4347
Fz - Peak [N]	5552	6922	7746	5868	6626	13717
Fz - Impulse Duration [ms]	42	42	23	24	48	21
Fz - Impulse [Ns]	46	40	38	39	54	49
Fz - Load Rate [kN/s]	10039	10986	14138	9711	10709	29866
Mx - Peak [Nm]	45	-30	86	43	69	368
My - Peak [Nm]	-175	113	-199	-161	-159	335

Table L.16: Injury strain and load-sharing data for load-condition specimens.

Specimen #	1206066	1206067	1207012	1207016	1207036	1208016
Rad Axial Strain Rate [με/s]	-	-	-	-	-19650	-
Rad Axial Strain - Peak [με]	-	-	-	-	-1895	-
Rad Axial Strain @ Fr Peak [με]	-	-	-	-	12	-
Ulna Axial Strain Rate [με/s]	-	-	-	-	-64682	-
Ulna Axial Strain - Peak [με]	-	-	-	-	-4353	-
Ulna Axial Strain @ Fr Peak [με]	-	-	-	-	-2	-
Rad LS Axial - 100%	-	-	-	-	95.5	-
Rad LS Axial - 75%	-	-	-	-	95.8	-
Rad LS Axial - 50%	-	-	-	-	91.3	-
Rad LS Axial - 25%	-	-	-	-	63.5	-
Rad Max Princ Strain Rate [με/s]	-	-	-	-	5480	-
Rad Max Princ - Peak [με]	-	-	-	-	1495	-
Rad Max Princ@ Fr Peak [με]	-	-	-	-	1	-
Ulna Max Princ Strain Rate [με/s]	-	-	-	-	32068	-
Ulna Max Princ Strain - Peak [με]	-	-	-	-	2058	-
Ulna Max Princ Strain @ Fr Peak [με]	-	-	-	-	0	-
Rad LS Max Princ - 100%	-	-	-	-	94.6	-
Rad LS Max Princ - 75%	-	-	-	-	96.5	-
Rad LS Max Princ - 50%	-	-	-	-	89.6	-
Rad LS Max Princ - 25%	-	-	-	-	57.4	-
Rad Min Princ Strain Rate [με/s]	-	-	-	-	-18751	-
Rad Min Princ - Peak [με]	-	-	-	-	-1948	-
Rad Min Princ @ Fr Peak [με]	-	-	-	-	11	-
Ulna Min Princ Strain Rate [με/s]	-	-	-	-	-67196	-

Ulna Min Princ Strain - Peak [με]	-	-	-	-	-4501	-
Ulna Min Princ Strain @ Fr Peak [με]	-	-	-	-	-2	-
Rad LS Min Princ - 100%	-	-	-	-	95.5	-
Rad LS Min Princ - 75%	-	-	-	-	95.8	-
Rad LS Min Princ - 50%	-	-	-	-	91.2	-
Rad LS Min Princ - 25%	-	-	-	-	93.3	-

L.6: INJURY DATA FOR NO LOAD-CONDITION SPECIMENS

Table L.17: Injury specimen, velocity and energy data for no load-condition specimens.

Specimen #	**1206066**	**1206067**	**1207012**	**1207016**	**1207036**	**1208016**
Pressure [psi]	16	16.1	20.1	16	16	16
Frequency [Hz]	9817	11326	9747	11303	11485	11439
Ballast [% BW]	46.0	43.2	47.0	48.0	47.0	47.9
Wrist Angle [°]	49.1	61.4	62.1	72.3	70.3	65.5
Ram Velocity [m/s]	8.2	5.9	9.3	6.2	6.2	6.1
Plate Velocity [m/s]	4.0	3.9	2.8	3.1	4.1	4.5
Ram Kinetic Energy [J]	223	116	285	130	127	122
Plate Kinetic Energy [J]	37	30	19	23	39	49

Table L.18: Injury force, moment and impulse data for no load-condition specimens.

Specimen #	1206066	1206067	1207016	1207036	1208016	1207012
Fr - Peak [N]	6049	6690	17839	6354	6396	8612
Fr - Impulse Duration [ms]	69	20	25	24	49	12
Fr - Impulse [Ns]	64	25	103	39	52	62
Fr - Load Rate [kN/s]	10951	10312	31242	10733	10483	3366
Fx - Peak [N]	2045	-2169	4586	1904	1956	2778
Fx - Impulse Duration [ms]	34	16	23	21	38	11
Fx - Impulse [Ns]	13	9	22	10	11	10
Fx - Load Rate [kN/s]	3839	-2659	3988	3200	3007	4471
Fy - Peak [N]	844	743	2009	841	787	999
Fy - Impulse Duration [ms]	20	18	18	24	44	11
Fy - Impulse [Ns]	3	3	11	4	4	3
Fy - Load Rate [kN/s]	1184	1035	3664	1168	1005	1085
Fz - Peak [N]	6018	6682	17318	6342	6378	8576
Fz - Impulse Duration [ms]	69	20	25	24	49	12
Fz - Impulse [Ns]	60	22	98	35	49	60
Fz - Load Rate [kN/s]	10932	10338	31836	10742	10480	3122
Mx - Peak [Nm]	-49	-44	-30	-57	49	-41
My - Peak [Nm]	-198	131	111	-154	-148	183

Table L.19: Injury strain and load-sharing data for no load-condition specimens.

Specimen #	1206066	1206067	1207012	1207016	1207036	1208016
Rad Axial Strain Rate [με/s]	-	-	-	-	-15375	-
Rad Axial Strain - Peak [με]	-	-	-	-	-848	-
Rad Axial Strain @ Fr Peak [με]	-	-	-	-	2	-
Ulna Axial Strain Rate [με/s]	-	-	-	-	-81910	-
Ulna Axial Strain - Peak [με]	-	-	-	-	-4842	-
Ulna Axial Strain @ Fr Peak [με]	-	-	-	-	2	-
Rad LS Axial - 100%	-	-	-	-	15.4	-
Rad LS Axial - 75%	-	-	-	-	19.7	-
Rad LS Axial - 50%	-	-	-	-	22.9	-
Rad LS Axial - 25%	-	-	-	-	26.7	-
Rad Max Princ Strain Rate [με/s]	-	-	-	-	2078	-
Rad Max Princ - Peak [με]	-	-	-	-	209	-
Rad Max Princ@ Fr Peak [με]	-	-	-	-	-7	-
Ulna Max Princ Strain Rate [με/s]	-	-	-	-	-7245	-
Ulna Max Princ Strain - Peak [με]	-	-	-	-	-1577	-
Ulna Max Princ Strain @ Fr Peak [με]	-	-	-	-	1	-
Rad LS Max Princ - 100%	-	-	-	-	36.6	-
Rad LS Max Princ - 75%	-	-	-	-	48.8	-
Rad LS Max Princ - 50%	-	-	-	-	14.6	-
Rad LS Max Princ - 25%	-	-	-	-	10.7	-
Rad Min Princ Strain Rate [με/s]	-	-	-	-	-18134	-
Rad Min Princ - Peak [με]	-	-	-	-	-1028	-
Rad Min Princ @ Fr Peak [με]	-	-	-	-	-5	-
Ulna Min Princ Strain Rate [με/s]	-	-	-	-	-86726	-

Ulna Min Princ Strain - Peak [με]	-	-	-	-	-4541	-
Ulna Min Princ Strain @ Fr Peak [με]	-	-	-	-	-6	-
Rad LS Min Princ - 100%	-	-	-	-	18.8	-
Rad LS Min Princ - 75%	-	-	-	-	23.8	-
Rad LS Min Princ - 50%	-	-	-	-	29.9	-
Rad LS Min Princ - 25%	-	-	-	-	56.1	-

L.7: STATIC MUSCLE PRELOAD DATA

Table L.20: Pre-injury and injury static muscle preload force data.

	Pre-injury				Injury			
Specimen	**ECU**	**ECRL**	**FCU**	**FCR**	**ECU**	**ECRL**	**FCU**	**FCR**
1206066L	28.6	64.8	16.1	11.7	27.2	62.8	15.3	12.0
	28.1	63.9	16.4	12.2	27.5	63.1	14.7	12.8
	27.5	63.7	14.7	10.3	27.2	62.8	14.2	10.3
1206067L	20.0	38.4	15.8	14.2	18.3	40.6	13.9	15.0
	19.5	37.0	13.1	13.9	17.5	40.3	13.1	15.6
	21.4	35.0	10.3	12.8	15.6	35.9	11.4	13.9
1207016L	27.0	65.1	14.2	11.4	30.0	64.2	14.7	11.4
	29.5	63.9	14.7	15.0	27.5	63.4	15.3	11.4
	28.1	65.3	11.4	10.8	29.5	63.9	14.7	11.1
1207036L	28.6	63.9	14.2	13.1	27.5	64.5	15.0	11.4
	27.5	63.7	15.8	11.1	28.6	62.8	16.1	11.4
	28.1	64.8	17.5	11.7	27.5	62.3	15.6	12.8
1208016L	28.9	65.1	15.0	12.2	28.4	63.9	15.3	11.7
	28.9	63.4	17.0	12.2	28.4	62.6	14.7	12.0
	29.7	65.6	16.4	10.3	29.7	63.1	15.6	12.2
1207012L	28.6	64.5	11.7	11.1	27.0	64.2	14.2	11.7
	28.4	63.9	15.6	10.6	27.5	63.9	14.7	12.8
	29.2	63.9	13.9	10.6	26.7	64.8	16.1	9.7
Mean	27.1	59.8	14.7	12.0	26.2	59.4	14.7	12.2
SD	3.2	10.6	2.0	1.4	4.3	9.5	1.1	1.5

VITAE

NAME	Jacob Mackenzie Reeves
PLACE OF BIRTH	London, Ontario
YEAR OF BIRTH	1990
POST SECONDARY	
EDUCATION AND DEGREES	The University of Western Ontario London, Ontario, Canada 2008 – 2012, BESc
HONOURS AND AWARDS	Ontario Graduate Scholarship 2012 John E. K. Foreman Gold Medal Award (Graduating with highest aggregate average in mechanical engineering) The Canadian Society for Mechanical Engineering Award (Demonstrating excellence in mechanical engineering) NSERC USRA 2011 Walker-wood Continuing Scholarship in Engineering 2008, 2009, 2010, 2011 UWO Continuing Entrance Scholarship 2008, 2009, 2010, 2011 Dean's Honours List 2008, 2009, 2010, 2011 UWO Faculty Association Scholarship 2009
TEACHING EXPERIENCE	**Teaching Assistant** Business 2299E: Business for Engineers Ivey Business School *Western University Canada* 2012 - 2013

CONFERENCES ATTENDED

The Ontario Biomechanics Conference
Barrie, Canada
March 2013

The Canadian Orthopedic Research Society
Ottawa, Canada
June 2012

PUBLICATIONS

Peer-reviewed Journal Articles:

1. Leitch K.M., Birmingham, T.R., **Reeves, J.M.**, Giffin, J.R., Dunning, C.E. (2011) Development of a multi-axis fixture to assess HTO plate design, Journal of Biomechanics. *(in preparation)*

Abstracts and Presentations at Peer-reviewed Professional Meetings:

2. Leitch KL, Birmingham TB, **Reeves J**, Giffin JR, Dunning CE: Development of a Materials-testing Fixture to Enable Asymmetric Loading of the Lower Limb: An application of in-vivo gait data, OARSI, Barcelona, Spain, April 26-29, 2012. *(poster)*
3. Leitch KL, Birmingham TB, **Reeves J**, Giffin JR, Dunning CE: Development of a Materials-testing Fixture to Enable Asymmetric Loading of the Lower Limb: An application of in-vivo gait data, Annual Meeting of the Canadian Orthopaedic Research Society, Ottawa, ON, June 8-10, 2012. *(podium)*

Other Abstracts and Presentations:

4. **Reeves JM**, Burkhart TA, McLachlin SM, Dunning CE: A Colour-Thresholding Technique to Quantify High-Speed Planar Motion of Isolated Distal Radii Specimens During Impact, Ontario Biomechanics Conference, Barrie, Ontario, March 15-17, 2013. (*podium*)
5. Leitch KL, Birmingham TB, **Reeves J**, Giffin JR, Dunning CE: Development of a Materials-testing Fixture to Enable Asymmetric Loading of the Lower Limb: An application of in-vivo gait data, Ontario Biomechanics Conference, Barrie, Ontario, March 16-18, 2012. *(poster)*